University of Canterbury

Ph.D Thesis

Two–Colour Excitation of Impurity Trapped Excitons in Wide Bandgap Insulators

Author:
Pubudu S Senanayake

Supervisor:
Assoc. Prof. Jon-Paul Wells

Co–supervisor:
Assoc. Prof. Mike Reid

Submitted in Partial Fulfillment of the Requirements for the Degree
Doctor of Philosophy in Physics

October 31, 2013

Abstract

Impurity trapped excitons (ITEs) occurring in divalent ytterbium doped calcium and strontium fluoride crystals have been investigated by exploiting the radically different radiative decay rates of the lowest exciton state and higher excited states, utilizing a novel two–colour transient photoluminescence enhancement experiment. The ITE energy levels have been directly measured with the observation of sharp transitions occurring from the changes of states of the localized hole and broad bands associated with changes of state of the delocalized electrons. The dynamic behaviour under excitation by time delayed ultra–violet (UV) and infrared (IR) pulses has been observed allowing for the identification of excitation and decay pathways between the ITE states.

The position and transition intensities of the sharp lines within the IR excitation spectrum have been successfully matched using a semi–empirical effective Hamiltonian crystal field model. In CaF_2:Yb^{2+} the lines occurring at 249 and 1145 cm^{-1} were matched with the crystal field parameter $B_4 = 800$ cm^{-1} and the exchange parameter $G^3(fs) = 5900$ cm^{-1}. In SrF_2:Yb^{2+} these lines were observed at 178 and 1284 cm^{-1} and matched with $B_4 = 600$ cm^{-1} and $G^3(fs) = 7278$ cm^{-1}. Local heating and direct absorption by intra–excitonic transitions are found to be the causes of the broad band observed in the spectrum and have been deconvolved by studying the dynamic behaviour of the monitored emission at different IR excitation frequencies. Through this modeling, higher lying ITE states have been identified occurring at 785 cm^{-1} in SrF_2:Yb^{2+} and in between 740 - 820 cm^{-1} in CaF_2:Yb^{2+}.

The dynamic model developed successfully simulates the temporal behaviour of the emission under IR excitation under a variety of parameters including IR fluence, excitation frequency, sample temperature and UV – IR pulse delay. Examination of the SrF_2:Yb^{2+} dynamic behaviour over a time scale of 100 ms shows UV driven trap population at a rate of approximately 3% per pulse, which are liberated and recycled to the Yb^{2+} ground state by the IR pulse.

The two–colour technique is applied to MgF_2:Yb^{2+}, a candidate for possible ITE emission. Temperature dependent emission spectra obtained under UV excitation indicates the possibility of an ITE state, independently populated from the $5d$ level of the Yb^{2+}. Typical $5d$ emission is also observed from this system. Under IR excitation, liberation of shallow traps and possible local heating is observed. No ITE emission is conclusively found with IR probing.

Acknowledgments

I would like to thank my supervisors Assoc. Prof. Jon-Paul Wells and Assoc. Prof. Mike Reid for their patience and support throughout the entire process of completing this thesis. Jon in particular was instrumental in keeping me focused on the task at hand, and stopping me from getting bogged down in often irrelevant detail. Mike was available for countless discussions that were instrumental to the success of the work in this thesis as well my general understanding of the topic.

Dr. Giel Berden at FELIX was of immense help in running all of the two–colour experiments and discussions with him led to much improvement in the technique utilized in this study, especially in the data recording. Thank you for staying for many hours beyond the scheduled shut down time helping us gather more data than would have been otherwise possible. Thanks are also extended to the Dutch FOM organization for providing FELIX beamtime and the FELIX staff for their assistance.

Prof. Roger Reeves provided valuable insight into the physics by asking tough questions during the many discussions, and it is much appreciated. Wayne Smith kept the RF furnace running with timely repairs and was of much help when any maintenance issue of equipment cropped up.

Dr. Andries Meijerink kindly provided the MgF_2:Yb^{2+} samples used in this study.

The support of the Department of Physics and Astronomy at the University of Canterbury through the provision of a studentship and teaching opportunities are acknowledged.

I would also like to thank my colleagues, Nishanthan Rabeendran, Sebastian Horvath, Rosa Hughes-Currie and Alex Salkeld for valuable discussion and general merriment, making the duration of my work at UoC truly memorable. Alex contributed his rendering expertise to make the lattice diagrams of the materials particularly striking. Thanks go to Sebastian for proof reading sections of this work.

Hanna Gunn set up a writing group and made sure that I stuck to my writing tasks, and proof read over a 100 pages of this thesis. Your support and your cooking is greatly appreciated.

To my brother, thanks for the music and feeding me throughout the last few months. Your support and belief was a key in making this happen. To the rest of my family, for their unwavering support and encouragement, there is no amount of thanks that is sufficient. To my father, explaining how day and night worked with a model and causing the start of this entire journey.

And last but certainly not least, to Dana for being the best possible distraction and stress relief in the last few months, especially during the write up. Thank you for being there at the most ridiculous of hours in the night and for the many talks till day break. Without you my sanity would have likely escaped long ago. Hopefully I can make it up in some small part in the coming months and sorry about the wait!

Contents

Figures

Tables

Chapter 1

Introduction

Rare-earth doped materials have found extensive use in a variety of applications ranging from fluorescent lighting and lasers to medical imaging due to their optical characteristics, high quantum efficiencies and durability [1]. Furthermore rare-earth doped bulk crystals allow complex ions to be placed in a variety of symmetry structures, depending on their host crystal. This allows the exploration of fundamental quantum mechanics of relatively complex systems with even simple spectroscopic experiments. With the parameter space explored, it is possible to build detailed models [2] which would be impossible to formulate or test without the data from experiment. The coupling of wide application in technology with the ability to explore fundamental science provides ample motivation to study these materials in as much detail as possible.

Accurate models already exist for the behavior of sharp optical transitions of the $4f$ configurations in rare-earth ions [1, 3]. However the transitions involving excited configurations such as $4f^n \rightarrow 4f^{n-1}5d^1$ are less well modeled due to the vibronic broadening of the spectra, leading to less information than the sharp lines observed in $4f$ spectra [4–6]. Probing the excited configurations via a two color excitation experiment would yield more information about these configurations [5]. This would be done by initially setting up an excited state population with a suitably absorbing excitation frequency (in this study ultra–violet radiation, or UV), then probing the states accessible to the excited population with a lower frequency (infra–red, or IR). Essentially one would be obtaining excitation spectra of the excited configuration.

There are already ab-initio methods for calculating excited state structures and bond length changes, giving good agreement with the broad spectra [2, 7]. These calculations suggest that there would be sharp line as well the broad vibronic transitions within the excited states. Experiments such as those proposed above would also allow for the testing and refinement of these models, as well as extension into other symmetry structures.

In addition to the $4f^{n-1}5d$ configuration, excited configurations can also occur with charge transfer from the rare-earth to the next nearest cations in the crystal. This leads to delocalized electrons, causing excitons to form, where the electron is bound to the $4f$ hole. Such excitons are termed impurity trapped excitons (ITEs) since they are unable to move from their local rare-earth site. ITEs can act as mediators for non radiative relaxation of the $4f^{n-1}5d$ excited configuration [2, 8]. ITEs exhibit broad emission meaning that little information can be gained from it directly and the energy structure properties have to be deduced via secondary methods such as temperature dependence and photoconductivity [9, 10]. However with a two color excitation experiment, it would be possible to probe the internal structure of ITEs directly.

Since ITEs play an important role in the optical pumping cycle it is crucial to extract dynamic information about them as well as gain an understanding of their energy level structure. This can be done through a *pulsed* two–colour excitation experiment, coupled with sufficiently fast detection to allow for ample time resolution.

In this study we directly probe the known ITEs occurring in CaF_2:Yb^{2+} and SrF_2:Yb^{2+} [9, 11, 12] with the two colour transient photoluminescence enhancement technique we have developed. In doing so crystal field parameters and Coulomb exchange parameters are extracted for intra-excitonic transitions through infra–red (IR) excitation spectra of the ITE. The dynamic behaviour of the ITE emission is observed when the system is perturbed by an IR pulse, and is comprehensively explained by invoking intra-excitonic transitions, IR induced local heating and trap liberation. MgF_2:Yb^{2+}, where it is not clear whether the system exhibits ITE behaviour or not, is explored using the same technique. The possibility of the occurrence of ITE emission is identified and IR induced trap liberation leading to enhancement of the emission is observed.

In addition to the specific application to the above materials, this study also serves as a demonstration for the versatility of this technique in probing the structure of energy states, where different emittive relaxation rates may occur. Furthermore the parameters extracted through this study can serve as a catalyst for advanced *ab-initio* calculations on both CaF_2:Yb^{2+} and SrF_2:Yb^{2+} systems similar to recent calculations for $SrCl_2$:Yb^{2+} [2, 7].

1.1 The crystal structure and physical properties of CaF_2

Calcium fluoride is a crystal with a molecular weight of 78.07 atomic units and a melting temperature of 1415 °C [13]. It has a face centered cubic structure with a lattice constant of 5.46 Å[14] and a ratio of 1:2 calcium to fluorine atoms, where the calcium occupies the center of an eight ion fluorine cage, with every other cage being empty. The divalent calcium ion has an ionic radius of 0.94 Å [15]. Figure 1.1 shows the arrangement and structure of the CaF_2 lattice.

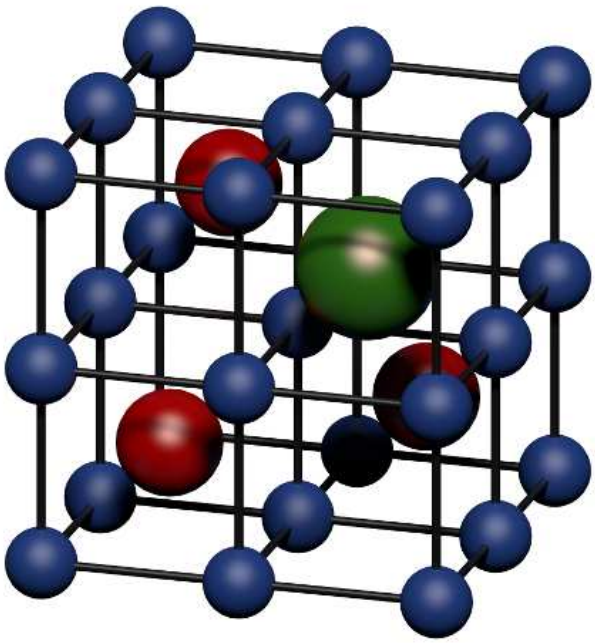

Figure 1.1 Structure of the CaF_2 and SrF_2 lattice showing the locations of the fluorine (in blue) cages and the calcium/strontium ions (in red). The calcium occupies the center of every other fluorine cage, giving an overall FCC structure. The positively charged ytterbium (Yb^{2+}) shown in green will occupy the Ca^{2+} (or Sr^{2+}) site. The black links between the fluorine ions are to indicate the cage structure and do not represent physical bonds.

CaF_2 has a conduction band made up of Ca^{2+} orbitals and a valence band of F^- orbitals. The resulting band gap has been reported as 11.6 [16] and 12.1 [17] eV (93600 and 97600 cm^{-1}), allowing for the transmission of a wide range of wavelengths from vacuum ultra violet (around 130 nm) to mid infra red (around 10 μm) [18]. The absorption of photons beyond 10 μm (1000 cm^{-1}) increases rapidly with wavelength due to the presence of phonons, with the absorption peaking at around 37 μm (270 cm^{-1}) [19].

At low temperatures CaF_2 displays very low heat capacity that is heavily dependent upon

the lattice temperature [20]. It also displays a heavily temperature dependent thermal conductivity [21, 22] which is influenced by the presence of impurities within the lattice [23].

Divalent impurities occupying the Ca^{2+} sites will experience cubic symmetry [24, 25], requiring two crystal–field parameters B^4 and B^6 [26] to parameterize the influence of the crystal. Trivalent impurities typically require charge compensation to occur in order to maintain crystal neutrality, breaking cubic symmetry. For example a F^- ion may occupy the interstitial site, leading to C_{4v} site symmetry at the trivalent impurity.

1.2 The crystal structure and physical properties of SrF_2

Strontium fluoride is a crystal with a has a molecular weight of 125.62 atomic units and a melting temperature of 1477°C [13], the highest of the materials grown at the University of Canterbury for this study. It has the same cubic structure as CaF_2 with a larger lattice, giving rise to a lattice constant of 5.79Å [27]. It has a ratio of 1:2 strontium to fluoride ions, and the strontium occupies the center of a fluoride cage, with every other cage being empty. The divalent strontium has an ionic radius of 1.10Å [15] and the Sr^{2+} — F^- bond length is 2.51Å [28]. The structure of SrF_2 is represented in figure 1.1.

SrF_2 has a band gap of 9.4 eV (75820 cm^{-1}) with a conduction band and the valence band made up of Sr^{2+} and F^- orbitals respectively. It transmits a wide range of wavelengths from vacuum ultra violet (around 150 nm) to mid infra red (around 10 μm) [29]. The absorption of photons beyond 10 μm (1000 cm^{-1}) increases rapidly with wavelength due to the presence of phonons, with the absorption peaking at around 45 μm (220 cm^{-1}) [19].

At low temperatures SrF_2 also displays very low heat capacity that is heavily dependent upon the lattice temperature [20], however, it has much greater heat capacity when compared to CaF_2 at a given temperature. It also displays heavily temperature dependent thermal conductivity properties [21, 22] which is also influenced by the presence of impurities within the lattice [30].

Similar to CaF_2 divalent impurities occupying the Sr^{2+} sites will experience cubic symmetry [24, 25], however the crystal field parameters will be smaller in comparison to CaF_2 due to the increased lattice size of SrF_2 [25].

1.3 The crystal structure and physical properties of MgF_2

Magnesium fluoride is a crystal with a molecular weight of 62.3 atomic units and a melting temperature of 1263 °C [13]. It has a rutile structure with lattice constants of $a = 4.62$ and $c = 3.02$ Å [31]. The unit cell of MgF_2 is tetragonal with the Mg^{2+} ion surrounded by six F^- ions occupying the tops of distorted octahedra of D_{2h} site symmetry [32]. The divalent magnesium ion has an ionic radius of 0.65 Å [33] and the Mg—F bond length is 1.98 Å [34]. The structure of MgF_2 with a divalent dopant present, is shown in figure 1.2.

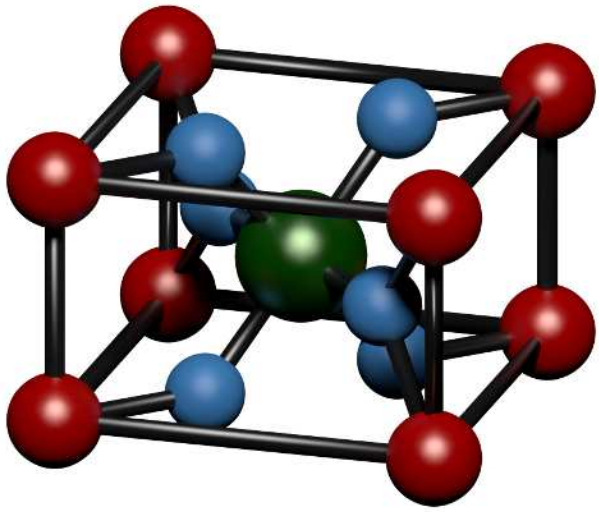

Figure 1.2 Structure of the rutile MgF_2 lattice showing the locations of the fluorine (in blue) and the magnesium ions (in red). The magnesium occupies the center of six fluoride ions arranged in a distorted octahedra. The positively charged ytterbium (Yb^{2+}) shown in green will occupy the Mg^{2+} site.

MgF_2 has the largest band gap of the hosts studied at 12.5 eV (100820 cm^{-1}) with a conduction band of Mg^{2+} orbitals and the valence band of F^- orbitals [35] and transmits a wide range of wavelengths from vacuum ultra violet (around 120 nm) to mid infra red (around 8 μm) [36]. The transmission of IR photons beyond 9 μm (1100 cm^{-1}) decreases rapidly with the minima occurring at around 21 μm (480 cm^{-1}) [37]. Associated with this an increase in the reflectance is observed, thus it is not clear whether MgF_2 absorbs heavily in this spectral region, or simply reflects a large fraction of the incident photons [37].

1.4 The rare–earth dopant

The rare–earth series is characterized by progressive filling of the $4f$ shell. In this study all the crystals are doped with ytterbium (Yb), in its divalent ionized state (Yb^{2+}). Yb is a lanthanide with a mass of 173 atomic units and has a nucleus comprising of 70 protons and a completely filled $4f$ shell of 14 electrons. Its electrons are configured as [Xe] $4f^{14}6s^2$ and it is these $6s$ electrons that it loses to form a divalent ion in our studies. However, the seed material used to provide the Yb is ytterbium tri-fluoride with a melting temperature of 1052°C [13]. The divalency is achieved through a reducing growth environment.

1.5 Outline of the thesis

The objectives of this study were to:

- Probe the energy structure of the ITE occurring within the CaF_2:Yb^{2+} system using the developed two colour technique. From the resultant IR excitation spectrum extract the crystal field and exchange parameters to fit an empirical effective Hamiltonian "crystal field" model to the transition frequencies. Use the model to compute transition intensities.
- Develop a dynamic model capable of explaining the observed temporal behaviour with varying IR excitation frequencies, powers and lattice temperatures in a consistent manner. One of the chief goals in this aspect was to minimize the number of free parameters and incorporate previously known dynamic rates and energy parameters.
- Probe the ITE occurring within SrF_2:Yb^{2+} with the same experimental technique in order to better understand its energy structure, but also to test the models that were developed to explain both the spectral and temporal behaviour of the ITE when excited by IR radiation.
- Explore the possibility of ITE emission occurring in MgF_2:Yb^{2+} and attempt to establish whether the IR radiation liberates traps that can contribute to the emission observed from MgF_2:Yb^{2+}.

Chapter 2 gives a brief outline of $4f \rightarrow 5d$ transitions in lanthanides, with a particular attention given to ytterbium. It then provides the historical context of the observation

of the ITEs as well as the theoretical interpretations presented to explain the observed behaviour, and presents the currently accepted model. Additionally the effective crystal field Hamiltonian that is employed in the empirical model explaining sharp lines in the IR excitation spectra is introduced. Finally the computation derived by Henderson and Imbusch [26] to determine bond length changes and ZPL locations using the bandwidth of an emission spectrum is outlined.

Chapter 3 introduces the growth and preparation process for the samples employed in this study. It then introduces the experimental technique that was employed in probing the ITEs as well as the MgF_2:Yb^{2+} emission. The equipment used is introduced, with particular attention given to FELIX, the Dutch Free Electron Laser, and the considerations when using it as an IR source.

Chapter 4 explains the details of the experiment as it applies to the CaF_2:Yb^{2+} case and presents the spectral and temporal details of the observations recorded. The empirical model is successfully employed to account for the observed sharp lines in the IR excitation spectrum. The dynamic model is developed with allowances made for local heating due to IR absorption into the lattice and the model is used to account for a range of dynamic behaviour successfully.

Chapter 5 explains the details of the experiments as it applies to SrF_2:Yb^{2+}. The models developed previously to account for spectral and temporal behaviour are employed without needing modification (the crystal field parameters are changed to reflect the different lattices in the spectral model). Direct observation of electron trapping caused by UV excitation and the subsequent liberation of these by the IR is also presented in this chapter.

Chapter 6 extends the study to MgF_2:Yb^{2+}. Here the possibility that emission is observed from an ITE state is presented. Under IR excitation it is found that there is no pronounced ITE behaviour (unlike the previous two cases), and trap liberation is observed throughout the excitation spectrum. The behaviour of the trap liberation is explored and it is found that they are likely extremely shallow traps.

Finally, chapter 7 summarizes the work and discusses the conclusions that can be drawn from this study.

Chapter 2

Theory and background

In this chapter we introduce general observations of $4f^n$ to $4f^{n-1}5d$ transitions in divalent lanthanides and introduce anomalous emission that has been seen in some cases of excitation of the $4f^n \rightarrow 4f^{n-1}5d^1$ transition. A brief history of the attempts at explaining this emission is provided along with the currently accepted model of the impurity trapped exciton which provides an explanation to the aforementioned emission. The theoretical framework for this model is briefly discussed.

The effective Hamiltonian method is introduced and a crystal field Hamiltonian is constructed in order to model the sharp lines in the excited state absorption (or secondary IR excitation) spectra of the ITEs. Additional equations based on the relationship between the Huang–Rhys parameters, emission bandwidth and configurational coordinate offsets are introduced to allow for the calculation of bond length changes and zero phonon lines (ZPLs) from observed emission spectra.

2.1 $4f$ to $5d$ transitions in divalent rare–earths

General surveys of $4f^n \rightarrow 4f^{n-1}5d^1$ transitions in divalent lanthanides were carried out in early works by authors such as McClure [38] and Loh [39] and extensive reviews were conducted by Rubio [24] or systematically analysed for trends by Dorenbos [40]. A vast collection of information is available on these transitions and here we provide brief outlines of the $4f^n \rightarrow 4f^{n-1}5d^1$ absorption and $4f^{n-1}5d^1 \rightarrow 4f^n$ emission as well as some properties relating to the divalent lanthanide of interest in this study (Yb^{2+}).

In the lanthanides the $4f$ shell is contracted inside the closed $5s$ and $5p$ shells [41] and is therefore shielded from the surrounding crystal environment, leading to only weak interactions with the lattice. Because of this, the transitions do not show extensive deviation from the free–ion values and absorption spectra consist of a superposition of sharp lines

resulting from discrete centres with a given point group symmetry [26]. However, the $5d$ levels are not contracted and they extend much further and therefore are heavily influenced by their surroundings, leading to strong interactions with the lattice [40].

Due to the lack of shielding, transitions between the $4f^n$ and $4f^{n-1}5d$ configurations can have drastically different peak frequencies depending upon the surrounding lattice. As an example consider Sm^{2+} which has the lowest $5d$ absorption frequencies varying from 9520 cm^{-1} in MgS to 21700 cm^{-1} in $NaMgF_3$ [40]. Similarly for emission it has frequencies ranging from 6200 cm^{-1} in SrS to 14400 cm^{-1} in $SrCl_2$ [40]. Additionally the transitions are vibronically broadened and the spectral peak variation coupled with the broadening of the lines make it difficult to interpret the observed spectra, thus leading to difficulties in assigning parameters of the extended effective Hamiltonian model [4]. Because of these reasons the experimental technique explored in this thesis (which has only been used in probing ITEs so far) may prove quite useful [5].

2.1.1 Transitions between $4f^n$ and $4f^{n-1}5d$ in Yb^{2+}

The 13 electrons in the $4f$ shell in the $4f^{n-1}5d$ configuration can be thought of as a single hole in the $4f$ shell. The exchange interaction between the hole and the $5d$ electron leads to a splitting of the $5d$ level into high spin (HS) and low spin (LS) states. The HS state has the lowest energy, while the LS state is typically located about 2000 cm^{-1} above that [40].

Depending upon the spin of the two states involved, the transition will be either spin allowed (SA) or spin forbidden (SF). For example a HS to LS transition is SF. As the $4f$ occupancy increases in the series beyond Eu^{2+}, the $4f$ level has a lower spin in comparison to the HS state, and in Yb^{2+} the $4f$ ground state is a LS state. Therefore the transition from the lower $5d$ state (HS) to the $4f$ ground state (LS) is spin–forbidden (SF). Figure 2.1 illustrates the SA and SF transitions between $4f$ and $5d$ states in Yb^{2+}. The solid arrows indicate transitions that are more likely to occur in comparison to the transitions represented by the dashed arrows. Since absorption predominantly occurs into the SA state, and emission typically occurs from the lowest state (SF for the Yb^{2+}) a Stokes shift approximately equal to the splitting is introduced into the spectrum.

Examining the absorption spectra of Yb^{2+} in several hosts show the large spread in peak positions. For example in $NaMgF_3$ the SA absorption occurs at a frequency of 32800 cm^{-1} [42], where as in $Y_3Al_5O_{12}$ the corresponding frequency is only 15300 cm^{-1} [43].

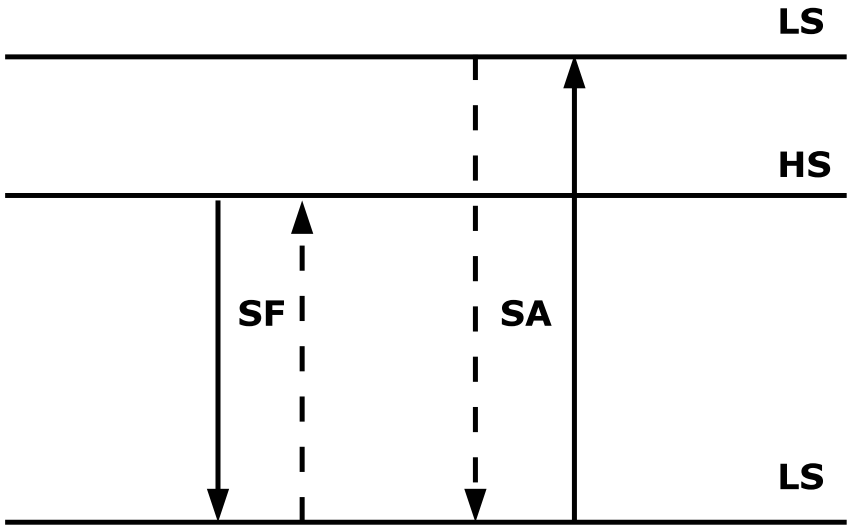

Figure 2.1 The $5d$ of levels are split into the high and low spin states due to the exchange interaction between the $4f$ hole and $5d$ electron. The arrows show the spin allowed/forbidden (SA/SF) absorption and emission from the split states to the $4f$ ground state. A dashed arrow indicates the low probability transition. The solid arrow indicates the high probability transition. In this instance the splitting of 2000 cm^{-1} in Yb^{2+} is shown.

The SF absorption spectra are observed in fewer cases due to the difficulty in detecting the much smaller absorption peak. In $NaMgF_3$ the peak occurs at 30600 cm^{-1} (2000 cm^{-1} difference with the SA peak) showing an exchange splitting. The lowest energy observed for SF absorption is at 23600 cm^{-1} for a NaCl host [44].

Considering $4f^{13}5d^1 \rightarrow 4f^{14}$ emission, there are only a few cases of SA emission occurring, namely Yb^{2+} doped $SrCl_2$, KCl, NaCl, KBr and KI [40]. However, in comparison the SF transition is observed in more hosts. The SA allowed state relaxes non–radiatively to the SF state in the $4f^n \rightarrow 4f^{n-1}5d^1$ configuration at a faster rate than the SA transition to the $4f$ ground state. When considering the peaks (of both SA and SF emission) a multitude of the hosts display emission as expected in relation to their absorption when the Stokes shift is accounted for (see table 3 and figure 6 in reference [40]).

2.2 Impurity Trapped Excitons

In addition to the $4f^{n-1}5d^1 \rightarrow 4f^n$ emission observed from the divalent lanthanide ions discussed above, emission that is heavily red shifted from the expected frequency position (beyond what the Stokes shift observed in $4f^{n-1}5d^1 \rightarrow 4f^n$ transitions can account for) was initially observed for CaF_2:Yb^{2+} and BaF_2:Eu^{2+} [45]. The observed emission,

rather than being an inverse of the absorption processes to the lowest states of the divalent lanthanide, was red shifted by 9700 and 7900 cm^{-1} in CaF_2:Yb^{2+} and BaF_2:Eu^{2+} respectively. In the case of BaF_2:Eu^{2+} emission was also observed from the $5d$ states, thus the red shift was directly measured. In the case of the CaF_2:Yb^{2+} $5d$ emission was not observed. Emission that was even further red shifted in comparison was reported in SrF_2:Yb^{2+} [46] and like the CaF_2:Yb^{2+} case, $5d$ emission was not observed from this system.

This emission, termed 'anomalous' (due to the displacement from the expected frequency), was initially suggested by Kaplyanskii and Feofilov to involve the $6s$ states (of the divalent lanthanide centre) [45]. Upon further consideration of the CaF_2:Yb^{2+} emission, it was conjectured to be due to a complex centre containing a Yb^{2+} ion by Witzke [24] while Reut ascribed the observations to a charge transfer effect [47].

Kaplyanskii et al. carried out more detailed experimental work on the CaF_2:Yb^{2+} system and examining the excitation spectra and fluorescence decay properties they concluded that the above explanations were incorrect and ascribed the observations to a Jahn-Teller effect [48, 49]. They were also able to construct a phenomenological scheme, where the anomalous centre was purported to have two emitting states separated by 30 cm^{-1}. This is remarkably close to the current two emitting state model of the ITE, where in CaF_2:Yb^{2+} it has a separation of 40 cm^{-1} [9] between the levels. Reut applied the same model to SrF_2:Yb^{2+} data, where emission peaks were observed at 12670 cm^{-1} at 4.2 K and 13700 at 77 K, and concluded that the energy gap between the two emitting states was 27 cm^{-1}.

Photoconductivity studies conducted on other divalent lanthanides in CaF_2, SrF_2 and BaF_2 allowed for an estimation of the location of the impurity states with respect to the conduction band of the host crystal [50, 51]. Using this technique McClure and Pedrini were able to show that the anomalous emission was present when the $5d$ states of the divalent lanthanide were close to or in the conduction band of the host crystal [52]. In the case of SrF_2:Yb^{2+} it was shown that excitation of the $4f^{14} \rightarrow 4f^{n-1}5d^1$ transitions led to the autoionization of the excited electron [52]. This leads to delocalization of the electron over the next nearest neighbour cations, and a trapped exciton like formation occurs about the now trivalent lanthanide centre [11].

Further measurements made by Moine et al. on CaF_2:Yb^{2+}, SrF_2:Yb^{2+}, and BaF_2:Eu^{2+} have confirmed the above model [9, 12, 53]. Figure 2.2 provides a schematic representation of the currently accepted model of the impurity trapped exciton (ITE) formation and energy level structure of the emitting states.

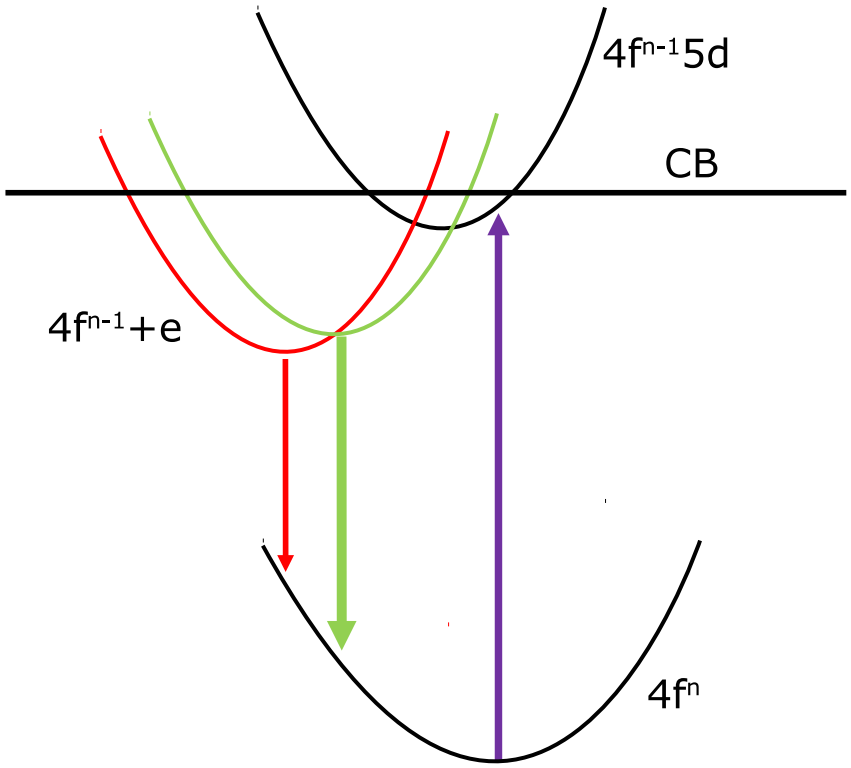

Figure 2.2 Schematic of impurity trapped exciton and its formation. Figure is adapted from [9] and the model as developed by McClure and Pedrini [52]. The $4f^{n-1} + e$ indicates the ITE, with the occupancy rare earth $4f$ level reduced by one as the electron is delocalized over the next nearest neighbours. The red and green indicates the two different emitting states of the ITE, with the colours signifying the difference in spectral peak position from the two states. The horizontal axis is in reduced configurational coordinates, although the diagram is not to scale.

Notice that this schematic diagram is only concerned with the structure of the ITE. Typical $5d$ emission which can also occur in cases where the $5d$ state is close to but not in the conduction band itself, and only a fraction of the excited electrons are autoionized [53, 54]. The reason that some lanthanide/host combinations, especially Yb^{2+} doped SrF_2 and BaF_2, do not exhibit any $5d$ emission is that the $5d$ states appear to lie entirely within the conduction band, meaning that the excitation of the $4f^{14} \rightarrow 4f^{13}5d^1$ transition causes the ionization of most of the electrons, which then decay to the ITE state via the conduction band [9, 12]. CaF_2:Yb^{2+} has $5d$ states that lie below the conduction band, however it does not exhibit any $5d$ emission [9].

Since there is a change in the valency of the lanthanide centre the fluoride cage undergoes a contraction, as it experiences a greater attractive force due to the extra positive charge now present at the centre of the cage. However, this configurational change does not manifest

itself in the absorption spectra, since the excitation is not directly into the ITE states. As the ITE recombines with the trivalent lanthanide, reducing it to its divalent $4f^n$ ground state, the fluorine cage expands to its original volume as the force collapsing it vanishes. This change in bond length causes vibronic broadening in the emission spectrum of the ITE as the lattice settles into its original configuration. ITE emission appears broad and featureless because of this configurational change. Additionally, as the delocalized electron influences bonding, changes within its state can also lead to configurational changes of the system. In such instances the emission peak position and width are seen to shift significantly, and the emission is still vibronically broadened as the lattice settles [9].

Subsequent to the above studies, further occurrences of anomalous emission likely resulting from ITE behaviour have been documented [42, 55–58]. Dorenbos, in his 2003 paper [11], provides a comprehensive list of possible and highly probable host materials where anomalous emission is observed when doped with divalent europium and ytterbium and attempts to establish general trends for the occurrence of ITEs.

It is found that the probability of anomalous emission increases with increasing cation size, with a decrease in the binding strength of the oxygen (for oxide compounds) and for a decrease in the lanthanide ion size.[1] Additionally it is found that normal $4f^{n-1}5d^1 \rightarrow 4f^n$ emission is observed for divalent lanthanides on monovalent cation sites [11].

2.2.1 ITEs in Yb^{2+} doped CaF_2 and SrF_2 hosts

The details that are specific to each of the ITEs occurring in CaF_2:Yb^{2+} and SrF_2:Yb^{2+} are discussed in chapters 4 and 5 respectively. However, there are also properties common to both cases, because of the similarity of the crystal structure of the two hosts. Since a large part of this thesis involves the study of these two ITEs information additional to the general outline of anomalous emission and ITEs will be presented.

Measurements made by Moine et al. suggests that in both the cases the ITEs are also formed through a tunneling process from the lower $5d$ levels to the ITE states. They come to this conclusion because (especially in CaF_2:Yb^{2+}) the photoconductivity measurements reveal that the lowest $5d$ levels lie very close to but below the conduction band of the host material, made up of the divalent cation wavefunctions [9].

As the ITE forms around a Yb^{3+} centre experiencing a cubic field, the $^2F_{7/2}$ multiplet

[1] Although the study primarily focuses on Yb^{2+} and Eu^{2+} doped hosts, Dorenbos establishes the lanthanide ion size trend through reports in literature.

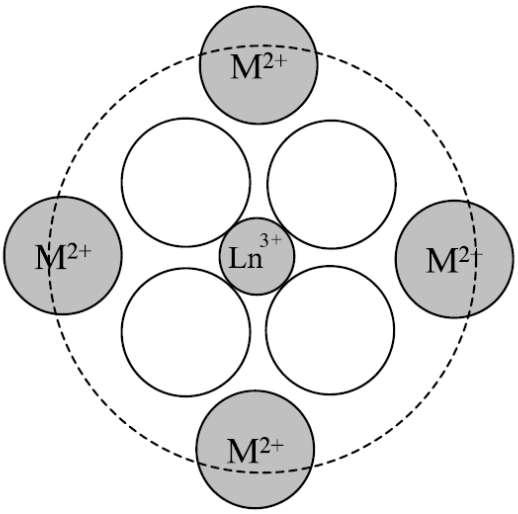

Figure 2.3 Simple model of the impurity trapped exciton as explained by Dorenbos [11] and also used by Moine et al. in their interpretation of the delocalization [9]. This shows the delocalization of the electron over the next nearest cations (denoted by M^{2+}). The now trivalent lanthanide centre is indicated by the Ln^{3+}. Figure is from reference [11].

of the Yb^{3+} splits into three levels. The hole–electron coupling of the lowest hole state results in the two excited states of the ITE (A_2 and T_2) that are a singlet and triplet states respectively. The hole and the electron are identified as being $4f$ like and s like in character. Moine's temperature dependent life time analysis places the triplet state (T_2) above the singlet state [9, 12]. In our study we have assumed that this interpretation of ITE state degeneracies to be correct.

For both systems Moine uses a model where the delocalized electron is primarily located over the next nearest neighbour cations, although detailed calculations conducted in $SrCl_2$:Yb^{2+} [2] suggest that the delocalization is over the nearest interstitial sites. No such detailed calculations exist for the CaF_2:Yb^{2+} or SrF_2:Yb^{2+} systems. Figure 2.3 shows the differences in the physical locations within the different models.

2.3 Crystal field Hamiltonian for modeling $4f$ hole transitions

Excitation of the ITE with the appropriate frequency radiation would allow for measurement of excitation spectra that reflect changes of either the delocalized electron or the $4f$ hole at the lanthanide site. Modeling the changes occurring at the delocalized electron would require detailed calculations such as those presented in references [2, 7] and are not within the scope of this study.

However, changes occurring within the $4f$ hole can be modeled by the construction of a crystal field Hamiltonian for an s electron and a $4f$ hole in a cubic crystal field. To do so one can essentially adapt the effective Hamiltonian for $4f^{13}6s$ transitions.

Note that while an involvment of the $6s$ levels of the divalent lanthanide ion causing the anomalous emission has been dismissed, the ITE exhibits s like character (see section 2.2). Because of this the modification of the effective Hamiltonian for $4f^{13}6s$, as outlined below will allow for the computation of the location and strength of the sharp spectral lines resulting from changes within the $4f$ hole.

2.3.1 The effective Hamiltonian method

For a given Hamiltonian H, with eigenstates ψ_i and eigenvalues E_i, the effective Hamiltonian H_{eff}, for its eigenstates ϕ_i has the same eigenvalues as H [59–61]. Expressed mathematically,

$$H\psi_i = E_i\psi_i, \tag{2.1}$$

$$H_{\text{eff}}\phi_i = E_i\phi_i. \tag{2.2}$$

The effective Hamiltonian within a $4f^n$ configuration is well known [3] and following its example it is possible to express the additional elements to account for the $6s$ orbitals, or the $4f^{13}6s$ effective Hamiltonian as,

$$\begin{aligned} H_{4f^{13}6s} &= \zeta(f)A_{\text{so}}(f) \\ &+ \sum_{k=4,6} B_q^k(f)C_q^{(k)}(f) + G^3(fs)g_3(fs) \end{aligned} \tag{2.3}$$

where the $\zeta(f)$ parameter (and the corresponding A_{so} operator) accounts for the spin–orbit effects on the $4f$ electrons and the $G^3(fs)$ is the exchange parameter for the Coulomb interaction between $4f$ and $6s$ electrons. The B_q^k parameters describe the crystal field effects experienced by the f electrons. Notice that, in contrast to the traditional $4f^n$ effective Hamiltonian, equation 2.3 contains no $F^k f_k$ terms. This is because we are dealing with a single hole with $4f$ character. Using these factors and that both CaF_2 and SrF_2 have cubic symmetry equation 2.3 can be reduced to,

$$H_{\mathrm{cf}} = \zeta A_{\mathrm{so}} + B^4 \left(C_0^4 + \sqrt{\frac{5}{14}} \left[C_4^4 + C_{-4}^4 \right] \right)$$
$$+ B^6 \left(C_0^6 - \sqrt{\frac{7}{2}} \left[C_4^6 + C_{-4}^6 \right] \right) + G^3(fs) g_3(fs), \tag{2.4}$$

because of the reduction in the number of crystal field parameters due to site symmetry experienced by the Yb^{3+} [4, 26]. If ITEs experiencing different symmetry conditions are to be modeled as above, then the Hamiltonian will reflect the relevant point group symmetry.

2.4 Bond length changes and their manifestations

ITE emission is broadband due to the configurational change of the lattice as the valency of the lanthanide centre changes under the electron–hole recombination. By measuring the bandwidth of an ITE emission spectrum it is possible to extract information about the physical changes that are occurring within the system.

Henderson and Imbusch (from pages 202 – 207) [26] outline a method for estimating the configurational shift for the bandwidth of any given transition. The relationship between the Huang–Rhys parameter, S and the bandwidth for a 0 K transition (i.e. with no thermal broadening) is given by,

$$S = \left(\frac{\Gamma}{2.36\nu} \right)^2, \tag{2.5}$$

where Γ is the bandwidth of the transition and ν is the effective phonon frequency for the host material. In wavenumber units for the phonon frequency the configurational coordinate change between the emitting and ground states for a given Huang–Rhys parameter is given by

$$\Delta Q^2 = \frac{S\hbar}{\pi c \mu \nu}, \tag{2.6}$$

where μ is the effective ligand mass. A bond length change ΔR can be extracted by converting the normal coordinates ΔQ to actual coordinates by division with the square root of the coordination number n_l, which depends upon the number of surrounding

ligands. Combining equations 2.5 and 2.6 the bond length changes for a given bandwidth (in units of cm^{-1}) can be expressed as,

$$\Delta R = \frac{\Gamma}{2.36}\sqrt{\frac{\hbar}{\pi c}}\sqrt{\frac{1}{\mu n_l \nu^3}}, \tag{2.7}$$

where the symbols have their usual meanings. Notice the additional factors employed to enable a wavenumber (cm^{-1}) unit of bandwidth to be used in the computation. As the bandwidth, and therefore the Huang–Rhys parameter of a given recombination transition grows, this interpretation implies that the system experiences a greater change in bond lengths. This shows that typically one would expect much broader emission profiles from the ITE recombination in comparison to $4f^{n-1}5d^1 \rightarrow 4f^n$ emission, given that the anion cage experiences a much greater contraction and expansion in the former case.

Additionally a transition with a large shift in configuration will cause a shift in the emission energy from the zero phonon line (ZPL)[2], as some of the transition energy will be lost to vibronic relaxation to the lowest vibrational level for a given state. Assuming that the vibrational frequencies of the initial and final states are the same, the shift in the centre of the emission energy from the ZPL can also be estimated from the emission bandwidth,

$$E_{\mathrm{ZPL}} = E_{\mathrm{centre}} + \left((\frac{\Gamma}{2.36\nu})^2 - \frac{1}{2} \right), \tag{2.8}$$

where the E_{ZPL} is the ZPL frequency and E_{centre} is the peak frequency of the emission. Notice that again, a large bandwidth leads to a large shift from the ZPL of a transition, which is again a feature of ITE emission.[3]

[2]Note that in the ITEs there is no zero phonon line. In this instance the calculation provides the energy gap between the minima of the two involved states. However throughout the rest of this thesis ZPL is used to refer to this energy gap.

[3]Although it should be noted that the red–shift in ITE emission is not only due to a configurational change, but rather in many cases, the ITE states occurring well below the corresponding $5d$ states.

Chapter 3

Experimental details

The focus of this thesis is two–colour experiments conducted on several metal fluoride hosts doped with ytterbium. Specifically calcium, strontium and magnesium fluoride, with the CaF_2:Yb^{2+} and SrF_2:Yb^{2+} being grown locally at the University of Canterbury. The MgF_2:Yb^{2+} crystals were grown by Andries Meijerink at the University of Utrecht. This chapter will provide the details of the experimental setup and devices used to conduct these studies.

3.1 Growth and preparation of the samples

The crystals were grown using the vertical Bridgman method in a 40 kW radio frequency (RF) furnace (figure 3.1) under vacuum. In this method the starting materials for the growth, namely pure metal fluoride crystals and ytterbium fluoride powder (3N purity), are mixed and placed in a graphite crucible. The crucible is then placed within a coil carrying the RF current, located in a chamber capable of attaining a vacuum of around 2×10^{-5} torr. Insulation is placed between the crucible and the RF coil to retain heat.

As the high frequency alternating current flows through the surrounding coil the resulting electric field across the carbon crucible causes it to heat resistively. By increasing the power output of the amplification system, the temperature of the crucible is increased to the melting point of the mixture contained within. Convection in the molten mixture evenly mixes the dopant atoms throughout the mixture. The crucible is then slowly lowered out of the coil, causing the temperature to drop as it exits the RF field. As portions of the crucible that are outside the coil begin to cool, the molten mixture freezes into crystalline form. Eventually the entire crucible is lowered beneath the coil and crystals as seen in figure 3.2 are formed. The rate of lowering can be adjusted, with slower lowering resulting in higher quality crystals.

Figure 3.1 The RF furnace used to grow the Yb doped CaF_2 and SrF_2 crystals. The chamber is capable of achieving a vacuum of less than 10^{-5} torr, while the furnace itself can achieve temperatures greater than 1500 °C.

The growth temperature is primarily dependent upon the melting point of the host crystal. The calcium, strontium and ytterbium fluorides have melting temperatures of 1415, 1473 and 1052 °C, respectively [13]. Often lead fluoride (PbF_2), with a melting temperature of 855 °C, is added to the mixture to getter residual oxygen. Care had to be taken when increasing the temperature through the regions where PbF_2 and YbF_3 are molten, with the host crystals still in crystalline form. If the mixture is heated too rapidly, the sudden increase in pressure can cause the crucible to open, leading to a loss of growth material.

Several crystals of both host materials were grown with Yb concentrations ranging from 0.005 to 2 molar percent. Since our primary focus in this project was to explore the Yb^{2+} ions in these materials, care had to be taken as the concentration of YbF_3 increases reduction to Yb^{2+} is less effective leading to increased Yb^{3+} centres forming [62]. At high enough concentrations these can then form Yb^{3+} clusters [63].

The as grown crystals were not suitable for experiments. These were cut into samples with a thickness of approximately 2 mm with the use of a Struers Minitom diamond saw. The cut samples were then polished down to approximately 1 - 1.5 mm using a Struers LaboPol-

Figure 3.2 (Left)The Yb doped CaF_2 and SrF_2 crystals as grown. The right most two crystals have had samples cut from them. (Right) The crystals cut and polished, ready to be used in experiments. The left most two samples are Yb doped CaF_2 , the right most two samples are Yb doped SrF_2. The crystals are between 8 – 10 mm in diameter and cut to between 1 – 2 mm thickness. Typically a boule weighs between 7 – 10 g, and a cut sample typically weighs between 0.2 – 0.4 g.

2 polisher, initially employing progressively finer grades of Silicon Carbide (SiC) paper and subsequently diamond suspension activated fiber with progressively finer particulate sizes. The polishing was crucial in reducing scattering of the illuminating lasers into the detection equipment.

The CaF_2 crystals were typically grown at a RF output power of 9.9 kW, to achieve a nominal temperature of 1415 °C across the carbon crucible. This power setting was established via a melt test. Since CaF_2 has a higher melting temperature than YbF_3 care had to be taken when increasing the mixture temperature beyond that of YbF_3 to avoid the possible loss of the melted material. A range of samples at dopant molar concentrations from 0.001% to 1% were grown with most of the measurements carried out using a dopant concentration of 0.05%.

The individual samples were prepared from the grown crystals as described previously with care taken to establish two parallel surfaces devoid of large scattering areas. For CaF_2 the diamond edged cutting blade was set to an intermediate speed, allowing for the blade to cut through the 8 mm diameter boule in 15 minutes. The samples were cut to a thickness of 2 mm then polished. In the polishing phase a roughing grind was applied with 1000 Grit SiC paper for 30 seconds per side, followed by a polish with 4000 Grit SiC paper for 120 seconds per side. This was then followed by a diamond suspension polish with diamond particulates of 9 and 6 μm for 240 seconds and 300 seconds per side

respectively.

The SrF_2 crystals were typically grown at a RF output power of 10.6 kW, to achieve a nominal temperature of 1473 °C across the carbon crucible. As with CaF_2 this power setting was established via a melt test. As before care had to be taken when increasing the mixture temperature beyond that of YbF_3. Again, a range of samples at dopant molar concentrations from 0.001% to 1% were grown with most of the measurements carried out using the 0.05% molar concentration.

In the case of SrF_2 the diamond edged cutting blade was set to a slower speed than CaF_2:Yb^{2+}, allowing for the blade to cut through the 8 mm diameter boule in 25 minutes. The samples were cut to a thickness of 2 mm then polished. The roughing grind was applied with the 1000 Grit SiC paper for 25 seconds per side, followed by a polish with 4000 Grit SiC paper for 100 seconds per side. This was then followed by the same diamond suspension polish applied to CaF_2.

3.2 Two–colour photoluminescence enhancement experiments

The two–colour photoluminescence enhancement technique involves employing time delayed UV and IR pulses to directly probe the internal energy structure of ITEs.

Figure 3.3 shows the general principles of the experiment:

1. A UV pulse excites the $4f^{14} \rightarrow 4f^{13}5d^1$ transition in Yb^{2+}.

2. The excited electron delocalizes via the conduction band or tunneling and forms an ITE centred at the now trivalent ytterbium with two emitting states separated by energy ϵ. The decay from the $5d$ state to the ITE can be to any state within the ITE, the dashed arrow simply indicates the formation of the ITE itself.

3. A slowly decaying population of oscillators is set up in the lower level of the ITE, which emits either visible or near–IR radiation.

4. A wavelength tunable IR pulse (electronically delayed from the UV pulse) excites the oscillators in the lowest level to higher energy states of the ITE via direct absorption of the IR photons. These oscillators decay non–radiatively to the faster emitting state.

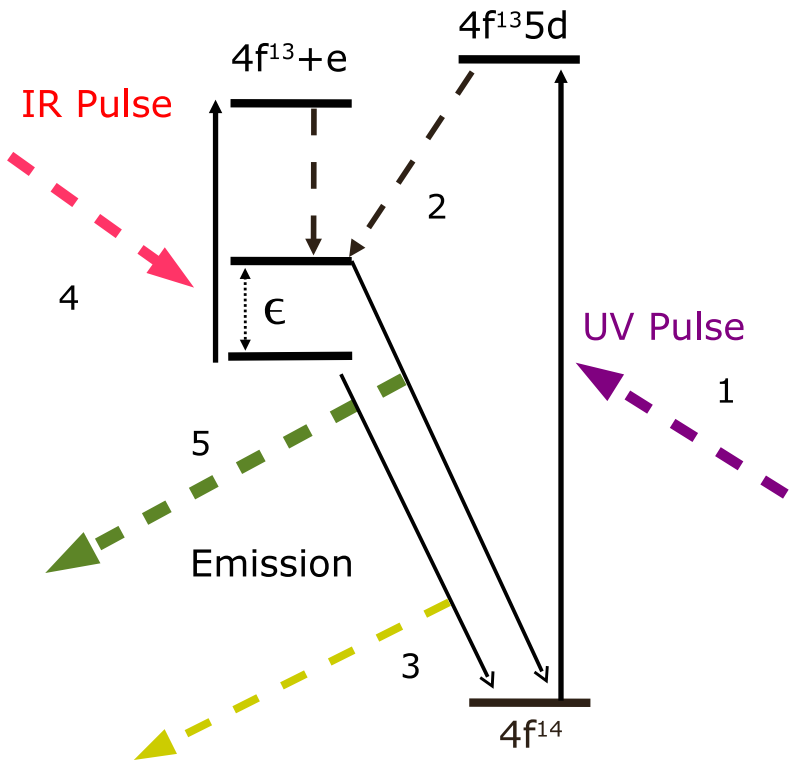

Figure 3.3 Schematic of the two-colour photoluminescence enhancement technique describing the sequence of major events.

5. This state decays with a much more rapid radiative relaxation to the system ground state (in comparison to the lowest ITE level), leading to an *enhancement* in the emission from the ITE.

By recording the dynamic behaviour of the emission over a range of excitation frequencies the energy structure of the ITE states can be determined.

3.2.1 The UV radiation source

A RegA regenerative amplifier seeded by a MIRA 900F Ti-Sapphire oscillator pumps a Quantronix TOPAS Optical Parametric Amplifier (OPA) which provided tunable UV laser radiation output from 250 to 400 nm (figure 3.4). The pulse width of of the OPA was around 3 ps with a repetition rate of 1 kHz. The average power output at the laser was typically 10 - 15 mW, with a maximum pulse fluence of approximately 0.13 Jcm^{-2}. The tunability of the UV output was essential as the materials studied had different peak absorption wavelengths (table 3.1).

Figure 3.4 (Left) The TOPAS traveling wave optical parametric amplifier, providing the tunable UV laser radiation. (Right) A MIRA 900F Ti-Sapphire oscillator seeds a RegA regenerative amplifier to pump the OPA.

Table 3.1 Peak absorption wavelengths and frequencies of the CaF_2:Yb^{2+}, SrF_2:Yb^{2+} and MgF_2:Yb^{2+} samples used in this study.

Material	Absorption wavelength (nm)	Absorption frequency (cm^{-1})
CaF_2:Yb^{2+}	365	27400
SrF_2:Yb^{2+}	360	27780
MgF_2:Yb^{2+}	335	29860

3.2.2 The Dutch free electron laser (FELIX)

The infrared (IR) radiation was provided by the Dutch Free Electron Laser for Infrared eXperiments (FELIX), located at FOM Rijnhuizen in Nieuwegein, the Netherlands. FELIX has a tunable wavelength range from 3 - 250 μm, and is able to scan continuously for large parts of its wavelength range. It is a pulsed laser, consisting of a macro–pulse with a width of 4 - 10 μs with a repetition rate of 5 or 10 Hz. The macro-pulse contains a comb of micro-pulses, of variable width (0.3 – 10 ps) with a repetition rate of either 25 MHz or 1 GHz [64]. A beamline of FELIX is shown in figure 3.5.

FELIX, like all free electron lasers, achieves radiation output by initially accelerating a beam of electrons to relativistic speeds and then directing the beam through a series of magnets with alternating poles [66, 67]. Called undulators, this arrangement of magnets cause the electron beam to wiggle as it travels through the transverse magnetic field (Figure 3.6). This acceleration causes radiation to be emitted which is in phase with the

Figure 3.5 The Dutch Free Electron Laser for Infrared eXperiments (FELIX) with one of the beam-lines clearly visible in the foreground. FELIX has two separate beam-lines depending on desired wavelength range. Photo from [65].

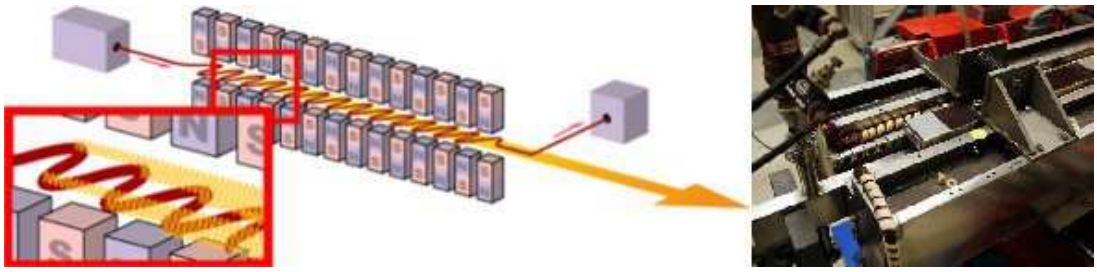

Figure 3.6 (Left) A schematic of the manner in which a FEL achieves the output of radiation from manipulating the motion of relativistic electrons. Photo from [68]. (Right) A close up of the undulators on one of the FELIX beam-lines. Photo from [69].

motion of the electrons [67]. The wavelength of the resultant radiation can be tuned by changing the distance of the magnets from the beam, thus allowing continuous tuning.

FELIX has two beam lines depending upon the required wavelength range. FEL2 allows for IR wavelengths between 3 to 45 μm, and can be setup to have a flat power output over a relatively large scan range, especially from 10 μm onward. FEL1 allows for much longer wavelengths, ranging from 45 to 250 μm. However, FEL1 does not have a flat power output, especially above 50 μm and has to be continuously adjusted to allow for lasing at a given wavelength. This makes continuous scans difficult at excitation wavelengths beyond 50 μm.

Figure 3.7 Photograph of the experimental setup. The UV and IR paths are indicated with the blue and red lines respectively. The yellow lines indicate the path of the emitted light from the sample.

The timing electronics available at FELIX allows the UV pulses to be synchronized with the FEL pulse, and a variable delay can be introduced between them. However due to the repetition rate of the UV pulse, the maximum possible delay is about 900 μs.

3.2.3 Experimental set up

The experiment was set up as shown in figure 3.7 with the samples held at cryogenic temperatures within an Oxford instruments microstat, operating under a vacuum of 10^{-6} torr, which was cooled using liquid helium. A heating unit was also attached to the microstat, and using this and the variability of helium flow rate, stable temperature control could be achieved. We estimate that the coldest possible temperature achievable in this setup to be approximately 8 K. The front window, transparent to the UV excitation and visible to near IR emission from the sample, was made of either CaF_2 or barium fluoride (BaF_2). The rear window transparent to the IR radiation utilized BaF_2, zinc selenide (ZnSe) and polythene windows dependent upon the IR wavelength range employed.

The emitted light from the sample was dispersed via a TRIAX 320 spectrometer and detected using a C31034 photo multiplier tube (PMT). The PMT was typically run with a voltage of -2000 to -1600 V. The signal from the PMT was passed through a Stanford Instruments SR 570 current amplifier to an oscilloscope where the data was captured via

a GPIB interface, using LabView®. Various long pass optical filters were placed in front of the input slit of the spectrometer to exclude possible UV laser scatter as this could saturate the PMT. When obtaining emission spectra the slit width of the TRIAX was set to 1 mm giving a maximum resolution of 2.6 nm. Given the width of the observed peaks this was sufficient. When operating in 0 – order (gathering all emission) the slit width was set to a maximum of 7 mm.

The UV and IR beams were focused and spatially overlapped using a pinhole with a maximum diameter of 100 μm. While the UV was focused using traditional optical lenses, the IR cannot be focused in such a way due to its long wavelength. Therefore gold plated off axis parabolic mirrors were used to focus the IR beam.

Using the timing electronics, a delay was introduced between the UV and IR pulses, with the UV arriving at the sample between 50 to 800 μs prior to the IR. In the case of CaF_2:Yb^{2+} the UV – IR delay was typically set to between 50 to 200 μs. Given the comparitively slow decay of the UV induced emission such a variance in delay did have an influence on the physics of the system. In the case of SrF_2:Yb^{2+} the delay was typically set to 100 μs except for the case where the influence of the delay was specifically examined. The details of this is discussed specifically in section 5.7.

The data acquisition recorded the transient response of the sample to the two pulses. The maximum time span of a single transient was limited to 1 ms by the repetition rate of the UV pulse. FELIX was operated under the 10 Hz repetition rate, and by triggering the data acquisition hardware with the FELIX pulse it was possible to exclude the UV pulses which did not have an IR pulse following it.

Typically FELIX was scanned through a range of wavelengths and the transients were recorded at each scan point, giving a two dimensional data set containing the spectral and temporal responses of the sample to the IR excitation wavelength. Band pass filters were placed between the IR entry point into the experimental station and the sample to avoid higher harmonics of FELIX leaking through on to the PMT. Such filters were available up to a wavelength of 20 μm, however they had sharp cutoffs complicating the scanning process.

Further to this, power and temperature dependent responses of the transients were also recorded. Power was varied with filters to attenuate the beam and the temperature was varied by using the cryostat heaters (PID controlled) and controlling the He gas flow (manual). It was also possible to measure the response of various delays between the

UV and IR pulses by setting these electronically. These variations gave a comprehensive parameter space to explore with these experiments.

3.3 Considerations when scanning the FEL

FELIX is only continuously tunable for a limited range due to the beam energy and undulator scan limitations, as these must be set up to operate over a certain range of wavelengths. Additionally, towards the wavelength extremes of a set range the IR power tends to drop off as the lasing becomes less efficient for the set up. Because of this care needed to be taken in ensuring that the different regions of the IR scans were accurately represented when combining them to form excitation spectra.

Figure 3.8 shows a measured power curve of FEL2, when operating over a wavelength range between 5 to 25 μm. The power shows a sharp drop off towards the lower wavelength region, and such behaviour is fairly typical. The effective scan range in this situation is therefore diminished with the start point approximately at 10 μm. Typically a correction can be applied by normalizing to the IR power curve if the power changes are not too extreme. However, in later chapters we will see that the response to IR power within our systems is not linear, and therefore in cases where the power differential is large such normalization becomes invalid. In such situations the power curve is presented along with the observed spectra to allow for comparison.

Wherever possible overlap was sought in the scan regimes so that the data could be intensity matched between them with a scale factor. Whenever this was not possible extrapolation was used to match the different scan regions.

While extrapolation was acceptable for spectral data, the dynamic data could not be realistically extrapolated. We were thus able to achieve fairly continuous spectral data plots, however, the dynamic data was only compared within a given dynamic regime where sufficient overlap was achieved.

In some instances (especially when filters were changed) scaling of the data was required in post processing to allow for the slight changes in effective IR power. In these instances the overlapping transients were checked to ensure consistency.

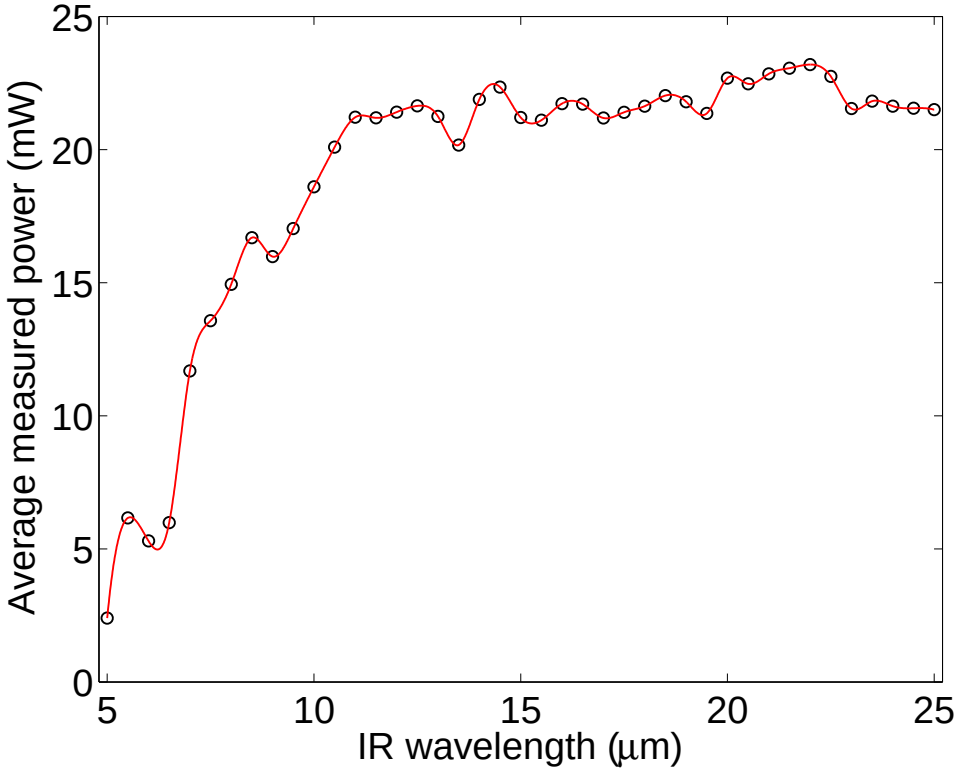

Figure 3.8 The recorded power curve at the sample for FEL2 operating over a range of 5 to 25 μm.

3.3.1 Operation of FEL at wavelengths beyond 50 μm

Operation of FEL1, for IR wavelengths beyond 50 μm proved challenging due to the extremely narrow scan regions attainable. Often a scan of 2 μm would cause the FEL to stop lasing, and within that region the power would fluctuate significantly. Because of this careful monitoring of the power at the sample was required, as shown on figure 3.9. The fluctuations observed rendered normalization almost impossible, instead peaks were identified by ensuring that there was no matching power increase at the location of the observed intensity peak. After such a peak was identified the scan range was narrowed, and the power response was flattened as much as possible.

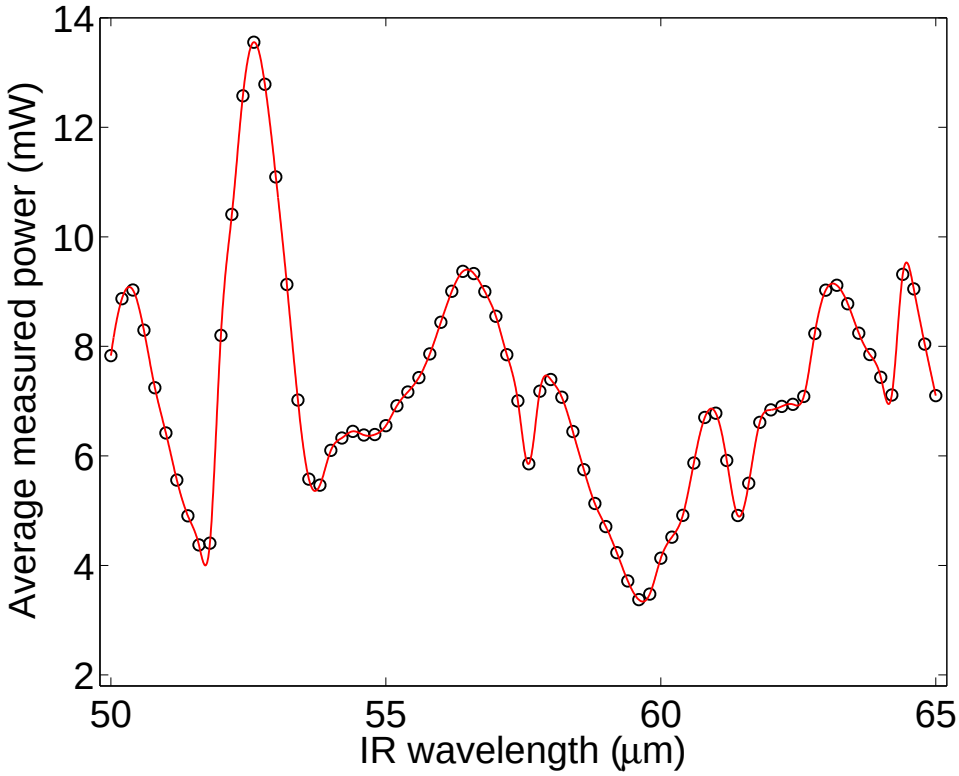

Figure 3.9 The recorded power curve at the sample for FEL1 operating over a range of 50 to 65 μm.

Chapter 4

Two–colour excitation experiment directly probing Impurity Trapped Excitons in CaF_2:Yb^{2+}

In previous work the known properties of the CaF_2:Yb^{2+} ITE have been determined through single colour excitation in conjunction with indirect methods such as temperature dependent emission life times and intensity measurements [9]. By utilizing the meta–stability of the ITE ground state and placing a population of oscillators in this state (via ultra–violet excitation) we directly probe the energy structure and its dynamics via tunable, secondary infra–red excitation of the ITE.

In this chapter we present the specific details of the two–colour experiments done on CaF_2:Yb^{2+}. We give a brief description of the ITE observed in CaF_2:Yb^{2+} and then describe the aspects of the experiments conducted that uniquely apply to CaF_2:Yb^{2+}, present the detailed observations and provide descriptions of the data. We analyse the spectral properties of both the observed emission and excitation and provide a model describing observed sharp peaks in the excitation spectrum. We also present detailed analysis and modeling of the dynamic properties observed in the system under a variety of conditions.

4.1 Impurity Trapped Excitons in CaF_2:Yb^{2+}

Previous studies [9, 12] have identified the anomalous emission from CaF_2:Yb^{2+} after excitation of the $4f \rightarrow 4f^{n-1}5d$ absorption at 27400 cm^{-1} as originating from an ITE occurring locally upon the Yb^{2+} sites. In this study Moine's et al. model of the ITE is used as a starting point and its details are presented here.

Figure 4.1 shows a schematic of the energy level distribution of the ITE (adapted from Moine et al.) [9]. There are two known emitting energy levels (which we have denoted states 2 and 3), separated by a gap of $\epsilon = 40$ cm^{-1}, with the upper level (state 3) having

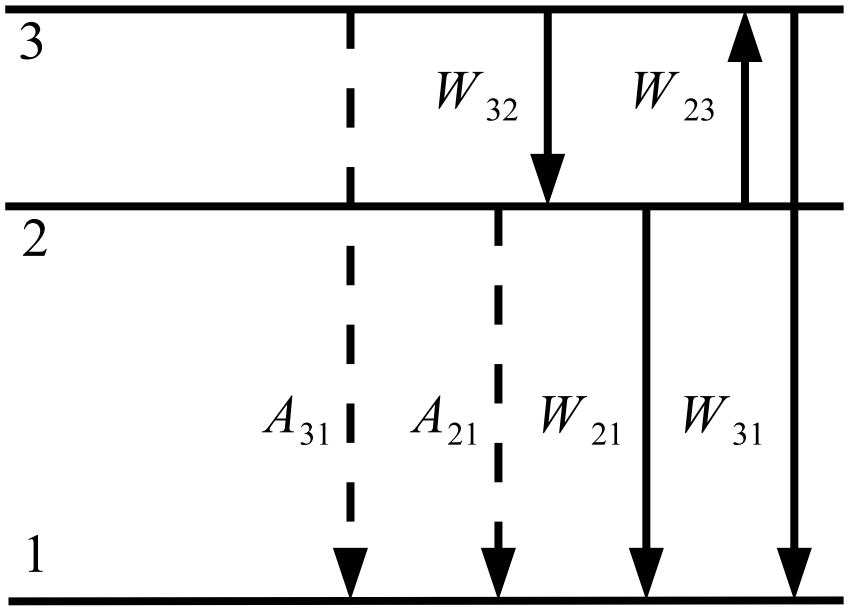

Figure 4.1 A schematic representation of the energy levels and associated rates in CaF_2:Yb^{2+}. The rates are described in table 4.1 and are obtained from references [9, 12]. The broken arrows represent radiative decay pathways and the solid arrows represent non–radiative decay pathways.

a much faster radiative rate at $A_{31} = 3800$ s^{-1} compared to the lower level (state 2) at $A_{21} = 18$ s^{-1}. Both levels have associated 'thermal' barriers which influence the non–radiative rates from the emitting states to the ground state of the system dependent upon the sample temperature. Their heights have been determined by the temperature dependent intensity and decay lifetime of the system. The barrier heights are $\epsilon_{21} = 1$ and $\epsilon_{31} = 2300$ cm^{-1}. The dependence of the non–radiative rates on the barrier heights are expressed by,

$$W_i = W_{i0} e^{-\epsilon/k_b T} \tag{4.1}$$

where W_i is the rate at a given temperature T and W_{i0} is the rate at $T = \infty$.

The non–radiative rate from state 2 at 8 K is $W_{21} = 48$ s^{-1}. Because ϵ_{21} is only 1 cm^{-1} this transition is always active and is not significantly influenced by temperature. The initial non–radiative rate from state 3 to the ground state has been set to $W_{31} = 10^{13}$ s^{-1}. Given the large associated barrier, W_{31} at 8 K is 0.94 s^{-1}, and remains negligibly low for temperatures that are used in our study (8 to 50 K).

The non–radiative rate from state 3 to 2 , W_{32}, and the rate from state 2 to 3, W_{23} are

related by,

$$W_{23} = \frac{g_3}{g_2} W_{32} e^{-\epsilon/k_b T} \tag{4.2}$$

where the degeneracies are $g_2 = 1$ and $g_3 = 3$ and T is the sample temperature. The degeneracies are used to account for the singlet and triplet nature of the two emitting levels, where they determine the ordering through the temperature dependent emission life time fit. Moine et al. only deal with the total decay rate of the observed emission from the ITE. Since the temperature dependent *ratio* of the non–radiative rates between states 2 to 3, (W_{32} and W_{23}), accounts for the thermal equilibrium of the oscillator population between the states the only requirement is that they are faster than the resolution of the lifetime data. Therefore W_{32} is set to 10^8 s^{-1}.

In our study we extract W_{32} from an initial fit to transient data at an IR excitation frequency of 900 cm^{-1} and keep this value constant at 50000 s^{-1}.[1]

Table 4.1 summarizes the rates discussed above. Where there is a potential barrier involved in computing the rates (e.g. W_{31}) a sample temperature of 8 K has been used. However, as discussed above, given the sizes of the barriers involved, at 8 K there is no significant deviation from the 'initial rates' used within the literature.

Table 4.1 Rates obtained from previous experiments for the CaF_2:Yb^{2+} ITE. The non–radiative parameters (W_i) with associated potential barriers have been calculated from Moine et al. [12], via equation 4.1 for a temperature of 8.0 K. W_{32}, the non–radiative relaxation rate from state 3 to 2 was determined through fitting, since the values presented in the previous studies are arbitrarily fast.

Parameter	**Rate (s^{-1})**	**Equivalent time constant (μs)**
A_{21}	18	55000
A_{31}	3800	263
W_{21}	48	21000
W_{31}	0	Inf
W_{32}	50000	20

As the sample temperature increases state 3 is increasingly populated due to the increase

[1] Keeping W_{32} is justified because of the temperature dependent dynamic behaviour, this is discussed in the modeling section later in the chapter. Refer to section 4.11.4

in the ratio of W_{23} to W_{32}. The emission intensity increases, as the system is radiatively decaying faster because $A_{31} \gg A_{21}$. However, if the temperature became sufficiently large such that W_{31} became much larger than A_{31} (for example, at $T = 180$ K, $W_{31} = 90000$ s^{-1}) the emission intensity will decrease, since most of the excited oscillators will decay out of state 3 non–radiatively. In such a situation the emission will arise out of the radiative decay from state 2, since the non–radiative rate out of state 2 (W_{21}) remains unchanged with temperature. Thermal quenching is observed above 180 K as the population of oscillators predominantly occupy state 3 and decay non–radiatively.

4.2 Experimental details

A two–colour excitation transient photoluminescence enhancement experiment (as detailed in section 3.2) was carried out on CaF_2:Yb^{2+} in order to directly ascertain the structure and dynamic properties of the ITE known to exist within that system. CaF_2 samples of 1.5 mm thickness doped with 0.05 molar percent of Yb^{2+} were used and excited by UV radiation at 27400 cm^{-1} (365 nm) and variable frequencies of IR radiation.[2] Both the beams were focused to a spot size of 100 μm giving a fluence of 0.13 Jcm^{-2} for the UV pulse and between 5 to 11 Jcm^{-2} for the IR pulse under the 25 MHz micro pulse regime.

4.3 Spectra of the impurity trapped exciton emission

Under excitation with only the UV pulses, emission previously identified as originating from the Yb^{2+} ITE system was observed, in agreement with Moine et al. [9]. Previous studies show that under initial excitation at a sample temperature of 8 K, the emission decays with a lifetime of approximately 15 ms. However, because the UV radiation repeats much faster (at 1 ms between pulses) the decay time of the emission could not be accurately determined in order to ascertain congruency with previous measurement.

4.3.1 Temperature dependent emission spectrum

The emission spectra for sample temperatures of 8 and 40 K are shown in figure 4.2. A least squares fitting was carried out on a Gaussian line shape function computing the

[2]Samples with Yb^{2+} concentrations between 0.01% to 0.1% were also tested, however detailed experiments were carried out at a concentration of 0.05%. All samples showed similar behaviour.

intensity $I(\omega)$ (given in arbitrary units) as defined below:

$$I(\omega) = A_0 e^{2\sqrt{\ln 2}(\frac{\omega-\omega_0}{\Gamma})^2} \tag{4.3}$$

where A_0 in the peak intensity, ω_0 the peak position and Γ is the full width at half maximum (FWHM). From this fitting the peak position was determined to be at 17800 cm^{-1} at 8 K, in agreement with Moine et al. [9]. The spectrum was broad with a FWHM of 3500 cm^{-1} and featureless, as is typical of ITE emission [9, 11, 12, 42].

With the sample temperature increased to 40 K the emission intensity increased by a factor of 2.5 and the spectral peak blue shifted by 600 cm^{-1} to 18400 cm^{-1} and the spectral width narrowed by 300 cm^{-1} to 3200 cm^{-1}. The emission intensity increase is due to a greater ratio of the population of oscillators occupying the radiatively faster state 3 at 40 K. The blue shift in peak position that is 15 times greater when compared to ϵ_{23}, indicates a configuration change occurs between states 2 and 3.

Table 4.2 Parameters from least squares fitting of single Gaussians to temperature dependent emission spectra from CaF_2:Yb^{2+} under UV excitation. The maximum intensity value (A_0) of the 8 K emission was fixed at 1 for the fitting. All other parameters were freely varied.

Parameter	$T = 8$ K	$T = 40$ K
A_0 (a.u)	1	2.41 ± 0.03
ω_0 (cm^{-1})	17800 ± 14	18400 ± 20
FWHM (cm^{-1})	3500 ± 50	3200 ± 60

4.3.2 Response of the ITE emission to IR excitation

Pulsed UV excitation followed by a spatially overlapped but time delayed IR pulse led to significant enhancement in the emission intensity from the sample. By recording the response transients to the excitation at points across the ITE emission spectrum the time–frequency plots shown in figures 4.3 (a) and (b) were obtained. These show the temporal evolution of the spectrum at IR excitation frequencies of 800 cm^{-1} and 625 cm^{-1} respectively. The UV pulse occurs at $t = 0$ μs with the IR pulse delayed by 100 μs. At $t = 100$ μs, the enhancement begins and rises, with the peak emission showing an

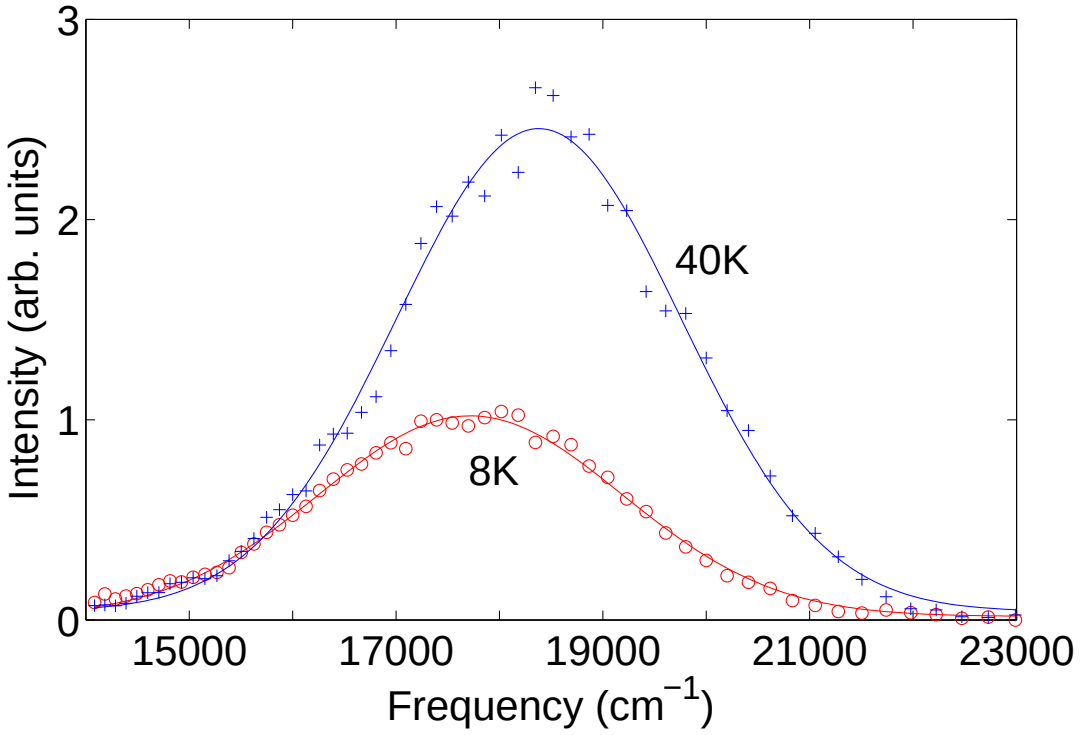

Figure 4.2 Emission spectra observed from CaF_2:Yb^{2+} under UV excitation at 27400 cm^{-1}. The emission at 8 K appears to be a single broad Gaussian peaking at 17700 cm^{-1} with a FWHM of 3500 cm^{-1}. At a sample temperature of 40 K the peak shifts to 18400 cm^{-1} and narrows slightly with a FWHM of 3200 cm^{-1}. The solid lines are fitted Gaussian curves. The spectra have been normalized such that the peak intensity of the 8 K spectrum is 1. Details of the fitted parameters are presented in table 4.2.

increase by a factor of 10. It should be noted that the signal is normalized such that the peak spectral intensity prior to the onset of the IR pulse is unity. There was a change of filters between the two scans to eliminate possible emission from europium contaminants in the sample and second order UV laser scatter seen in figure 4.3 (a).

The dynamic behaviour of the system is vastly different for the two IR excitation frequencies. Under 800 cm^{-1} excitation (figure 4.3), the rise in the enhancement is fast, and appears to be simply due to the FELIX pulse shape and time distribution (see section 3.2). The enhancement decays with a time constant of approximately 40 μs and the emission intensity appears to fall close to the pre–IR levels within the time frame of the UV pulse repetition (i.e. before 1 ms has elapsed since the previous UV pulse).

At an IR excitation frequency of 625 cm^{-1} the rise becomes slower, increasing to approximately 30 μs and the decay time constant becomes slower at approximately 160 μs. This causes a change in the overall transient shape in comparison to the excitation at 800 cm^{-1}.

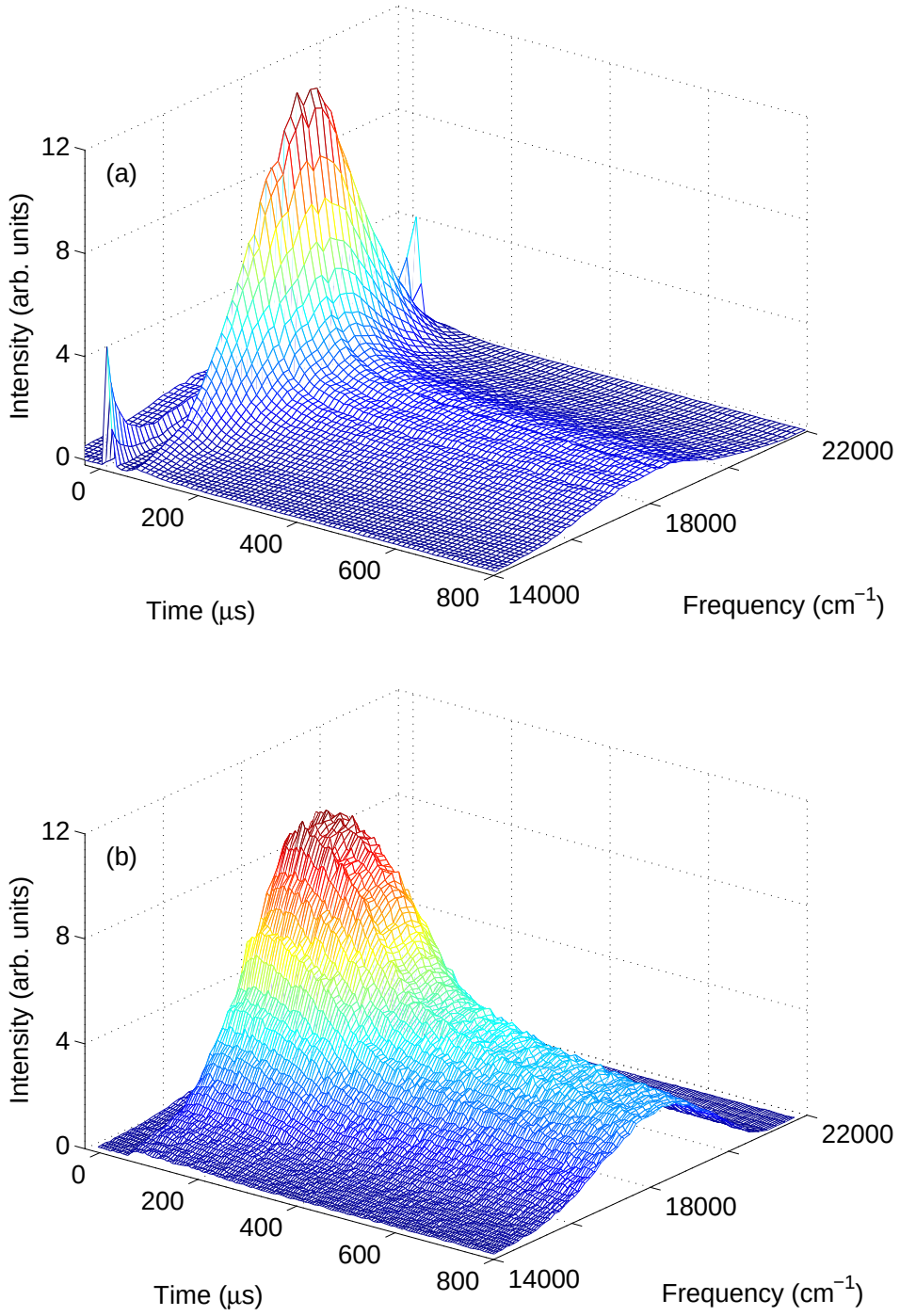

Figure 4.3 Emission spectra obtained at a sample temperature of 8 K, showing the enhancement caused by the IR. The UV and IR pulses occur at $t = 0$ and $t = 100$ μs respectively. (a) Shows the response at an IR frequency of 800 cm^{-1} with the decay in enhancement occurring rapidly after the termination of the IR pulse. The peaks appearing at $t = 0$ μs are likely due to europium impurities present and the second order UV scatter. (b) Shows the response at 625 cm^{-1} excitation. The enhancement lasts for longer and has a larger rise time. Additionally the emission intensity does not return to the pre–IR levels. A change in filters eliminated the peaks at $t = 0$ μs.

Additionally the emission intensity does not fall to the pre–IR level, and thus an offset appears in the spectral intensity profile. Additionally under this excitation frequency the overall emitting population fraction some time after the initial enhancement (for example from 600 to 800 μs) is greater than for the same time frame under an excitation of 800 cm^{-1}.

From the spectral results presented in section 4.3.2 it can be seen that a significant difference exists in the dynamic behaviour of the ITE emission spectrum at different IR excitation frequencies. However it is not immediately clear from the raw results how the emission behaves spectrally under such excitation. Specific time slices of the emission spectra presented in figures 4.3 (a) and 4.3 (b) give a deeper view of the spectral changes that the IR excitation causes.

Figures 4.4 (a) and 4.4 (b) show the behaviour of the emission at different times in the excitation sequence for IR excitation at 800 cm^{-1} and 625 cm^{-1} respectively. The pre–IR spectrum (i.e. spectrum under UV excitation alone) is essentially identical in both cases. There is a discrepancy in the amplitude of the emission peak, however this is due to slight differences in the PMT signal amplification and different filters in use to exclude UV scatter during the two scans (Note that the spectra presented are in raw form, i.e. they have not been normalized with respect to each other, since the key comparison being made is not of the absolute spectral intensity between the two excitation regimes, but of peak position, width and their behaviour in the time domain).

By fitting a single Gaussian to each of the spectra (as was done in section 4.3.1), we extract the peak positions and widths at the different time points along the excitation sequence. The parameters extracted from these fits are presented in tables 4.3 and 4.4.

For 800 cm^{-1} IR excitation (figure 4.4 (a) and table 4.3) at $t = 20$ μs the peak has blue shifted by 540 cm^{-1} (from 17800 to 18340 cm^{-1}) and narrowed by 300 cm^{-1} (from 3500 to 3200 cm^{-1}). The blue shift and the change in spectral width is in agreement with the shift and narrowing observed when the sample was heated to 40 K (comparing the parameters presented in tables 4.2 and 4.3). Thus the IR excitation at 800 cm^{-1} is likely placing population into the faster emitting state 3. As time progresses the spectrum evolves back to the pre–IR spectrum in both peak position and width, indicating that the emission out of state 3 has diminished while state 2 continues to emit. There is a slight difference in peak position and intensity, indicating that the emission out of state 3 has not completely vanished.

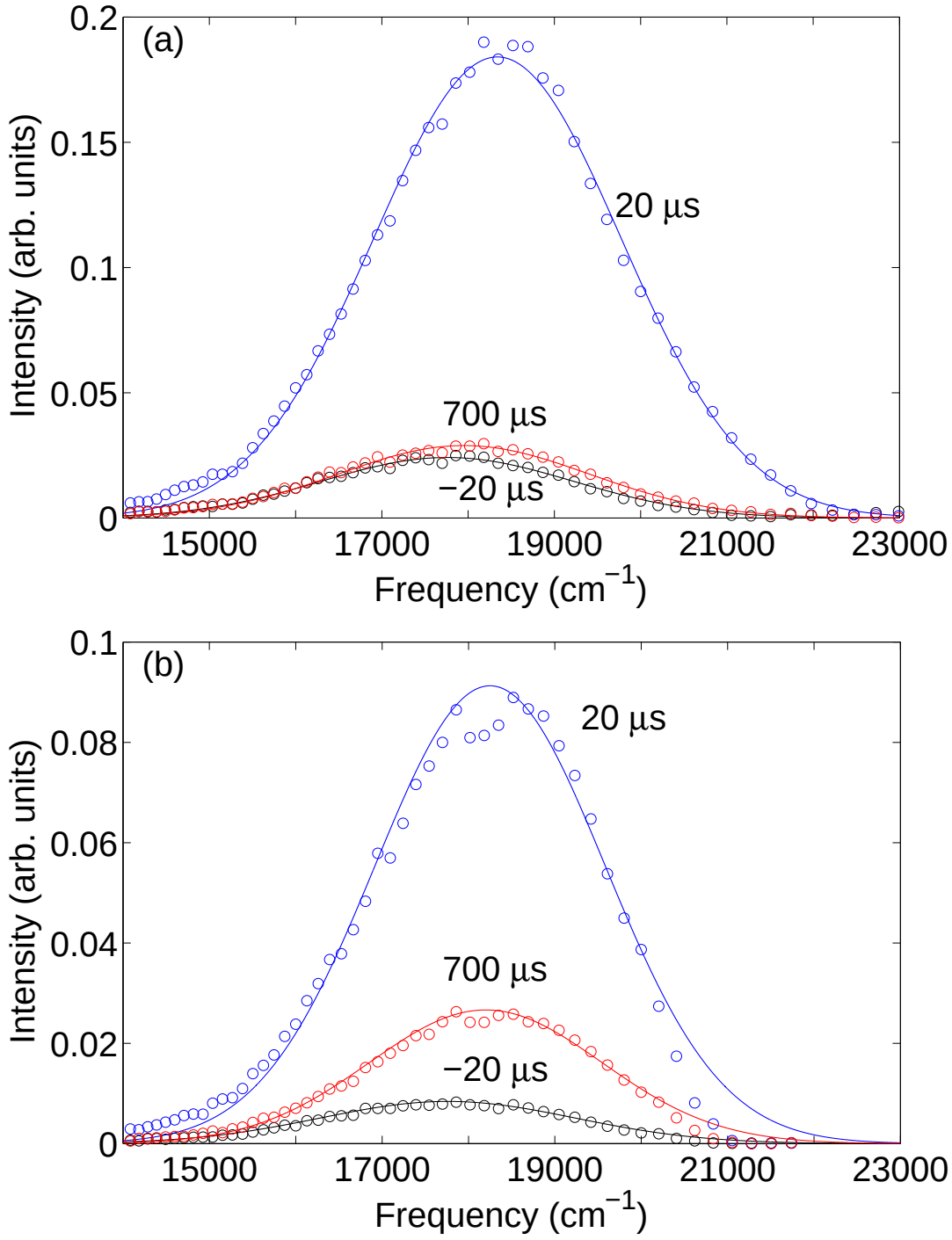

Figure 4.4 The changes in the emission spectrum at 8 K for IR excitation at (a) 800 cm^{-1} immediately after the IR excitation (20 μs) and towards the end of the excitation cycle (700 μs). Notice that the peak positions move significantly, first blue shifting then red shifting back to the UV only emission spectrum (in black labeled -20 μs), (b) 625 cm^{-1}, the peak positions blue shift significantly, however they do not shift back to the UV only emission spectrum. The fall in intensity occurring at 21000 cm^{-1} is due to filters used for excluding UV scatter.

Table 4.3 Parameters from least squares fitting of single Gaussians to changes in the emission spectrum under IR excitation at 800 cm^{-1} immediately after the IR excitation (20 μs) and towards the end of the excitation cycle (700 μs). The values for the spectrum prior to the IR pulse (UV only) is also shown at $t = -20$ μs for comparison.

Parameter	-20 μs	20 μs	700 μs
A_0 (a.u)	0.0242 ± 0.004	0.1841 ± 0.003	0.0289 ± 0.006
ω_0 (cm^{-1})	17800 ± 60	18340 ± 40	17900 ± 50
FWHM (cm^{-1})	3500 ± 80	3300 ± 30	3500 ± 50

The dynamic behaviour of the emission (see figure 4.3) shows a fast decay of the enhancement, which is in contrast to what would be observed under heating (see section 4.6 for details). Therefore the mechanism for the population transfer in to state 3 is likely different between the IR excitation and increasing the sample temperature.

Table 4.4 Parameters from least squares fitting of single Gaussians to changes in the emission spectrum under IR excitation at 625 cm^{-1} immediately after the IR excitation (20 μs) and towards the end of the excitation cycle (700 μs). The values for the spectrum prior to the IR pulse (UV only) is also shown at $t = -20$ μs for comparison.

Parameter	-20 μs	20 μs	700 μs
A_0 (a.u)	0.00840 ± 0.0002	0.0941 ± 0.004	0.0267 ± 0.006
ω_0 (cm^{-1})	17800 ± 60	18300 ± 100	18200 ± 60
FWHM (cm^{-1})	3500 ± 80	3100 ± 150	3200 ± 100

In the case of IR excitation at 625 cm^{-1} (figure 4.4 (b) and table 4.4) the peak blue shifts by 500 cm^{-1} (from 17800 to 18300 cm^{-1}) and narrows by 400 cm^{-1} (from 3500 to 3100 cm^{-1}) at $t = 20$ μs, in agreement with the shift and narrowing observed with the sample at 40 K. The spectral behaviour is also similar to that observed for IR excitation at 800 cm^{-1} and the fitted parameters are in agreement (compare tables 4.3 and 4.4). The IR excitation at this frequency is still placing population into state 3.

At $t = 700$ μs the behaviour differs from the spectrum obtained for excitation at 800 cm^{-1}. The spectrum does not evolve back to the pre–IR spectrum, instead it slowly decays, while retaining both peak position and width, indicating that the emission out of state 3 while diminishing, remains dominant.

Examination of the figures pertaining to the two excitation frequencies shows the dynamic behaviour is also divergent at long time scales. These factors indicate that IR excitation at 625 cm^{-1} causes a change that is long lasting in comparison to the decay processes involved in excitation at 800 cm^{-1}. A possible explanation is that the IR is causing local heating through absorption of the IR radiation by the lattice, given that the IR absorption at 600 cm^{-1} is greater than at 800 cm^{-1} [70] (see section A.1).

4.3.3 Configurational changes within the ITE

From figures 4.2 and 4.4 it is clear that there are significant changes in the spectra associated with the two emitting states of the exciton. By examining the peak position and band width changes that occur in the emission as the state of origin changes it is possible to extract some information about the physical changes that are occurring within the ITE system. Utilizing equation 2.7 from section 2.4 with an effective phonon frequency $\nu = 325$ cm^{-1} the bond length changes the system undergoes during recombination from states 2 and 3 were computed and the results are presented in table 4.5.[3]

Additionally the ZPLs can be computed with equation 2.8 allowing for an estimation of the energy displacement in the transitions (indicated by the emission peak). From table 4.5 we can see that while the ZPLs are significantly blue shifted in comparison to the emission peaks, they are indistinguishable from one another. Even though this calculation is only approximate it does illustrate that both state 2 and 3 are configurationally shifted from the ground state of the system. Additionally it shows that state 3 has greater configurational alignment with the $4f^{14}$ ground state in comparison with state 2. Note that the two excitation regimes (thermal and IR induced) show peak shifts that are in agreement with each other. This allows for the treatment of states 2 and 3 as the only detectable emitting states that are being accessed by the ITE within our experiments.

The ΔR of -0.169 ± 0.002 Å computed for the emission occurring at 8 K under UV excitation only (i.e. from state 2) is in agreement with previous calculations by Moine et al. [9]. The negative ΔR is assigned because when the ITE forms, the Yb is trivalent, thus *contracting* the Yb – F bond.

As with the peak position, the bond length changes calculated for all the enhanced emission spectra are in agreement with each other and show a smaller change than the bond

[3]The choice of ν is from the calculations conducted by Moine et al. in computing bond lengths in reference [9].

Table 4.5 Summary of the computed values for bond length changes and locations of the zero phonon lines (ZPL) as a function of temperature and IR excitation frequency. The emission spectra peak and FWHM values were obtained from the fits summarized in tables 4.2, 4.3 and 4.4. ΔR indicates the change in bond length the system experiences under recombination with its ground state, ending at the $4f^{14}$ configuration. E_{ZPL} indicates the zero phonon line for the respective emissive state that recombined with the ground state. Recall that 8 and 40 K spectra were obtained under excitation with UV alone. The peak positions (Peak) are indicated for easier comparison between the spectra and to the ZPLs.

	8 K	**40 K**	**800 cm^{-1}**	**625 cm^{-1}**
Peak (cm^{-1})	17800 ± 14	18400 ± 20	18340 ± 40	18300 ± 100
E_{ZPL} (cm^{-1})	24400 ± 700	23900 ± 900	23800 ± 500	23000 ± 2000
ΔR (Å)	-0.169 ± 0.002	-0.154 ± 0.003	-0.158 ± 0.001	-0.15 ± 0.01

length change that occurs when oscillators in state 2 decay to the ground state. Because the bond length changes are *negative* this implies that when the system is in state 3 the bond length is *longer* than when it is in state 2, and closer to the bond length of the Yb^{2+} ground state $4f^{14}$.

4.4 IR excitation frequency dependence of the excitonic emission

By scanning the FEL and recording the temporal response of the emission (monitored at 17800 cm^{-1}) at each IR excitation frequency point a time–frequency data set was obtained. The delay between the UV and IR was set to 200 μs to minimize scattered UV light.

The transient response of the emission is heavily dependent upon excitation frequency, as shown in figure 4.5 over an excitation region between 400 – 900 cm^{-1}. At higher frequencies a sharper temporal response is evident, with the decay time of the enhancement at the higher energies being 20 μs slowing to 160 μs as the excitation frequency approaches 600 cm^{-1}.

There are two distinct regions of behaviour, separated by the transient behaviour of the emission. A peak appears at around 800 cm^{-1} and a broader one is present with an onset

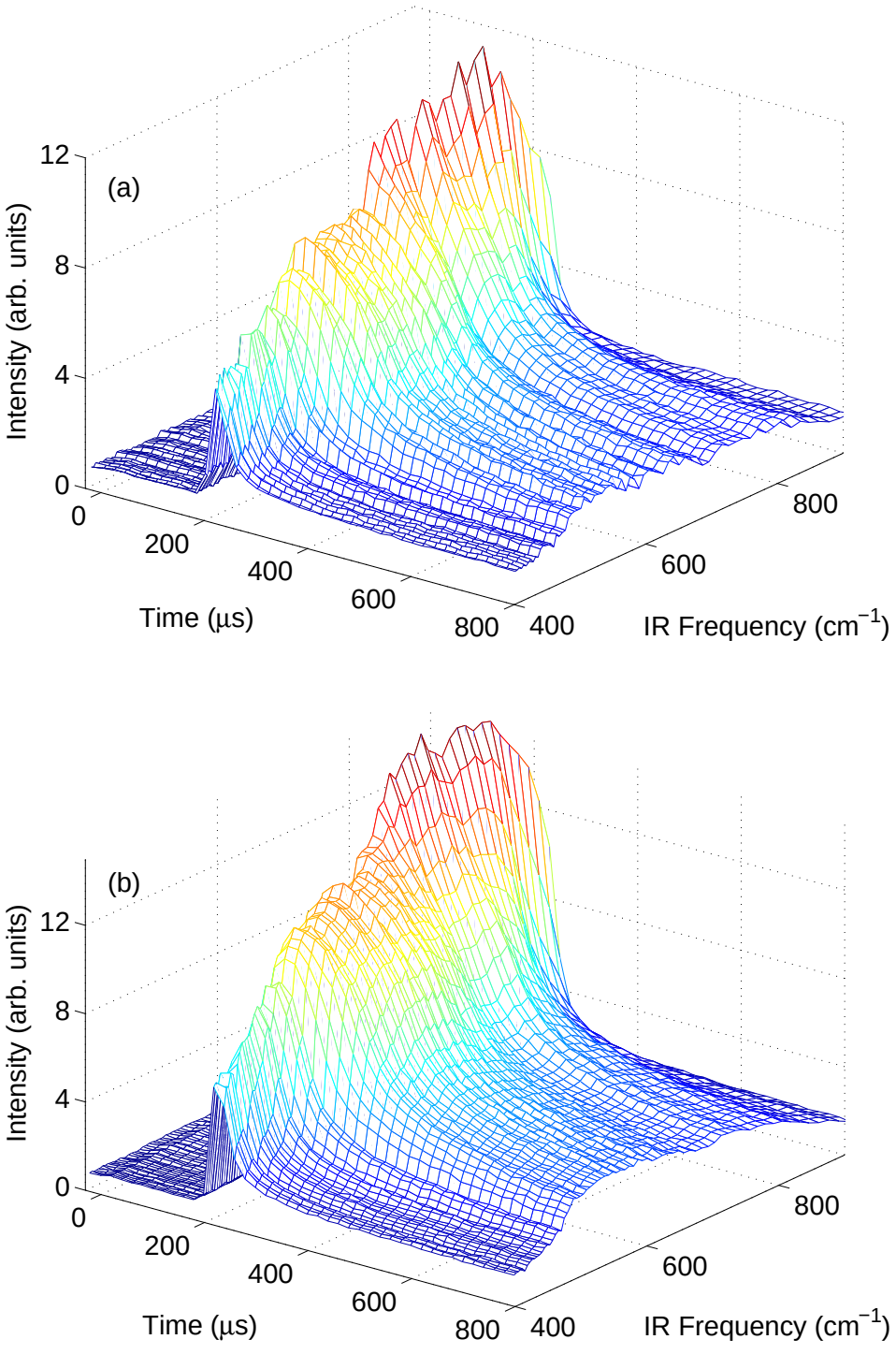

Figure 4.5 Transient behaviour under an IR excitation scan from 400 – 900 cm^{-1} at a sample temperature of 8 K, with the emission monitored at (a) 17800 cm^{-1} and (b) 18500 cm^{-1}. A distinct variation in the dynamic behaviour can be seen at the excitation frequency decreases, with an increasing rise and decay of the enhancement building into the transients. The peak enhancement appears to diminish as the IR frequency decreases.

at about 700 cm^{-1} reaching its maximum intensity at around 600 cm^{-1}. The post– IR offset in the long time decay profile coincides with the lower excitation frequency, and thus the broader peak, gradually diminishing as the excitation frequency increases.

As the excitation frequency decreases beyond 450 cm^{-1} towards 400 cm^{-1} the decay times also fall back towards 40 μs making the transient profile sharper. The offset at long times has also decreased with a sharp decline starting at an excitation frequency of 480 cm^{-1}.

Since there is a blue shift in the emission under excitation by the IR pulse (as discussed in section 4.3.2) the excitation scan from 400 to 900 cm^{-1} was repeated, with the emission detection set closer to the blue shifted emission peak at 18500 cm^{-1}. Figure 4.5 (b) shows that the general response to the IR excitation frequency is similar to what is observed under emission monitoring at 17800 cm^{-1}. The overall intensity of the emission has increased (both figure 4.5 (a) and (b) are normalized by the same factor to allow for comparison) and there is a relative change in intensity of the long term (800 μs) behaviour of the transient response.

The frequency response of the offset is better defined, with a steeper decline as the excitation frequency decreases from 650 to 500 cm^{-1} and the relative intensity of the offset (i.e. the magnitude of the offset in comparison to the peak enhancement in time) is greater. By examining the emission spectra, in section 4.3.2, it was determined that the offset in the emission (at 625 cm^{-1}) was due to the population transferred into state 3, rather than simply an increase in the total number of oscillators. Accordingly the behaviour of the offset in the excitation spectra when monitoring near the emission peak is not surprising.

Figure 4.6 (a) shows IR excitation scans from 300 down to 225 cm^{-1} (the limit of FELIX ability in the configuration in use during the experimental run). An enhancement increase was found at 280 cm^{-1} which reached a maximum at 250 cm^{-1} and remained approximately constant beyond that. Unlike the broad features present in the earlier scan region, there was a gradual change of transient behaviour in the time domain, with the decay times increasing as the excitation frequency decreased toward 250 cm^{-1}. As the excitation frequency decreased beyond 250 cm^{-1} the enhancement decay hastened, although the maximum enhancement intensity did not vary significantly. The long term behaviour of the emission (near t = 800 μs) appears flat in relation to the excitation frequency beyond the initial rise similar in nature to the short time enhancement response.

Figure 4.6 (b) shows the transients from figure 4.6 (a) terminated at $t = 300$ μs. In comparison to the time–frequency plot of the full transients a much larger variation in

the emission intensity with excitation frequency is evident.

The emission rises rapidly from 260 cm^{-1} peaking at 250 cm^{-1} and gradually diminishes as the excitation frequency decreases towards 220 cm^{-1}. This trend stems from the frequency dependent variation in decay times across the scan. However given the relatively fast decays of the enhancement (on the order of tens of microseconds), at 800 μs the detail present at the intermediate time scale appears to wash out, leading to the relatively flat response observed in figure 4.6(a).

4.4.1 Time integrated IR excitation spectrum

The difference in the emission observed in figures 4.6 (a) and 4.6 (b) indicates that the IR excitation response of the system can be washed out when directly examining the transient plots in the manner displayed. Even though there is a change in the magnitude of the emission under IR excitation in this frequency region, it is not obvious from a collection of the transients as presented. Thus it is beneficial to construct an IR excitation spectrum across all the scanned regions, which will reflect the true change in emission magnitude under a given frequency of IR excitation.

An IR excitation spectrum of the emission response was constructed by integrating over the IR induced change in the emission by employing a software based boxcar via the LabView® interface used for data acquisition.

The boxcar gate (G_1) was placed between 10 μs after the incidence of the IR pulse[4] and 690 μs after that. An additional gate (G_0) was placed before the UV pulse coupled to the IR pulse (with the start and end points at -199 μs and -10 μs respectively), to account for any possibility of emission fluctuations due to UV power fluctuations. The final integrated intensity I was defined as $I = (G_1/G_0) - 1$.[5]

This effectively captured the entire enhancement in the emission caused by the IR pulse. Because the integration was essentially occurring over the entire transient of the enhancement, different decay responses (as displayed in section 4.4) would be taken into account, as they would cause different instantaneous intensities in time.

The scans were done in small spectral regions, and these were matched to obtain a com-

[4]This was done to avoid the initial rise in the enhancement due to the FEL pulse width which varied between 6 – 8 μs.

[5]For example if there was no enhancement this would return a value of 0. Large fluctuations in UV fluence would be tempered by the division by G_0.

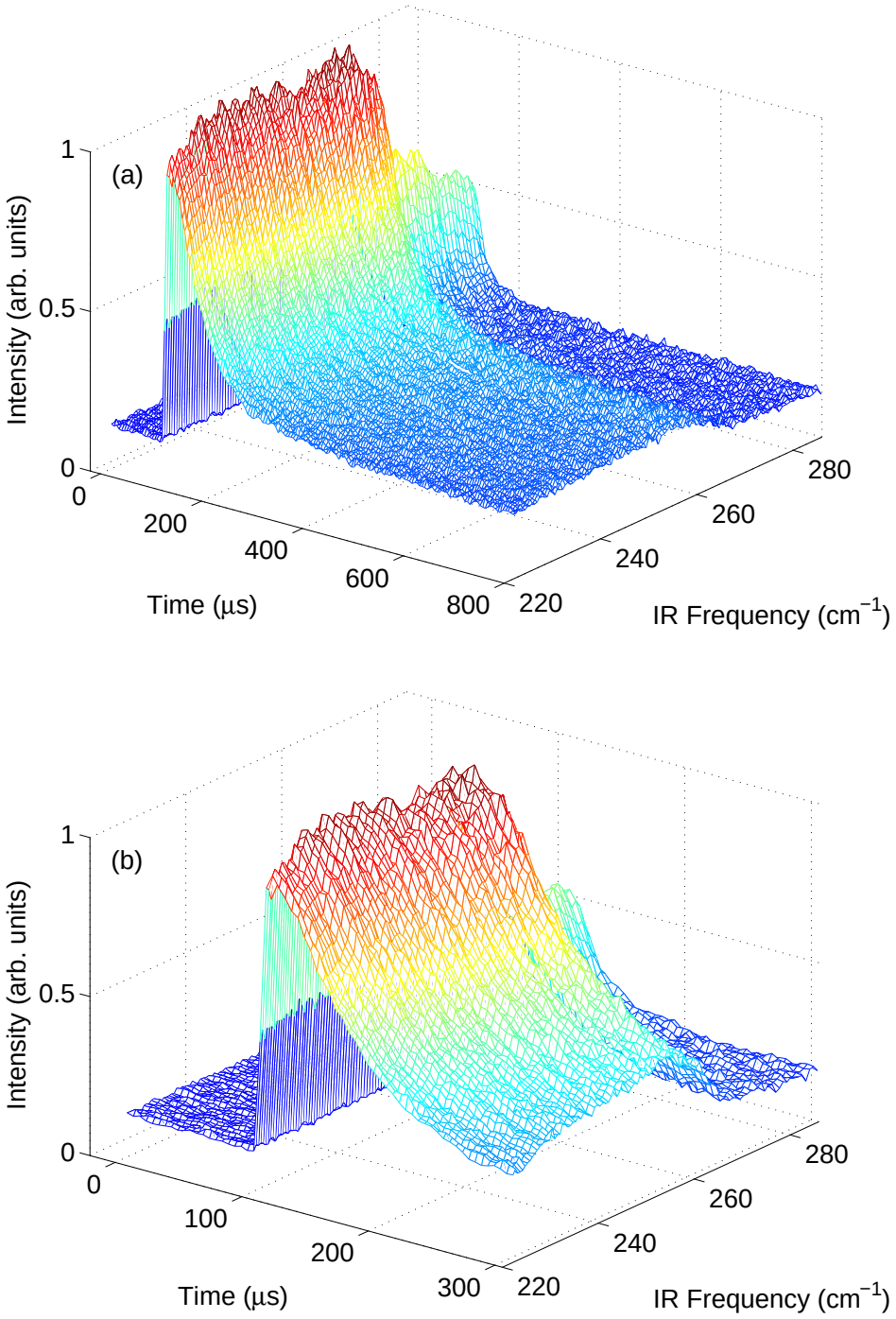

Figure 4.6 IR excitation scan from 220 – 280 cm^{-1} at a sample temperature of 8 K, monitored at 17700 cm^{-1}. (a) In the full transient the maximum enhancement response appears flat beyond 260 cm^{-1}, as does the emission at 800 μs. (b) With the time axis shortened to 300 μs an IR excitation frequency dependence that is different from both the initial enhancement magnitude and long term emission is observed. The emission rises rapidly from 260 cm^{-1} to peak at 250 cm^{-1} and diminishes as the excitation frequency decreases toward 220 cm^{-1}.

plete excitation spectrum between 200 – 1400 cm^{-1}. Figure 4.7 shows the emission response with all emission frequencies monitored. A small sharp peak is visible at 1145 cm^{-1} and a larger peak is visible at 249 cm^{-1}. Both these peaks are narrow, with FWHMs of 13 ± 3 and 18 ± 4 cm^{-1} respectively. Note that the low energy peak, while being close to the phonon peak of bulk CaF_2 (which occurs at 257 cm^{-1}) [70], does not occur at the same frequency, and is much narrower than the phonon peak (see section A.1).

The positions and the widths are determined through fitting with Gaussian functions. For the 1145 cm^{-1} line, a background trend which causes a distortion in the peak shape is present. This was dealt with by fitting the background with a quadratic and subtracting the fitted polynomial from the data. The parameters for the Gaussian fits are summarized in table 4.6. While the positions of the peaks are well defined the widths are less precise. Within the achieved precision, both the peaks are of similar sharpness. The low frequency peak is an order of magnitude greater in size when compared to the high frequency peak.

Particular attention should be directed at the shape of the low frequency peak. Under comparison with the time–frequency representation in figure 4.6(a) there is a clear difference in the shape of the peak, with the integrated peak appearing much sharper. This behaviour is in concord with the trend observed at the intermediate time scale presented in figure 4.6(b). Therefore variation in dynamic behaviour has a greater influence on the peak shape than the magnitude of the initial enhancement.

In between the two peaks a broad excitation region, extending from 400 – 1000 cm^{-1} is present. This region can be divided into two distinct regions by considering the dynamic behaviour of the emission.

Toward the high frequency end of the broad peak (at around 800 cm^{-1}) we see what is likely a feature due to intra–excitonic transitions via direct absorption of the IR by the ITE. This is characterized by fast rise times (on the same order as the temporal width of the IR pulse) and fast decay times (approximately 40 μs) and such dynamic behaviour is amply evident in this excitation region when the spectrum is considered in conjunction with the time–frequency spectrum, given in figure 4.5.

Toward the low frequency end of the broad peak (at around 600 cm^{-1}) the observed features are temporally slower. The behaviour is likely due to population transfer induced by local heating through the absorption of the IR radiation by the CaF_2 lattice. This possibility is discussed further in section 4.9.3.

The intensity of the excitation spectrum peaks towards the low frequency end of the broad

feature, at about 570 cm^{-1}. However, figure 4.5 indicates that the initial enhancement amplitude is greater at about 800 cm^{-1} IR excitation. It is also clear that this enhancement decays much faster when compared to the low frequency enhancement. This illustrates the value of obtaining both a time integrated and a time resolved spectrum as it reveals that differences in dynamics is most likely causing the observed peak shapes.

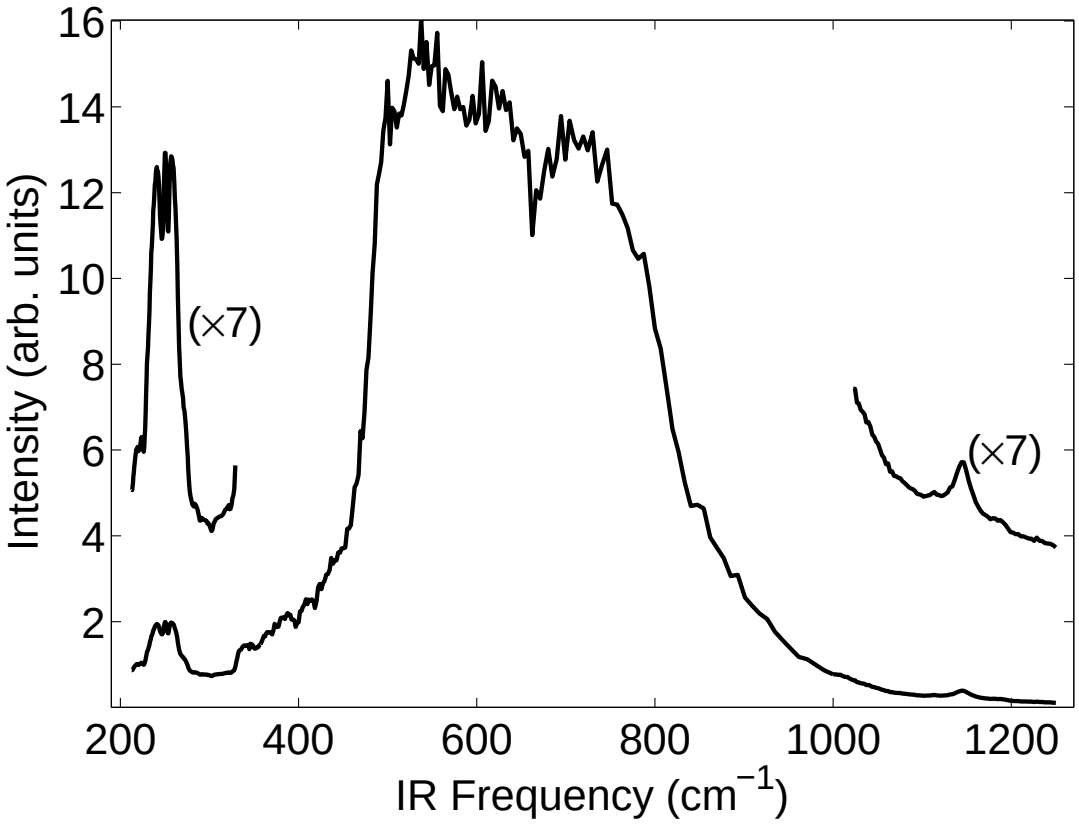

Figure 4.7 Time integrated excitation spectrum induced by the IR pulse in CaF_2:Yb^{2+} at a sample temperature of 8 K. The dips appearing throughout the spectrum are due to atmospheric absorption of the IR radiation.

Table 4.6 Parameters from fitting single Gaussians to sharp peaks present in the IR excitation spectrum of CaF_2:Yb^{2+}. A_0 of the high frequency peak was set at 1 to allow for easy comparison.

Parameter	**High frequency**	**Low frequency**
A_0 (a.u)	1	11 ± 4
ω_0 (cm^{-1})	1145 ± 2	249.1 ± 0.6
FWHM (cm^{-1})	13 ± 3	18 ± 5

4.4.2 Physical origins of the IR excitation features

By considering the model of the ITE (see chapter 2), a Yb^{3+} ion with a $4f$ hole ($4f^{13}$) and a delocalized electron, we are able to understand the broad band feature in terms of intra-excitonic transitions. Since there is a bond length change in the transition between the two excited states of the exciton [9] as shown by the analysis presented in section 4.3.3, such transitions would be vibronically broadened. Furthermore, such change will occur depending on the states occupied by the delocalized electron, since it is this electron that can affect bonding. The entire broad band is likely due to transitions that change the orbital of the delocalized electron. The intra-excitonic component of this band is associated with the excitation spectrum from 650 to 900 cm^{-1} by considering the dynamic behaviour previously observed.

The width of the direct excitation band is similar to that of the CaF_2 phonon spectrum [71], and gives a $\Delta R = 0.01$ Å using equation 2.7, for the transition from state 2 to a higher lying excitonic level. The difference in ΔR between transitions from states 2 and 3 to the ground state (see table 4.5) is also approximately 0.01 Å. This implies that the higher lying ITE state and state 3 are configurationally aligned and that the bond length change for the transition is small. A large bond length change would induce greater broadening as the lattice would undergo a greater perturbation, causing the nuclei of the neighbouring centres to move further, whose movement would in turn also take longer to dampen out [72].

While we can infer qualitatively that a configurational change has occurred under IR excitation and provide an estimate for the change in bonding, we are not able to provide an accurate model underscoring the position and width of the band. However detailed calculations with an *ab initio* approach as those done in ref [2] should yield such a model. Such a model would also be able to predict the expected position and line width in a material of similar properties to CaF_2:Yb^{2+} such as SrF_2:Yb^{2+} allowing for experimental verification of a sophisticated model.

The dips present within this broad band are due to atmospheric water absorption of the IR radiation along its beam path. Although purging the beam path with dry nitrogen helped alleviate the problem, it did not completely remove the highly sensitive absorption.

The sharp lines observed in CaF_2:Yb^{2+} (at 250 and 1145 cm^{-1}) can also be attributed to intra-excitonic transitions. However, given their line widths its clear they cannot involve a change in bonding, thus they must be as a result of changes within the $4f$ hole or

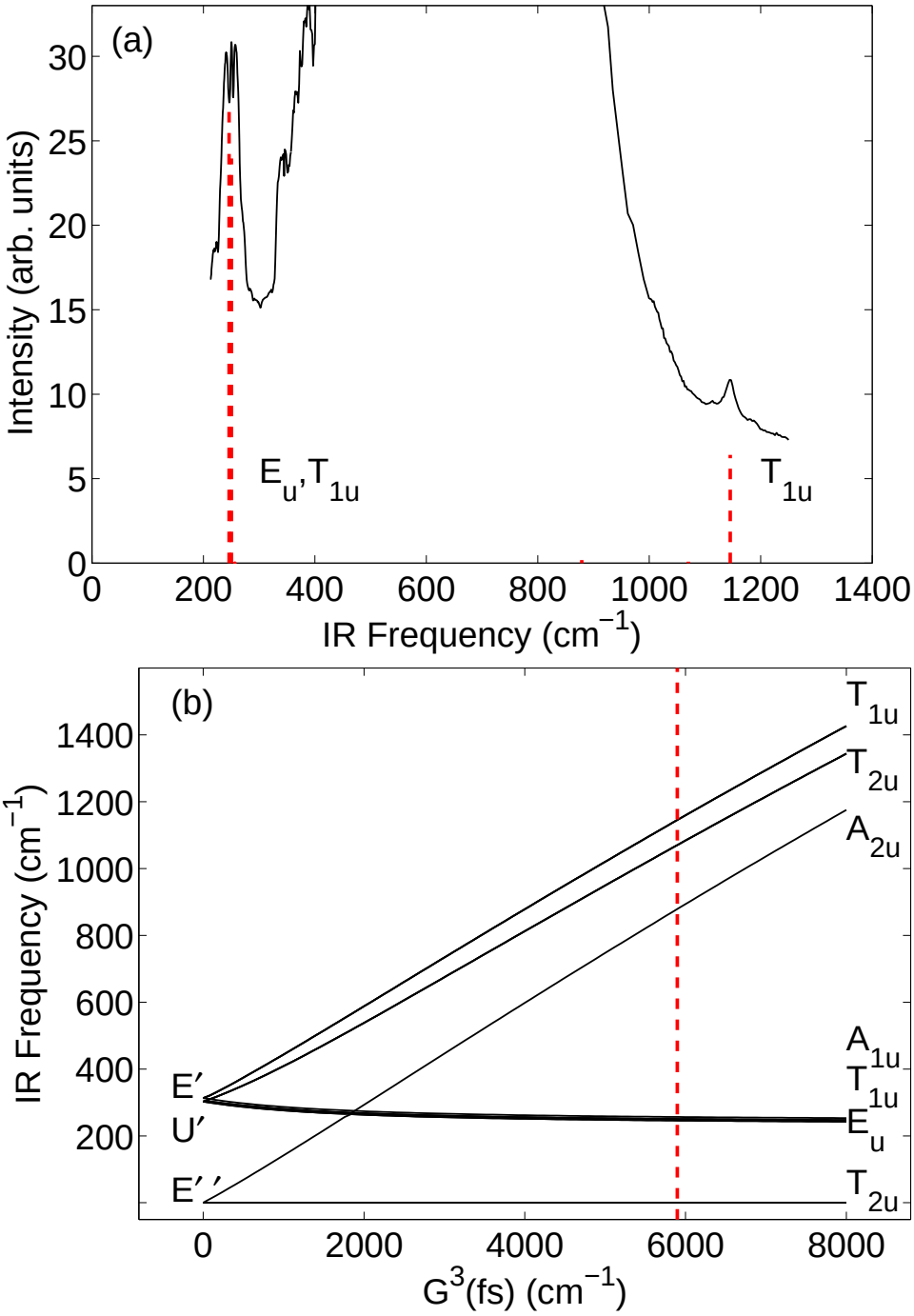

Figure 4.8 (a) IR excitation spectrum for CaF_2:Yb^{2+} including the calculated oscillator strengths for the transitions observed and (b) dependence of the exciton energy levels on the exchange parameter G^3(fs).

the relative spin of the $4f$ hole and delocalized electron (which involves an exchange interaction). If the transitions involved a bond length change, then as in the previously explored case, vibronic broadening of the line should occur.

Previous work by Sánchez-Sanz et al. [2] indicates that the excitons include a combination of $5d$ and $6s$ orbitals. While detailed calculations are available for the $SrCl_2$:Yb^{2+} system [7], as stated previously there are no detailed calculations available for CaF_2:Yb^{2+}.

However, using the semi-empirical model detailed in chapter 2, which constructs a Hamiltonian for a $4f$ hole and an s electron in a cubic crystal field,

$$H_{\rm cf} = \zeta A_{\rm so} + B^4 \left(C_0^4 + \sqrt{\frac{5}{14}} \left[C_4^4 + C_{-4}^4 \right] \right) + B^6 \left(C_0^6 - \sqrt{\frac{7}{2}} \left[C_4^6 + C_{-4}^6 \right] \right) + G^3(fs) g_3(fs), \tag{4.4}$$

where ζ is the spin-orbit interaction for the $4f$ electrons, B^4 and B^6 are crystal-field parameters for the $4f$ electrons, and $G^3(fs)$ is the exchange interaction between the $4f$ and the delocalized electron, we may model the energies and relative intensities of the sharp lines.

Since only two sharp lines were observed, not all the parameters in the model can be determined exclusively using the data. These were set using values obtained from the literature (see table 4.7). With these settings and using $B^4 = -800$ cm^{-1} and $G^3(fs) = 5900$ cm^{-1} the observed sharp peaks were matched.

Table 4.7 Fitted parameters for the sharp lines observed in the CaF_2:Yb^{2+} IR excitation spectrum. The ζ value is from ref [3] and $\frac{B^6}{B^4}$ values are from reference [73].

Parameter	**CaF_2:Yb^{2+}(cm^{-1})**
ζ	2928
B^4	-800
$\frac{B^6}{B^4}$	-0.34
$G^3(fs)$	5900

The energy splittings and the manner in which the exchange parameter affects the excitonic energy levels in the particular case of CaF_2:Yb^{2+} is demonstrated in figure 4.8(b).

When the $G^3(fs)$ parameter is set to zero the $^2F_{7/2}$ multiplet of $4f^{13}$ splits into E'', U' and E' irreducible representations of the octahedral group [26], shown on the left hand side of figure 4.8(b). As $G^3(fs)$ is increased these states couple with ^{2}S (from the s like electron). Since the system has cubic symmetry only magnetic dipole transitions will be allowed. Calculated oscillator strengths for the absorption are compared with experiment in figure 4.8(a), which illustrates that for the 16 total possible levels, several transitions are forbidden or calculated to be very small. For the allowed transitions that are observed the oscillator strengths appear to be in agreement with the intensity of the observed excitation peaks.

The B^4 parameter is similar to -725 cm^{-1}, the value determined in ref [6] for $SrCl_2$:Yb^{2+} in a $4f^{13}5d^1$ configuration. A Hartree-Fock calculation for the $4f^{13}6s^1$ configuration of Yb^{2+} provides a value of $G^3(fs) = 3167$ cm^{-1} (employing code established by Cowan [74]) which is smaller than what is found in the peak position matching done above. This discrepancy can be explained by considering the likely nature of the exciton itself.

Recall that while the simple model of the exciton [11] has it delocalized over the next nearest Ca^{2+} ions, the more detailed calculations carried out in reference [2] on $SrCl_2$:Yb^{2+} suggest that it occupies the next nearest interstitial sites of the fluoride cage. It also indicates that the exciton, instead of being purely $4f^{13}6s^1$ like in character, has some coupling with the $4f^{13}5d^1$ states. Although these calculations also reveal that the delocalized electron exhibits s like symmetry, the exchange parameter must take into account the coupled structure of the delocalization. From Pan et al. [6] we see that the exchange splitting for $4f^{13}5d^1$ is greater than 2000 cm^{-1}. The relevant exchange parameters can range between 5000 - 7800 cm^{-1} (using the values from [6] and those adapted from [75] by Pan et al.). Given these factors, and considering a splitting of 1145 cm^{-1} observed in this system, the fitted exchange parameter is reasonable (note that the electron in our case occupies a more delocalized orbital than $5d$).

This analysis provides insight into the physical origin of the transitions observed in the excitation spectrum in CaF_2:Yb^{2+} and the parameters confirm that the model reflects a reasonable approach to understanding the ITE behaviour under IR excitation. This model can now be extended to other materials to test its robustness under differing lattice conditions. Such an extension is discussed in the case of SrF_2:Yb^{2+} in Chapter 5.

4.5 Dynamic behaviour of the ITE under IR excitation

Investigation of the temporal behaviour for varying IR excitation frequencies will provide deeper insight into the properties of the ITE. For that purpose we study the transients at three representative excitation frequencies from the broad excitation feature and compare their behaviour. From figure 4.9 it is immediately clear that there is considerable variation dependent upon the IR excitation frequency.

It can be seen that at 625 cm^{-1} excitation the decay times are much larger than at any of the other excitation frequencies presented. However, the rise times of the transients gets progressively larger with decreasing excitation frequency.

This trend was not immediately obvious from the time–frequency plots of the data presented in figure 4.5. Figure 4.9 (b) illustrates the rise time trend by allowing direct comparison of the rise times via normalization. The shaded area indicates the length of the IR pulse and illustrates that even at an excitation frequency of 875 cm^{-1} there is a rise in the emission beyond the termination of the IR pulse.

Drastic changes in dynamic properties, such as those above, may be interpreted as excitation into completely different ITE states displaying varying life times and excitation pathways. However one must consider the transient properties in conjunction with the emission spectra presented previously (in section 4.3.2). From these we know that the emitting state (under the excitation frequencies presented here) is likely state 3 of the ITE (there is also a contribution from state 2 which is much smaller). What is evident in examining the data acquired for varying IR excitation frequencies is that there are different dynamic mechanisms driving the population changes of the two emitting states in the ITE.

4.6 Mechanisms of oscillator population changes in the ITE system

The dynamic properties of a system must ultimately be modeled via a set of rate equations that take into account the possible transitions and their likelihoods. However, before this can be done due consideration must be given to the origin of the particular properties exhibited by the transient within the search space traversed by the experiment.

From section 4.1 it is clear that once a population transfer occurs from state 2 to state 3,

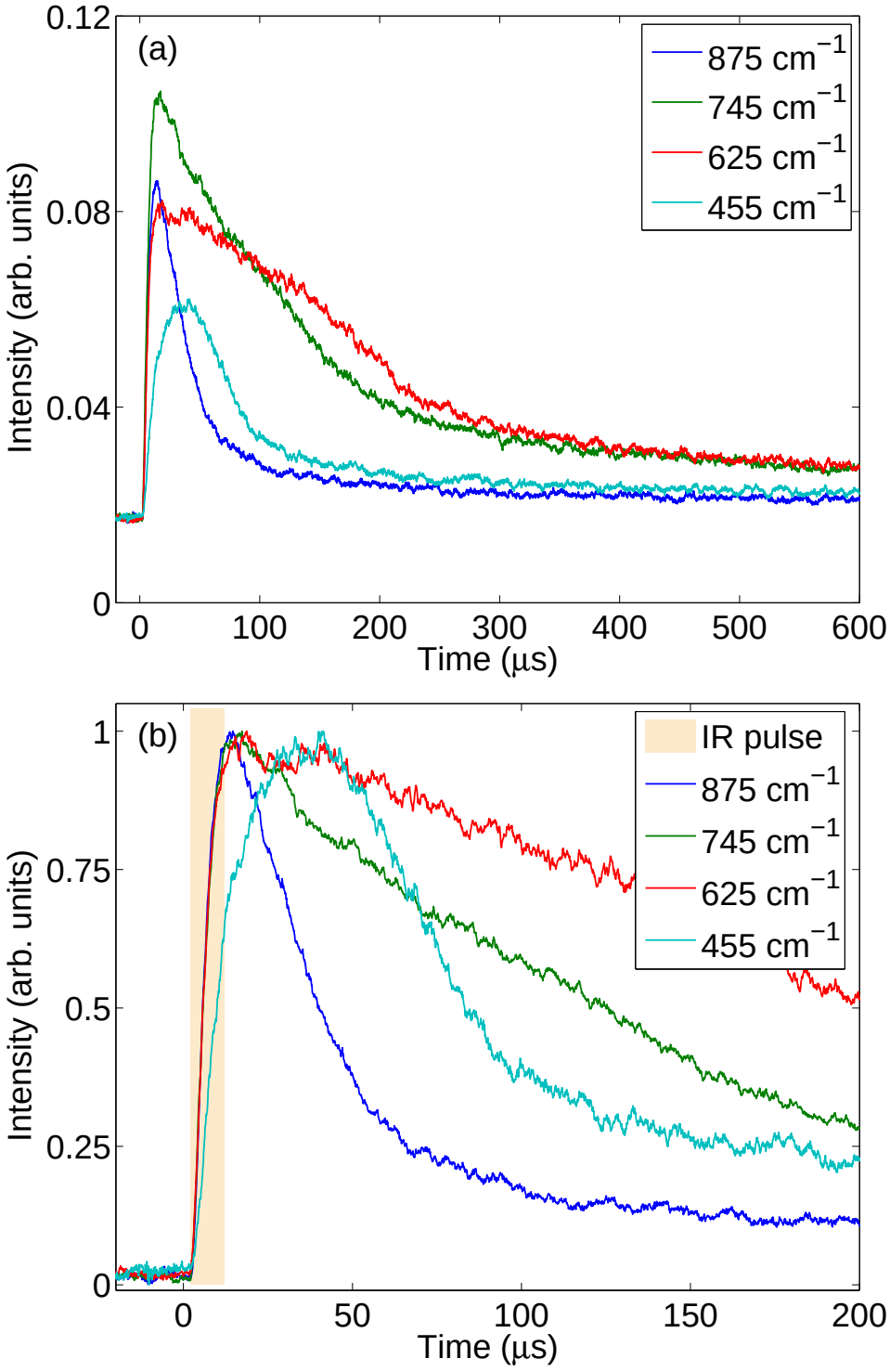

Figure 4.9 (a) 8 K transient photoluminescence enhancement representing the four regions of the broad band discussed in section 4.4. (b) The transients from (a) normalized such that their domain is $[0, 1]$ to allow for easier comparison. The shaded area indicates the length of the IR pulse as recorded.

an increase in the emission will occur. Population placed within state 3 will also decay to state 2 at a rate of W_{32} in addition to radiatively decaying to the ground state of the Yb^{2+} ($4f^{14}$). The coupling that exists between W_{32} and W_{23}, governed by equation 4.2, means the system will exhibit a temperature dependent change in emission as the overall radiative rate will depend upon the population distribution among states 2 and 3. From these factors it can be seen that there are two regimes under which state 3 can be populated.

The first is **equilibrium population of the state**, where a steady state sample temperature causes the existence of a steady population ratio between states 2 and 3. This ratio is determined purely by W_{32} and the sample temperature of the system and will not change throughout the decay process, thus leading to a steady rate of emission. The rate of emission will change with temperature as this drives the ratio of populations in the two states.

The second regime is **non–equilibrium population of state 3**, where the ratio of the population of state 3 to state 2 is greater than what is established by the sample temperature. In such a case the primary decay pathway of the population of state 3 will depend upon the relative sizes of W_{32} and A_{31}.

Three possible origins for the oscillators that result in the non–equilibrium population of state 3 are considered:

1. Intra-excitonic transitions induced by the IR pulse, where oscillators in state 2 are excited into state 3, through an intermediate level within the ITE. The emission may rise beyond the termination of the IR pulse if the intermediate level has a large enough transition time to state 3. However this rise time will be independent of IR fluence. The decay rate would be a combination of the radiative (A_{31}) and non–radiative (W_{32}) rates. Because the rates involved with depopulation of state 2 into the ground state are much smaller than the rates of depopulating state 3 (irrespective of the final state of the transition), given enough time the emission would return to the pre–IR intensity.

2. Local heating of the sample where the IR beam is incident could cause the local temperature of the sample to rise, such that state 3 is thermally populated in a small region of the sample. As the heat conducts away and the area local to the incidence of the IR beam cools to the sample conditions, the rate of population of state 3 will diminish. The rise and decay of the emission would depend upon the

local temperature changes, governed by the heat capacity and thermal conductivity of the sample. Both of these properties are heavily temperature dependent in CaF_2 [20, 21] thus the behaviour of the transients will change significantly with the IR absorption of the lattice.

3. States 2 and 3 may be populated from sources external to the ITE system. For example the liberation of electron traps by the IR radiation into the conduction band could cause them to decay to the ITE excited states, leading to a greater population in state 3 than would be present at equilibrium conditions. There are numerous examples in literature documenting the liberation of traps as a source of electrons that ultimately lead to emission [76–81]. These traps are often identified via thermoluminescence and photoluminescence after irradiation under high energy radiation (for example x - ray, electron beam irradiation) [78–80, 82]. In this scenario, the electrons are likely liberated in to the conduction band [83] of the CaF_2, where they tumble to the ITE states through a mechanism that is similar to manner in which the ITEs are formed in the first place [9, 11], as explained in section 2.2.

It is likely that a combination of the scenarios described above take place under illumination by the IR pulse. Before proceeding to modeling of the dynamic properties, it would be pertinent to identify the described scenarios taking place within the ITE system and this can be achieved by examining the transients obtained throughout the experiment over a variety of additional search parameters (e.g. IR fluence, sample temperature).

4.7 Dependence of transients on IR fluence

Power dependent transient measurements were taken at an excitation frequency of 800 cm^{-1} shown in figure 4.10. The rise time of the enhancement appears to increase with power and the decay rates of the initial enhancement also appear to decrease. The peak intensity also appears to saturate, with the increase in IR fluence from 4.8 to 9.6 Jcm^{-2} not corresponding to a doubling of the peak intensity.

Figure 4.10 (b) illustrates the behaviour of the transient with emphasis placed upon the enhancement. Here there transients are normalized to a domain spanning $[0, 1]$ to allow for easier comparison between them. The shaded area indicates the duration of the IR pulse as recorded during the experiment. While no discernible rise is observed at an IR fluence of 1.4 Jcm^{-2} at the full IR fluence of 9.6 Jcm^{-2} it is clear a significant rise has built in.

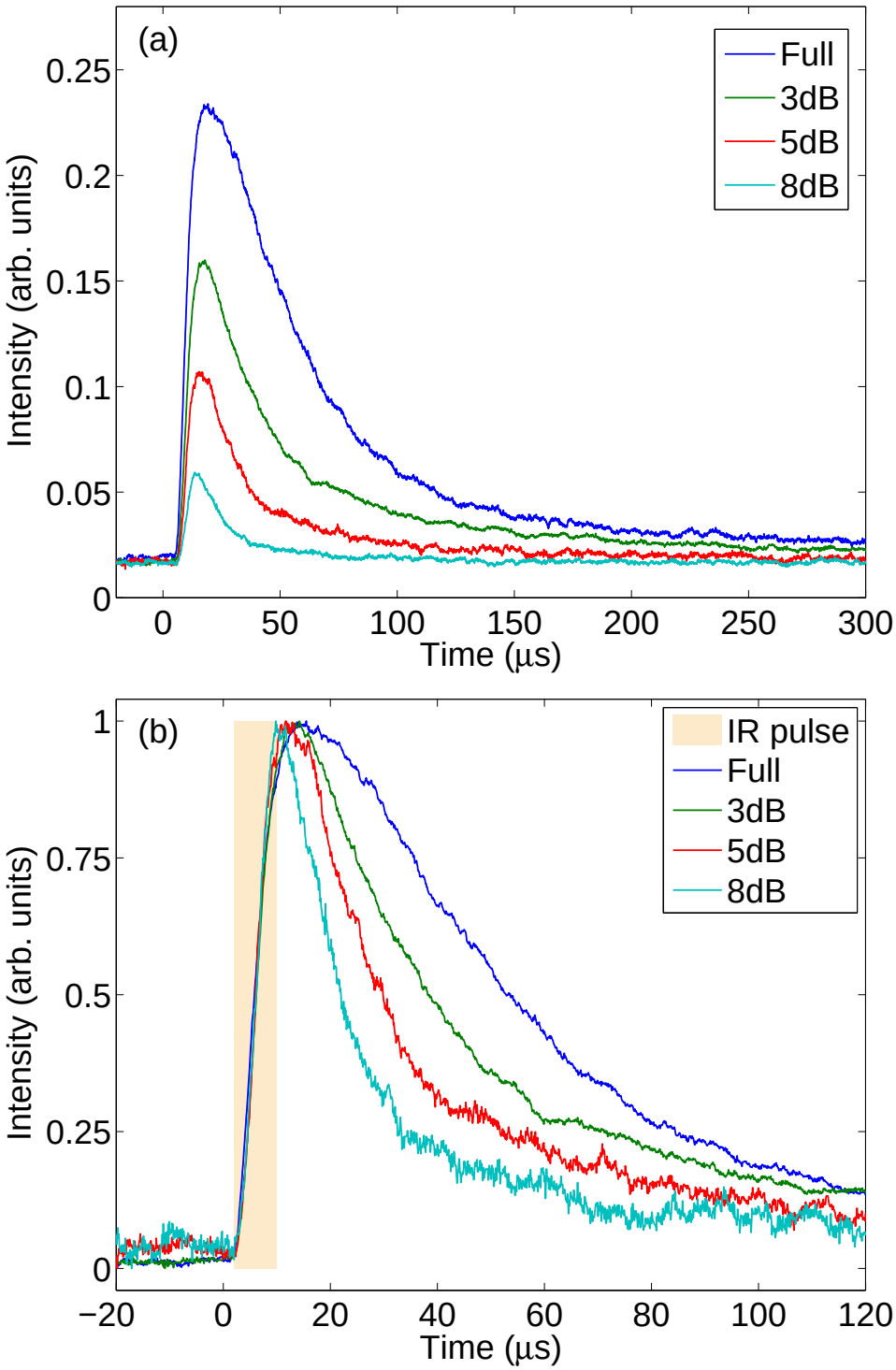

Figure 4.10 (a)The 8 K transients at different IR excitation powers for a frequency of 800 cm^{-1} monitored at 18500 cm^{-1} are presented for comparison. The maximum IR fluence was 9.6 Jcm^{-2}, at 3 dB attenuation the IR fluence was 4.8 Jcm^{-2}, at 5 dB it was 2.9 Jcm^{-2} and at 8 dB it was 1.4 Jcm^{-2}. (b) The transients normalized to a domain of $[0, 1]$. The shaded area indicates the IR pulse length.

Figure 4.10 (b) also reinforces the large differences in decay rates with changes in the IR fluence. It is clear that as the IR fluence increases the decay rate of the emission decreases. This raises the question of what relationship the total enhancement intensity has with IR fluence. Figure 4.11 shows that both the peak and total enhancement (with the transient integrated from 0 to 150 μs) appear to be sublinear with IR fluence. However when considering the total enhancement the sublinearity is far less pronounced than in the case of the peak intensity.

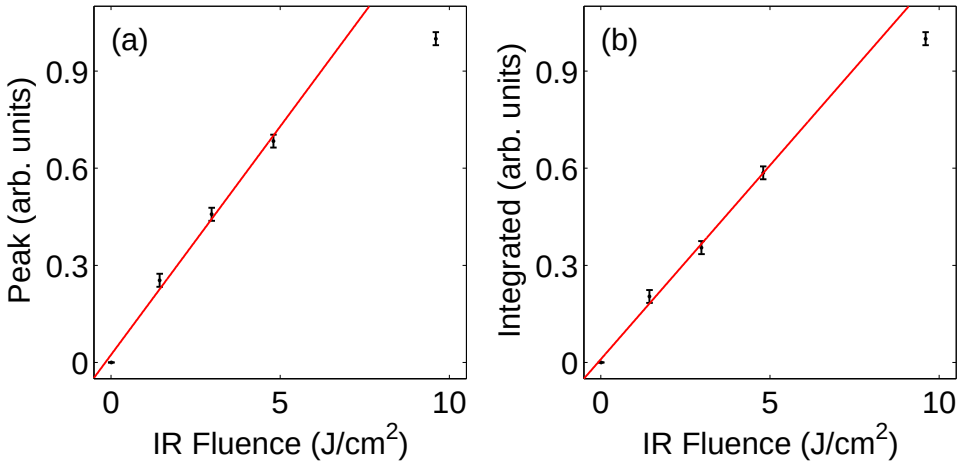

Figure 4.11 The behaviour of the emission enhancement under changing IR fluence is presented, with (a) representing the peak intensity of the enhancement at a given fluence, while (b) shows the total integrated intensity over the entire enhancement (the integration was taken from $0 < t < 120$ μs). Both plots have been normalized such that the maximum value is 1 to allow for ready comparison.

While the behaviour of the peak enhancement indicates possible saturation of the population transition under IR excitation, the total enhancement indicates the likely involvement of a process additional to the direct electronic transitions. If the transitions were truly saturating the integrated total intensity of the enhancement would not tend towards linearity. As we shall see later (in section 4.9.3) the additional process is likely heating caused by the absorption of the IR radiation.

4.7.1 Transient behaviour at extreme IR fluence

As previously mentioned FELIX can operate in two pulse train modes (see section 3.2), with micro pulse repetition at 25 MHz or 1 GHz. The 1 GHz regime applies 40 times the power of the 25 MHz regime at a given excitation frequency.

Chronologically the 1 GHz experimental runs were conducted prior to many of the runs

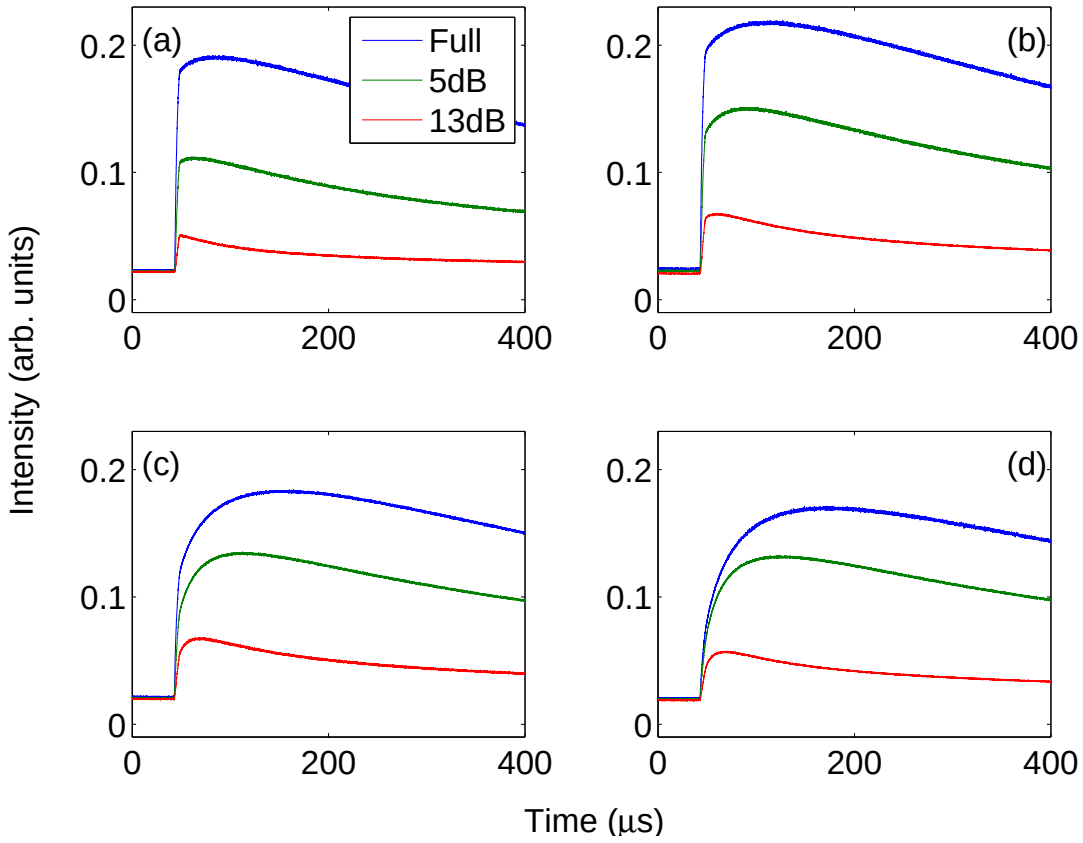

Figure 4.12 Transients observed under IR excitation with the micro–pulse repetition rate set to 1 GHz across four different frequencies with (a) at 833 cm^{-1}, (b) at 714 cm^{-1}, (c) at 625 cm^{-1} and (d) at 500 cm^{-1}. Multiple IR attenuations are also presented at each frequency with 0 attenuation (full) corresponding to an IR fluence of 100 Jcm^{-2}, a 3 dB attenuation to 50 Jcm^{-2} and an 8 dB attenuation to 15 Jcm^{-2}.

at 25 MHz contributing to a majority of the data presented in this chapter. The chief reason for this was that with the increased power delivered under the 1 GHz regime, the enhancement was easier to locate when setting up the experiment. Additionally the signal to noise ratio also benefited from the extra available power.

When considering the 1 GHz data collectively with other observations they can provide valuable qualitative insight into the dynamic behaviour of the CaF_2:Yb^{2+} ITE system. From figure 4.12 it is clear that the IR fluence dependent rise times are consistent across a wide range of IR powers. The behaviour observed in the 25 MHz transients is again on display here, with the rise times growing prominent as the IR fluence increases. The decay rates also slow with increasing power (consistent with the 25 MHz regime) however, in this case the fast decay in the enhancement is not observed, except minimally at an IR attenuation of 13 dB (a decrease in the pulse energy by a factor of 20 which still

provides twice as much energy as the maximum at 25 MHz). Instead a decay rate that is substantially greater than A_{21}, but smaller than A_{31} is observed, indicating that a sustainable population ratio shift has occurred between states 2 and 3 subsequent to the IR pulse.

Additionally, the IR excitation frequency dependence of the transient behaviour is reinforced, with an increase in the rise times and slowing of decay rates observed as the IR frequency decreases towards 400 cm^{-1}. Notably at maximum power, with decreasing frequency the decay slope appears to become somewhat shallower, likely due to an increased ratio W_{23}/W_{32} being sustained for longer through slow cooling (see section 4.11.3).

4.8 Temperature dependent transient photoluminescence enhancement

We have already seen that the emission spectrum changes in a similar manner with both increases in sample temperature and IR excitation (section 4.3.1). Given this similarity one would expect to see the influence of the IR diminishing with increasing sample temperature. Figure 4.13 shows that this is indeed the case. Here the transients are presented from the incidence of the UV pulse (at $t = 0$ μs in this case) to illustrate the influence the sample temperature has upon the dynamic behaviour.

Prior to the IR pulse the transients show increasing emission intensity with increasing temperature, as well as an increasing decay rate. This is due to the increasing population of state 3.

As the temperature increases the influence of the IR excitation also diminishes. Assuming the interaction cross section between the IR radiation and an oscillator in state 2 remains unchanged with temperature, as the number of oscillators in state 2 decreases the number of transitions into state 3 via the absorption of the IR into the ITE decreases, leading to the observed effect. At 50 K the influence of the IR is not discernible.

Examining the initial emission intensity of the 50 K transient upon excitation with the UV pulse also provides an indication that the IR does not cause saturation[6] of the transition into state 3. Examining the peak height of the emission enhancement (at 10 K) it is clear that the maximum intensity caused by the IR is smaller than the peak intensity of the

[6]Here saturation is defined as the IR completely depleting the population of state 2, such that any additional IR photons would not cause an increase in the observed enhancement

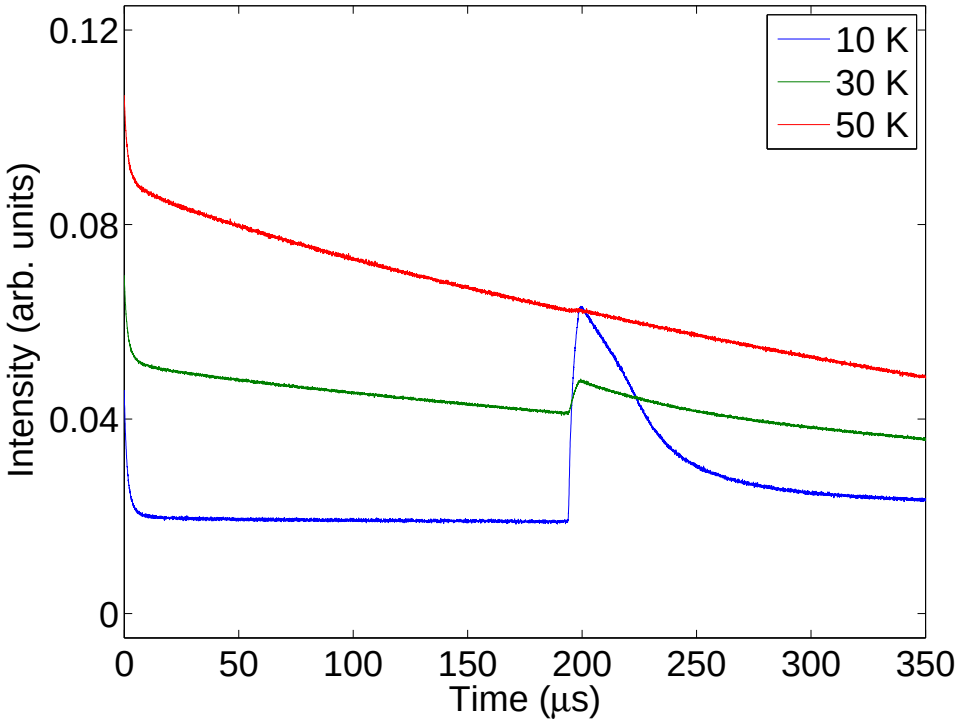

Figure 4.13 Temperature dependent behaviour of the transients under IR excitation at 714 cm^{-1}.

emission at 50 K. This indicates that a temperature of 50 K creates a larger population of oscillators in state 3 than the IR pulse does. Given this is possible, the IR cannot be causing saturation.[7]

It should be noted that even at 50 K the population of oscillators is not entirely in state 3. This can be inferred by examining the ratio $W_{23}/W_{32} = 0.94$ at 50 K. Therefore the non–radiative transition from state 3 to state 2 is still slightly favoured, meaning the equilibrium population distribution is in favour of state 2. This is reinforced by extracting the decay rate of the 50 K transient through an exponential fit, giving $\tau = 1600 \pm 30$ s^{-1}, slower than $A_{31} = 3800$ s^{-1}.

[7]Note that while some of the oscillators have decayed to the ground state before the incidence of the IR pulse, given the UV – IR delay of at most 200 μs and decay constant of ITE emission of 15 ms, this effect is negligible. Also note that the comparison being made is between the maximum number of oscillators excited into state 3 by a sample temperature of 50 K and the maximum number of oscillators the IR excites into state 3.

4.9 Identification of oscillator population transfer mechanisms in CaF_2:Yb^{2+}

4.9.1 Evidence for direct transitions present in the transients

The dependence of the PL enhancement on IR excitation frequency demonstrates the vast differences in their rise and decay profiles (see figure 4.5). Since the transients show fast rise times at the higher excitation frequencies by examining the rise characteristics at these frequencies (with provision made for the IR pulse profile) it is possible to determine whether intra–excitonic excitation or local heating gives rise to the enhancement.

From figure 4.9 (b) it can be seen that at an excitation frequency of 875 cm^{-1} the rise in the enhancement does not proceed beyond the termination of the IR pulse. As the IR pulse ends the enhancement begins to decay rapidly and the emission has reached a pre–IR intensity at approximately 600 μs. The lack of a rise time greater than the duration of the IR pulse indicates that it is unlikely that local non–equilibrium heating plays a major role in the enhancement at this frequency. Given the thermal conductivity of CaF_2 it is unlikely that a temperature rise sufficient to provide the observed enhancement would dissipate at a rate required for no rise time to be observable in the transient. The lack of a distinct offset in emission intensity towards the latter region of the transient indicates that liberated traps are unlikely to be contributing in a significant manner to the enhancement at this frequency.

When considering these factors it is likely that there is transfer of population occurring within the ITE under IR excitation. The IR pulse places the oscillators in an ITE state at a greater energy, which has good configurational overlap with state 3, allowing for fast population of state 3. The analysis of the IR excitation spectrum in section 4.4.2 indicates the possibility of a higher energy ITE state. The bond length calculations conducted therein supports the higher ITE state and state 3 having similar configurations. Furthermore analysis conducted on the temperature dependent intensity and lifetimes of the ITE emission based on a method adapted from that employed by Moine et al. for analysing the ITE in SrF_2:Yb^{2+} [12] indicated the possibility of a higher ITE state in CaF_2:Yb^{2+}.[8]

Naturally, the question of whether the fast component of the emission enhancement is

[8]This work was conducted by Rosa Hughes-Currie for her BSc. Honours project and has been acquired through personal communication by the author. The work is not included in this thesis.

simply due to emission from this proposed higher state arises. However the evidence suggests that this is not the case. From examining the blue shift in the emission spectra under IR excitation at 800 cm^{-1} (section 4.3.2, figure 4.4 (a)), where the transients display fast behaviour, it can be seen that that both the peak position and its width immediately after excitation by the IR pulse correspond favourably with the behaviour of the spectrum under a sample temperature rise from 8 to 40 K (refer to tables 4.2 and 4.3 for specific numbers). A sample temperature of 40 K is not large enough to populate the exciton state accessed by the IR pulse at a frequency of 800 cm^{-1}, yet the spectral properties of the emission resulting from the two cases are statistically identical, indicating that the emission emanates from the same state (state 3) in both the cases.

4.9.2 Do liberated traps contribute to the enhancement?

Mainly informed by the behaviour observed in our experiments with MgF_2:Yb^{2+} (see chapter 6) [81] the initial interpretation of the observed offsets in the emission transients of CaF_2:Yb^{2+} under IR excitation was that they were caused by an overall increase in the population of state 2. The origin of these 'extra' oscillators was assigned to electron traps that become liberated under illumination with the IR pulse [81, 84, 85].

Upon examination of the offset distribution with respect to IR excitation frequency, we were able to provide an approximate matching to a Coulomb trap with a threshold 390 cm^{-1} in CaF_2:Yb^{2+} (see figures 4 and 7 in ref [85]). The Coulomb trap model can be described as follows:

$$\rho(\omega) = \gamma \frac{(\omega - E_d)^{3/2}}{\omega^5} \tag{4.5}$$

where ρ is proportional to the ionization cross section of the traps, but translated to intensity of light from liberated traps via the constant γ. E_d denotes the trap threshold and ω is the IR frequency. The equation is adapted from equation 3 of reference [86].

It should be noted that the Coulomb trap model was not able to account for the relatively sharp drop off in emission offset towards the higher excitation frequencies [85] nor match the peak of the emission offset precisely.

Additionally there is direct evidence of trapping induced by the UV illumination of the sample in the case of SrF_2:Yb^{2+}. In the case of SrF_2:Yb^{2+} the IR pulse does cause a liberation of these traps, however they appear to decay to the ground state of the system

rather than populating any excited ITE states (please see chapter 5 for more details on the observations recorded in SrF_2:Yb^{2+}). This leads to the reinforcement of the above interpretation as the source of the observed emission offset.

However there were oversights in the analysis done that led to the above interpretation. Chief among which was the neglect of the rates of decay of the emission towards the end of the transients (i.e. the region responsible for the emission offset). Furthermore the transient shapes suggest that the ratio of populations of state 2 and 3 are changing (i.e. the emission is decaying towards the pre–IR intensities, rather than to 0). This is achievable by liberated traps that populate state 3 very slowly (i.e. on the order of 100s of μs), however there is then an inconsistency in the intermediate components of the transients (i.e. between the fast direct transitions and the offset).

It is possible that the liberated electrons populate state 3 via a distribution of higher ITE states with a continuous spread of decay rates in to state 3, however a simpler explanation for the observed phenomenon is that the sample undergoes local (thus non–equilibrium) heating.

4.9.3 Evidence for non–equilibrium heating under IR illumination

CaF_2 exhibits significant absorption in the frequency range used in the IR scans [19, 70] (see appendix A.1 for details). As explained in reference [19], this is due to the phonon population that exists at these frequencies. As the frequency decreases from 1000 cm^{-1} towards 200 cm^{-1} the phonon density of states grows rapidly, and as does the concomitant IR absorption. The resultant phonon population is equivalent to a local heating effect. The rest of the sample is held at a fixed temperature (in our experiment indicated to be approximately 8 K by the cryogenic equipment), thus the heat will dissipate continuously out of the region illuminated by the IR beam. This region will thus experience varying temperature across the time spanned by the transients. The temperature change of this region can be computed by knowledge of the energy the IR pulse contains (measured) and the heat capacity of the lattice, known from previous studies of the material [20]. The decay of the non–equilibrium local temperature will be dependent upon the conductivity of CaF_2 and this will determine the time scales over which the ratios of the populations in state 2 and 3 will change. Because there is a frequency dependence on the absorption of the IR into the CaF_2 lattice, there will also be a frequency dependence in the amount of local heating that the sample experiences.

If the emission offsets described previously are to be examined in this context, where local non–equilibrium heating can occur, some measure of the occurrence of heating is required. As we know from sections 4.1 and 4.6, under changing temperatures the population ratios of states 2 and 3 change, thus the decay rate of the emission also changes. Examining the decay rate well away from the initial enhancement, and close (in time) to the end of the transient (between 500 and 800 μs) allows for identification of the population ratio change and provides an indication of possible local heating within the sample. From the changing decay rates we can thus infer what changes are occurring in temperature.

The decay rates towards the end of the transients were taken into account by examining the slopes in the time region $500 < t < 800$ μs under a logarithmic transformation of the transient curve. As figure 4.14 shows, the intensity of the emission offset appears to be well correlated with the decay rates. This correlation indicates the emission offset that is observed is likely due to emission occurring from state 3 rather than an increase in oscillators in state 2.

The trend observed is even more pronounced when considering the IR excitation scans with emission being monitored at 18500 cm^{-1} as illustrated by figure 4.14 (b) (this is near the peak of the emission resulting from state 3). This reinforces the notion that the offset is primarily due to emission out of state 3.

It should be made clear that the *direct implication* of these correlations is simply that the origin of the observed offset in emission is due to a considerable population existing in state 3, well after the initial enhancement has occurred. However given the observed longevity of the population of oscillators in state 3, combined with the knowledge that out of equilibrium population decays to state 2 rapidly (section 4.9.1) the observed offset can be inferred to be due to local heating. Furthermore the observed increase in intensity as the IR frequency lowers matches with the IR absorption properties observed.

Additionally examining the transients directly shows that at IR frequencies where the offset is greatest, the rise time in the initial enhancement appears to extend further in time than the termination of the IR pulse. In combination with this, greater decay times (thus smaller decay rates) in the enhancement are also observed in this excitation region. Figure 4.9 (b) illustrates the rise beyond the IR pulse length and the decreasing decay rates observed over a variety of IR excitation frequencies, and it is clear that as the frequency decreases (i.e. the IR absorption by CaF_2 increases) the rise time becomes more pronounced. This correlation increases the plausibility of local non–equilibrium heating. For the population of state 3 to continue to rise beyond the initial excitation by the IR

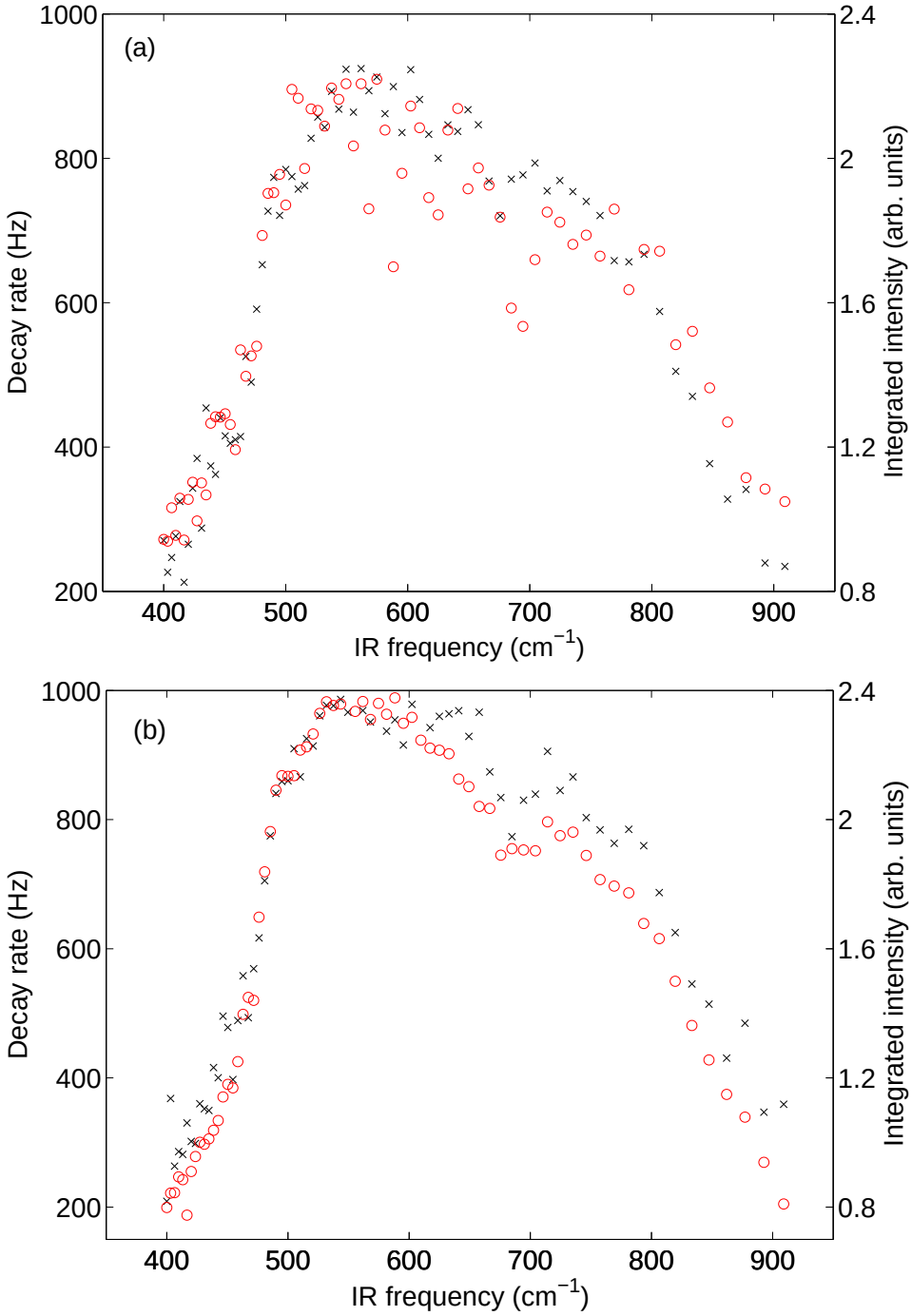

Figure 4.14 IR frequency dependence of the long time decay rates (black crosses), showing strong correlation with the emission offset intensity (red open circles), illustrating that the offset observed in the emission is due to the population of state 3. (a) The emission is being monitored at 17700 cm^{-1} and (b) with emission monitored at the 18500 cm^{-1}, nearer to the peak of the emission resulting from state 3.

pulse requires a positive change in temperature, driving W_{23} higher via its Boltzmann coupling to W_{32}.

The power dependent behaviour of the transients is also indicative of heating, with the rise times increasing and decay rates decreasing as the power increases. The observed trend where the enhancement appears to saturate with increasing power can also be explained with heating when one considers that there is a temperature dependent rise in the thermal conductivity of CaF_2 [20] and thus the temperature will reach a saturation point with increasing power.

The transients observed under IR excitation with the micro pulse repetition set to 1 GHz provides further evidence of heating. In these transients (presented in section 4.7.1) rapid decay from state 3 to 2 is not seen, and the rise time is pronounced. The rate of emission appears to tend towards $A_{31} = 3800$ s^{-1}. The power dependent observations are still consistent even at this regime, with both the changing rise times and the slowing decay rates observed as power is increased. The saturation effect is also seen when considering the peak emission intensity in time.

A key question now arises. Why does the rise time appear to increase as the energy available for heating is increased (be it through dialing up the IR power or through greater absorption)? Surely, given the relationship between W_{23} and W_{32} it is reasonable to expect the rise to speed up as the power increases? This expectation would be valid if the sample did not begin cooling toward the ambient temperature of the rest of the sample immediately at the termination of the IR pulse. Because of this cooling, slower rates are immediately overshadowed by the rate at which the sample cools, and the value of W_{23} simply is not large enough to create a significant increase to the emission enhancement to overcome the fast decay out of state 3. Additionally the rise effect is influenced by the potential of the IR excitation frequency to directly excite the oscillators. The ratio of this rate to W_{23} also plays a role in determining the rise time.

4.9.4 Why was heating initially dismissed?

It is prudent to provide an explanation for what informed the decision to discount heating as a possibility for some of the observations in our initial interpretation of the data. As both figures 4.14 (a) and (b) show, the offset and indeed the enhancement diminishes towards 400 cm^{-1}, while the absorption increases (section A.1). Therefore we assumed that if the properties displayed by IR excitation around the 600 cm^{-1} region were due

to heating, they would have to increase toward the peak of the IR absorption and the enhancement would not diminish as observed.

Upon first consideration this appears to be a sound argument, however it overlooks an important factor in that the heating required for the observations is local to the volume of the crystal *where both the UV and IR are interacting* with each other. Because of this an account must be made of the penetration depth of the IR through the crystal to determine how much heating power it can deliver to a particular region where the UV beam is also present. As the IR absorption rapidly increases towards 225 cm^{-1} the beam loses the ability to deliver heating to the region of the sample that is producing the greatest intensity of emission.

It should be noted however that if there are direct resonant transitions present in excitation frequency regions where the IR cannot deliver heating power, these may still be prominently observed. The number of photons required for resonant transitions is far fewer when compared to the number required for heating a region within the spot size of the IR beam.

4.10 Thermal effects due to IR absorption

The evidence presented in section 4.9.3 means that local non–equilibrium heating and the subsequent dissipation of that heat must be examined and taken into account in detail if the dynamic properties of the transients are to be modeled with accuracy. The heating of the lattice by the IR and the subsequent cooling are modeled. Details of the modeling are presented in appendix C.

The volume V where the local heating occurs is defined as shown in figure 4.15. The IR beam, assumed to be TEM_{00}, is centered on and propagates along the z axis. The centre of the cylinder experiences the maximum IR fluence which decreases diametrically due to the Gaussian beam shape of TEM_{00}.

The time dependent energy imparted within V can be expressed by,

$$Q(x, y, t) = E_m f(t) g(x, y), \tag{4.6}$$

where E_m is the maximum total energy imparted by the beam over both space and time (thus dependent upon both IR fluence and absorption by the lattice), $f(t)$ is the

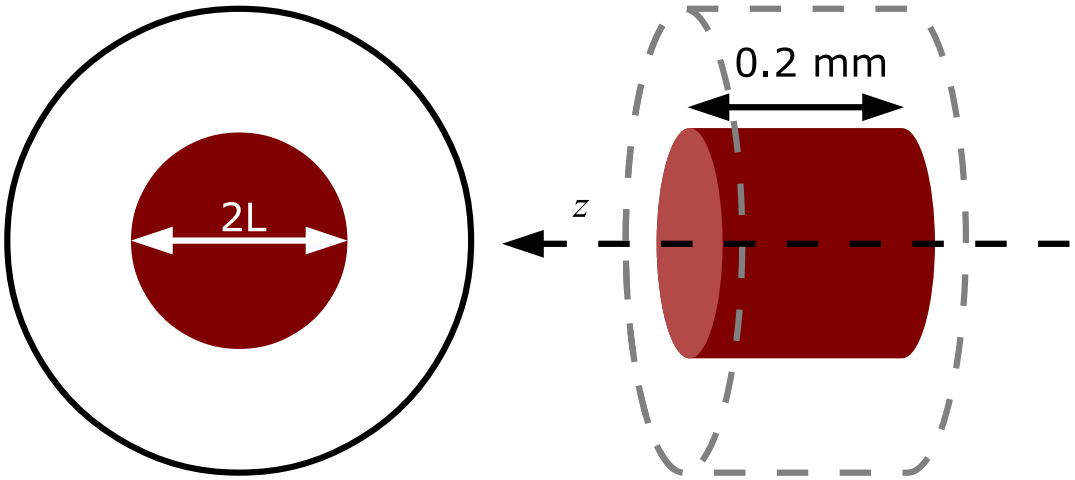

Figure 4.15 Schematic of the volume where the local heating is assumed to occur. The z axis arrow defines the direction of IR propagation with the beam centered upon the axis. The plan view on the left is looking down the axis, with $L = 100$ μm. The diameter of the cylinder is twice the spot size of the IR beam.

normalized time dependent pulse shape of FELIX,[9] and $g(x, y)$ is the normalized beam energy at a given point (x, y) over a region A enclosed by $-L < x < L$ and $-L < y < L$, with $L = 100$ μm for a Gaussian beam shape.[10]

Division of equation 4.6 by the temperature dependent heat capacity of CaF_2, $c(T(x, y, t_{n-1}))$, defined over all points within A gives the following equation for the change in temperature:

$$\frac{dT}{dt_n} = E_m \frac{f(t_n)g(x, y)}{c(T(x, y, t_{n-1}))}, \tag{4.7}$$

where c is also time dependent due to the time dependence of T. Note that equation 4.7 is in discrete form (with n being the time step) to allow it to be used in numerical computation.

Because $c(T)$ is heavily temperature dependent at low temperatures [20] the temperature distribution over A is a distorted Gaussian shape with a width that is dependent upon the total energy input E_m. Therefore different E_m values with identical beam FWHMs will cause different temperature distribution widths.

The dissipation of the local temperature perturbation is modeled by solving the heat equation [87],

[9] The time integral of $f(t)$ over its duration is unity.
[10] The volume integral of $g(x, y)$ over the region A is unity.

$$\frac{\partial T}{\partial t} = \alpha(T)\nabla^2 T, \tag{4.8}$$

where $\alpha(T) = k(T)/c(T)$. Here $k(T)$ is the temperature dependent thermal conductivity. Since T is dependent upon (x, y, t), α is a surface defined over the region A and is time dependent. Because of the temperature dependences involved equation 4.8 must be solved numerically. A *Forward-Time Central-Space* (FTCS) algorithm [88, 89] generalized to two-dimensions was used for the computation. A geometric mesh with a typical grid spacing $(\Delta x, \Delta y)$ of between 1 – 3 μm was employed. The forward time step was sufficiently small to satisfy the Courant-Friedrichs-Lewy (CFL) [90, 91] condition for numerical stability of the model. This condition, as it applies to the employed algorithm, can be stated as,

$$\alpha(T)\frac{\Delta t}{\Delta x^2} < 0.5, \tag{4.9}$$

where Δt is the length of the time step and Δx^2 is the square of the mesh spacing. Refer to appendix C.2 for the reasons behind the choice of algorithm, its details and the manner in which numerical stability was maintained.

Because $\alpha(T)$ is heavily temperature dependent for $T < 120$ K [21] the temperature distribution will influence the dissipation of heat from V. Thus variation in E_m leads to variations in how both the heating and cooling of the local region occurs.

Computing the average temperature of the region $(x, y) = (0 \pm 10, 0 \pm 10)$, determined by solving equations 4.7 and 4.8, a single time dependent local temperature can be obtained. Figure 4.16 shows the behaviour of the temperature in time as the energy input changes for a beam FWHM set at 60 μm to reflect the FELIX beam profile. Note that since the temperature distribution width is an inherent property of the system it is not free to be set.

Of particular importance is the failure of the temperature to return to the pre–IR value within the time frame of the recorded transients. Since the rate ratio W_{23}/W_{32}, and hence the population ratio between state 2 and 3, is influenced *only* by the temperature of the emitting region such an offset in temperature reinforces the supposition that the observed offset in the emission transients is likely due to heating. The cooling curves are different at different input energies, suggesting that the longevity of the thermal population of state 3 will be dependent upon the amount of IR radiation absorbed by the lattice. The maximum temperature reached by the system shows a sublinear dependence to E_m.

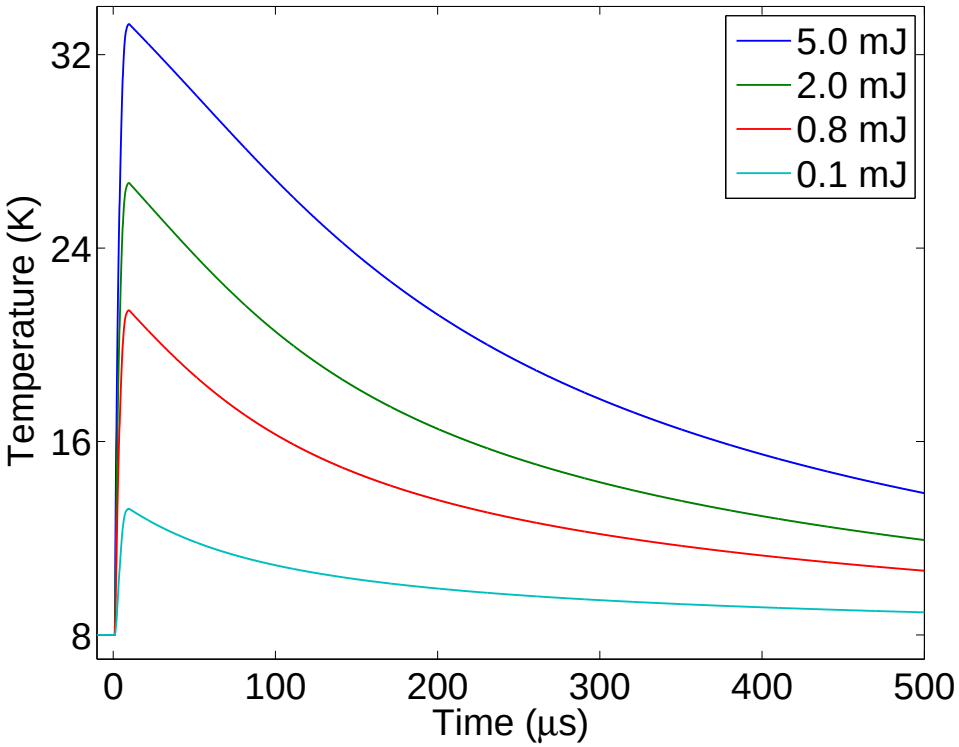

Figure 4.16 Temperature dissipation curves showing the variations in the time dependent shapes with input energy magnitude. The initial temperature distribution for these curves are seen in figure C.4. Note the behaviour of the peak temperature, and its clear sublinear dependence upon input energy. Also note the slight changes in the shape of the decay of temperature as the input energy increases. An offset in the local temperature is also observed where the system does not cool back down to the pre–IR ambient temperature of the sample.

4.10.1 The frequency dependence of IR heating

The energy that is available for local heating (E_m) depends upon the energy that is deposited into the lattice, which is determined by the frequency dependent absorption coefficient (as shown in figure A.1). Thus, one would expect that the greatest thermal influences would occur at 257 cm^{-1}, the peak of the IR absorption in CaF_2.

However, there is another aspect of the absorption that must be taken into account. As the absorption coefficient rises with the decrease in IR frequency, the beam gets attenuated through the sample and in order to cause changes in emission through heating a significant amount of energy is required *at the volume of the sample which has been pre excited by the incident UV beam.* As described in section 3.2 the UV and IR beams only overlap over a small volume (previously defined as V) in the middle of the sample. If the absorption

within the sample is too high, not enough photons will arrive at the volume of the sample where the two beams overlap, thus diminishing the potential of the IR pulse to cause thermally induced changes in the observed emission. Similarly, if the absorption within the sample is too small, not enough IR photons will be deposited into the lattice over the volume where the beams overlap, again reducing the thermal influences upon the emission. Because of this there will be an optimal IR frequency that causes the greatest thermal effects upon the emission.

It is possible to approximate the absorbed IR fluence across a certain length of propagation through the crystal using Beer's law [92] and the absorption coefficient β obtained from the data presented in figure A.1. This allows for the computation of the relative energy deposited into the volume V across the IR excitation frequency range. The volume V defined in figure 4.15 was used, with its rear surface at 0.4 mm from the rear of the sample along z.

The frequency dependent energy deposition is calculated by estimating the relative strength of the IR radiation at the rear surface of volume V with,

$$E_r = \frac{E(\omega)}{E_0(\omega)} = 1 - e^{\beta(\omega)\Delta z} \tag{4.10}$$

where ω is the IR frequency, $E_r = E(\omega)/E_0(\omega)$ is the relative IR energy and δz is the distance of propagation (in this case $\Delta z = 0.2$ mm).

Subsequently the absorption of the remaining energy E_r into the lattice across 0.2 mm is computed by again using Beer's law with $\Delta z = 0.2$ mm. The frequency dependent curve computed is presented in figure 4.17 and illustrates the vast differences in the deposited energy. Within the broad excitation peak region, the greatest amount of heating occurs between $\approx$ 500 to 650 cm^{-1} and very little heating occurs beyond 800 cm^{-1}. This is consistent with the emission offset observations discussed in section 4.4.

4.11 Modeling the dynamics of the ITE with rate equations

By combining understanding of the physical origins of the observed effects in the transients, qualitatively described in section 4.6, with a model of the time evolution of non–equilibrium thermal effects due to the IR radiation pulse, it is possible to model the transients describing the dynamic properties of the ITE emission directly. As with any

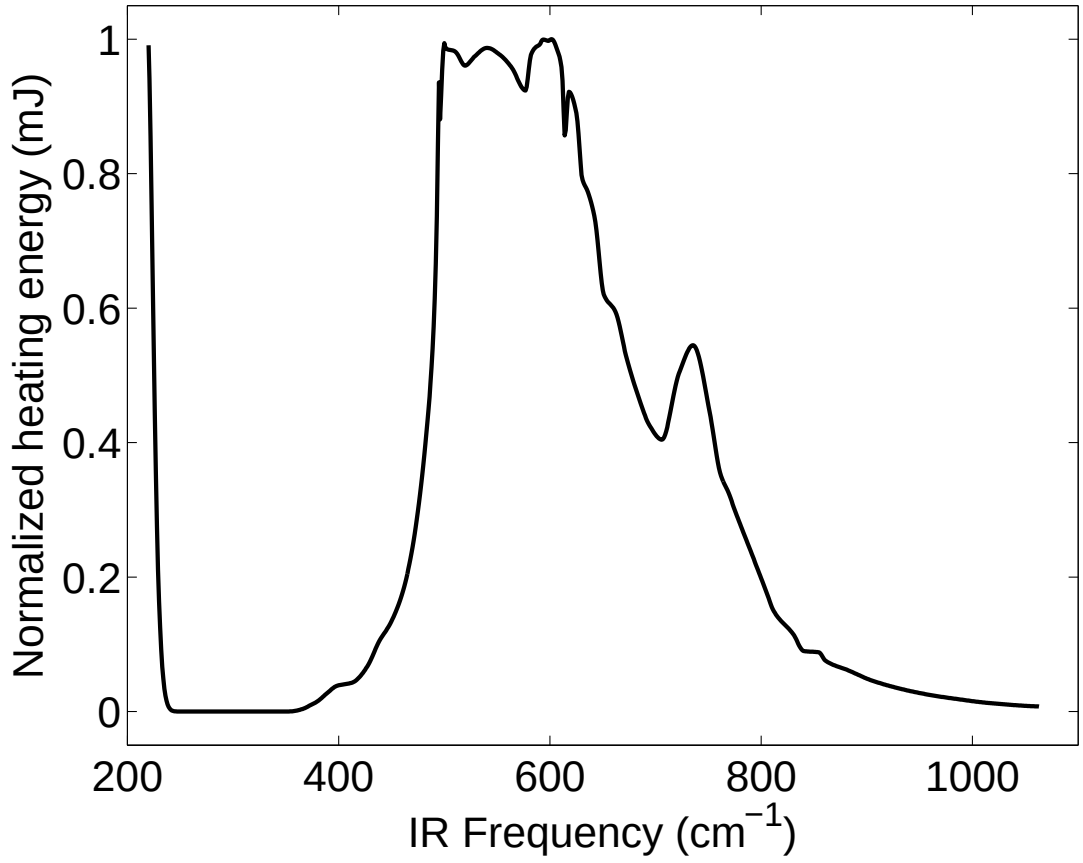

Figure 4.17 The frequency dependence of the energy deposited into the CaF_2 lattice volume V by the IR excitation pulse is presented here. The energy has been normalized such that its maximum value is 1 mJ. The relative differences in the amount of energy available for heating at different IR frequencies is illustrated, with the energy peaking at 600 cm^{-1} rather than at the peak of the IR absorption spectrum.

description of a dynamic system involving optical, non–radiative and thermal transfers of oscillators a set of rate equations may be employed. The schematic in figure 4.18 is an extension of the ITE schematic presented in figure 4.1, with the addition of the direct transfer process under IR excitation.

A majority of the rates described in figure 4.18 have been previously established in section 4.1 from the literature [9, 12]. The rates are used to establish a model where the population changes of the oscillators are described by,

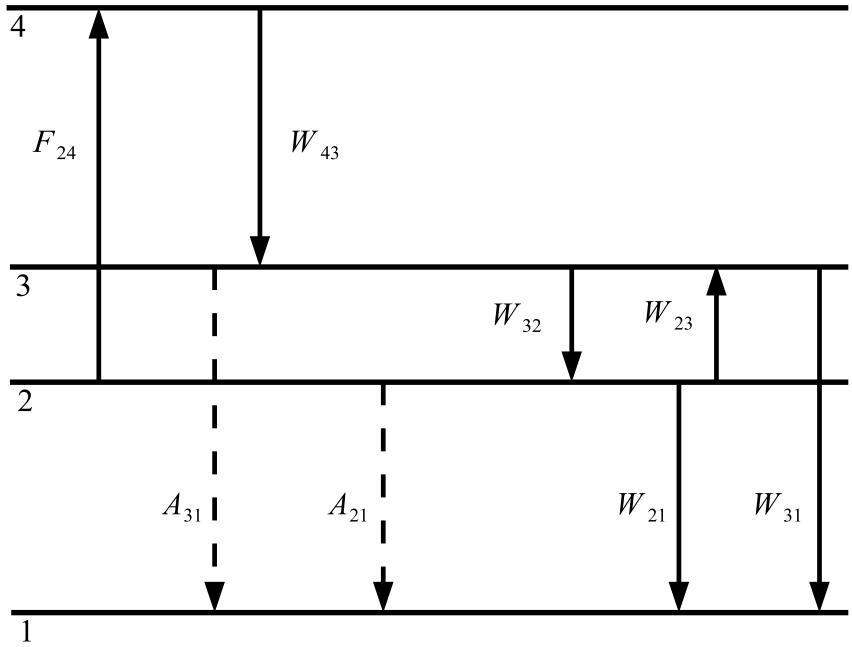

Figure 4.18 A schematic representation of the rates to be used in modeling the dynamic properties of the emission observed in CaF_2:Yb^{2+}. The known energy levels associated with the CaF_2:Yb^{2+} ITE are presented with additions made to model the direct intra–excitonic absorption under IR excitation. The scheme follows the convention set up by the previous ITE energy schematic from section 4.1.

$$\begin{aligned}
\frac{dN_1}{dt} =& A_{21}N_2 + A_{31}N_2 + W_{21}N_2 \\
&+ W_{31}N_3 \\
\frac{dN_2}{dt} =& - A_{21}N_2 - W_{21}N_2 - F_{24}f(t)N_2 \\
&- W_{23}(T)N_2 + W_{32}N_3 \\
\frac{dN_3}{dt} =& - A_{31}N_3 - W_{31}N_3 - W_{32}N_3 \\
&+ W_{23}(T)N_2 + W_{43}N_4 \\
\frac{dN_4}{dt} =& - W_{43}N_4 + F_{24}f(t)N_2
\end{aligned} \tag{4.11}$$

where N_k is the population of oscillators in a given state k, F_{24} is the rate of IR induced direct excitation into state 4, which decays to state 3 via the non–radiative rate W_{43}. All other symbols retain their definitions from previous sections.

In the modeling W_{43} rate is set to ≤ 0.1 μs (i.e. the model resolution), and therefore the transfer of population from state 4 to 3 is essentially instantaneous. While it is possible

that W_{43} is slower and causes a component of the rise time observed, the low IR fluence transients do not display any significant rise beyond the termination of the IR pulse (see the 8 dB normalized transient in figure 4.10 (b)). Additionally W_{43} cannot account for an increasing rise time with IR fluence. Therefore the selection of W_{43} is justified.

These equations are numerically solved with a forward Euler method, the time evolution scheme employed by the adapted FTCS algorithm described in section C.2 with equations C.10 and C.11. At each time step the instantaneous population of each radiative state is multiplied by the respective Einstein coefficient (A_k) to determine the relative emission from that state, thus establishing the temporal behaviour of the emission intensity. The required temperatures are calculated prior to the evolution of equations 4.11 for a given amount of heating energy E_m using the model described in section 4.10. This is done for a time frame that is identical to that used to solve the rate equations.[11] The temperature is then picked at each point during the forward time march of the rate equation model, and the thermally influenced rates are calculated at each instance. This approach to temperature based rate changes allows for the consideration of both non–equilibrium thermal effects and temperature changes of the sample. To deal with changes in the temperature the boundary condition of the temperature distribution is changed as well as the initial (pre–IR) temperature surface.

The parameters are then fitted with the use of a least squares fitting algorithm, typically an extended version of the Levenberg–Marquardt algorithm [93] as employed by MATLAB in its non-linear fitting and optimization tool boxes. When dealing with IR frequency changes the parameters F_{24} and E_m are allowed to vary during the fitting, however the E_m value is given a limited range through which it is allowed to vary, based upon the expected absorption at a given frequency as discussed previously (see section 4.10.1). The maximum value for E_m in the frequency range is determined by fitting the transient at 625 cm^{-1} while keeping E_m unbound. The initial values for subsequent fittings are determined by multiplying this maximum value by the normalized heating energy at the relevant IR excitation frequency (see figure 4.17). For variations in IR fluence the transient resulting from unattenuated IR excitation is fitted to, allowing F_{24} and E_m to change as before, however the transients resulting from the attenuated IR pulses are computed by decreasing F_{24} and E_m such that they reflect the fractional change in IR fluence. All other rates are

[11] Given that the solution scheme for the IR thermal influences is far more sensitive to the time resolution in terms of numerical stability, this value is set by the requirements of the thermal modeling rather than the rate equations. The resolution required by the thermal modeling is always higher due to the $1/\Delta x^2$ factor present in the stability condition.

held constant at the values obtained from literature (see section 4.1). However, because W_{32} is not directly available in literature, it was obtained via an exponential decay fit to the high frequency end of the IR excitation (at 900 cm^{-1}) to determine the fast decay rate in the enhancement. This value is presented in table 4.1, and it is allowed to vary by ±5% during the fitting process.[12] There was no systematic change in this variation.

It should be noted that the rate equations presented by 4.11 are describing the behaviour of the ITE after excitation with the UV pulse. The ITE is already in its meta stable excited state (state 2) before the modeling commences. The relative populations of state 2 and 3 prior to the incidence of the IR pulse are set by the sample temperature (taken to be 8 K in most cases) and the ratio established by equation 4.2.

4.11.1 Modeling the IR frequency dependent behaviour of the transients

Applying the set of equations 4.11 combined with the thermal effects already discussed the transient behaviour across the broad excitation spectrum was fitted at key points along the IR frequency range. Although fitting to each excitation point along the frequency axis would have been ideal, the computation time for such an exercise would have been immense. The points, with IR excitation frequencies of 455, 625, 714 and 833 cm^{-1} were chosen to allow an examination the variety of trends observed in the dynamics of the IR excitation spectrum (see section 4.4). 833 cm^{-1} is an excitation frequency where the direct intra-excitonic transitions are dominant (and is also a value at which emission spectra was recorded). The transients at 625 cm^{-1} excitation show the greatest potential for influence from thermal effects. Excitation at 714 cm^{-1} provides an intermediate mix of the two influences. 455 cm^{-1} excitation reflects the diminishing IR excitation influence, which also presents a long rise time.

The fits obtained at these IR frequencies are displayed in figure 4.19 with the fitted parameters summarized in table 4.8. It is clear that while the modeling is providing for the basic behaviour adequately, some of the fits are not perfect. This is especially so in the 625 cm^{-1} transient (figure 4.19c), where the shape of the emission enhancement is not well matched. The uncertainties of the parameters for the particular fit (table 4.8) reflect the mismatch showing greater relative variation when compared to other excitation

[12]The variation allowed was the uncertainty obtained from the exponential fitting to the the high frequency decay. Even though the decay rate can be determined with greater accuracy, because of the possibility of minute thermal effects mixing with the transient even at 900 cm^{-1} the uncertainty was left as obtained from the simple fit.

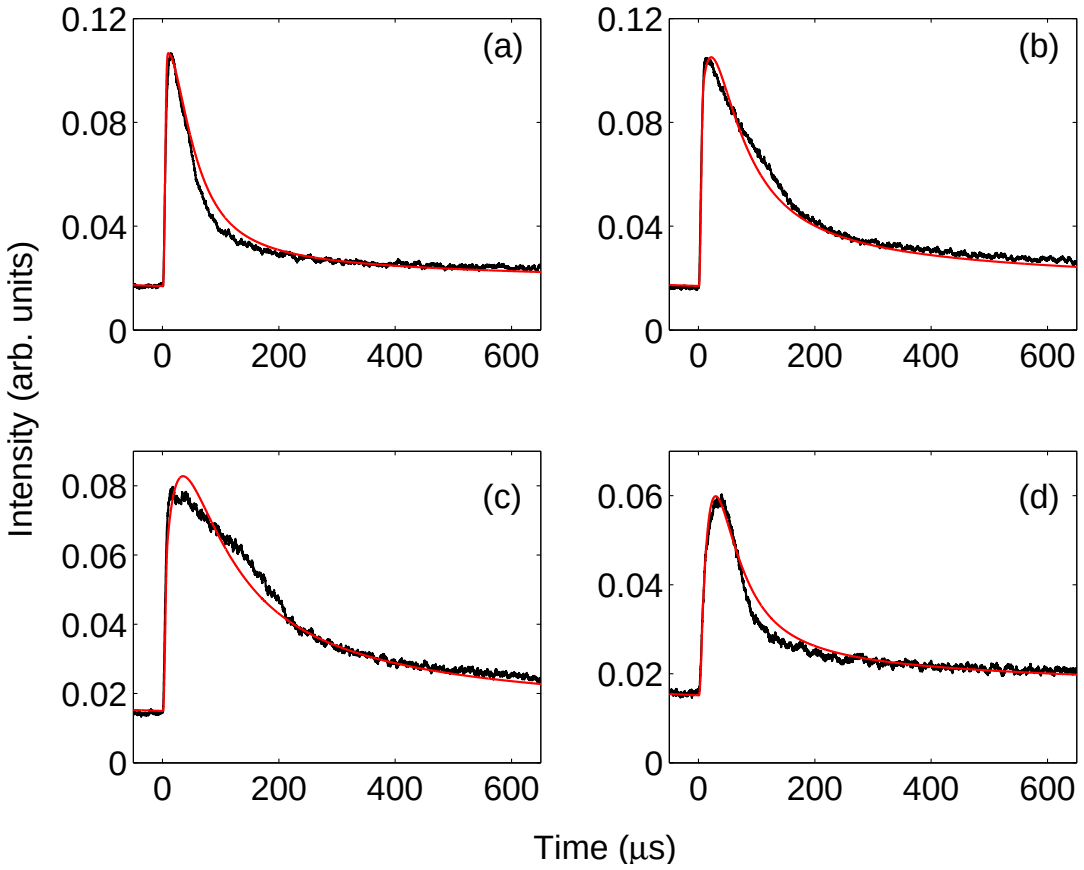

Figure 4.19 The transients at different IR excitation frequencies are simulated using the rate equations discussed previously, while also taking into account the heating aspects associated with the IR radiation being absorbed into the CaF_2 lattice. The data is presented in black, while the simulated transient is presented in red. Four representative transients are displayed (from across the broad peak discussed in sections 4.4 and 4.4.1) where (a) has an IR excitation frequency of 833 cm^{-1}, (b) has a frequency of 714 cm^{-1}, (c) has a frequency of 625 cm^{-1} and (d) has a frequency of 455 cm^{-1}.

frequencies. The behaviour past 200 μs in time is well matched, with the emission offset well accounted for across the four fits. The fits where heating is not as prominent as at an excitation frequency of 625 cm^{-1} are better matched, leading to the possible implication that the modeling of the heating and heat dissipation is not entirely accurate.

There *is* inaccuracy in the way the current model deals with the heating process arising from the use of a single average temperature over a small region, rather than computing transients from all (x, y) points relating to the temperature distribution. Because the ITE emission is sensitive to temperature, the resultant transients across the distribution will have differences between them. The final transient curve that is recorded is a composite of all these different transients, thus there will be some discrepancy when the modeling

does not compute an array of transients and form a composite. However, even exploiting the symmetry of the system, such a calculation involves an increase in computation time by factor of approximately 60 (for the typical geometric mesh employed in our modeling).

Table 4.8 Parameters from least squares fitting of IR excitation frequency dependent transients with the rate equation model presented above. F_{24} represents the intra excitonic transitions rate, and is an indication of the intensity of the direct transition absorption of the IR pulse into the ITE. E_m is the total energy deposited into the lattice by the IR pulse that contributed to local heating under the modeling described in section 4.10. Computed E_m indicates the calculated value for E_m based on the curve presented in figure 4.17 and the fitted value at an IR excitation of 625 cm^{-1}. T_{max} indicates the maximum temperature reached by the local region under the IR induced heating. A temperature of 8 K was used through all the fits.

IR frequency (cm^{-1})	F_{24} (s^{-1})	E_m (mJ)	Computed E_m	T_{max} (K)
833	13200 ± 400	0.34 ± 0.01	$0.32 \pm 8\%$	15.1 ± 0.4
714	10400 ± 500	1.02 ± 0.05	1.11	19.5 ± 0.6
625	5900 ± 300	2.5 ± 0.2	2.50	24.2 ± 1.2
455	1450 ± 70	0.25 ± 0.007	0.27	14.2 ± 0.3

With decreasing excitation frequency the rate of the direct transition diminishes indicating that the resonance is toward the higher end of the broad band in the IR excitation spectrum. This also shows that the integrated excitation spectrum presented by figure 4.7 in section 4.4.1 has two distinct regions within the broad band that are influenced by different processes despite having similar peak intensities. The behaviour of the parameter E_m confirms that the transient behaviour observed between the IR frequencies of 500 to 650 cm^{-1} (in figure 4.5 (a) and (b)) is due to local heating via the absorption of radiation into the lattice.

Although the E_m values were seeded using the computed values in table 4.8 a $\pm 25\%$ variance was allowed within the fitting algorithm. This was done in an attempt to establish the validity of the heating model as a plausible explanation for the observed dynamic properties. If the parameter values varied to the extremes of their bounds it would be an indication that there was an inconsistency in the modeling process. However, the fitted values and computed values are in agreement within their uncertainty ranges,[13] and this provides credibility to the modeling of the heating effect.

[13]The uncertainty in the computed E_m values arise from the uncertainty of the fitted value at an IR

The rise time behaviour of the transients is also of particular interest. The main driver of the rise time could reasonably be assumed to be the amount of heating, and thus maximum temperature. Contrary to expectation, the greatest rise time is observed for the transient with the least local heating, at an excitation frequency of 455 cm^{-1}. As explained in section 4.6 the behaviour is determined by a multitude of factors, and the above observation provides an indication of a major factor. Notice that at this frequency, while T_{max} is at its lowest, so is F_{24}, giving a maximum ratio $R_{455} = W_{23}/F_{24} = 1.7$. Similarly the other respective ratios can be computed to be, $R_{625} = 2.1$, $R_{714} = 0.74$ and $R_{833} = 0.24$. R_{455} is the second largest ratio, and this ratio appears to be a major factor in determining the location of the peak intensity of the transient in time. It should be noted that even though R_{625} is greater, from figure 4.19(c) it can be seen that the model overestimates the rise time in this case, with the modeled curve having a similar peak location (in time) to the 455 cm^{-1} excitation.

The dependence of the rise time on the ratio $R_k = W_{23}/F_{24}$ can be understood as follows. For a given value of temperature, and thus W_{23}, there exists a specific oscillator population ratio between states 2 and 3. If F_{24} is large enough to drive the system beyond this ratio, the process of thermally populating state 3 will be overshadowed by the non-equilibrium depopulation of the extra oscillators back to state 2, driven by the unchanging W_{32}. Thus as the ratio R_k becomes larger, the thermal population process gains prominence in comparison to the direct population of state 3.

4.11.2 Modeling the IR fluence dependent behaviour

As with the IR frequency dependent data, transients dependent upon the IR fluence at a frequency of 800 cm^{-1} were modeled by the methods previously discussed. At maximum fluence the parameter F_{24} was allowed to vary freely and as was E_m. However E_m was seeded by a value obtained through calculation (see section 4.11.1) at 0.65 mJ. The obtained fits and the relevant data are presented in figure 4.20 and the parameters for the fits are shown in table 4.9.

Notice that because of the excitation frequency, the absorption of IR radiation into the lattice is small, thus heating is not prominent at this frequency. However due to the very low thermal capacity of CaF_2 at low temperatures, the sample experiences a temperature

frequency of 625 cm^{-1} as this was employed to compute the remaining values. The uncertainties of the fitted E_m values are from the least squares fitting algorithm, which computes them by taking the diagonal values of the covariance matrix.

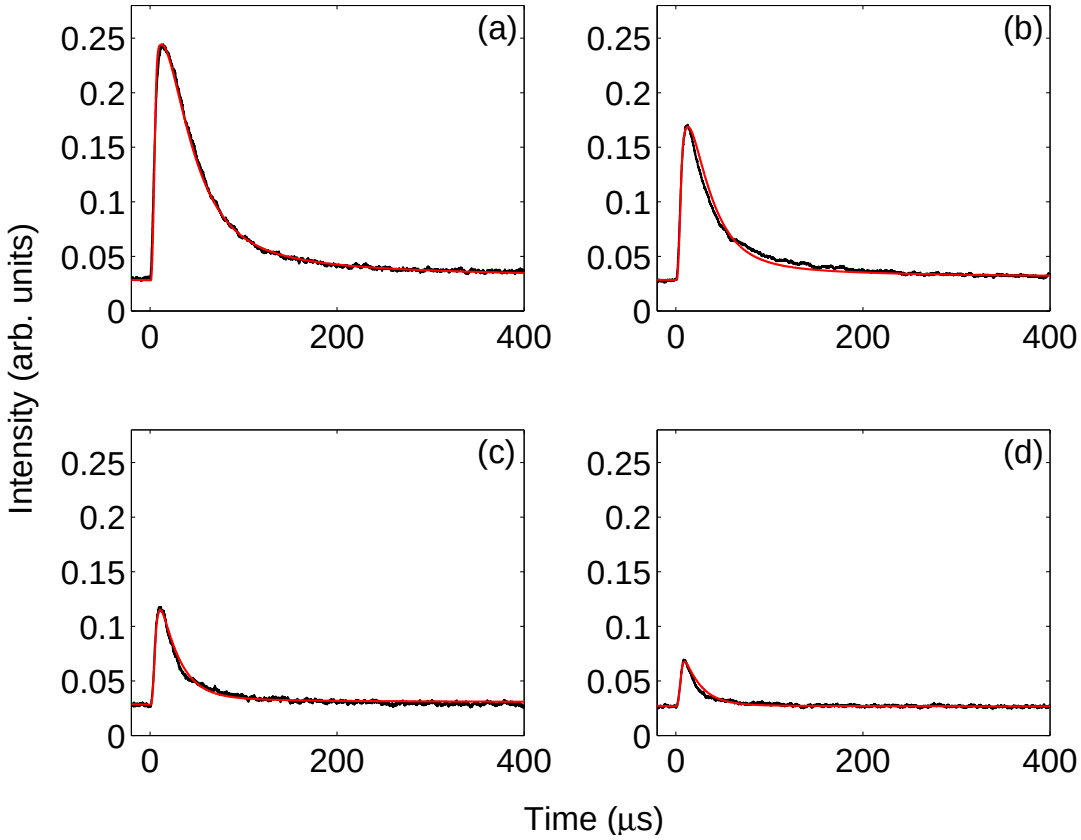

Figure 4.20 The transients and the least squares fits obtained through the rate equation modeling process at different IR fluences for a frequency of 800 cm^{-1}. The data is presented in black, while the simulated transient is presented in red. Four representative transients are displayed where the IR fluences are (a) 9.6 Jcm^{-2}, (b) 4.8 Jcm^{-2}, (c) 3.0 Jcm^{-2} and (d) 1.5 Jcm^{-2}. Note that only (a) has fitted parameters, with the values for the other curves being computed from the values for (a).

increase of 11.5 K at the IR beam spot. However the source of the emission enhancement is dominantly the direct transition with an $R_{800} = 0.32$. Additionally examining the fits, it is clear that the direct transition does not saturate, as scaling the F_{24} parameter linearly with IR fluence allows for acceptable fitting to the data.

The behaviour of the temperature with increasing fluence as a source of the *appearance* of saturation can be confirmed by examining the temperature curves for the above modeling.

Figure 4.21(a) presents the temperature curves with the now familiar trend of sublinear dependence of the maximum temperature values upon the energy deposited into the lattice by the IR pulse. Examining the maximum possible W_{23} values for a given IR fluence, shown in figure 4.21(b), illuminates the situation further. While the three lowest values for W_{23} display a linear dependence on fluence (indicated by the fitted red line), the rate for

Table 4.9 Parameters from least squares fitting of rate equation model to transients with varying IR excitation fluence at 800 cm^{-1} in CaF_2:Yb^{2+}. Note that the rate W_{23} is the maximum reached during the transient.

Atten (dB)	Fluence (Jcm^{-2})	F_{24} (s^{-1})	E_m (mJ)	T_{max}(K)	W_{23} (s^{-1})
0	9.6 ± 0.1	26000 ± 800	0.70 ± 0.02	20.4 ± 0.6	8300
3	4.8	13000 ± 400	0.35 ± 0.01	17.0 ± 0.5	4800
5	3.0	8500 ± 250	0.21 ± 0.006	14.0 ± 0.4	2700
8	1.5	4300 ± 120	0.11 ± 0.003	11.4 ± 0.3	900

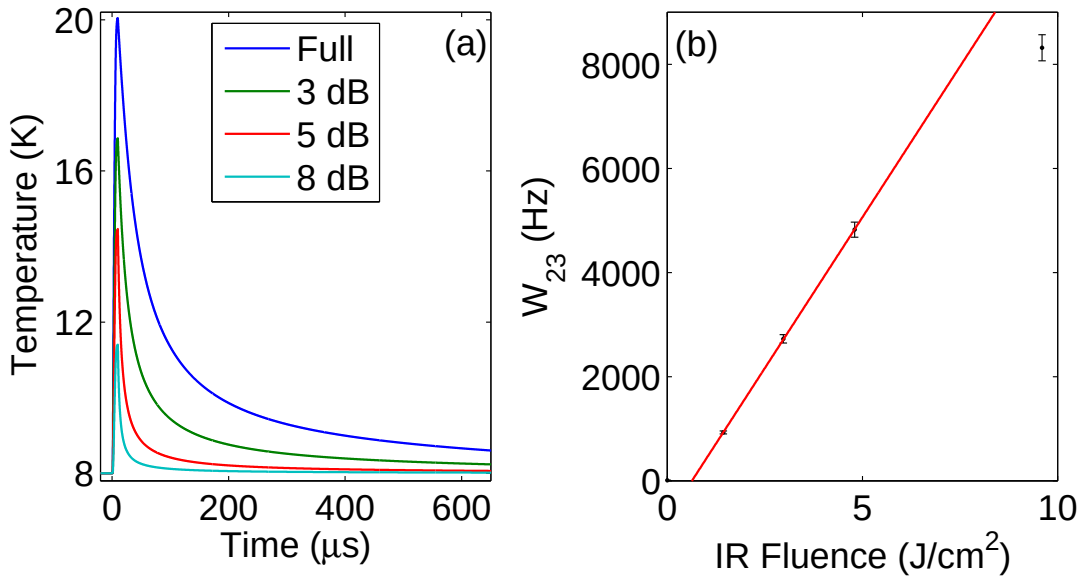

Figure 4.21 The behaviour of the temperature curves under changing IR fluence is presented in (a), while (b) presents the manner in which the maximum possible W_{23} rate is governed by the specific maximum temperature at a given IR fluence. Notice the sublinear value of W_{23} at maximum fluence.

maximum fluence is well below linearity. This follows the trend of the emission enhancement dependence on IR fluence presented in figure 4.11, where the lower values displayed linearity. This points to the positive proportionality of the heat capacity with increasing temperature as the reason for the observed "saturation" effects in the enhancement.

While decay of the enhancement is dominated by the rate W_{32}, being 6 times greater than the maximum W_{23} reached, because $A_{31} \gg A_{21}$ the influence of the thermal population of state 3 is significant to the overall temporal shape of the emission enhancement. Therefore any changes in the manner in which the temperature of the local region dissipates influences the shape of the enhancement, and this is clearly evident when comparing the normalized decay profiles presented in figure 4.10 (b). The differences in the temperature dissipation as the IR fluence changes provides an explanation for the changes with the temperature falling faster as the fluence decreases. Recall from sections 4.1 and 4.6 that as the sample cools its W_{23}/W_{32} ratio falls, and with that the population in state 3 falls. This reasoning is also obviously applicable in the local heating case. Additionally as the *rate* of cooling increases the time frame available for the system to sustain a given population ratio decreases, thus causing the enhancement to decay faster at lower powers. It should be noted that while the peak temperature has an impact upon this decay, the major contribution of the peak temperature is in determining the number of oscillators that are thermally excited into state 3 before the cooling and decay process becomes apparent at the termination of the IR pulse.[14]

4.11.3 Modeling transients excited with the 1 GHz micro–pulse repetition–rate of the IR at a frequency of 625 cm^{-1}

While we have shown that the modeling process works across both IR frequency changes and IR fluence changes, it should be tested for consistency across a variety of possible search parameters. For that purpose an attempt to model the behaviour of the transients at extreme fluence values with the data presented in section 4.7.1 has been made. Even though experimental exploration of the GHz micro pulse regime was curtailed due to concerns of over complicating the experiment, and the subsequent analysis, if the above rate equation and heating models are correct, they should be able to consistently simulate at least the general characteristics of GHz transients.

[14]One should keep in mind that the cooling and the decay of oscillators are happening throughout the IR excitation phase as well. However while the IR pulse is illuminating the sample these process are not readily apparent. The model begins the decay process as soon as there is any population in state 3 that can decay.

To this end the transients resulting from varying the IR fluence at an excitation frequency of 625 cm^{-1} was chosen for the fitting process. The maximum IR fluence was 100 Jcm^{-2}, lower than a 40 fold increase from the 25 MHz regime due to a larger spot size (at 200 μm). The total pulse energy however was on the order of 40 times larger. As before the parameters were allowed to vary freely for the transient under maximum fluence and scaling of these fitted parameters were applied to the transients resulting from the attenuated IR pulse.

The fits obtained are presented in figure 4.22 with the corresponding parameters summarized in table 4.10. Notice that the F_{24} parameter is only 8.5 times as great as the corresponding value in the 25 MHz regime. Similarly E_m is only a factor of 30 greater (rather than 40).

Table 4.10 Parameters from least squares fitting of rate equation model to transients with an IR micro pulse repetition rate of 1 GHz and fluence variation at an excitation frequency of 625 cm^{-1} in CaF_2:Yb^{2+}.

IR attenuation (dB)	IR fluence (Jcm^{-2})	F_{24} (s^{-1})	E_m (mJ)
0	100 ± 1	50000 ± 2000	72 ± 4
3	50	25000 ± 1000	36 ± 2
8	15	7500 ± 300	11.0 ± 0.6

The heat modeling took into account the larger spot size, and thus had a wider temperature distribution for the input energy. This resulted in lower maximum temperatures than what would have been achieved had the spot size remained the same. For example at maximum fluence the maximum temperature was 51 K, however with a spot size of 100 μm this jumps to 66 K. At these high temperatures the heat conductivity is quite low, thus the temperature dissipation was also slow, resulting in the local region retaining relatively high temperatures for far longer than was the case under the 25 MHz regime. The sustained emission enhancement observed is because of this sustained high temperature.

The changes in the decay rates are also accounted for by the longevity of the temperatures with increasing IR energy put into the system. As IR energy decreases (as with the 25 MHz case) the local region cools faster thus decreasing the population ratio of state 3 to 2, in turn leading to a decay in the emission.

Such considerations also account for the frequency dependent rise and decay behaviour

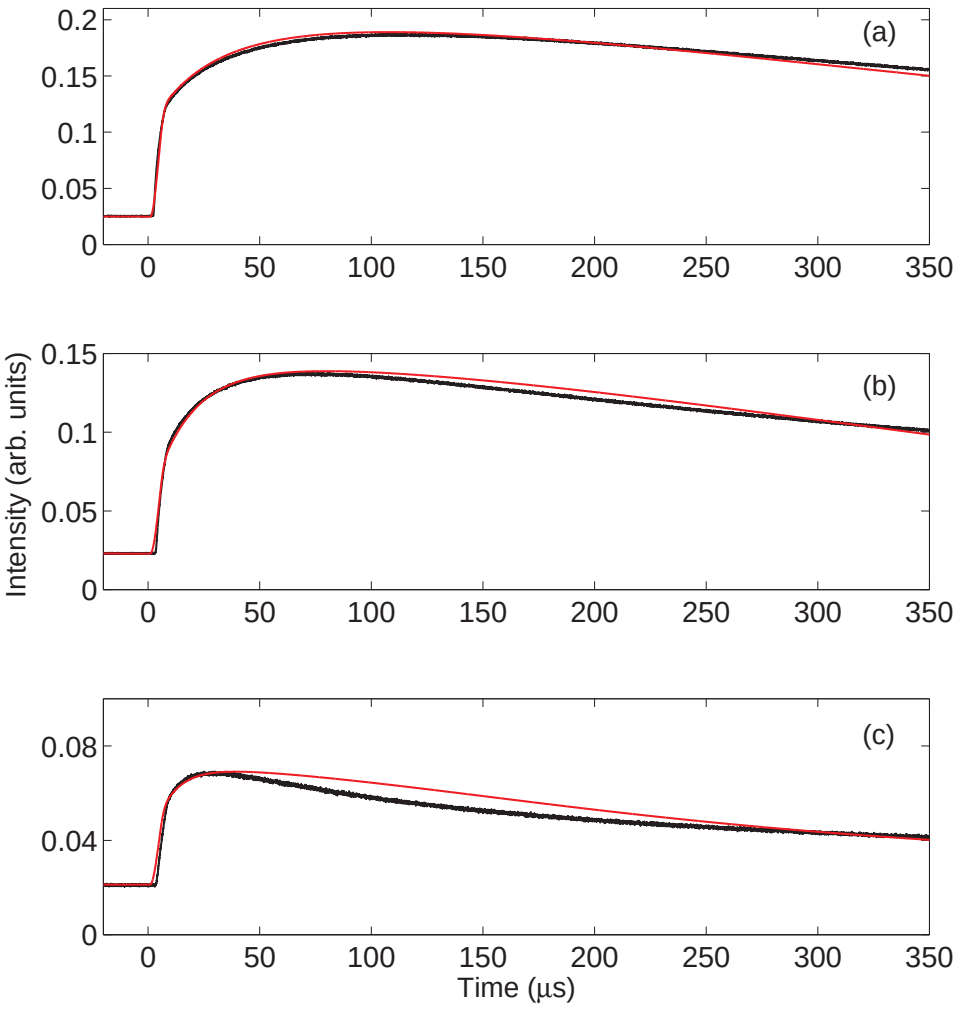

Figure 4.22 Fits to transients at an IR excitation frequency of 625 cm^{-1} with the micro-pulse repetition rate at 1 GHz, with the data is presented in black and the fits in red. Three representative transients across varying IR fluence are displayed where, (a) has a fluence of 100 J/cm^2, (b) has a fluence of 50 J/cm^2 and (c) has a fluence of 15 J/cm^2.

reported in section 4.7.1, since the IR induced heating increases (see section 4.10.1) across the range of frequencies presented.[15]

Comparisons between the two regimes should be made only tentatively however, since the detection set up and gathering optics were not identical between the two runs. However, the ability of the model to take into account the extreme IR fluence variation shows that it is consistent, and likely an accurate representation of the true dynamic behaviour of the system.

[15]This is effectively the same as dialing up the IR power, since the amount of energy deposited in to the local volume V is simply increasing within as the frequency decreases.

4.11.4 Modeling the transients under changes in equilibrium lattice temperature

The temperature dependent transients presented in section 4.8 were also modeled by varying the ambient temperature input of the heating model previously presented. Since the IR excitation for these transients were at 714 cm^{-1} the F_{24} and E_m parameters were held constant at the previously fitted values (shown in table 4.8). Figure 4.23 shows the achieved fits. The time axis has been modified such that $t = 0$ μs corresponds to the start of the IR pulse to account for the manner in which the coding implements the modeling process.

The increase in the ambient temperature causes the population available for IR induced transitions to diminish, thus rendering both direct transitions and heating of the local volume V ineffective. By keeping the IR related parameters constant, yet still modeling the observed transients we can see that there is no temperature dependent cross sectional change within the ITE. It should be noted however that in the 50 K modeling (figure 4.23 c) the IR induces a minor bump that is not seen in the data. This suggests that perhaps some other suppression of direct population transfer is occurring as the temperature of the sample increases. At this temperature the IR induced heating was far too minimal to cause any noticeable changes to the ambient temperature of the sample (due to the relatively high heat capacity at 50 K).

One key aspect when modeling the higher temperatures is to match the delay between when the system is initialized (with the UV pulse) and when it is illuminated with the IR pulse. At low temperatures ($\leq$ 15 K) this is not vital as the population decay from state 2 is far too slow to be an influential factor within the delay time frames of the experiment. However as the temperature rises and the population ratio between states 3 and 2 increases, the oscillator population that decays to the ground state becomes significant. Beginning the modeling process at the incidence of the UV (recall that the transitions due to the UV are not modeled) and setting the correct thermally induced initial population ratio between state 3 and 2 (this essentially happens automatically as the ratio W_{23}/W_{32} is computed instantaneously) allows for the satisfactory modeling of the decay rates through out the temperature range explored.

The behaviour of the temperature dependent transients also informed the choice to hold W_{32} constant in the modeling process. As can be seen a constant value accounts accurately for the observed temperature dependent decay rate changes in the system. Additionally, given there is no indication of a thermal barrier that determines W_{32}, inferring and mod-

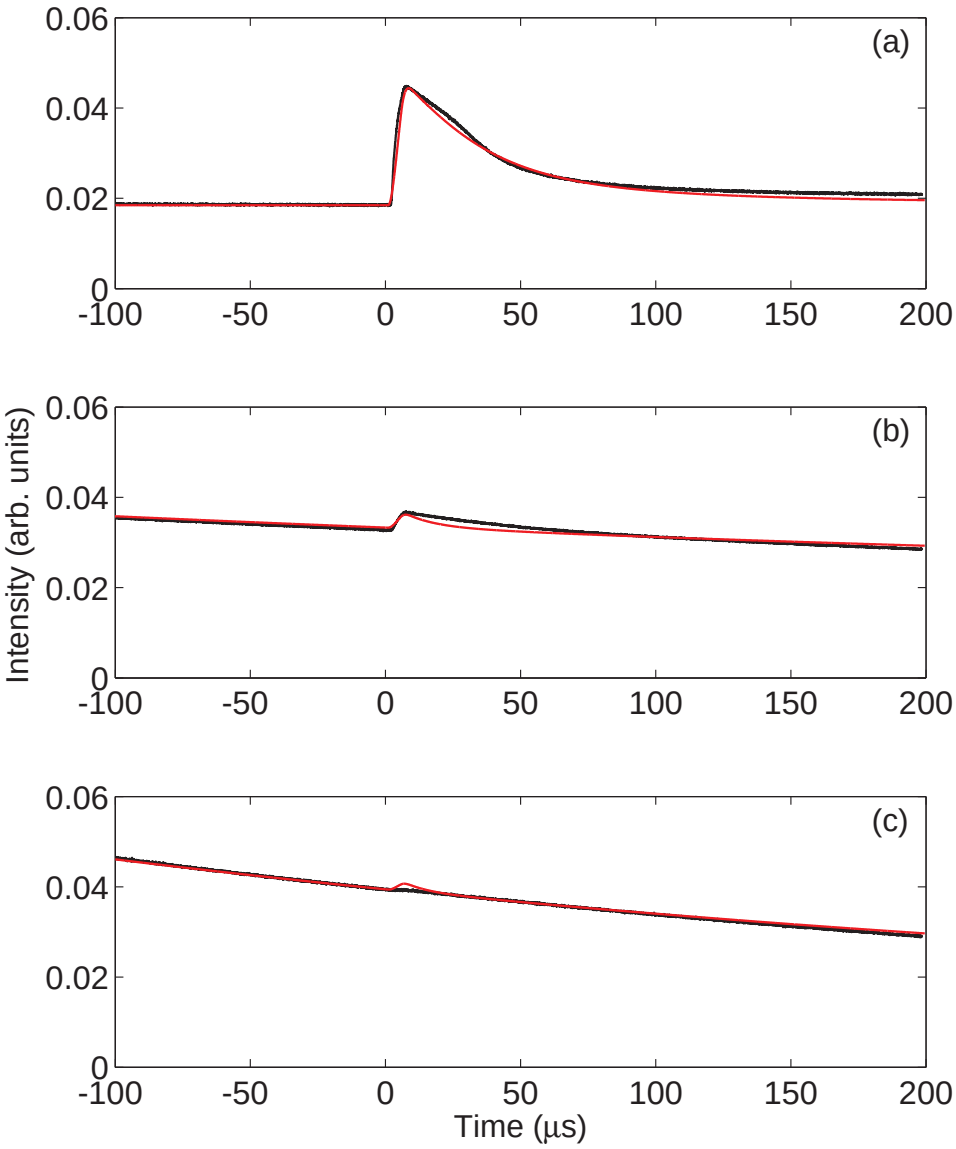

Figure 4.23 Fits to transients at an IR excitation frequency of 714 cm^{-1} as the ambient sample temperature was changed with (a) having a temperature of 10 K (b) 30 K (c) 50 K. Notice that the influence of direct transitions due to the IR is diminishing as well as the local heating induced by the absorption of IR radiation.

eling a process that changes the rate for a transition only a few wavenumbers below it would simply have added extra degrees of freedom to the model.

The ability of the model to account for the changes observed for sample temperature changes does show that it is consistent in all the domains it seeks to address and therefore we can be confident of the physical information extracted from this modeling process.

4.12 The dynamics of the sharp lines in the IR excitation spectrum

The higher energy sharp line with its peak at 1145 cm^{-1} did not prove conducive for obtaining transients with a satisfactory signal to noise ratio. The peak itself is a result of averaging over both time and IR excitation scans, and because of this we cannot make any conclusive statements about the nature of the dynamics in this particular transition.

Because it was possible to obtain transients of the low energy sharp line at 249 cm^{-1} this line is of greater interest in this context. As we see from examining figure 4.6(b) the peak appears to be a result of changing dynamics across the excitation range. The width of the peak shows that the broadening is inhomogeneous (rather than due to transition life time broadening of the emitting state), indicating that multiple electronic transitions are feeding the emitting state. Given this the changes occurring in the dynamics as resonance is approached is not surprising. Because it is possible to assign a multitude of states with different lifetimes that feed the optically active transitions it is possible to account for the behaviour with a rate equation model as previously discussed. However modeling such behaviour in this method is not overly useful as the freedom in the system is too great, thus making the modeling somewhat redundant. Particular attention should drawn to the fact that under the interpretation presented here for the manner in which heating is influenced by the IR excitation frequency (in section 4.10.1) the sharp transitions are not overly affected by heating.

4.13 Extracting the exciton spectrum

Removing the estimated contribution of the heating to the IR excitation spectrum by employing the heating spectrum from figure 4.17 allows for the extraction of intra–excitonic transitions through the absorption of the IR by the ITE. Assuming that at the peak of

the heating spectrum the total energy of the IR pulse is used for local heating a simulated emission transient can be constructed. Integrating the simulated transient with the same gate settings employed for the IR excitation spectrum in section 4.4.1 an estimate of the maximum possible contribution due to heating is obtained. The normalized heating spectrum is scaled by this contribution to estimate the influence of heating across the IR excitation range. Figure 4.24 shows the result of subtracting the modified heating spectrum from the IR excitation spectrum.

In comparison to the measured spectrum it can be seen that the peak is now higher in energy, between 740 to 820 cm^{-1} and has narrowed. The presence of the spike in the heating contribution at 750 cm^{-1} makes the estimation of an exact peak position difficult. The width of the peak indicates that in this excitation range the IR pulse is primarily causing a rearrangement of the delocalized electron state. Both sharp peaks retain their shape and position, indicating that these peaks *are* primarily due to intra–excitonic transitions.

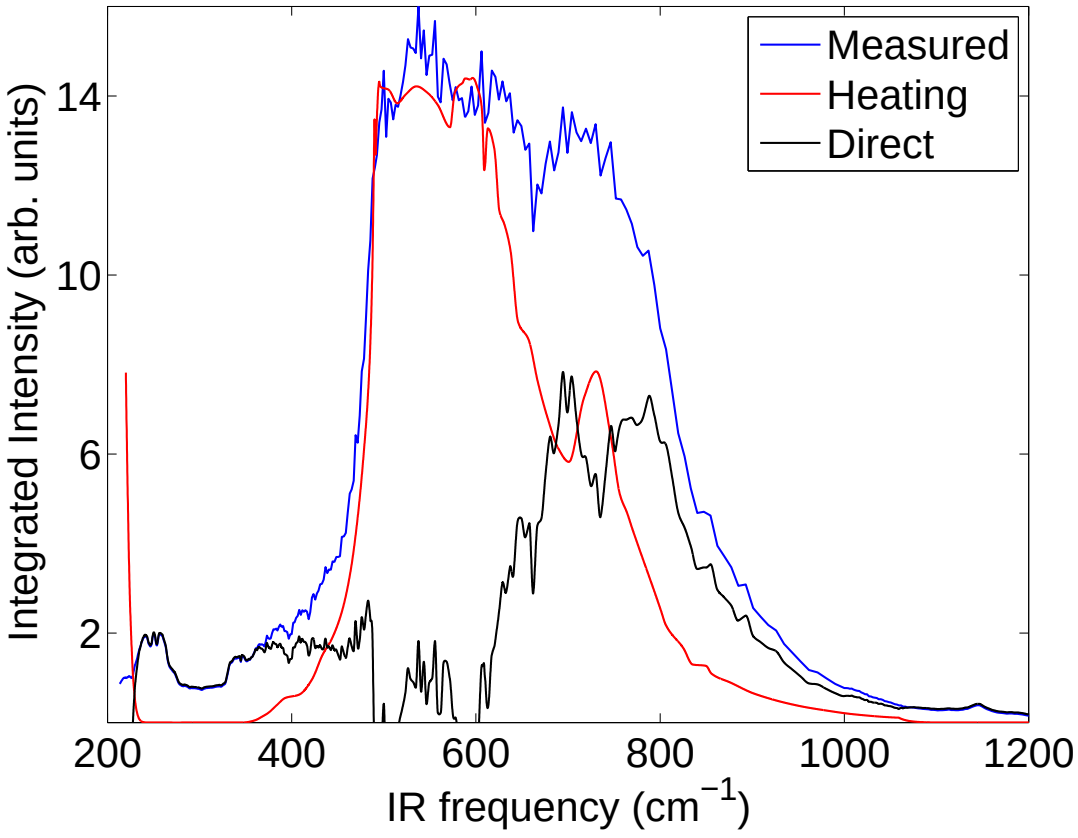

Figure 4.24 The IR excitation spectrum of CaF_2:Yb^{2+} with the calculated heating effects removed. Measured indicates the experimentally obtained spectrum. Direct shows the calculated IR induced intra–excitonic transition spectrum.

The peak in the excitation spectrum between 500 to 650 cm^{-1} is due primarily to heating of the lattice by IR absorption, and this is confirmed by the nature of the dynamic behaviour of the emission within this region.

The computed heating curve is heavily dependent upon data extracted (via plots) from previous studies for IR absorption in CaF_2 (Kaiser [70] and Denham [19]), heat capacity (Collocott [20]) and thermal conductivity (Harrington [21]). As a consequence it is difficult to deconvolve the contribution to the measured spectrum from heating with great precision. The fine structure present on the trace labeled 'Direct' in figure 4.24 are artifacts of the deconvolution.

4.14 Conclusion

Through the analysis of data obtained in two–colour experiments exploring the properties of ITEs in CaF_2:Yb^{2+} we have shown that it is possible to construct physically consistent models that describe both the spectral and temporal features observed. From this we have extracted physical interpretations and attributes of the ITE that were previously not known.

We have demonstrated that while the tunable IR radiation is able to directly access electronic states within the ITE, there are likely only two emitting states contained within it. This is shown through the similarity of the emission spectral behaviour under increasing temperature and under secondary excitation with the IR pulse. Using this spectral behaviour we have shown that state 3 of the ITE is configurationally different to state 2. A greater bond length change of ΔR of -0.169 ± 0.002 Å occurs when state 2 decays to the $4f^{14}$ ground state in comparison to state 3 at ΔR of -0.15 ± 0.01 Å. This implies that the bond lengths of state 3 and the ground state are longer than that of state 2. The ZPL frequencies for both transitions are in agreement with each other within the established uncertainties and show that both state 2 and 3 are configurationally shifted with respect to the $4f^{14}$ ground state. State 3 shows a smaller shift than state 2.

The time integrated IR excitation spectrum revealed two sharp peaks at 249 and 1145 cm^{-1} that are likely due to changes within the $4f$ hole. The positions and the oscillator strengths for these transitions were well matched with a semi empirical model based on the coupling of the $4f$ states to an s like symmetric delocalized state with an exchange parameter $G^3(fs) = 5900$ cm^{-1}. This was was found to be acceptable when considering the $5d$ and $6s$ coupled nature of the delocalization and when considering the exchange

parameters for $4f$ and $5d$ found in previous studies.

Dynamically the ITE emission showed significant dependence upon the IR excitation frequency. Preliminary analysis of this behaviour indicated that transients consisted of a mixture of direct transitions via IR absorption within the ITE and population transfer due to localized heating via the absorption of IR radiation by the lattice. By taking into account these factors the observations have been modeled with a four level system and a comprehensive heat dissipation model. At the four excitation frequencies modeled we found the intra–exciton absorption to be largest at the highest frequency with $F_{24} = 13200 \pm 400$ s^{-1}. This suggests the peak of the intra-excitonic absorption lies in the higher energy region of the broad excitation, and by deconvolving the influence of the local heating on the IR excitation spectrum with the use of a computed heating spectrum the intra–excitonic peak was estimated to be between 740 - 820 cm^{-1}. The calculation also confirmed that the low frequency peak in the broad band of the IR excitation is due to local heating effects.

The modeling was also able to account for the observed IR fluence dependent behaviour of the ITE emission transients. What initially appeared to be saturation of the direct transitions was shown to be heating effects, and no saturation was found under the modeling. It was found that maximum heating occurs at around 600 to 630 cm^{-1} and the local temperature can be as high as 16 K above the rest of the sample.

A consistency check of the model was conducted by modeling transients obtained at sample temperatures of 10, 30 and 50 K. The model was able to consistently account for the observations at these temperatures.

The IR excitation spectral models and the modeling of the dynamics will now be employed in the case of SrF_2:Yb^{2+} allowing for both a physical understanding of that system as well as further checking of the consistency of the models presented.

Chapter 5

Two–colour experiment to probe impurity trapped excitons in SrF_2:Yb^{2+}

In this chapter we extend our investigations to SrF_2:Yb^{2+}. Since SrF_2:Yb^{2+} also exhibits anomalous emission due to the formation of an ITE for excitation of the $4f \rightarrow 5d$ absorption in Yb^{2+}, the same PL enhancement experimental technique will be able to probe its structure. SrF_2 is isomorphic with CaF_2. Therefore the ITE will experience the same point group symmetry. This allows for further investigation of the ITE energy level structure, as well as providing an additional platform upon which the models developed in the previous chapter can be tested.

5.1 Impurity trapped excitons in SrF_2:Yb^{2+}

As in CaF_2:Yb^{2+} previous studies [9, 12] have identified the anomalous emission originating from SrF_2:Yb^{2+} after excitation of the $4f \rightarrow 4f^{n-1}5d$ absorption at 27800 cm^{-1} as originating from an ITE with the emission strongly red shifted in comparison to CaF_2:Yb^{2+}. Structurally the ITE appears to be similar to that found in CaF_2:Yb^{2+}, and figure 4.1 provides a valid schematic for the current case.

Previous temperature dependence studies identified two excited energy levels (which we have again denoted states 2 and 3), separated by a gap of $\epsilon = 26$ cm^{-1}, with the upper level (state 3) having a radiative rate of $A_{31} = 49000$ s^{-1} compared to the lower level (state 2) at $A_{21} = 40$ s^{-1} [12]. Both these rates are far greater than the corresponding rates in CaF_2:Yb^{2+} and allows for the possibility of additional measurements such as varying the time delay between the UV and IR pulses in the two–colour experiment. Additionally both levels have associated non–radiative rates that are far greater than those in the CaF_2:Yb^{2+} ITE system. State 2 has a non–radiative rate $W_{21} = 1500$ s^{-1}. The barrier associated with this transition has been set at 0.1 cm^{-1} indicating that it is always active

and that this transition is even more likely compared to that of CaF_2:Yb^{2+}. Because of the barrier size the temperature dependent variance of W_{21} is insignificant.

The non–radiative rate for the transition from state 3 to the $4f^{14}$ ground state has greater significance in SrF_2:Yb^{2+} due to its associated barrier height of only 100 cm^{-1} (an order of magnitude smaller when compared to CaF_2:Yb^{2+}). At a sample temperature of 8 K, employing equation 4.1 W_{31} is found to be 0.94 s^{-1}. In the temperatures used in the study of SrF_2:Yb^{2+} (up to 40 K) this rate does not increase significantly and can be assumed to be negligible in comparison to the other rates.

The non–radiative rate between the states 2 and 3, is set at $W_{32} = 10^8$ s^{-1} (similar to the CaF_2:Yb^{2+} case). In our study we extract this parameter from an initial fit to transient data we have recorded and keep this value constant through the rest of the modeling at 40000 s^{-1}. W_{23} is determined by equation 4.2, with the ITE system having identical degeneracies in states 2 and 3 to that of CaF_2:Yb^{2+}. Table 5.1 summarizes the rates discussed above. Where there is a potential barrier involved in computing the rates (e.g. W_{31}) a sample temperature of 8 K has been used.

Table 5.1 Rates obtained from previous experiments for SrF_2:Yb^{2+} ITE [12]. The non–radiative parameters (W_i) with associated potential barriers have been calculated from Moine et al., via a Boltzmann factor for a temperature of 8.0 K. W_{32}, the non–radiative relaxation rate from state 3 to 2 was determined through fitting, since the values presented in the previous studies are arbitrarily fast.

Parameter	**Rate (s^{-1})**	**Equivalent time constant (μs)**
A_{21}	40	25000
A_{31}	49000	20
W_{21}	1500	660
W_{31}	0.94	1000000
W_{32}	40000	25

Compared to the ITE system in CaF_2:Yb^{2+} the emission decays at a much faster rate, owing to the higher rates associated (both radiative and non–radiative) with states 2 and 3. Additionally due to the smaller barrier moderating W_{31} the onset of thermal quenching of the emission occurs at a lower temperature than in the SrF_2:Yb^{2+} ITE (140 K when compared to 180 K for the CaF_2:Yb^{2+}). Because of the smaller energy gap between states 2 and 3, the overall dynamics of the emission are also sensitive to much smaller

temperatures changes than in the case of CaF_2:Yb^{2+}.

5.2 Issues encountered in extending the two–colour experiment to SrF_2:Yb^{2+}

One of the major issues with SrF_2:Yb^{2+} is that its ITE emission peaks in the near infra red, around 12500 cm^{-1} (800 nm) [9] and was therefore difficult to detect with the visible PMTs that were employed in the experiment. The PMT used in our experiments has a sensitivity which falls off at around 750 nm, and is therefore only sensitive to the tail of the emission. Furthermore the emission is weaker than that observed in the other materials studied. The emission was also extremely sensitive to the UV excitation frequency.

Initial investigations suggested that emission could not be obtained from Yb^{2+} doped SrF_2 with several excitation experiments unable to to reproduce the emission described in reference [9]. During those attempts the excitation frequency was set to either 28170 cm^{-1} (355 nm Nd:YAG laser line) or 27400 cm^{-1} (365 nm - the excitation wavelength used in CaF_2:Yb^{2+}). However, emission was finally detected under excitation at 27780 cm^{-1} (360 nm) in a sample with a Yb concentration of 0.1%. Subsequently emission was also achieved from samples of other concentrations. The excitation wavelength proved crucial, as even a slight drift (to 27620 cm^{-1} or 362 nm) caused the emission to become undetectable.

Since the experiments were predominantly excitation experiments the emission was simply monitored at a set wavelength. Emission scans proved particularly unhelpful, since the detector was not sensitive to the necessary wavelengths to gain useful information. In our initial experiments we monitored the emission at the peak of the signal (note that this was an artificial peak as a result of the sensitivity curve of the detection), however subsequently we switched to monitoring all wavelengths (with relevant filters to isolate the emission from the excitation laser's scatter) for two reasons.

As discussed previously, the emission peak may blue shift under secondary excitation with the IR radiation. By monitoring all the emitted wavelengths details in the excitation spectrum would be more clearly observable than monitoring a narrow band of wavelengths. In addition to this, monitoring all wavelengths caused an increase in the overall signal, which improved the signal to noise ratio of the setup, thereby improving the data.

However, one must consider whether the observations and results recorded are consistent

between the two regimes of detection. Since the emission is a featureless Gaussian broad band [9], shifting the position at which the monitoring occurs should not pose a problem. In addition the data from the two regimes were compared to verify that there was consistency between the results.

5.3 The experimental details

The experiments were conducted on samples with a nominal dopant concentration of 0.05 mol% Yb^{2+}. The sample measuring approximately 1.5 mm in thickness and held at a temperature of 8 K, was initially illuminated with a UV pulse at 27780 cm^{-1} followed by an IR pulse with a variable time delay between them. Both the beams were focused to a spot size of 100 μm giving a fluence of 0.13 Jcm^{-2} for the UV pulse and between 5 to 11 Jcm^{-2} for the IR pulse under the 25 MHz micro pulse regime.

The IR radiation was scanned between 150 cm^{-1} to 1400 cm^{-1} (7 μm to 65 μm). These scans were conducted with relative UV - IR delays of 150 μs and 800 μs (except for excitation wavelengths below 220 cm^{-1}, which were only done with a delay of 150 μs).

Due to the rapid emission decay in SrF_2:Yb^{2+}, in addition to the parameter space explored under for the CaF_2:Yb^{2+} ITE, we were able to explore the change in behaviour of the emission enhancement for variations in the delay between UV and IR pulses. Measurements of the transients at long time scales of 100 ms were also taken. We thus recorded the transients observed for an entire IR excitation cycle. Within this there were 100 cycles of UV excitation, allowing us to observe the long term effects the IR excitation had on the sample.

Qualitatively the effect of the UV and IR beam overlap upon the transients was explored by optimizing the alignment of the two excitation beams and then displacing them slightly with respect to each other. No quantitative measurements were taken in this regard.

5.4 General observations

For UV excitation at 360 nm deep red emission exhibiting a single exponential decay with a lifetime of 660 μs was observed from the sample, consistent with previous observations [9]. With subsequent IR excitation an enhancement in the emission by a factor of up to 10 was observed, with the magnitude of the enhancement depending upon the excitation

wavelength of the IR radiation. This enhancement decayed far more rapidly than the emission resulting from UV excitation alone, with decay times varying from 20 to 70 μs. There also appeared a rise time varying from the instrument resolution limit of 6 μs up to 30 μs. This also depended upon the IR excitation wavelength.

5.5 Dependence of the excitonic emission upon IR excitation frequency

Scanning the IR excitation revealed both the dynamic and spectral dependence of the excitonic emission upon excitation frequency. The scans were conducted monitoring all emission frequencies. Because of this additional effects due to FELIX harmonics and unexpected artifacts were encountered during the scans. However, due to the nature of their dynamic behaviour, it was possible to separate these from the excitonic effects that were being explored.

Figure 5.1 (a) shows the enhancement in the IR excitation range from 500 to 1400 cm^{-1} with UV – IR delay of 150 μs. The time base in the detection has been set to a range of 100 μs in total to give a better view of the enhancement and its dynamics. While there is a small amount of enhancement happening at the higher end of the frequency scale, it rapidly increases as the excitation frequency approaches 800 cm^{-1}. However the decrease seen from around 570 cm^{-1} is due to the IR filter cutting off towards 500 cm^{-1}. Therefore it should be emphasized that the peak appearing here at 700 cm^{-1} is not a true peak, but an artifact due to the nature of the particular experiment. To obtain a true estimate of a possible peak a complete excitation spectrum must be reconstructed, and this will be discussed later in this chapter. As the enhancement increases with the excitation frequency approaching 600 cm^{-1}, a rise time builds within the transients. The decay rate also appears to decrease correspondingly leading to the enhancement persisting for longer.

Figure 5.1 (b) shows the enhancement in the same IR excitation range (500 to 1400 cm^{-1}) with a UV – IR delay of 800 μs. The UV only signal has now diminished significantly and the enhancement is much smaller than before. There is now a distinct temporally sharp structure on top of the transients, originating at approximately 1000 cm^{-1} with a very small rise time and a fast decay. Initially it was thought that this was the FELIX's higher harmonics getting through the IR filter, possibly through a burnt hole. The UV excitation beam was blocked and it was observed that the fast structure remained (while

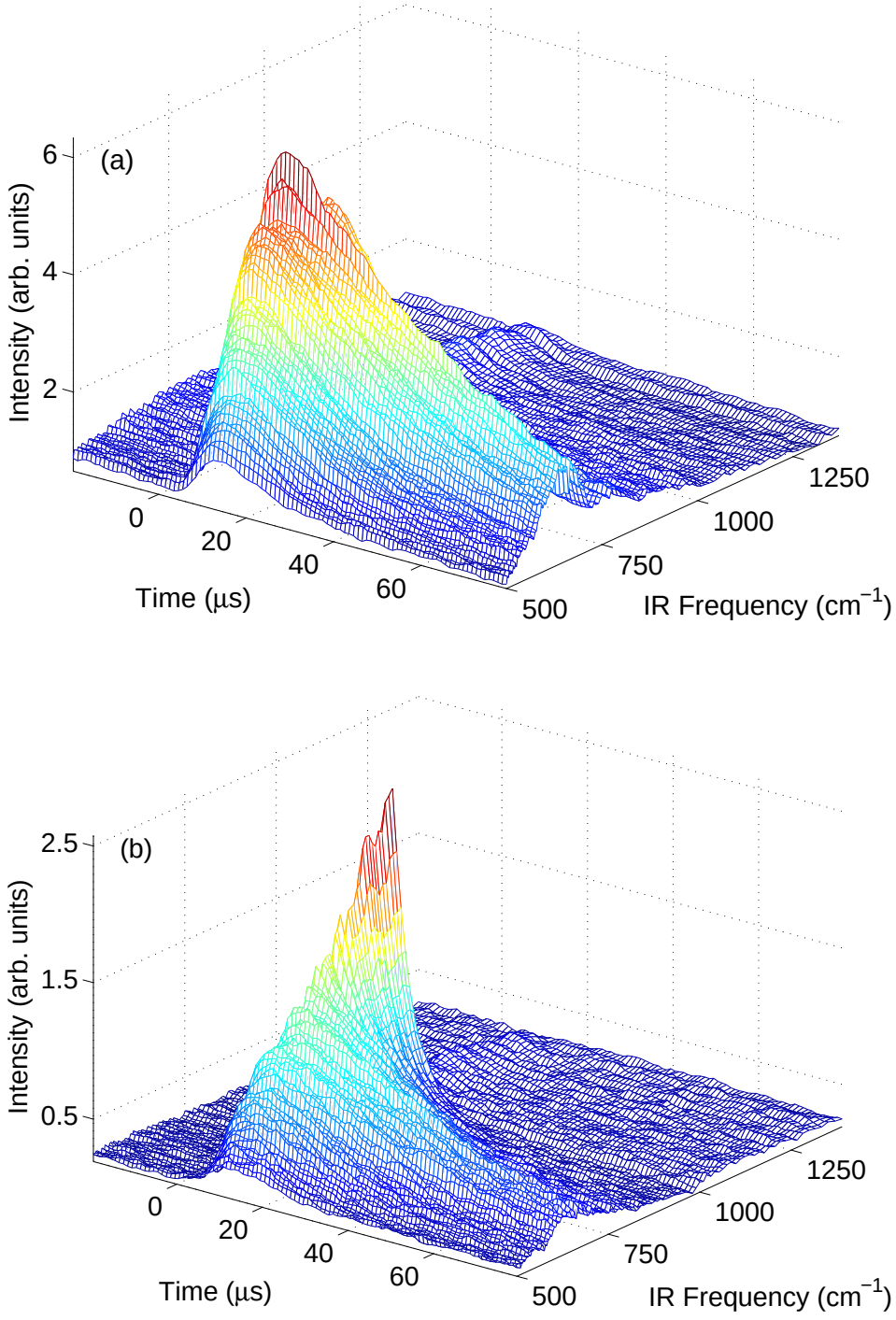

Figure 5.1 Enhancement in the SrF_2:Yb^{2+} ITE emission for an IR excitation scan from 500 – 1400 cm^{-1} with a UV – IR delay of (a) 150 μs and (b) 800 μs at a sample temperature of 8 K. The enhancement intensity has decreased in (b) compared to (a). The origin of the temporally sharp structure appearing in (b) has not been identified, however due to its dynamic properties its is unlikely to be related to the ITE emission. The cutoff in emission occurring towards 500 cm^{-1} is due to IR filter used.

the rest of the enhancement vanished). This was convincing evidence that it was simply an artifact, however placing a bandpass filter in the visible range in the IR beam path caused the effect to vanish. When the same filter was placed *after* the sample the signal shown still remained. This indicates that the effect is real and originates from the sample. The transients had an instrument limited rise time and a decay of < 5 μs. It was decided in the interest of optimizing the beam time available not to pursue this in detail, however a minor investigation was conducted and will be discussed at the end of this chapter.

It is puzzling that the temporally sharp structure only appears in the long delay data. The most likely reason is that the intensity of the standard enhancement is much larger with a short delay, so the effect is likely washed out. Another possibility is that the appearance depends on the total exposure time of the sample to UV radiation, and the longer delay scans were performed much further into the experimental run, meaning the sample had been exposed to UV irradiation for a longer time than in the short delay scans. The typical enhancement one observes appears to maintain a consistent shape between the two delay settings. Again, the fall off and peak appearing (ignoring the temporally sharp structure) in the data is due to the IR filter cutting off towards 500 cm^{-1}.

Figure 5.2 (a) shows the transient properties in the IR excitation range from 220 to 500 cm^{-1} with a delay of 150 μs. In this and subsequent scans no IR filters were employed due to the unavailability of sufficiently long pass filters. The enhancement is steadily declining toward the lower excitation frequency, as the FEL frequency moves away from the main enhancement peak. Note that the region corresponding to 500 cm^{-1}, where previously a rapid decrease in enhancement was seen (see figure 5.1) appears relatively flat and confirms the previous effect was due to filter cut off. It should also be noted that the data is *not* scaled to match the different scan regimes. Therefore comparisons on the intensity can only be made within the specific regimes. Again we see fast temporally sharp structures appearing around 470 cm^{-1} and again around 350 cm^{-1}. As before, these have instrument limited rise times and very fast decay times (< 5 μs). Since the excitonic emission is much slower than this we can safely separate these from the explored exciton dynamics. In addition to the real structures, there is also a component arising due to higher harmonics from FELIX, and with no filter in the way, these get through to the PMT. They can be distinguished by examining their time structure, with the peak in signal only lasting for the duration of the FEL pulse. The highest peak in figure 5.2 (a) appears to have such components.

Figure 5.2 (b) shows the transient properties in the IR excitation range from 220 to 500

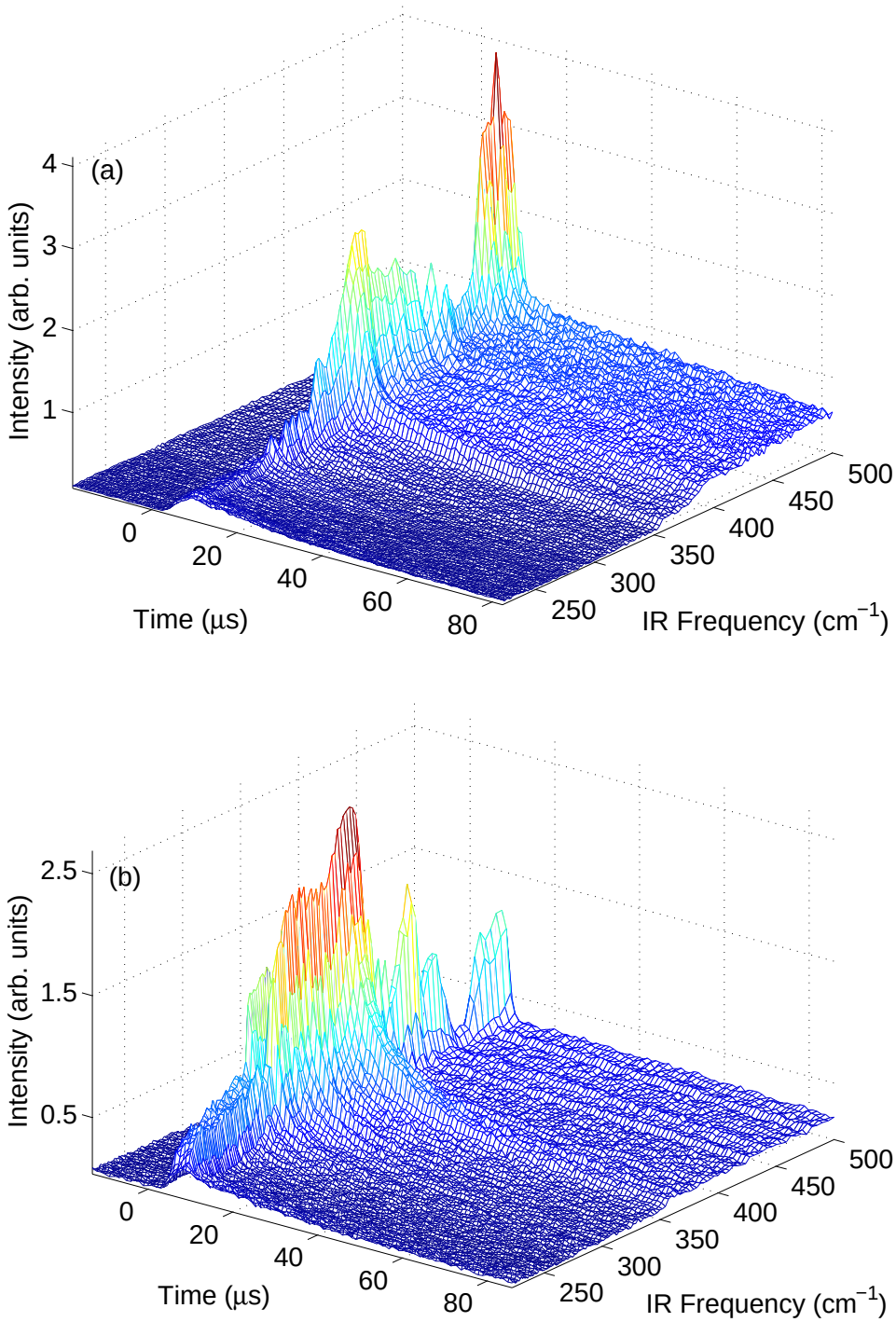

Figure 5.2 ITE emission for an IR excitation scan from 500 – 1400 cm^{-1} with a UV – IR delay of (a) 150 μs and (b) 800 μs at a sample temperature of 8 K. The emission enhancement intensity has decreased in (b) compared with (a). The intensity is seen to decrease as the excitation frequency falls from 500 towards 250 cm^{-1}. Because this scan is contaminated by higher harmonics of FELIX, seen as fast high intensity peaks it is not useful for studying the faster aspects of the ITE dynamics.

cm^{-1} with a delay of 800 μs. The enhancement has diminished, and this has led to the temporally sharp structures becoming relatively more prominent, since these do not appear to be related to the actual SrF_2:Yb^{2+} exciton emission. Interestingly there appears to be a relatively slow feature occurring at 350 cm^{-1}, however analysis has shown that this is caused by the fast structure residing on top of the typical enhancement. Included in this structure are FELIX harmonic effects as well. The excitation peaks occurring above 375 cm^{-1} are mainly due to FELIX harmonics. Unfortunately since this set of data is dominated by FELIX effects and fast temporal features, it is not overly useful.

Figure 5.3 shows the transient properties in the IR excitation range from 155 to 205 cm^{-1} with a delay of 150 μs. There is a sharp excitation peak in the enhancement at around 178 cm^{-1}. The intensity fluctuations occurring throughout the excitation range are due to FELIX power fluctuations in scanning. As described in section 3.2 scanning at these frequencies is not ideal, as one must tune the FEL cavity for a given wavelength of IR radiation. As this changes, the output power of the IR radiation fluctuates, causing the observed signal fluctuations. Because of this it was extremely important to verify that the peak observed was not simply a power fluctuation. It was found that FELIX's power was actually at a local minimum over the region of the peak, which suggests that the peak is real.

5.5.1 Time integrated IR excitation spectrum

Through the integration of the transient signal over the enhancement region an IR excitation spectrum of SrF_2:Yb^{2+} was obtained as shown in figure 5.4. As noted previously, the excitation scans were conducted in segments and these were put together to construct the overall excitation spectrum. To obtain correct scaling in the different scan regimes the intensities of the start and end points of the excitation regions were matched post integration. The gating was selected such that the fast features encountered and shown in figures 5.1 (b) and 5.2 were omitted from the integration.

As with CaF_2:Yb^{2+} the spectrum can be divided into three distinct regions, with a high energy peak centered at (1284 ± 8) cm^{-1} with a width of (40 ± 10) cm^{-1}, a broad band from 950 to 400 cm^{-1} and a low energy peak at (178 ± 3) cm^{-1} with a FWHM of (12 ± 2) cm^{-1}. Unlike the CaF_2:Yb^{2+} case the excitation transient data does not immediately show distinct dynamic behaviour in relation to excitation frequency within the broad band. Comparing figures 4.5 and 5.1 illustrates this. However, extending the interpretation employed in the case of the CaF_2:Yb^{2+} we can infer that the broad band is made up of

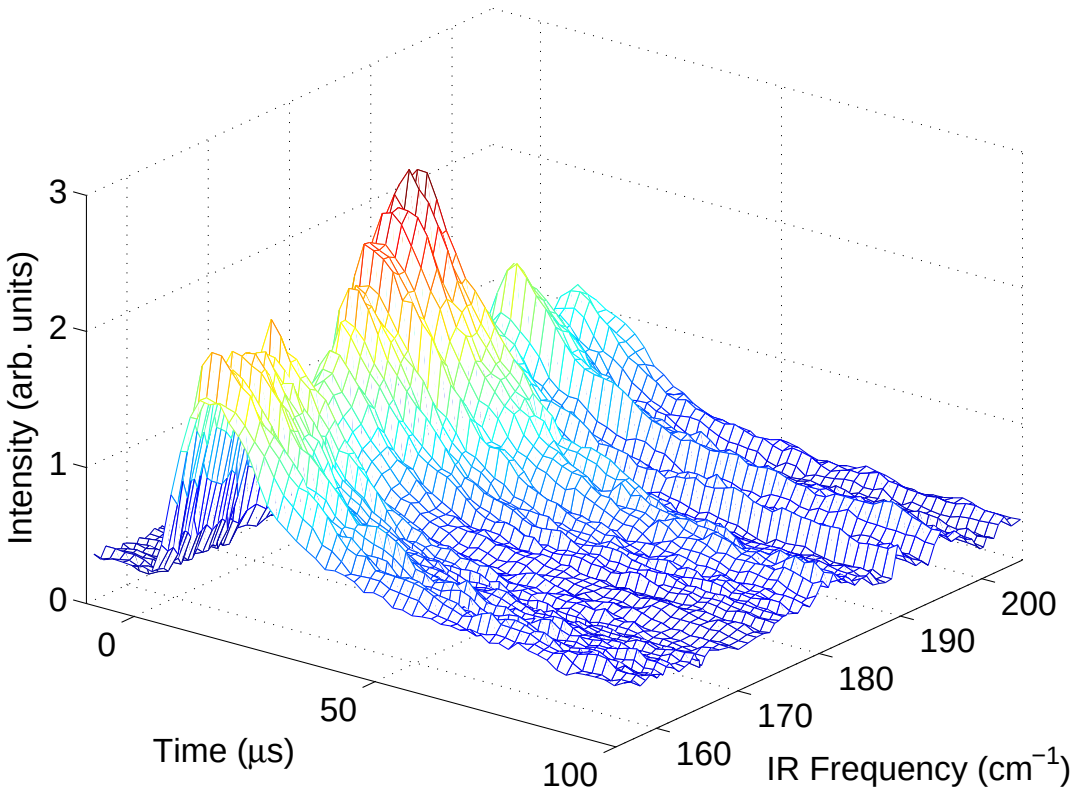

Figure 5.3 Emission enhancement induced in SrF_2:Yb^{2+} by IR excitation from 155 – 210 cm^{-1} with a UV – IR delay of 150 μs showing the low energy sharp peak occurring at 178 cm^{-1}. The dynamic behaviour does not appear to vary across the IR excitation range and the minor intensity fluctuations are due to IR fluence fluctuations. The emission was monitored at all frequencies. The sample temperature was 8 K.

transitions that alter the state of the delocalized electron. The total width of the broad band is similar to that of CaF_2:Yb^{2+} although the direct IR absorption intra–excitonic transitions have shifted to a lower energy in comparison here. Since there is a bond length change, transitions involving the delocalized electron are vibronically broadened. Such a bond length change occurs depending on the states occupied by the delocalized electron. So, the vibronically broadened band is due to transitions that change the orbital of the delocalized electron. The dips present within this broad band are due to atmospheric water absorption of the IR radiation causing an effective lowering in the incident IR power upon the sample. Although purging the beam path with dry nitrogen helped alleviate the problem, it did not completely remove the highly sensitive absorption.

The SrF_2:Yb^{2+} sharp lines display a greater spread in energy in comparison to the CaF_2:Yb^{2+} case, with the low energy line occurring at a lower energy (178 cm^{-1} compared

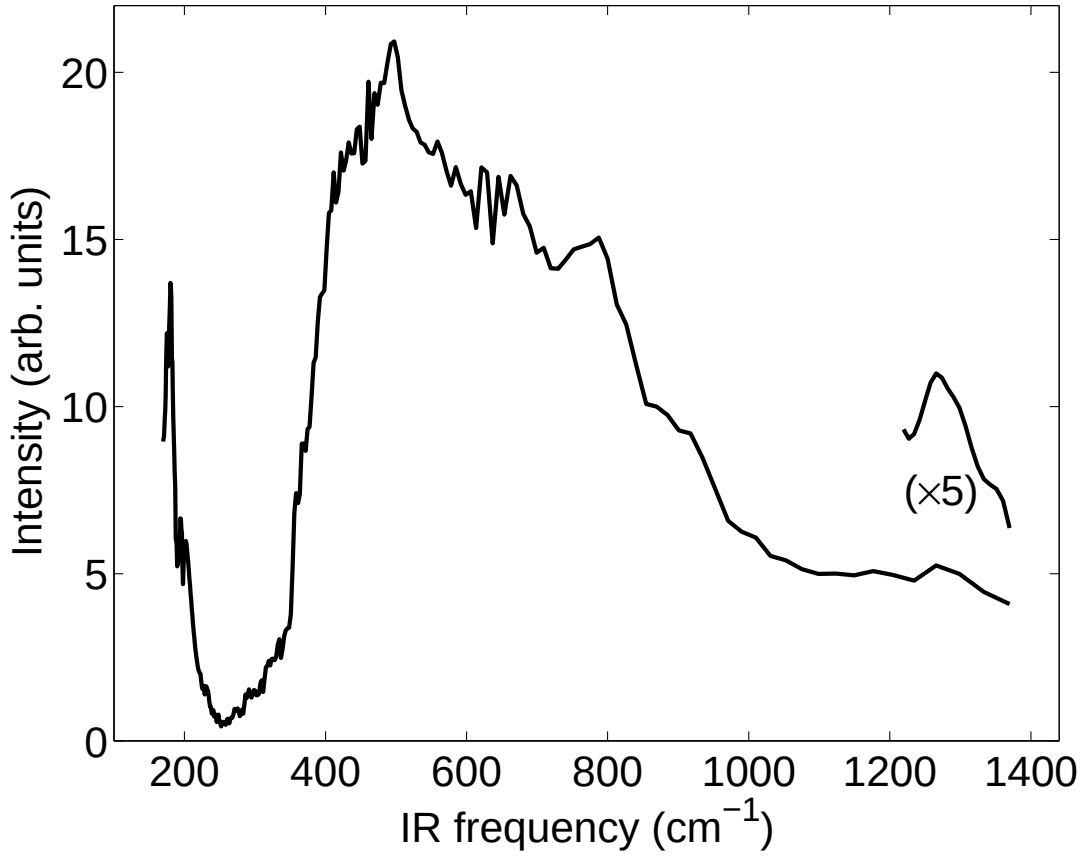

Figure 5.4 8 K excitation spectrum obtained through integrating over the emission enhancement induced by the IR pulse in SrF_2:Yb^{2+}. Two sharp peaks are present at 178 cm^{-1} and 1284 cm^{-1} respectively. Within the broad feature between 400 to 1000 cm^{-1} the higher frequency features are likely a result of direct transitions with the lower frequency features originating from local heating. The dips appearing throughout the spectrum are due to atmospheric absorption of the IR radiation. Details of the sharp peaks are presented in table 5.2.

Table 5.2 Parameters from fitting single Gaussians to sharp peaks present in the IR excitation spectrum of SrF_2:Yb^{2+}. The background was first removed with a polynomial subtraction from the relevant segment of the spectrum. A_0 of the high frequency peak was set at 1 to allow for easy comparison.

Parameter	High frequency	Low frequency
A_0	1	12 ± 4
x_0	1284 ± 8	178 ± 3
FWHM	40 ± 10	12 ± 2

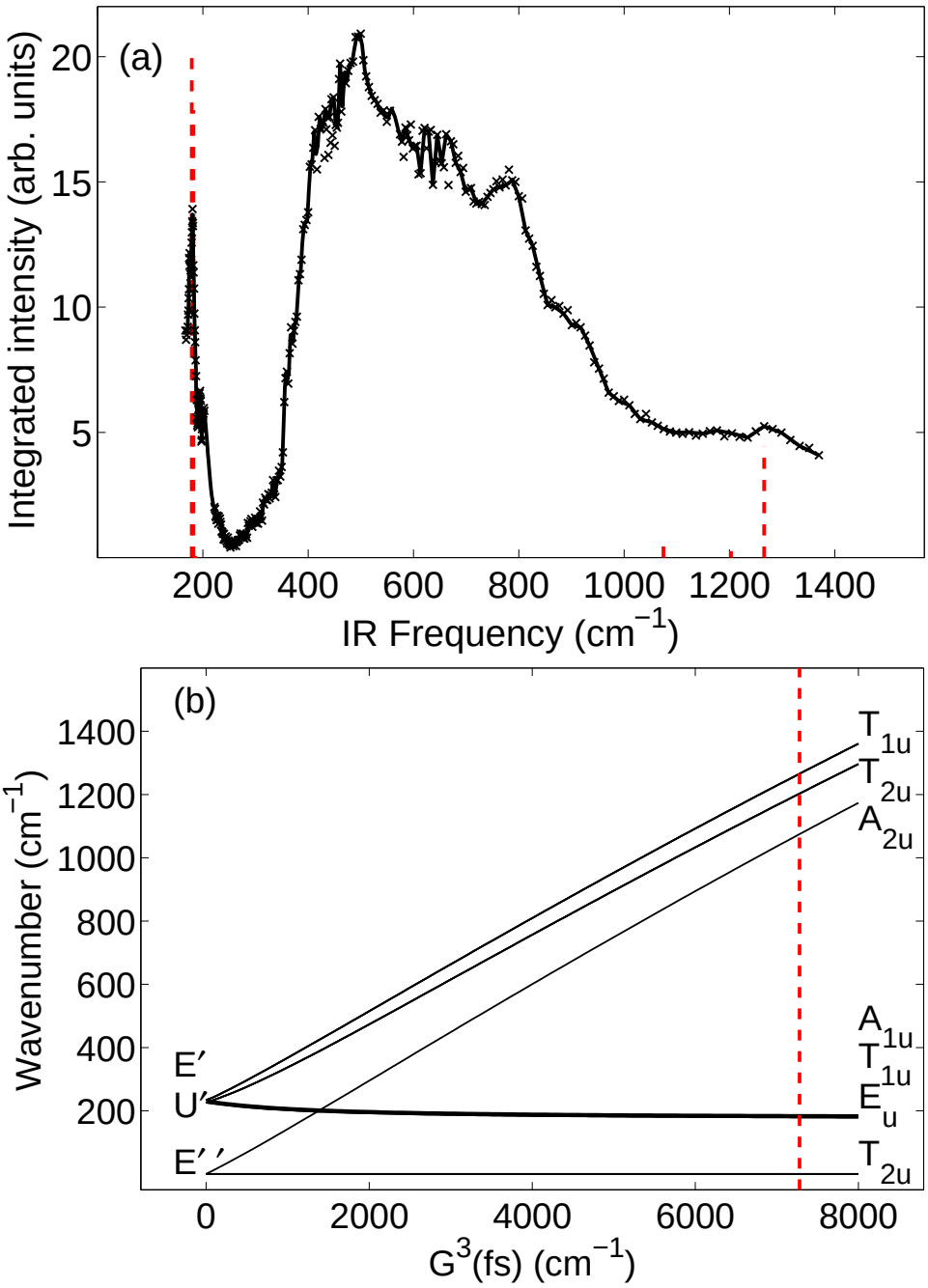

Figure 5.5 (a) 8 K IR excitation spectrum for SrF_2:Yb^{2+} including the calculated oscillator strengths for the transitions observed and (b) dependence of the exciton energy levels on the exchange parameter G^3(fs).

to 249 cm^{-1}) and the high energy line occurring at a higher energy (1284 cm^{-1} compared to 1145 cm^{-1}). In SrF_2 the phonon peak occurs at 220 cm^{-1} and is wider than the low energy sharp peak observed here [19]. These lines can be explained using the same interpretation as in the CaF_2:Yb^{2+} case. Again, note that due to the narrowness of the sharp lines they cannot involve a change in bonding, thus they must be as a result of changes within the $4f$ hole. The semi-empirical model described by equation 4.4, and employed to model the sharp lines in CaF_2:Yb^{2+} can be extended to account for the observations in SrF_2:Yb^{2+} with appropriate modification of some parameters. Even though both systems have cubic symmetry, due to the difference in the size of Sr^{2+} in comparison to Ca^{2+} the exchange and crystal field parameters will be different. If the interpretation is to remain consistent changing these parameters should allow for the modeling of the greater spread in the two observed sharp lines as well as their specific frequencies.

With $B_4 = -600$ cm^{-1} and $G^3(fs) = 7278$ cm^{-1} the observed sharp lines were matched. While the crystal field parameter B_4 is lower than the corresponding value of -800 cm^{-1} for CaF_2 given the larger size of the SrF_2 lattice [15, 94], this is reasonable and matches favourably with previous studies on SrF_2 containing erbium and dysprosium impurities [25, 73]. The B_4 is also close to the value determined in reference [6] for $SrCl_2$:Yb^{2+}, which was -725 cm^{-1}. Additionally the model provides oscillator strengths that reasonably match the observed relative intensities of the two sharp lines. Both the frequency and intensity matching of the model to data is shown in figure 5.5 (a). The comparatively large exchange parameter indicates that the ITE electron is more localized on the Yb^{3+} than in the CaF_2 case. Due to the larger lattice size in SrF_2, this behavior is expected. A summary of the values used in matching the sharp lines is presented in table 5.3, with CaF_2 for comparison.

The energy splittings and the manner in which the exchange parameter affects the excitonic energy levels in the particular case of SrF_2:Yb^{2+} is demonstrated in figure 5.5 (b). This illustrates that the greater exchange parameter allows the model to account for the greater spread observed between the two sharp lines. The general details of this calculation is identical to the case of CaF_2:Yb^{2+}.

Table 5.3 Comparison of parameters in matching the sharp lines observed in SrF_2:Yb^{2+} and CaF_2:Yb^{2+}. The ζ and $\frac{B_6}{B_4}$ values are from ref [73].

Parameter	**SrF_2:Yb^{2+}(cm^{-1})**	**CaF_2:Yb^{2+}(cm^{-1})**
ζ	2928	2928
B_4	-600	-800
$\frac{B_6}{B_4}$	-0.34	-0.34
$G^3(fs)$	7278	5900

5.6 Dynamic behaviour of the SrF_2:Yb^{2+} ITE under IR excitation

Although at first glance the time–frequency plots of the transients under varying IR excitation frequencies do not seem to show a great deal of variation in the dynamics, closer examination reveals that there are significant differences across the broad band region of the excitation spectrum. Figure 5.6 illustrates these differences. The overall shape does not change as dramatically with excitation frequency as in the CaF_2:Yb^{2+} case. However, it is clear that the transient at an excitation frequency of 500 cm^{-1} displays a much slower decay and a greater rise time in comparison with an excitation frequency of 770 cm^{-1}. As with the CaF_2:Yb^{2+} the lower excitation frequency (in this case at 420 cm^{-1}) shows a significant rise, but a smaller enhancement in comparison to the other transients. In the current case its rise time is similar to the 500 cm^{-1}, however its decay is much faster.[1]

Given the IR absorption spectrum of SrF_2 (refer to appendix B.1 for details) is similar to that of CaF_2 with the peak shifted to 220 cm^{-1} it is likely that local heating under absorption of the IR radiation by the lattice plays a significant role in the current case as well. Furthermore, given that the absorption peak is shifted to a lower frequency and that the absorption curve is essentially a monotonically increasing function towards the peak, the maximum of the thermally induced peak would be expected to red shift in comparison with CaF_2:Yb^{2+}. Examining the excitation spectra (figures 4.7 and 5.4), we see that the "second" peak within the broad band occurs at 500 cm^{-1} in SrF_2:Yb^{2+} while it is closer to 600 cm^{-1} in CaF_2:Yb^{2+}.

[1] In the case of the CaF_2:Yb^{2+} the rise time at 455 cm^{-1} was much larger than the all the other transients.

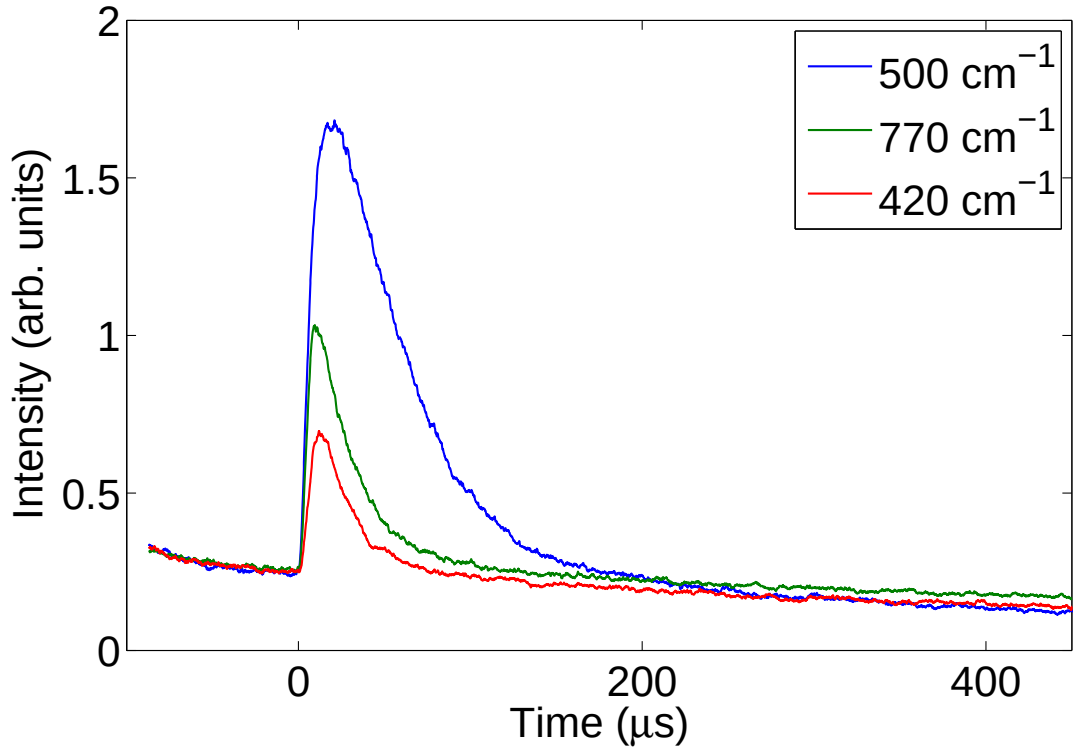

Figure 5.6 Comparison between the full IR excitation power transients at frequencies of 500 cm^{-1}, 770 cm^{-1} and 420 cm^{-1} at a sample temperature of 8 K.

5.6.1 Occurrence of UV induced electron trapping and their liberation by IR irradiation

Examining the behaviour of the emission over a time scale of 100 ms, the UV induced emission intensity over several excitation cycles was observed to undergo sequential reduction with each pulse. Figure 5.7 shows that the emission intensity diminishes by about 50% over 80 ms, or 80 UV pulses.[2] FELIX was operated at a repetition rate of 10 Hz, thus figure 5.7 represents one complete cycle of the transient behaviour in between IR pulses. Upon irradiation by the IR pulse (operating at a frequency of 550 cm^{-1}) at $t = 0$ ms, the intensity of the emission induced by the subsequent UV pulse increases substantially. It should be noted that the large signal occurring at $t = 0$ ms is the IR induced emission enhancement previously explained.

The behaviour observed in figure 5.7 shows that the UV pulses are likely placing electrons from Yb^{2+} ions into trap states, thus decreasing the overall number of oscillators available to populate the optically active ITE states. The relatively steady level of emission observed for $-20 < t < 0$ ms indicates that the decreasing emission reaches a steady state

[2]The UV pulse repetition rate is 1 kHz, thus a UV pulse strikes the sample every millisecond.

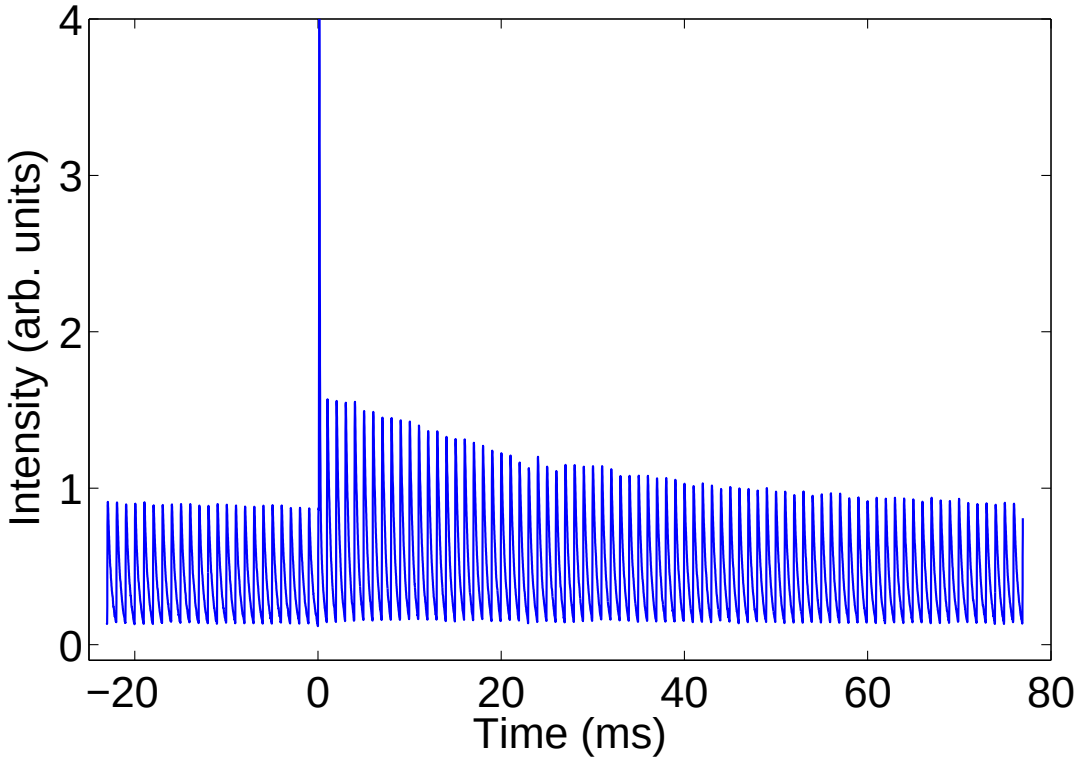

Figure 5.7 Behavior of the transients over a 100 ms timescale at a sample temperature of 8 K. The UV induced intensity reduces with each pulse, eventually leveling off. There is a constant emission level that is stable over this time scale. The IR pulse occurring at $t = 0$ ms causes an increase in the intensity of emission induced by the subsequent UV pulse.

as the number of pulses increase beyond 80. The IR pulse liberates the trapped electrons causing the UV induced emission to increase subsequent to the sample being irradiated by the IR. By examining the rate at which the maximum intensity of the emission diminishes at each pulse after this, an estimate of the fraction of oscillators lost to traps can be obtained.

In order to achieve this a peak finding algorithm was employed to determine the times at which the UV pulse was incident upon the sample. This also allowed for a measure of the emission intensity for each pulse. An exponential decay function was fitted with an offset included to account for the steady state emission intensity. The independent variable used in the function was pulse number (rather than time), allowing for the determination of traps populated per UV pulse. Figure 5.8 illustrates the calculation and the achieved fit to the decay of the intensity.

The fitted function takes the form:

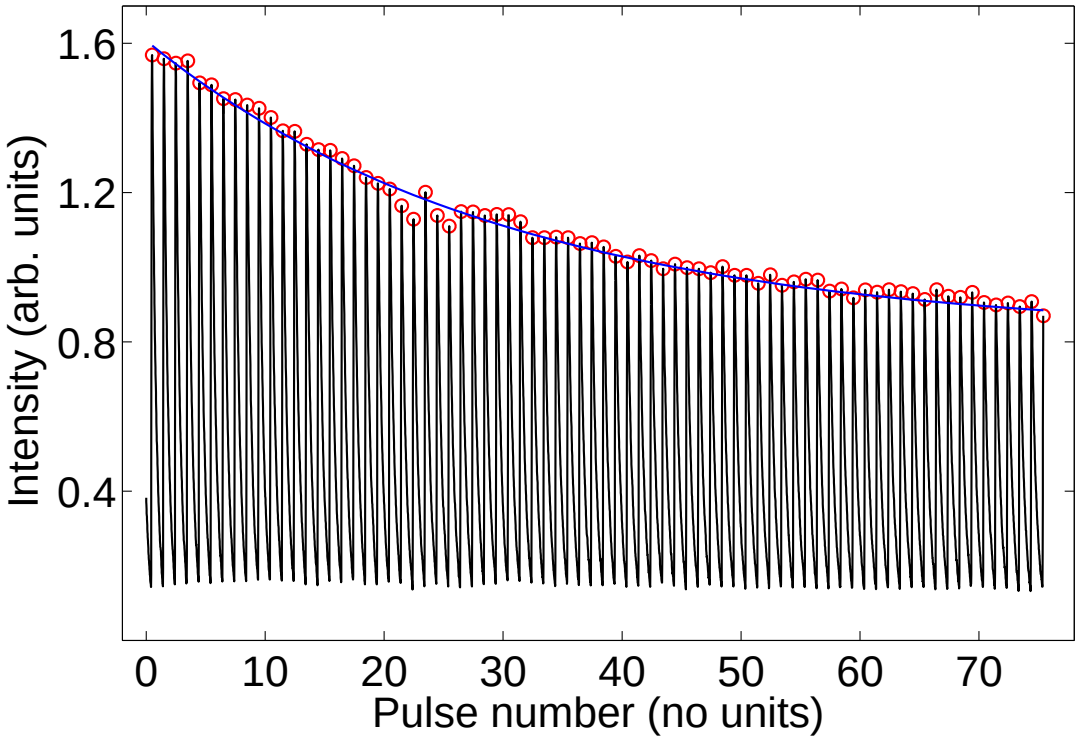

Figure 5.8 Demonstration of the calculation to determine the rate at which the UV populates traps. The red circles indicate the peak positions and intensity. The blue line is the fitted decay curve, fitted to the pulse number. This as been modified to match the indexing of the pulse position to show the decay clearly. The black transient is the same as that found in figure 5.7, post FEL pulse.

$$I(n) = I_0 e^{-\beta n} + y_0 \tag{5.1}$$

where $I_0 = 0.80 \pm 0.04$ (arb. units), $y_0 = 0.82 \pm 0.03$ (arb. units), $\beta = 0.033 \pm 0.002$ and n is the pulse number after the arrival of the FEL pulse. Since we are dealing with pulse numbers β has no units.

By examining the ratio of the offset (representing the steady state emission intensity) to I_0 we see that electrons from about half of the oscillators the UV can interact with are eventually lost to traps. The loss rate is approximately 3% of initially available oscillators per pulse. Assuming the trap liberation is a single photon process, from the IR excitation frequency we can estimate that the trap depth at most 550 cm^{-1}.

These observations indicate that the UV populates trap states by photoionizing electrons from Yb^{2+} sites.[3] The IR liberates these traps and they recombine with the Yb^{3+} left

[3]Since the emission occurs due to the UV interacting with the $4f$ electrons and creating ITEs via the

by the UV pulse(s), eventually returning the electron to the $4f^{14}$ state of the Yb^{2+}. The increase in the UV induced emission subsequent to the IR pulse supports this interpretation.

Measurement of changes in Yb^{3+} populations with respect to the number of incident UV pulses may shed light on the nature of the traps. This can be done with a simultaneous measurement of the $f - f$ absorption in Yb^{3+}, occuring at 10200 cm^{-1}. For example, an increase in Yb^{3+} would indicate that the UV photoionizes Yb^{2+} to trap states that are independent of the dopant. Additionally monitoring the $f - f$ absorption while scanning the IR excitation may provide a spectrum of the shallow traps occuring within the system. Similarly, such a measurement while exposing the sample to temperatures used for thermoluminscence experiments (where trap depths can be determined) may allow for the construction of a spectrum of the deeper traps occuring in the system.

The pathway through which the trapped electrons are recycled to the Yb ions remains unclear.[4]

However, because of the direct evidence of trap liberation the possibility must be investigated. In order to achieve this the transients must be examined in greater detail.

5.7 UV – IR delay dependence of the transients

The decay of the SrF_2:Yb^{2+} ITE emission is much faster in comparison to the CaF_2:Yb^{2+} case at 1500 s^{-1} to 66 s^{-1} (decay time constant of 660 μs compared with 15 ms). Since the emission decays a significantly within the repetition rate of the UV pulses, the influence of the delay between the UV and IR pulses on the dynamic properties of the transients can be explored.

Figures 5.9 (a) and (b) show the UV – IR delay dependent properties of the enhancement at excitation frequencies of 500 and 770 cm^{-1} respectively. The delay was varied between 200 μs to 800 μs in steps of 200 μs.

In general with an increase in the delay there is a decrease in the emission enhancement.

$5d$ states, a decrease in the UV induced emission indicates a decrease in the number of $4f$ electrons with which the UV can interact.

[4]For example, regardless of whether the electrons decayed from the conduction band straight to the $4f^{14}$ states or utilized the ITE decay as a pathway or decayed directly via a $5d$ transition, the increase in the emission at the subsequent UV pulse would be observed.

While it appears that the magnitude of the enhancement decays as the intensity of the emission just prior to the IR pulse diminishes, there is still a significant emission enhancement at a UV – IR delay of 800 μs. The shape of the enhancement (in line with the data presented previously) changes across the excitation frequencies, however, at a given frequency the shape does not change with delay. In addition to this the change in post enhancement decay of the transients remain consistent throughout the changing delays.

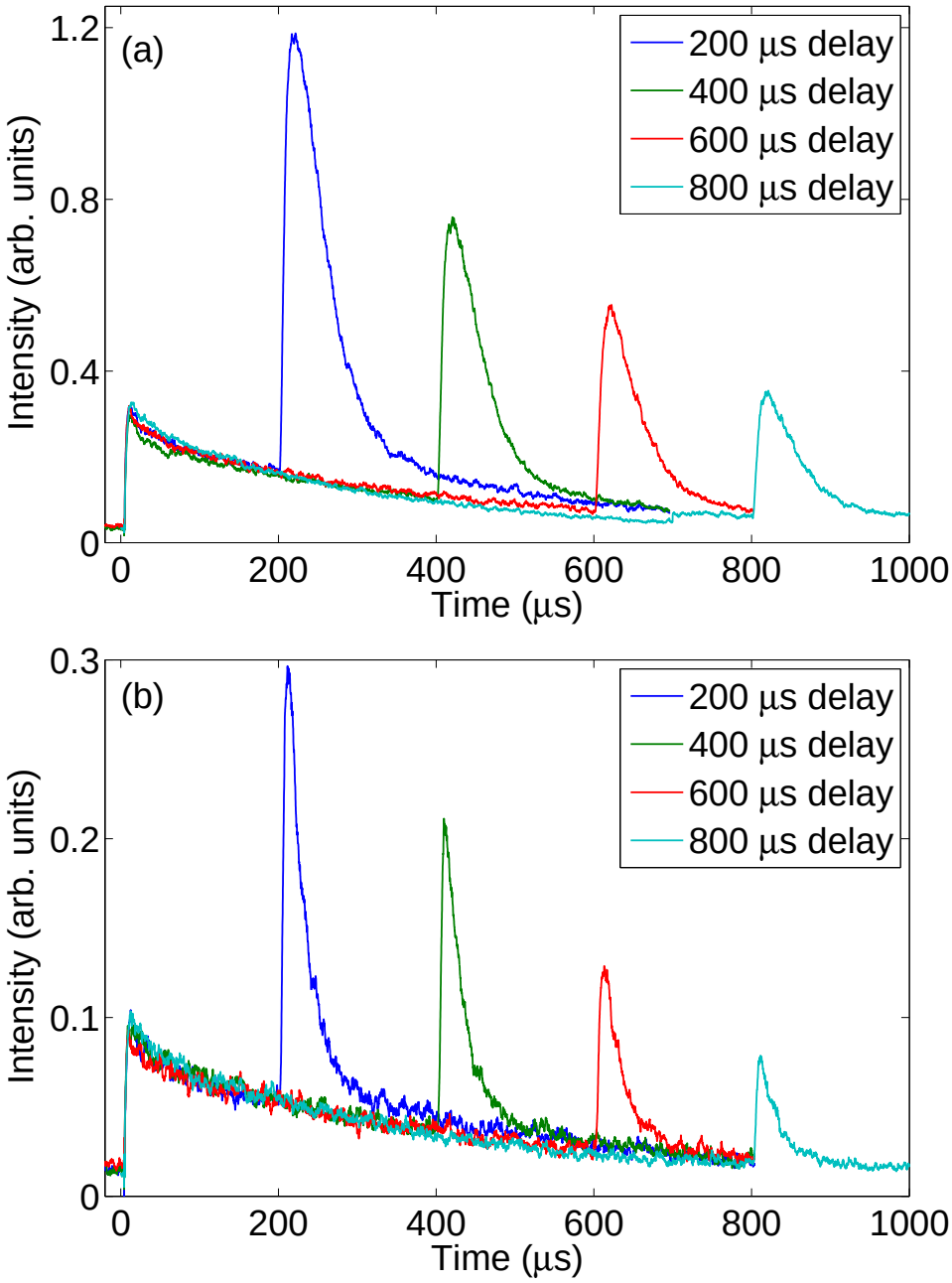

Figure 5.9 8 K transients observed for UV – IR delays between 200 – 800 μs at IR excitation frequencies of (a) 500 cm^{-1} and (b) 770 cm^{-1}. The shape of the transients retain their overall shape across the delay range in both cases. The UV pulse occurs at $t = 0$ μs.

By overlaying the transients at each of the delays and normalizing them to a domain $[0, 1]$ it is possible to directly compare the shape of the enhancement at a given delay, the post enhancement decay profile and the intensity of the emission post enhancement. Figure 5.10 shows that, apart from the total intensity of the emission enhancement, the transients appear to be identical irrespective of the delay between the UV and IR pulses.

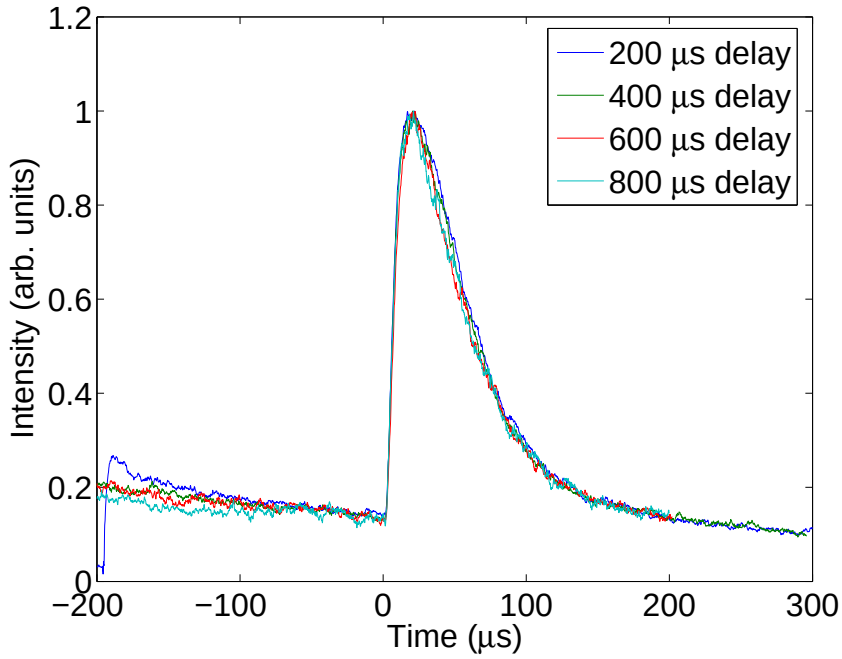

Figure 5.10 UV – IR delay dependent transients at an excitation frequency of 500 cm^{-1} overlaid and normalized to a domain of $[0, 1]$ to allow for comparison of the changes in shape.

The observations detailed in section 5.6.1 indicate that the traps are long lived on the scale of the experiment. Thus their contribution should not change with the relative delay of the UV and IR pulses. However as the delay increases the population of state 2 prior to the IR pulse diminishes and its contribution to the enhancement also decreases. Therefore the ratio of the contribution from the liberated traps increases. This will then lead to a change of the shape of the enhancement transient. Additionally the enhancement magnitude should level off with increasing delay. By computing the total enhancement (by integrating the intensity over the enhancement period) for each of the delays, and then comparing this to the relative delay is possible to ascertain whether such a leveling is occurring. If there is a leveling off then the total enhancement will decay at a slower rate than the decay of the UV only emission curve. We can further verify this by comparing the total enhancement to the pre–IR emission level. If there is a contribution from traps, then this should show a super linear relationship.

Figure 5.11 shows the relationships for IR excitation frequencies of 385, 500 and 770 cm^{-1}.

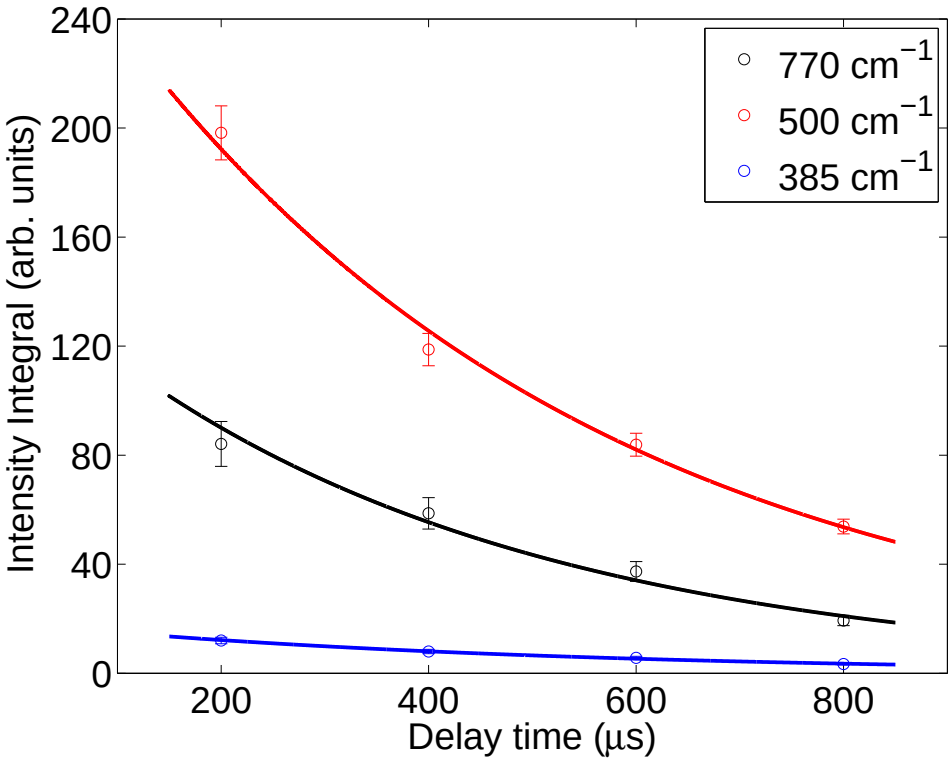

Figure 5.11 Change in the IR induced enhancement magnitude with varying UV – IR delay at different excitation frequencies. While the initial maximum enhancement magnitude is dependent upon the excitation frequency, the manner in which this changes with delay seems consistent across the IR excitation frequencies. The solid lines are exponential decay fits to the delay dependent enhancement.

Table 5.4 Parameters for the fitted exponentials to the enhancement magnitude decay points illustrated in figure 5.11.

f_{exc}(cm^{-1})	Rate (s^{-1})	Time (μs)
770	2400 ± 200	410 ± 40
500	2100 ± 100	470 ± 20
385	2100 ± 100	480 ± 30

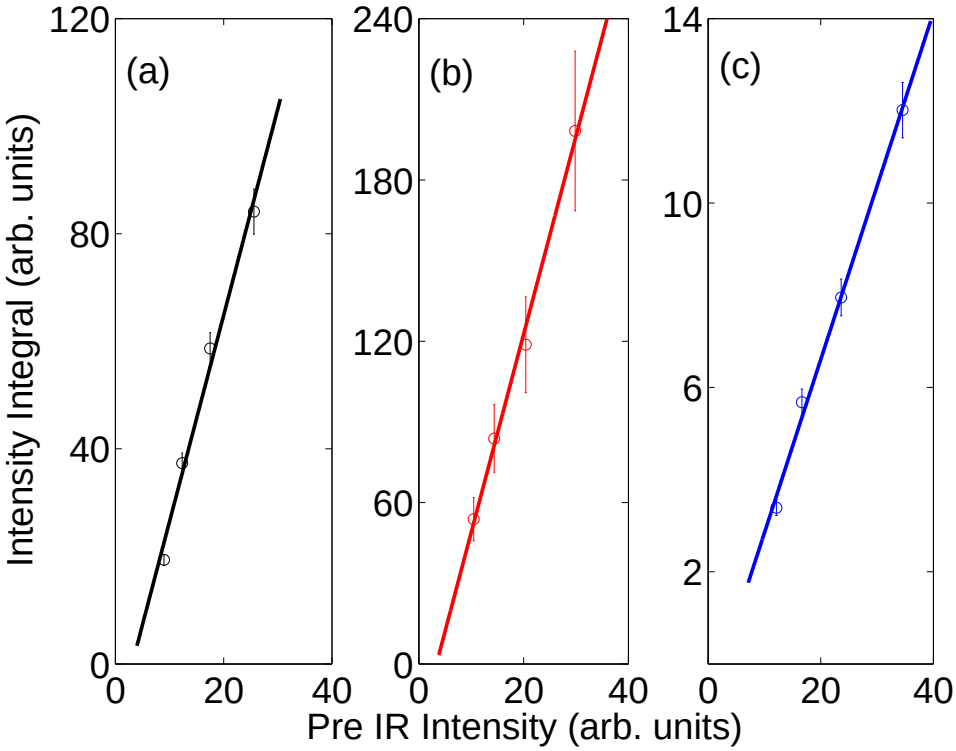

Figure 5.12 Change in the IR induced enhancement magnitude with pre-IR emission level (set up through varying delay) at different excitation frequencies (a) 770 cm^{-1}, (b) 500 cm^{-1} and (c) 385 cm^{-1}. The variation of the enhancement magnitude is linear with pre-IR emission level, indicating that the total number of excited oscillators probably does not change under IR excitation.

The rates and time constants for the fitted curves are presented in table 5.4 with their uncertainties. It appears that the decay is slightly faster than the observed decay of the UV only emission which remains consistent at 1700 ± 100 s^{-1} (time constant of 590 ± 30 μs). If liberated traps were making a contribution to the ITE emission the expectation is that the decay of the enhancement would be *slower* than the decay of the UV only emission level. Given the uncertainties associated with the decay values of enhancement decrease it is difficult to distinguish between them for different excitation frequencies.

Figure 5.12 shows the ratio of the enhancement magnitude to the pre–IR emission level. Across all the excitation frequencies the relationship is clearly linear and indicating that the enhancement magnitude is directly proportional to the pre IR population of state 2. This further reinforces the interpretation that liberated traps can not be identified as contributing to the ITE emission within the broad band.The behavior of the delay data suggests that the traps being liberated by the IR radiation do not recombine to form excited excitons.

5.8 IR fluence dependent behaviour of the transients

Figures 5.13 (a) and (b) show the IR fluence dependent transients at IR excitation frequencies of 500 and 770 cm^{-1} respectively. The IR fluence at the sample in both the cases is similar at approximately 10 Jcm^{-2}. The time axis has been shifted such that $t = 0$ now coincides with the UV pulse. During these measurements the UV – IR delay was set to 100 μs. A common feature between both excitation frequencies is an increasing rise time as the IR power increases. Additionally the 'bulge' in the decaying part of the transients also gets more prominent with an increase in power. The post enhancement decay also appears to become faster as the power increases. Across the excitation frequencies the transients under 770 cm^{-1} excitation have less prominent rise features when compared to the 500 cm^{-1} excitation, which is consistent with the earlier frequency dependent data. The post enhancement decay also appears slower on the 770 cm^{-1} excitation transients in comparison to the 500 cm^{-1} excitation. Saturation appears to occur with the maximum enhancement less than twice that of the 3 dB attenuated enhancement. If no saturation was occurring one would expect that the difference between the 0 dB and 3 dB transients to a factor of 2 (since an attenuation of 3 dB represents a halving of the incident IR fluence).

Such behaviour becomes clearly evident when considering the total integrated enhancement magnitude, as illustrated in figures 5.14 (a) and (b) at excitation frequencies of 500 and 770 cm^{-1} respectively. The trend, similar to that observed in the case of CaF_2:Yb^{2+} (figure 4.11), indicates that at maximum power the enhancement is less than expected for a linear relationship with IR fluence.

In the case of CaF_2:Yb^{2+} sublinearity of the enhancement with IR fluence was found to be due to thermal effects induced by the IR radiation being absorbed into the lattice coupled with the heavy temperature dependence of the heat capacity in CaF_2. SrF_2 also displays such absorption [19, 70] and thermal properties [21], and is likely undergoing similar heating to the CaF_2. The increase of the post enhancement decay rate is further evidence of heating, since even a small temperature change would cause a noticeable shift in the rates given the small energy gap (of 26 cm^{-1}) between states 2 and 3 and the large difference in the relaxation rates from these states to the $4f^{14}$ ground state (1720 compared to 49000 s^{-1}) [12].

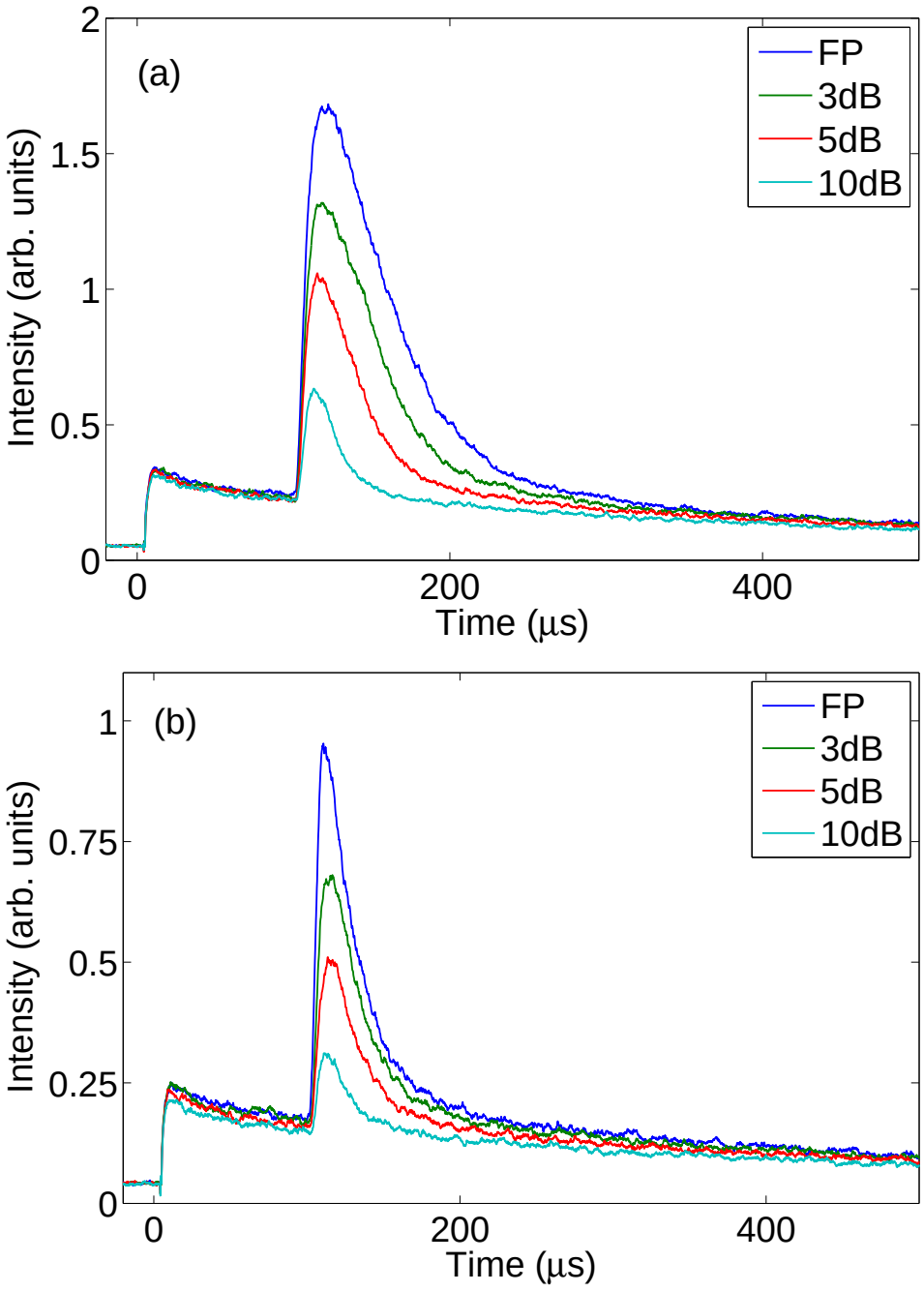

Figure 5.13 IR fluence dependent behaviour of the 8 K transients at an excitation frequency of (a) 500 cm^{-1} and (b) 770 cm^{-1}. FP indicates a fluence of 10 Jcm^{-2} with the successive attenuations decreasing the fluence to 5.0, 3.1 and 1.0 Jcm^{-2} respectively. In both cases with increasing power a rise time and a slowing of the enhancement decay builds into the transients. This effect is far more pronounced in the 500 cm^{-1} excitation case (a). The UV pulse occurs at $t = 0$ μs with the UV – IR delay at 100 μs.

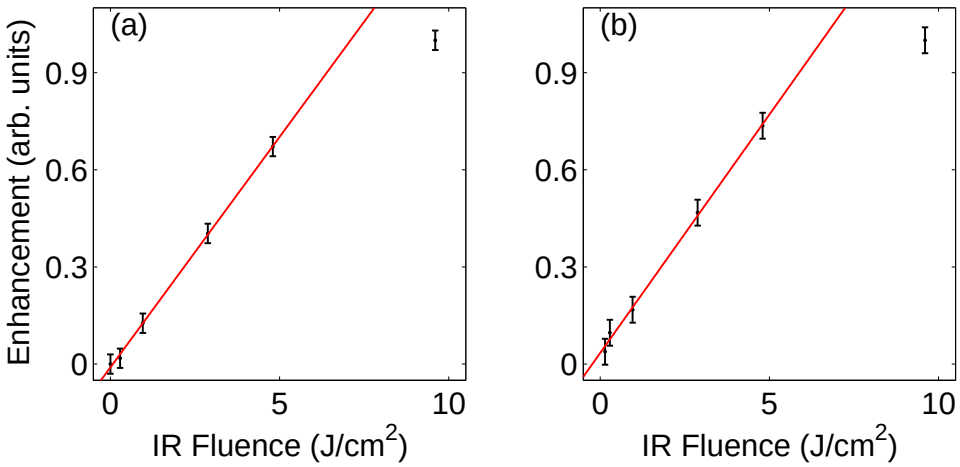

Figure 5.14 The behaviour of the integrated emission enhancement under changing IR fluence, with (a) showing the observed trend under an IR excitation frequency of 500 cm^{-1} and (b) showing the trend at 770 cm^{-1}. The integration was carried out for $100 < t < 250$ μs). Both plots have been normalized such that the maximum of the integrated value is 1 to allow for ready comparison.

5.9 Modeling the dynamics of the ITE

From the observations described above it appears that within the broad band of the IR excitation spectrum liberated traps are unlikely to make a contribution to the behaviour of the transients. The similarity of the thermal and absorption properties between CaF_2 and SrF_2 and the observed behaviour of the transients under IR fluence variation suggests that local heating will again play a part in explaining the dynamic behaviour of the SrF_2:Yb^{2+} ITE emission. Additionally, the excitation frequency dependent transients (shown in figure 5.6) suggests, as with CaF_2:Yb^{2+}, at higher excitation frequencies there are direct transitions occurring through absorption of the IR radiation within the ITE.

Given these factors the modeling conducted upon the CaF_2:Yb^{2+} ITE, described in sections 4.10 and 4.11 should be readily applicable to the SrF_2:Yb^{2+}. Modifications to the specific thermal properties and rates the modeling employs will have to be made to account for the differences between the materials. The thermal properties used for SrF_2:Yb^{2+} are summarized in appendix B. Rates previously identified by Moine et al. are used as summarized in table 5.1 [9, 12]. The energy gap between states 2 and 3 was set to 26 cm^{-1} [12].

A four level system as illustrated in figure 4.18 and described by equation(s) 4.11 was employed to model the emission transients observed. The time dependent temperature

changes due to absorption of the IR radiation and the dissipation induced heating was modeled by employing the algorithm described with a combination of equations C.7 and C.11 to ultimately solve the heat equation.

As with the modeling conducted on CaF_2:Yb^{2+}, the ITE is already in its meta stable state (2) before the modeling commences. The relative populations of state 2 and 3 prior to the incidence of the IR pulse are set by the sample temperature (taken to be 8 K in most cases) and the ratio established by equation 4.2.

5.9.1 Modeling the IR fluence dependent behaviour at different frequencies

IR fluence dependent transients presented previously at excitation frequencies of 500 and 770 cm^{-1} were modeled with the parameters F_{24} and E_m fitted to the maximum fluence transients through a least squares fitting. Subsequently these were scaled to match the IR fluence upon the sample for the respective attenuations. The value for E_m was seeded by the exact same manner employed in the case of CaF_2:Yb^{2+}.

Figure 5.15 shows that the fits obtained are well matched to the data, with only a slight discrepancy evident at around the 150 μs mark in the transients. Notice that the fluence dependent changes in the post enhancement decay rates are well modeled by taking into account the dissipation of the local heating. There is a large amount of heating occurring at this frequency as it is near the peak of the IR absorption into the lattice, and is a major contributor to the enhancement. The E_m parameter presented in table 5.5 illustrates this clearly.

Table 5.5 Parameters from least squares fitting of rate equation model to transients with varying IR excitation fluence at 500 cm^{-1} in SrF_2:Yb^{2+}. Note that the rate W_{23} is the maximum reached during the transient.

Atten (dB)	Fluence (Jcm^{-2})	F_{24} (s^{-1})	E_m (mJ)	T_{max}(K)	W_{23} (s^{-1})
0	10.0 ± 0.1	12500 ± 300	4.3 ± 0.1	18.2 ± 0.2	15000
3	5.0	6250 ± 130	2.15 ± 0.05	15.8 ± 0.2	12000
5	3.1	4160 ± 80	1.33 ± 0.04	14.5 ± 0.2	9800
10	1.0	1250 ± 30	0.43 ± 0.01	12.4 ± 0.1	5300

Additionally the maximum value reached for the rate W_{23} is consistently larger than the F_{24} rate, again indicating that local heating is the dominant driver of the oscillator

population transfer at this excitation frequency. It should be stressed that the W_{23} is an *instantaneous* maximum reached within the algorithm stepping through time, and as the fluence decreases it would be maintained for an ever shorter time.[5]

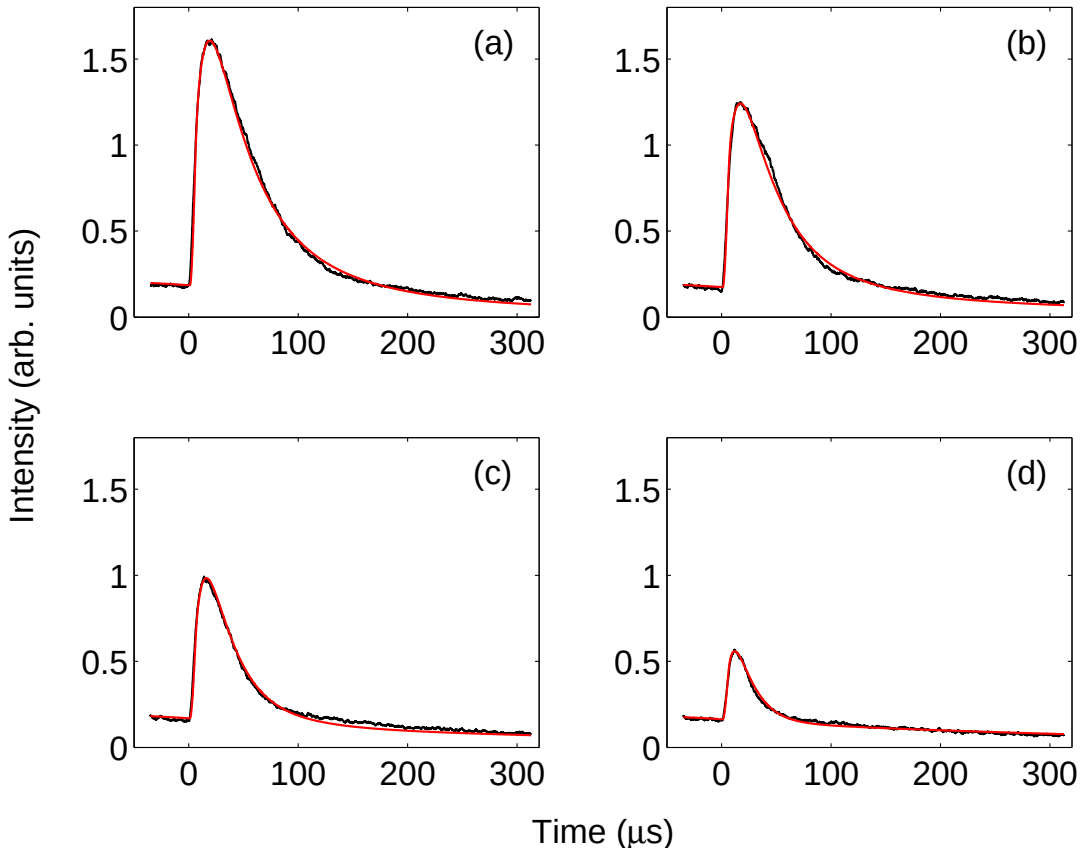

Figure 5.15 The 8 K transients and the least squares fits obtained through the rate equation modeling process at different IR fluences for a frequency of 500 cm^{-1}. The data is presented in black, while the simulated transients are presented in red. IR fluences of (a) 10 Jcm^{-2}, (b) 5.0 Jcm^{-2}, (c) 3.1 Jcm^{-2} and (d) 1.0 Jcm^{-2} were employed in obtaining the data. Note that only (a) has fitted parameters, with the values for the other curves being computed from the values for (a).

Even though the amount of energy deposited into the lattice is far higher in this instance compared to the fluence dependent observations obtained in CaF_2:Yb^{2+} (detailed in table 4.9) the maximum temperatures reached here is lower in comparison. This is because, although the temperature dependent heat capacity of both CaF_2 and SrF_2 follow a similar

[5]Recall that at low temperatures, because of the dependence of the thermal diffusivity upon temperature, the dissipation of the heat happens faster the lower the temperature above the sample conditions. As the fluence decreases the maximum temperature and the spread in the temperature distribution diminishes, this causing the heat to diffuse faster, in turn leading to an inability to sustain a given W_{23} rate. See section 4.10 for further details.

trend with temperature, SrF_2 has a capacity that is almost an order of magnitude greater than CaF_2 at low temperatures [20].

Figure 5.16 shows the fits obtained for an IR excitation frequency of 770 cm^{-1} with the obtained parameters summarized in table 5.6. It is immediately clear that local heating makes a much smaller contribution to the enhancement in comparison with the 500 cm^{-1} case. The F_{24} parameter is larger than the corresponding value under 500 cm^{-1} excitation, indicating that the direct intra–excitonic transition is stronger at an excitation frequency of 770 cm^{-1}, implying a greater interaction cross section at this frequency. This further indicates that the higher energy end of the excitation spectrum is likely due to direct transitions within the ITE itself. The W_{23} maxima are much smaller than before and is a reflection on the lower maximum temperature the local interaction volume reaches due to the diminished absorption of the IR radiation by the lattice.

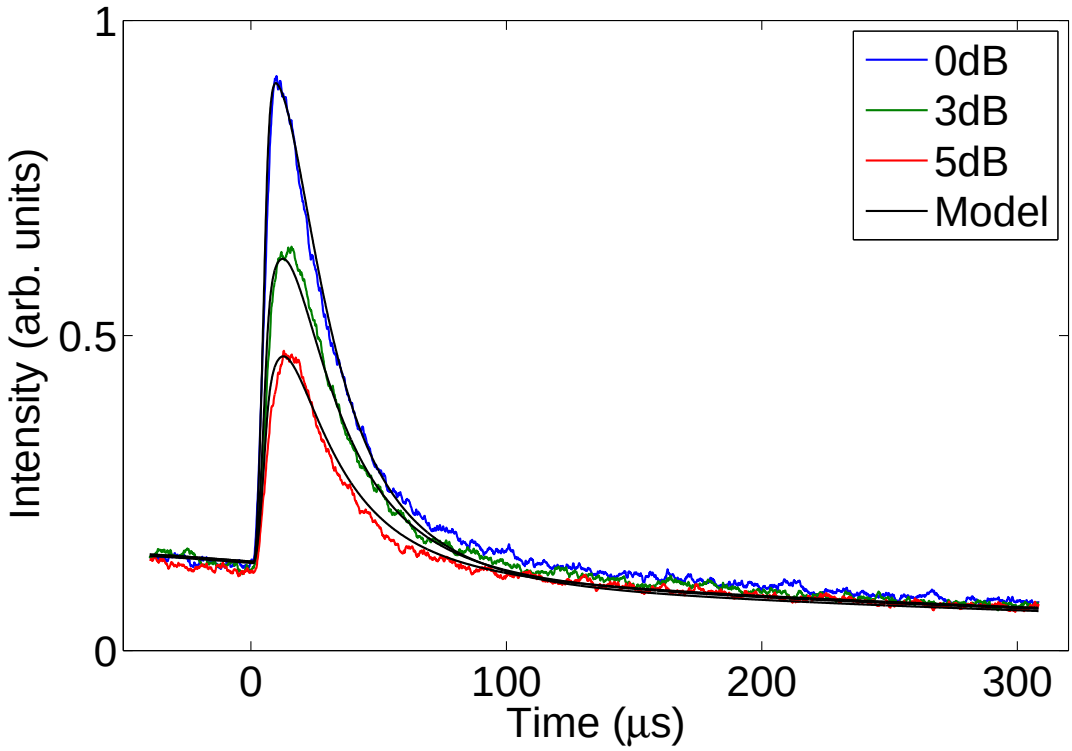

Figure 5.16 The 8 K transients and the least squares fits obtained through the rate equation modeling process at different IR fluences for a frequency of 770 cm^{-1}. IR fluences of 10 Jcm^{-2} at 0 dB, 5.0 Jcm^{-2} at 3 dB attenuation and 3.1 Jcm^{-2} at 5 dB attenuation were employed in obtaining the data. Note that only the unattenuated case has fitted parameters, with the values for the other curves being computed from the values for 0 dB.

The fits themselves are less well matched when compared to those expressed in figure 5.15, likely due to the smaller SNR given the diminishing signal away from the main peak

of the excitation. The post enhancement decay rate is well matched and as is the rise profile of the transients.

Table 5.6 Parameters from least squares fitting of rate equation model to transients with varying IR excitation fluence at 770 cm^{-1} in SrF_2:Yb^{2+}. Note that the rate F_{24} is larger in comparison to the 500 cm^{-1} excitation case.

Atten (dB)	Fluence (Jcm^{-2})	F_{24} (s^{-1})	E_m (mJ)	T_{max}(K)	W_{23} (s^{-1})
0	10.0 ± 0.1	16100 ± 600	0.85 ± 0.03	13.5 ± 0.3	7600
3	5.0	8100 ± 300	0.43 ± 0.02	12.4 ± 0.3	5900
5	3.1	5200 ± 100	0.27 ± 0.01	11.3 ± 0.3	4500

5.9.2 IR excitation frequency dependent time evolution of populations within the ITE

Since the modeling algorithm employed computes the relative population of each state at each time step, it was possible to extract the time evolution of the populations of the states along the transient. Additionally by setting up the algorithm to record the pathway of the population transfer between the states it was possible to obtain the relative influence of the two mechanisms being simulated.

Figure 5.17 (a) and (b) shows the time evolution of the population of the two emitting ITE states (2 & 3) and the $4f^{14}$ ground state at 500 and 770 cm^{-1} respectively. These figures confirm that just subsequent to the UV excitation the population is predominantly in state 2. Given that (with a sample temperature of 8 K) equation 4.2 provides a ratio 1 : 0.009 in favour of state 2 this is expected. In both cases only a small fraction of the total population present in state 2 becomes excited (between 5 to 10 %), however, due to the significantly faster radiative relaxation rate out of state 3 a large enhancement in the emission is observed. At 500 cm^{-1} excitation the population of state 3 is larger than 770 cm^{-1} and it is also sustained for a greater time. This is due to the previously discussed local heating. The population evolution of state 3 shows us why the two transients behave so differently to each other (see figure 5.6).

The individual pathways through which the population transfer occurs is examined in figure 5.18 (a) and (b) at 500 and 770 cm^{-1} respectively. In both cases the direct pathway transfers a a similar number of oscillators between states 2 and 3, with the transition being

slightly stronger in the 770 cm^{-1} excitation case. The population that is directly transferred decays immediately upon termination of the IR pulse while the thermal transfer continues, with the population reaching its maximum some time after the IR termination.

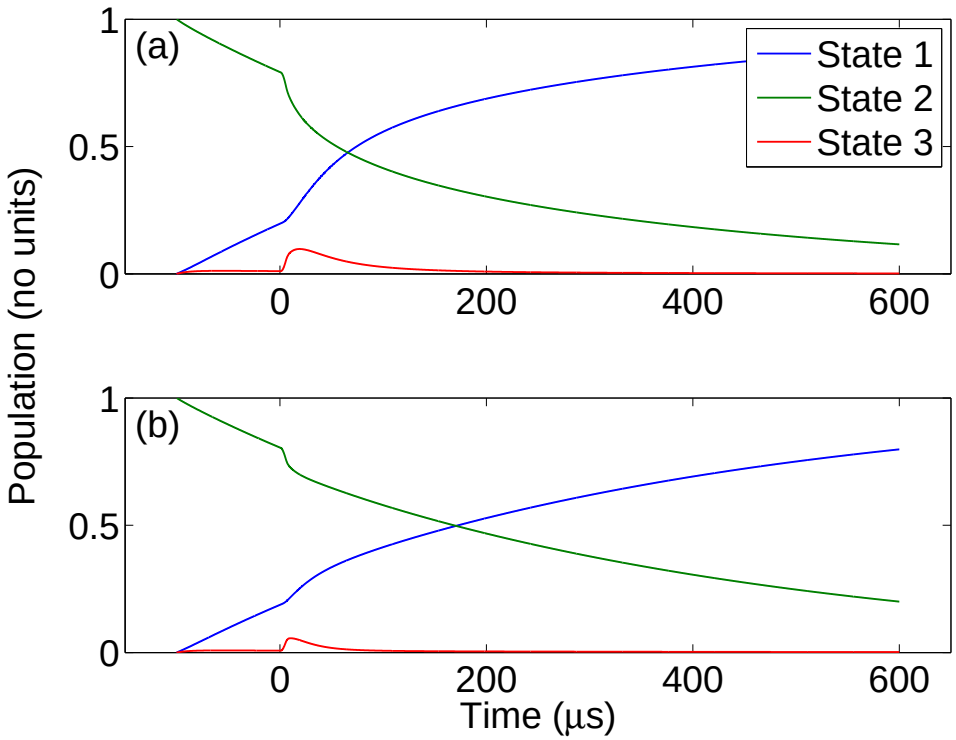

Figure 5.17 Change in the relative populations of states 1, 2 & 3 under IR excitation. The total population is 1, and the initial conditions place almost all the population in state 2. This is computed using the lattice temperature and employing equation 4.2 to obtain a ratio. (a) Shows the changes with the IR at 500 cm^{-1} and (b) shows the changes with the IR at 770 cm^{-1}. Note the difference in the relative populations of state 3 in (a) & (b).

In the case of IR excitation at 500 cm^{-1} its clear that a dominant proportion of the population transfer occurs due to heating, and the sustenance of the state 3 population for over 100 μs indicates that the cooling of the locally heated volume takes an appreciable time. This behaviour explains the *changing* post enhancement decay rate of the transients. In comparison with the IR excitation at 770 cm^{-1} both processes contribute significantly to the population transfer into state 3. Additionally the thermally transferred population peaks earlier than in the 500 cm^{-1} case. This, combined with the greater influence of the much faster direct transfer causes the overall peak of the population of state 3 to occur earlier than in the case where heating provides the dominant mechanism for the population change.

The population transfer mechanism analysis provides a pertinent illustration of the im-

portance of identifying the dynamic situation behind a particular spectral feature where possible. Considering the IR excitation spectrum without an insight into its dynamics could have led to the erroneous assignment of an electronic transfer to the peak occurring at 500 cm^{-1} or to an interpretation where the entire width of the broad peak is taken as a saturated single transfer.

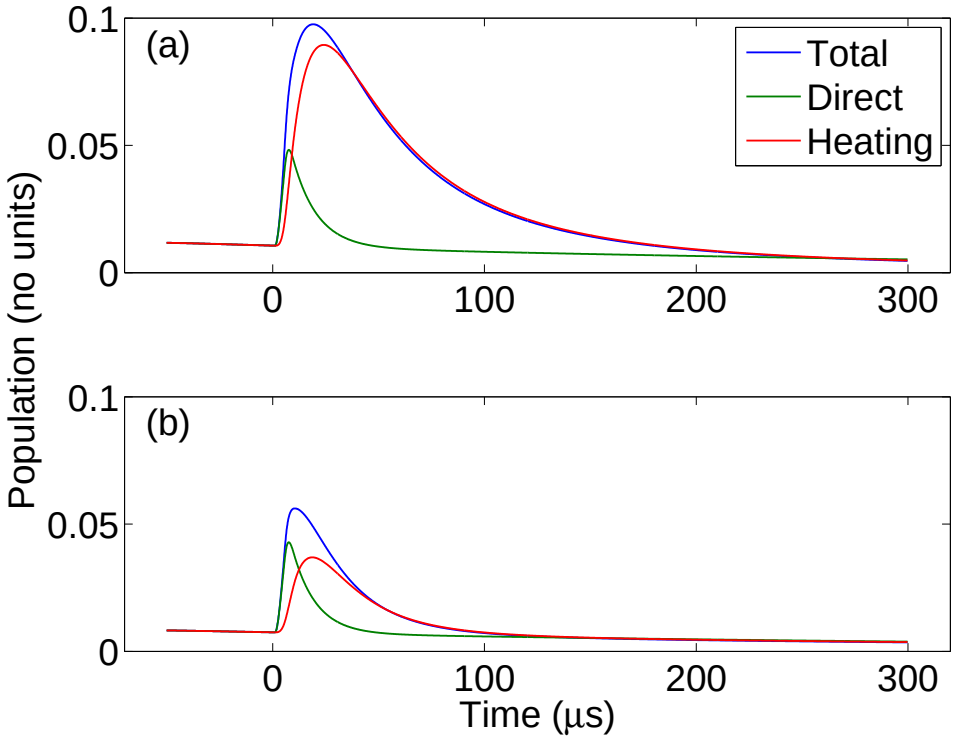

Figure 5.18 Comparison between the two pathways for transition from state 2 to 3, by examining the change in the population of state 3 under different excitation regimes. Total indicates the total population change in state 3. Heating indicates the population change due to thermalization from the IR induced heating. Direct indicates the population change via IR absorption into the exciton. (a) Shows the changes with the IR at 500 cm^{-1} and (b) shows the changes with the IR at 770 cm^{-1}. Note the significant difference in the relative strengths of the two different pathways in (a) & (b).

5.9.3 Modeling the UV – IR delay dependent behaviour of transients

Figure 5.10 showed that the shape of the transient appears independent of the delay between the UV and IR pulses, and the analysis conducted in section 5.7 indicated that the changes in enhancement magnitude were due to the decreasing population of state 2 with increasing delay. Given these facts the dynamic model that has been presented should be able to account for the delay observations by only changing the time taken

for the commencement of the IR pulse after the start of the modeling. This effectively introduces a delay between the UV and IR pulses into the model. Even though the model does not account for the dynamic behaviour due to the UV pulse, it initializes with population distributed among the states as arranged by the UV radiation and sample temperature.

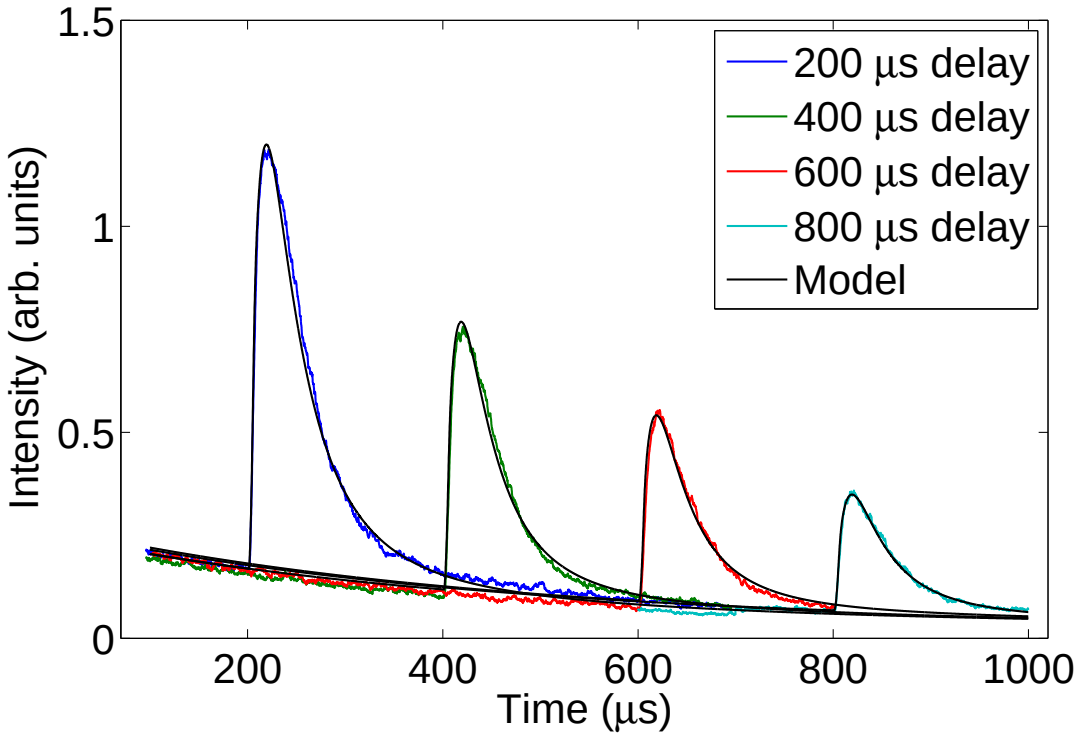

Figure 5.19 Comparison between the data (at 8 K) and model for various delays at an IR excitation frequency of 500 cm^{-1}. The rise and overall shape of the transient are well matched, however there is a slight difference in the matching of the peak of the enhancement. The parameters within the model remained constant and were identical to those presented in table 5.5 for a fluence of 10 Jcm^{-2}.

Figure 5.19 shows the fits obtained for the 500 cm^{-1} excitation case by changing the IR pulse commencement time to reflect the UV – IR delay while keeping the other parameters identical to the maximum fluence scenario. With $F_{24} = 12500\ s^{-1}$ and $E_m = 4.3$ mJ the the observations are well matched with the delay driven decrease in population just prior to the IR pulse accounting for the enhancement magnitude change. This provides strong evidence that liberated traps are not contributing significantly to the enhancement within the explored excitation frequencies of the broad band, reinforcing the interpretation that direct transitions and IR induced heating are its main drivers.

5.9.4 Modeling the temperature dependent behaviour of the transients

As in the CaF_2:Yb^{2+} case, modeling the sample temperature dependent behaviour of the transients will provide further confirmation for its accuracy and reinforce the physical interpretation of the dynamics observed within the ITE emission under IR excitation.

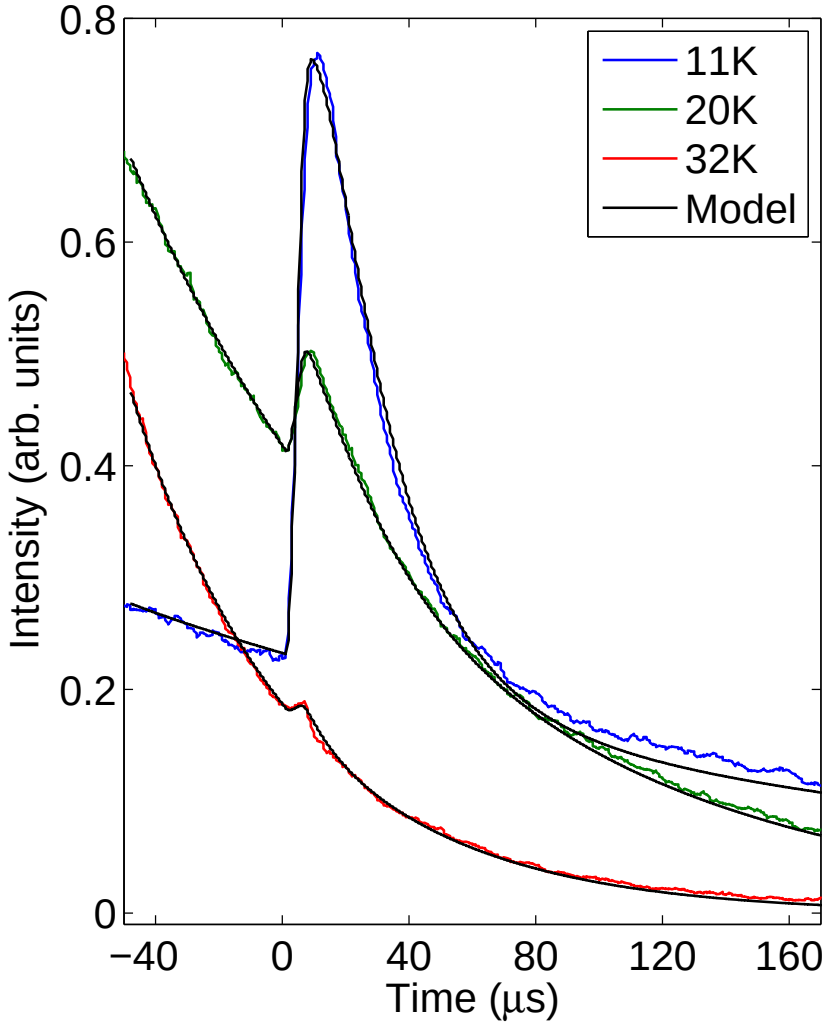

Figure 5.20 The behavior of the transients at different lattice temperatures at an IR excitation of 770 cm^{-1}. The data is time matched at the IR pulse incidence, represented by $t = 0$ μs. The modeled fit is shown in black. As the temperature increases the emission intensity increases while its decay time decreases due to thermal mixing between states 2 & 3. The UV – IR delay was set to 200 μs for these measurements.

The behaviour of the transients, as shown in figure 5.20, is as expected, with the decay becoming faster as the population ratio begins to favour state 3 with increasing temperatures. The emission intensity increases correspondingly. Note that in figure 5.20 the 32 K transient appears less intense than the other temperatures. This is because the figure

is focused upon the time region where the IR pulse interacts with the sample, which occurs 200 μs after the incidence of the UV pulse in these measurements. By this time the transient has already decayed significantly and is thus at a lower instantaneous intensity.

Table 5.7 Parameters from modeling the temperature dependent transients at an IR excitation frequency of 770 cm^{-1}. The lattice temperature (T_a) was varied in the model to reflect the indicated temperature of the cryostat, T_{max} is the maximum temperature the interaction volume reaches under the IR pulse with an energy of $E_m = 0.85 \pm 0.03$ mJ. Diff shows the increase in temperature from the ambient. F_{24} indicates the level to which the IR excitation causes an intra-excitonic population change, and shows no systematic change.

T_a (K)	T_{max}(K)	Diff (K)	F_{24} ($\pm$700) s^{-1}
11.0	14.2	3.2	16700
20.0	20.7	0.7	16600
32.0	32.2	0.2	16700

When fitting these transients the parameter F_{24} was allowed to vary, however, within its uncertainty it does not show any variation between the temperatures. This indicates that the interaction cross section did not change with temperature, rather the population available for interaction diminished as the temperature increased. The heating effect of the IR pulse also diminishes with increasing sample temperature due to the increasing heat capacity of the SrF_2 host lattice.

The behaviour seen here, both in modeling and the physical experiment is similar to the temperature dependent dynamic behaviour of the CaF_2:Yb^{2+} ITE, and given the similarity of the two systems the current observations are expected. It is worth noting that even though throughout the modeling the temperatures reached by the SrF_2 lattice were lower in comparison to CaF_2, because the SrF_2:Yb^{2+} ITE has a smaller energy gap between states 2 and 3, the ultimate behaviour was similar.

5.9.5 The dynamics of the 178 cm^{-1} sharp line

The model as outlined above was then applied to the sharp intra-exciton transition at 178 cm^{-1} yielding a good approximation to the measured enhancement. In this case the F_{24} parameter was inferred to be 12900 ± 600 s^{-1}, and E_m was found to be 0.4 mJ giving T_{max} = 12 K. However, as figure 5.21(a) shows, there is a long time offset that is not

well modeled with the above parameters. Unlike the dynamics modeled in the previous section, the slope of the long term transient does not cause it to converge to the pre - IR emission level in time indicating that it is not likely due to heating alone. Since an offset remains when heating is taken into account the possibility of liberated traps contributing to the emission must be considered at this excitation frequency.

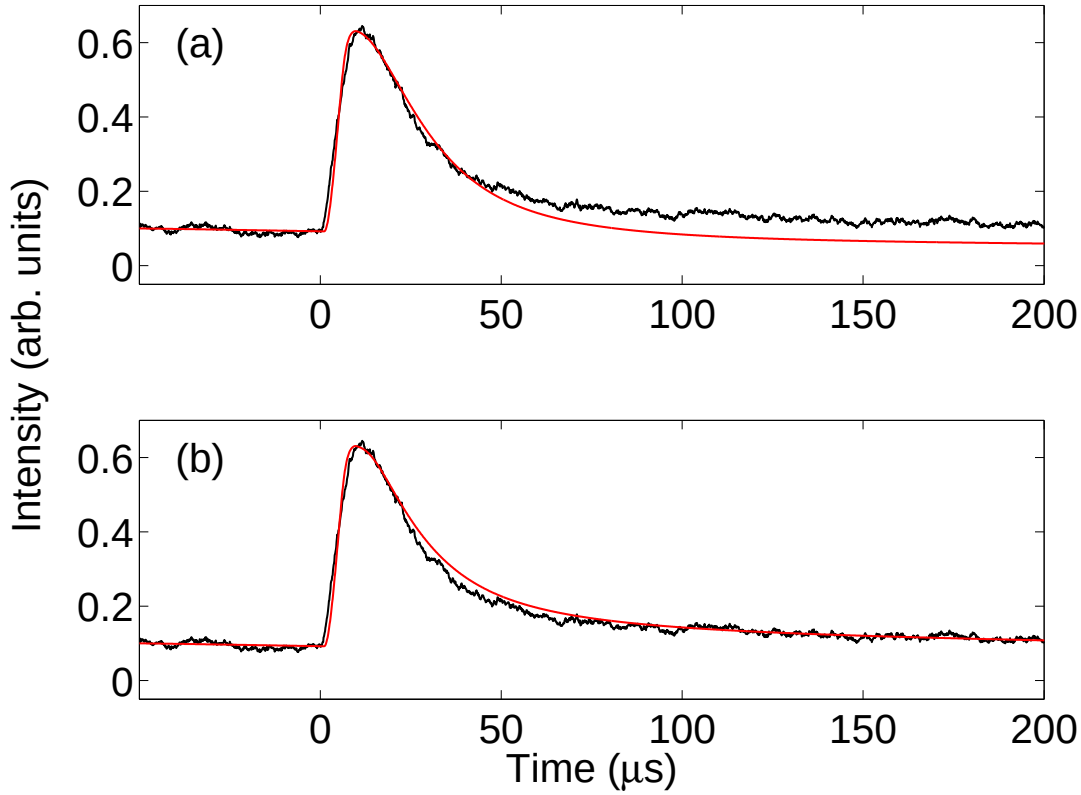

Figure 5.21 Modeling of the sharp peak at an IR excitation frequency of 178 cm^{-1} with $F_{24} = 12900 \pm 600$ and $E_m = 0.4$ mJ. It was found that an offset was present in the long time scale that is not accounted for via heating. (a) Shows the fitting achieved with heating alone and (b) shows the fitting achieved when in addition to the heating, liberated traps were allowed to populate state 2. Note that the enhancement itself is well matched in both cases, indicating that the direct transition and heating does account for the population that is placed in state 3. The sample temperature was 8 K.

The addition of an extra level to represent the conduction band via which electrons may populate the ITE states is necessary to enable the model to account for the liberated traps. It was assumed that there is an infinite reservoir of traps, such that no restriction is placed upon the number of liberated traps that can contribute to the ITE emission. A non–radiative free parameter W_{c2}, defined as a rate from the conduction band to the ITE state 2 was added to the model. The liberated traps are allowed to populate state 2 for the duration of the IR pulse.

Figure 5.21(b) shows the fit achieved by allowing IR liberated traps to populate state 2 at a rate of $W_{c2} = 100000$ s^{-1} from the onset of the IR pulse. The F_{24} and E_m values were unchanged between the two fits. The specific rate W_{c2} provides no real insight into the situation, it is simply set so that the appropriate number of oscillators are added to state 2 in the time available. With the liberated traps the population of state 2 is increased by 50% at the fitted rate. With this increase the offset present in the transient can be reproduced. The analysis carried out in section 5.6.1 showed that at an excitation of 550 cm^{-1} the IR pulse is able to liberate a sufficient number of traps such that the $4f^{14}$ ground state population is doubled. Given this, the fractional population increase required to account for the observed offset at an excitation of 178 cm^{-1} appears reasonable. To obtain a meaningful insight into the rates involved (and thus the relative interaction cross sections) in the trap liberation process a far more detailed experiment varying both the IR fluence and delay are required.

Since figure 5.7 shows that the liberation of traps does occur at higher excitation frequencies (and from the dynamic analysis it appears without contributing to the emission in a discernible manner), the configurational change in the ITE may be different under excitation at 178 cm^{-1} compared to the higher frequencies. This may lead to an appropriate overlap of ITE states with the conduction band allowing for the liberated electrons to recombine with the excited states of the ITE rather than decay to the ground state ($4f^{14}$) of the system (as in the higher frequency excitation, see figure 5.7).

Comparison of F_{24} for excitation at 178 cm^{-1} and 770 cm^{-1} shows that the transition moment is comparable in either case, and this is in good agreement with the calculated transition intensities from subsection 5.5.1.

5.10 The exciton spectrum

The time domain analysis provides a means to separate the pathways through which excited level (state 3) is populated and therefore we are able to infer the direct intra excitonic spectrum (i.e. without heating effects) by examination of the thermal contribution within the entire set of transients over the full excitation frequency range studied as shown in figure 5.22. By estimating the value of E_m at a given frequency with the employment of an IR absorption curve (as detailed in section 4.10.1) a heating spectrum can be estimated. The remainder from subtracting this from the measured IR excitation spectrum is likely the frequency dependent profile of the intra–excitonic transition(s).

In comparison to the as measured experimental spectrum the peak is now higher in energy, at around 785 cm^{-1}. While this peak has now narrowed considerably, it is still much wider than the two sharp lines. The width of this peak confirms that in this excitation range the IR pulse is primarily causing a rearrangement of the delocalized electron state. Both sharp peaks appear to be unaffected by heating retained their shape and position, indicating that these peaks *are* primarily due to intra-excitonic transitions.[6]

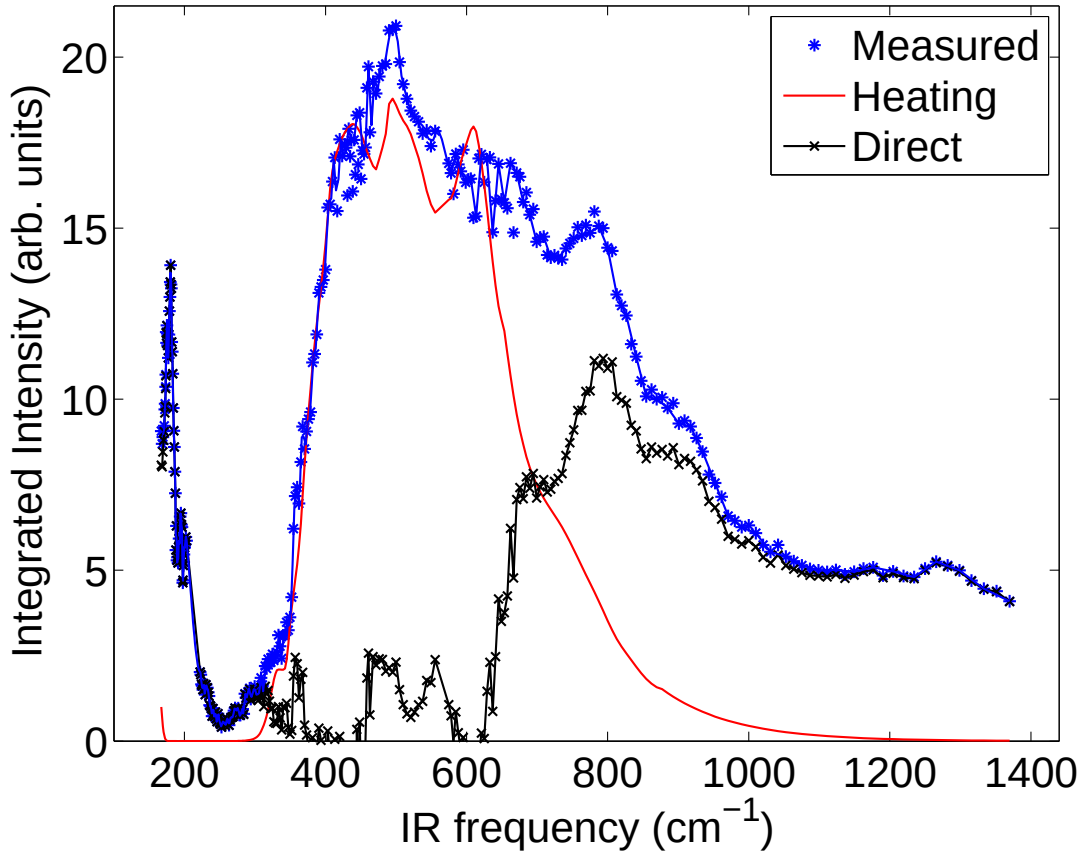

Figure 5.22 The IR excitation spectrum of SrF_2:Yb^{2+} with the calculated heating effects removed. Measured indicates the experimentally obtained spectrum. Heating effects are calculated using the absorption data adapted from Kaiser [70] and Denham [19]. The trace labeled "Direct" shows the calculated IR induced intra-excitonic transition spectrum, with the broad peak narrowing and blue shifting to 785 cm^{-1}. The sharp peaks retain their properties almost unaffected. The structure present between 300 to 600 cm^{-1} is likely due to the approximate nature of the heating curve.

The extracted direct absorption peak in SrF_2:Yb^{2+} is similar in position and width to that observed in CaF_2:Yb^{2+}, as shown in figure 4.24. However, it is difficult to make a precise

[6]Note that in the dynamic fitting of the 178 cm^{-1} sharp line a minor component due to heating was seen. The E_m used was computed using the heating spectrum, however this influence appears very small in the integrated spectrum to the point that it is not clearly visible.

comparison as the peak position in CaF_2:Yb^{2+} is not as well defined as in SrF_2:Yb^{2+}. It is clear that the observed comparative red shift in the broad peak in SrF_2:Yb^{2+} is primarily due to local heating. Given that the IR absorption peak is red shifted in SrF_2:Yb^{2+} in comparison to CaF_2:Yb^{2+} this is unsurprising.

As with CaF_2:Yb^{2+} the computed heating curve is heavily dependent upon data extracted from previous studies for IR absorption in SrF_2 (Kaiser [70] and Denham [19]) and thermal properties (Collocott [20], Harrington [21]) making the precise deconvolution of the heating influence from excitation spectra difficult. The fine structure present on the trace labeled 'Direct' in figure 5.22 between 300 to 600 cm^{-1} are likely artifacts of the deconvolution.

In a system where the dynamic shape of the transient does not provide an immediate indication of different population transfer mechanisms the ability to analyse the pathways through which its occurring and extract the true intra-excitonic excitation curve is valuable. Such an extraction is less vital in the case of CaF_2:Yb^{2+} in comparison, as the transient behaviour across the broad excitation band provides an indication of the ITE transitions.

5.11 Conclusion

Through the analysis of data obtained in two–colour experiments exploring the properties of ITEs in SrF_2:Yb^{2+} we have shown that it is possible to consistently extend the previously constructed physical models that describe both the spectral and temporal features observed. From this we have obtained physical parameters for the SrF_2:Yb^{2+} ITE that were previously not known.

The time integrated IR excitation spectrum revealed two sharp peaks at 178 and 1284 cm^{-1} that are due to changes within the $4f$ hole. The semi empirical model employed in the CaF_2:Yb^{2+} was extended to the current system by changing the B_4 and $G^3(fs)$ parameters to reflect the larger lattice size of SrF_2. The positions and the oscillator strengths for these transitions were well matched with $B_4 = 600$ cm^{-1} and $G^3(fs) = 7278$ cm^{-1}. The crystal field values for SrF_2 are well matched with previous studies. The exchange parameter being larger than in the CaF_2:Yb^{2+} case indicates that the electron spends less time around the next nearest neighbours in comparison.

Even though the dynamic behaviour of the emission showed significant deviation from

observations in CaF_2:Yb^{2+} the model developed previously was able to account for the transients seen in the SrF_2:Yb^{2+} ITE emission. Their behaviour was again heavily dependent upon the IR excitation frequency. The relatively fast decay rates of SrF_2:Yb^{2+} allowed for measurements of UV – IR delay dependence to be conducted, and these provided good evidence that liberated traps were unlikely to be contributing to the emission within the broad excitation peak. However, examining the dynamic behaviour over a time scale of 100 ms allowed for direct observations of UV driven trap population at a rate of approximately 3% per pulse. The IR pulse liberated these traps, causing them to populate the $4f^{14}$ ground states of the Yb^{2+} centres.

The transients were again found to consist of a mixture of direct transitions within the ITE and population transfer due to localized heating. Despite having a smaller emission enhancement at an IR excitation of 770 cm^{-1} the direct transition is stronger with $F_{24} =$ 16100 s^{-1} in comparison to 500 cm^{-1} excitation where $F_{24} = 12500$ s^{-1}. At 500 cm^{-1} excitation the main component of the enhancement was due to thermal population transfer through local heating. This showed that identification of the population transfer pathway was vital to ensure that the observed excitation peaks are correctly interpreted. The modeling was also able to account for the observed IR fluence dependent behaviour of the ITE emission transients. What initially appeared to be saturation of the direct transitions was shown to be due to local heating effects. It was found that maximum heating occurs at around 500 cm^{-1} and the local temperature can be as high as 10 K above the rest of the sample. The model was able to account for changing sample temperatures by simulating the transients obtained at sample temperatures of 11, 20 and 32.5 K.

Upon modeling the dynamic behaviour of the sharp excitation line at 178 cm^{-1} it was found that while direct transfer and local heating was able to account for the emission enhancement observed, an offset remained post enhancement, where its decay rate indicated that it was not due to local heating (as in the case of the offsets observed within the broad excitation band). This offset required the introduction of liberated traps into state 2, increasing its population by 50% to account for the observations. This ratio of population increase was reasonable given the IR pulse was directly observed to liberate populations of a similar order of magnitude in the 100 ms measurements.

Deconvolving the influence of the local heating on the IR excitation spectrum by identifying the excitation pathways through the constructed dynamic model the direct absorption intra–excitonic peak was estimated to be at 785 cm^{-1}. It was also shown to be much narrower than the time integrated excitation spectrum suggested. The calculation also

confirmed that the low frequency peak in the broad band of the IR excitation is due to local heating effects.

The IR excitation spectral models and the modeling of the dynamics were successfully employed in the case of SrF_2:Yb^{2+} showing that the current physical interpretation presented for the ITE behaviour is consistent across different systems.

Chapter 6

Two–colour excitation experiments on MgF_2:Yb^{2+}

In this chapter we present the specific details of the two–colour experiments performed on MgF_2:Yb^{2+}. Motivation for the study of MgF_2:Yb^{2+} and a brief description of the material is provided. The specific details of the emission observed in MgF_2:Yb^{2+} is introduced and the possibility of an ITE occurring in the system is discussed. The aspects of the experiments conducted that uniquely apply to MgF_2:Yb^{2+} are described. Detailed observations and descriptions of the data are then provided.

6.1 Motivation for the study

It is not clear whether, after $4f \rightarrow 5d$ excitation, Yb^{2+} doped MgF_2 exhibits emission from an ITE or if it is purely $4f^{13}5d^1 \rightarrow 4f^{14}$ emission. Dorenbos' analysis suggests that MgF_2:Yb^{2+} should display anomalous emission, with a smaller red shift than the clearly defined cases of CaF_2:Yb^{2+} and SrF_2:Yb^{2+}[11]. However work conducted by Lizzo et al. suggests that MgF_2:Yb^{2+} shows typical $5d \rightarrow 4f$ emission and does not present evidence of an ITE [95].

Using the experimental technique we have developed, which probes the ITEs directly, it may be possible to draw a conclusive picture in a case where there is ambiguity about their existence. Insight into the formation and behaviour of the ITEs may also be obtained from a situation where the ITE is barely forming. If emission from an ITE can be observed in MgF_2:Yb^{2+} this will allow for the extension of the previously detailed models as well as determination of a proportionality in the extent of the red shift in emission with the cation size in the host lattice. Since MgF_2 has a rutile lattice structure, and the Yb^{2+} experiences D_{2h} point symmetry [32] the discovery of ITE emission will also allow for the examination of symmetry dependent ITE behaviour. In the absence of an ITE it may be possible to use this experimental technique to directly probe the $5d$ structure of the

divalent ytterbium in MgF_2.[1]

6.2 The $4f \rightarrow 5d$ absorption of MgF_2:Yb^{2+}

The specific details pertaining to the $4f \rightarrow 5d$ transition of MgF_2:Yb^{2+} are found in the work conducted by Lizzo et al. [95]. MgF_2:Yb^{2+} displays absorption from 22900 to 43600 cm^{-1} with a number of distinct bands present within this range. At room temperature the largest excitation peak is seen at Lizzo's K band occurring at 39395 cm^{-1}. The G band at 29455 cm^{-1} also shows a prominent excitation peak. Lizzo assigns relative oscillator strengths of 0.006 and 0.002 to these bands respectively. At low temperature this behaviour is reversed, with the G band showing the greatest excitation peak while the K band decreases substantially in intensity. Of particular interest in the current case is the G band, as at low temperatures this resolves into various electronic and vibronic lines. Strong lines are observed at 30210, 30115, 29855 and 29455 cm^{-1}. In the current study the 29855 cm^{-1} (335 nm) line is excited by the OPA. Figure 6.1 shows the excitation and emission spectra obtained by Lizzo et al. including their assignments of bands.

Upon excitation into the $5d$ states emission is observed with a peak frequency of 21053 cm^{-1} originating from the lowest $5d$ level (labeled A). The emission spectrum observed with an excitation frequency of 29855 cm^{-1} shows a relatively small displacement from the zero phonon line with the emission peak red shifted by 1800 cm^{-1} (compare this with approximately 9700 cm^{-1} for CaF_2:Yb^{2+} and $>$ 13400 cm^{-1} for SrF_2:Yb^{2+}). ZPLs and discrete vibronic structure is observed in the emission, notably on the high energy shoulder of the emission spectrum. The quenching temperature for the emission is reported as 480 K and the intensity remains relatively stable from 4.2 K to room temperature. However, the emission spectrum undergoes significant broadening as the temperature increases.

The emission life time shows a rapid decline from 22 ms at 4.2 K to about 6 ms at 10 K, further reducing to about 2 ms at 120 K. Above 150 K it drops below 1 ms. This change is ascribed to thermal population of higher energy states with rapid emissive decay times. By fitting the temperature dependent lifetime Lizzo finds two emitting levels at frequencies of 6.2 and 343 cm^{-1} (labeled B and C) above the state A, with lifetimes of 2.3 ms and 13 μs respectively. The position of state C is different to that obtained by lifetime fits when considering an observed absorption at 494 cm^{-1} above state A. State B

[1] Assuming that the electronic levels have significantly different radiative lifetimes, work by Lizzo et al. suggests that they do.

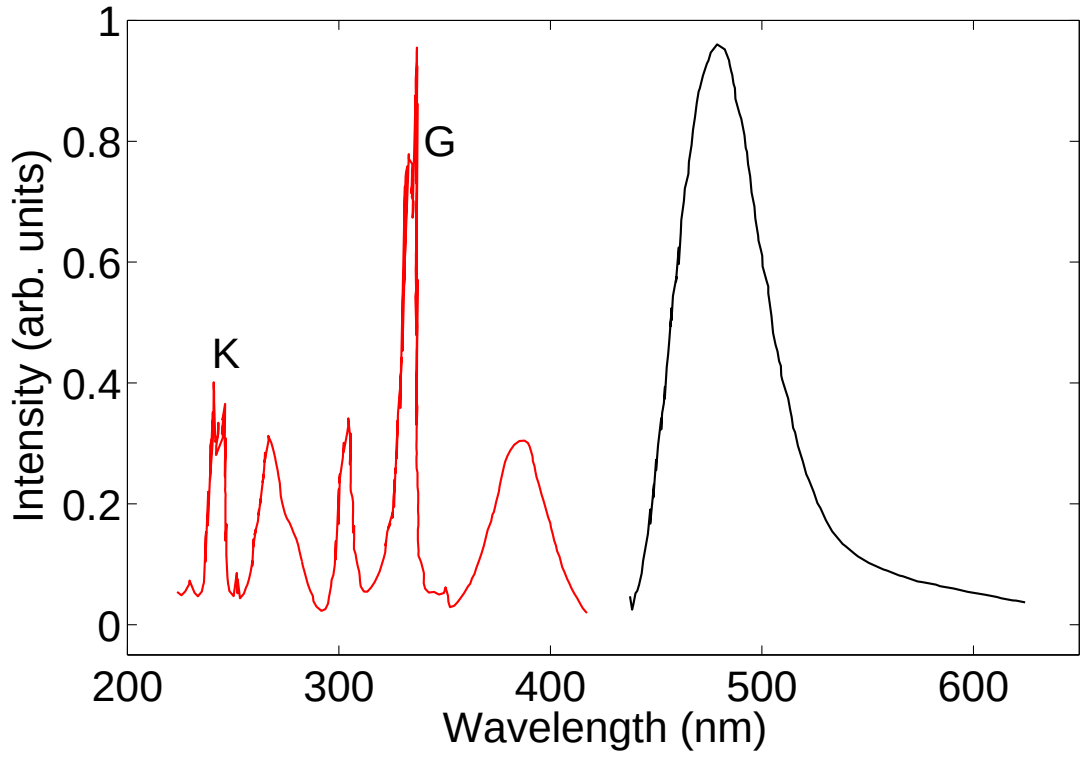

Figure 6.1 Excitation and emission spectra obtained by Lizzo et al. showing the K and G excitation bands and the broad emission observed at 4.2 K.

shows agreement with the observed spectral position.

Additionally Lizzo does not consider the possibility of multiple emitting sites within the observed emission spectrum, despite the considerably asymmetric shape of the curve even at 4.2 K. At room temperature this asymmetry is quite pronounced. It should be noted that while displaying an emission spectrum in wavelength units tends to skew its shape the presented spectra in Lizzo's study retains their asymmetry upon transformation to a frequency axis. Because vibronic bands are asymmetrical for small Huang-Rhys parameters (S), the observed asymmetry leads Lizzo to conclude that the emission is from $4f^{13}5d^1 \rightarrow 4f^{14}$.

6.3 Experimental details

A two–colour transient photoluminescence enhancement experiment (as detailed in section 3.2) was carried out on MgF_2:Yb^{2+} in order to directly determine the existence of an ITE within the system. Highly polished MgF_2:Yb^{2+} samples of 2.0 mm thickness doped with 0.6% molar mass of Yb^{2+} from the identical boule used by Lizzo et al. were employed

in this experiment. These were excited by UV radiation at 29855 cm^{-1} (335 nm) and variable frequencies of IR radiation. Both the beams were focused to a spot size of 100 μm giving a maximum fluence of 0.13 Jcm^{-2} for the UV pulse and between 5 to 11 Jcm^{-2} for the IR pulse.

6.4 Temperature dependent emission under UV excitation

For excitation with only the UV pulses, emission presented in figure 6.2 was observed. Spectrally, the emission at 10 K was in agreement with previous observations by Lizzo et al. [95]. At this temperature, within the time frame recorded, the emission did not show any discernible decay, however as the temperature was increased up to 180 K (figure 6.2 (d)) the decay rate showed a clear increase. With increasing temperature a rise began to build into the transients subsequent to illumination with the UV pulse and became prominent at 180 K. Additionally the emission spectrum broadened with the lower energy region increasing in intensity with temperature.

By time integrating the transients over $t = [10, 100]$ μs, an emission spectrum was constructed for each of the sample temperatures. Figure 6.3 shows the obtained temperature dependent emission spectra. The broadening of the line width is clearly evident here. With the exception of the 10 K emission spectrum, as the temperature increases the emission intensity also appears to increase. This behaviour is consistent with the general interpretation posed by Lizzo et al. with the faster higher states being thermally populated as the temperature rises.

The observed broadening is also expected from previous work which shows a much broader emission spectrum at room temperature in comparison to cryogenic temperatures. Lizzo et al. reports a broadening from approximately 2200 cm^{-1} at 4.2 K to 3800 cm^{-1} at 298 K.[2] From figure 6.3 it can be seen that the emission observed displays a linewidth of 2300 cm^{-1} at 10 K and approximately 3500 cm^{-1} at 180 K.

When fitting the observed spectra at a sample temperature of 10 K two Gaussians were required peaking at 20000 and 21300 cm^{-1} and with FWHM of 1600 and 1000 cm^{-1} respectively.[3] As the temperature increased the contribution from the lower frequency peak increased, leading to both the observed broadening and the increase in emission

[2]Note that these numbers are extracted from figure 2 in reference [95] and are therefore approximate.

[3]The observed shape did not match the typical Pekarian curve associated with low S vibronic broadening, thus a two Gaussian fit was employed.

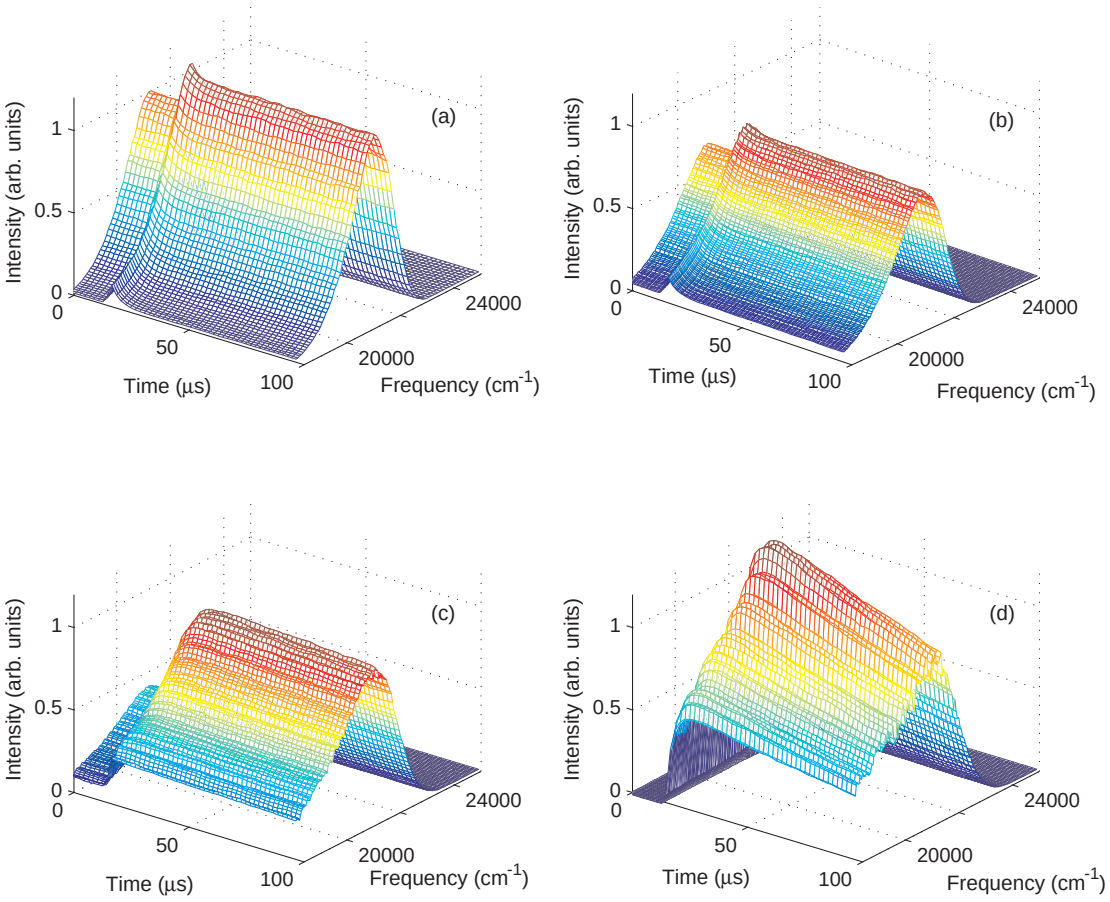

Figure 6.2 The temperature dependent behaviour of the MgF_2:Yb^{2+} emission under UV excitation at 29850 cm^{-1}. At a temperature of (a) 10 K, there is no obvious decay occurring over the time frame recorded. (b) Shows the recorded emission at 60 K, (c) at 120 K where the decay is becoming visible. At (d) 180 K the decay is clearly visible and the emission intensity has increased. Throughout the increase in temperature the emission spectrum broadens.

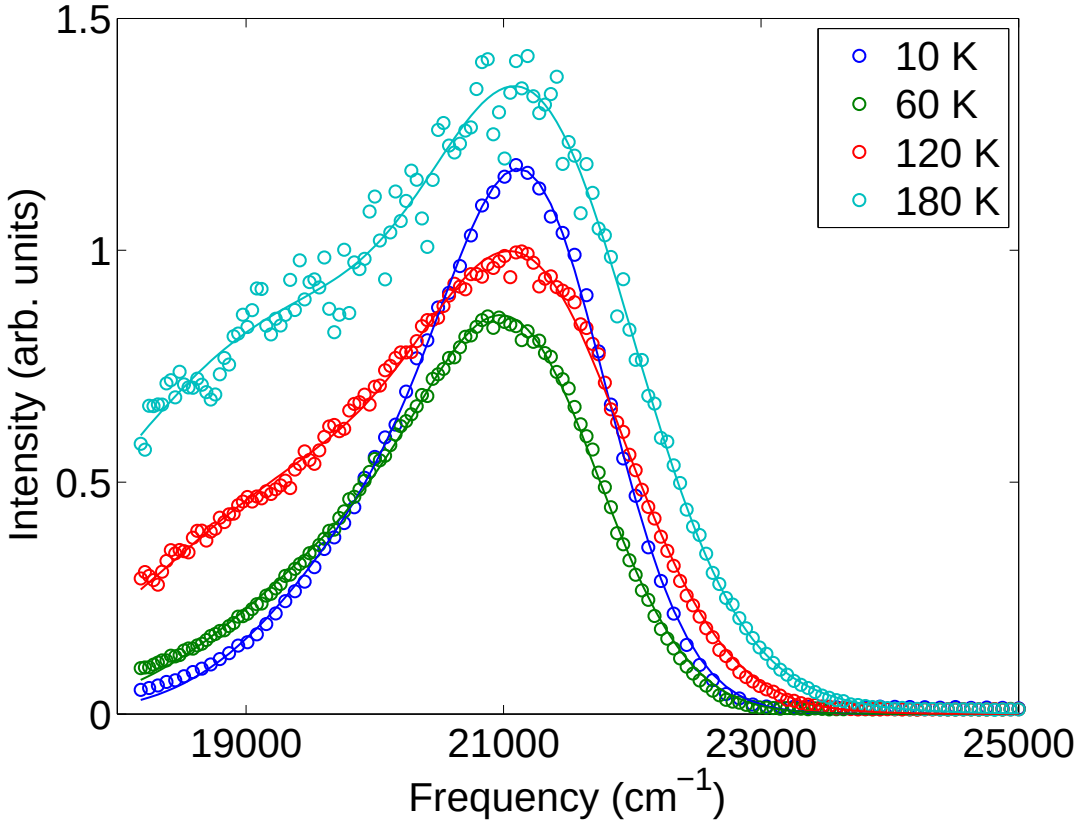

Figure 6.3 The time integrated temperature dependent emission spectra of the MgF_2:Yb^{2+} under UV excitation at 29850 cm^{-1} for temperatures ranging from 10 to 180 K. With increasing temperature the spectral lines broaden and the intensity also increases. The solid lines indicate the fitted curve employing two Gaussians.

intensity.

Figure 6.4 shows the manner in which the two individual Gaussians behave with increasing temperature. It is clear that the contribution from the lower frequency Gaussian increases as the temperature rises. This peak also appears to slightly red shift with increasing temperature, however, this behaviour is not conclusively discernible due to the broadening of the spectrum taking it beyond the scan range. While both peaks broaden with increasing temperature, the higher frequency peak remains stationary within the uncertainty of the peak position determination. The fitted parameters for each of the spectra are summarized in table 6.1.

From the relative scale factors of the two Gaussians, A_0 and A_1, it is clear that the low frequency peak grows at a greater rate in comparison to the high frequency peak. Its fractional contribution to the emission also increases at a greater rate due to its greater FWHM and greater temperature dependent broadening. It seems unlikely that the low

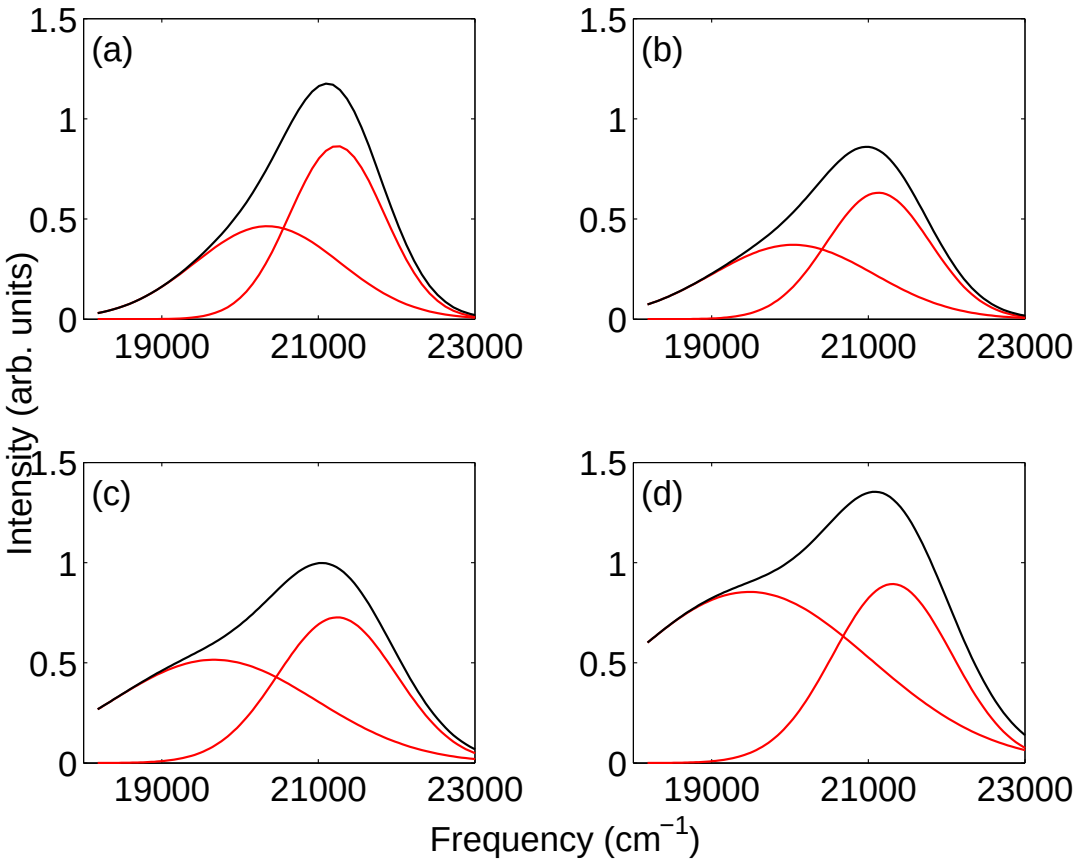

Figure 6.4 The fits to the time integrated temperature dependent emission spectra of the MgF_2:Yb^{2+} showing the behaviour of the individual Gaussians with temperature increase. The low frequency peak rapidly gets stronger as the temperature increases from (a) 10 K through (b) 60 K, (c) 120 K to (d) 180 K. Throughout the increase in temperature both the lines broaden.

Table 6.1 Summary of parameters for the fits achieved to the temperature dependent emission spectra shown in figure 6.3 with a two Gaussian model. A_i denotes the coefficient of each Gaussian, ω_i is the peak positions and FWHM is the Full Width at Half Maximum for each of the Gaussians. FWHM and ω_i are in units of cm^{-1}.

	High Frequency			**Low Frequency**		
T (K)	A_0 (a.u.)	ω_0	FWHM	A_1 (a.u.)	ω_1	FWHM
10	0.8 ± 0.1	21300 ± 100	1000 ± 80	0.5 ± 0.1	20300 ± 400	1600 ± 200
60	0.6	21200 ± 100	1100 ± 70	0.4	20000 ± 300	1700 ± 200
120	0.7	21200 ± 100	1260 ± 70	0.5	19700 ± 300	2200 ± 300
180	0.9	21300 ± 200	1300 ± 90	0.9	19500 ± 200	2600 ± 300

frequency peak is a $5d \rightarrow 4f$ emission, because it has a lower energy than the lowest known fd transition in MgF_2:Yb^{2+} [95]. Although the number of data points in the temperature dependence is sparse here, it appears that A_1 shows a large increase starting at 120 K (compared to the increase in A_0). This suggests that the source of the low frequency emission may have several levels that are thermally populated. Given that the low frequency peak is active at 10 K it is likely that this source is populated independently of the $5d$ states, at least at low temperature.

Lizzo et al. models the changing decay rates with a four level system that is assumed to be states within the $4f^{13}5d^1$ configuration. While this successfully accounts for the changing lifetimes, it appears that the possibility of two peaks existing within the main emission spectrum has been overlooked in their analysis. Additionally there is a discrepancy in their assignment of the fastest emitting level (with a time constant of 13 μs), where the excitation spectra places it 494 cm^{-1} above the lowest $5d$ state while the temperature dependent modeling places it at 343 cm^{-1}.

Excitonic emission is a possible candidate in explaining both the low frequency peak and the discrepancy in the fastest emitting level. Emission occurring out of both the $5d$ states and ITE states have been previously observed in BaF_2:Eu^{2+} [54, 96]. It is possible that MgF_2:Yb^{2+} exhibits similar behaviour, and the second fitted peak is originating from the ITE recombination with the $4f^{14}$ ground state. It is possible that the two fitted Gaussians represent $5d$ emission from Yb^{2+} centres at different symmetry sites. However, this is unlikely given that the rate at which the two spectral peaks change with temperature is drastically different.

In BaF_2:Eu^{2+} the ITE state is located below the $5d$ states [8, 96]. Given that the relative broadening of the low frequency peak is almost twice that of the high frequency peak, it is possible that the ZPL of the low frequency peak is located at a higher energy, but the emission has a large red shift, leading to the observed peak positions. The MgF_2:Yb^{2+} ITE ZPL is possibly located between 300 – 400 cm^{-1} above the $5d$ state's ZPLs (from Lizzo's dynamic model).It has already been established that ITEs exhibit such configurational changes causing red shifted behaviour, as previously addressed [9, 11, 12, 42, 96]. Such an interpretation is also supported by the analysis carried out by Dorenbos [11], which places the MgF_2:Yb^{2+} emission characteristics within the realms of the anomalous emission associated with ITE behaviour.

Although the ITE (if it exists as described above) would have to be independently populated at low temperature it may also gain population from the $5d$ states at high temper-

ature, which consistently explains the observed temperature dependent change in A_1 as well as the increased emission in the overall peak. Notice that the high frequency peak does not show a positional shift with temperature. If the increasing emission is a result of a higher $5d$ state being populated a shift in the peak position would be expected. Despite these factors, in order to establish whether an ITE exists within the MgF_2:Yb^{2+} system with certainty more experimental evidence is required.

6.5 Photoluminescence enhancement

In contrast to CaF_2:Yb^{2+} and SrF_2:Yb^{2+}, excitation with a time delayed IR pulse caused a small increase in emission which vanished at a temperature of 20 K. Figure 6.5 (a) shows the response of the system when the sample is illuminated with a UV pulse at $t = 0$ μs and the IR pulse, at a frequency of 1000 cm^{-1}, incident upon the sample at $t = 50$ μs. The emission spectra before and after the IR pulse are shown in figure 6.5 (b) and a small increase in the peak intensity is observed. The peak position and line width of the emission band remains unchanged after IR excitation. The parameters for the fitted double Gaussian curves are identical to those in the 10 K UV only excitation case apart from A_0 and A_1. A_0 showed an increase of 6% while A_1 showed an increase of 3%.

The spectral behaviour indicates that after illumination with the IR pulse the emission is originating from the same state as before the IR, but that the contribution from the $5d$ state has increased relatively. Examination of the the decay rates of the emission before and after IR, as shown in figure 6.6 (a) and (b), reinforces this interpretation. The decay rates appear to change slightly post–IR (150 ± 8 s^{-1}) in comparison to the pre–IR rate (140 ± 10 s^{-1}). The post–IR rate shows a 7% increase, which is very similar to the overall emission increase from the $5d$ state. However, given the uncertainties of the two values it is difficult to be certain about the increase.

6.6 UV – IR delay measurements

Varying the delay between the UV and IR pulses causes no change in the enhancement intensity. Figure 6.7 shows the magnitude of the enhancement for delays of 40, 300 and 600 μs with the inset showing the integrated enhancement value. It appears that the enhancement behaves almost identically at each of the delays. Although at a delay of 600

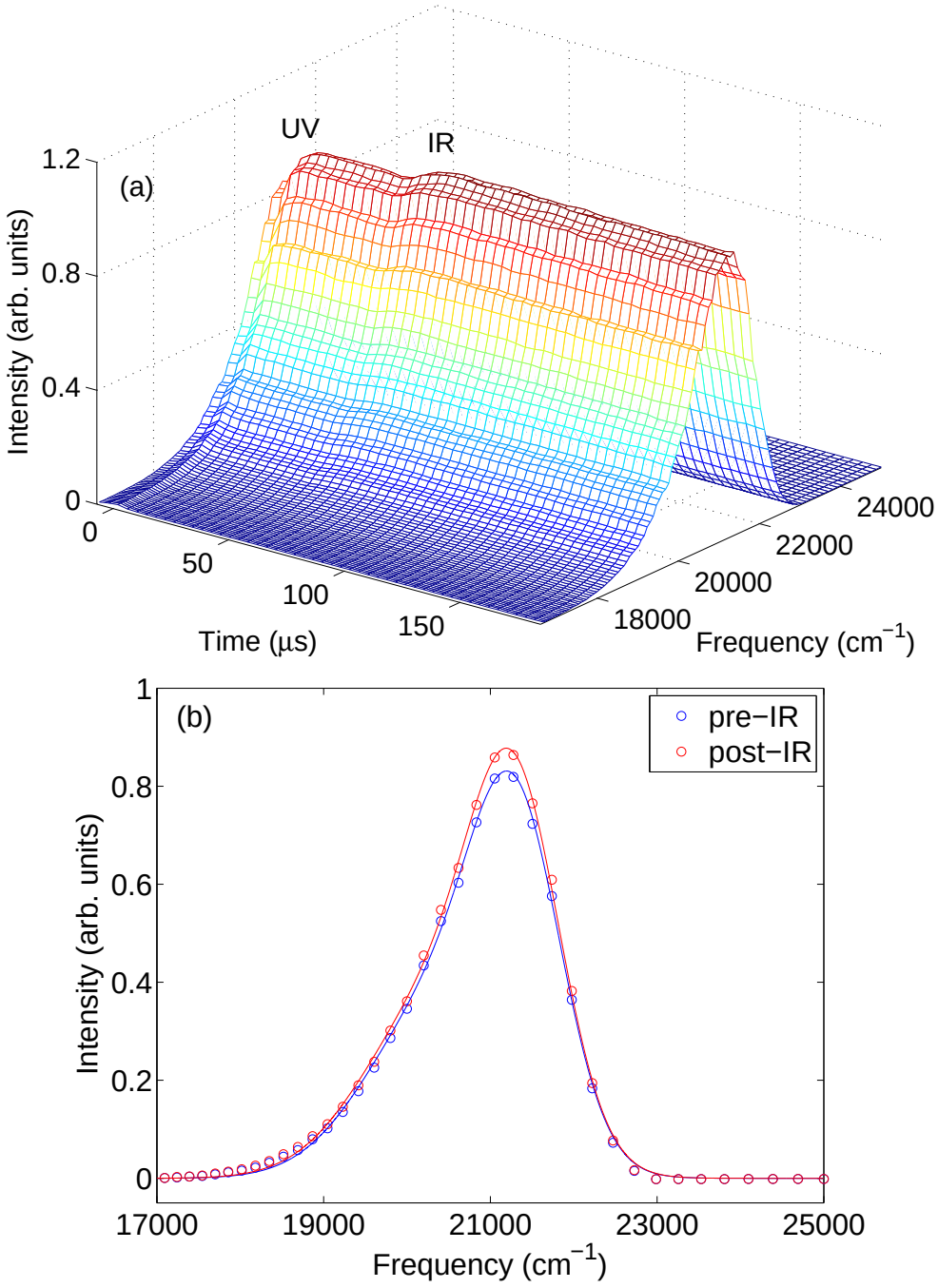

Figure 6.5 MgF_2:Yb^{2+} emission spectrum obtained at a sample temperature of 10 K with IR excitation at 1000 cm^{-1} (a) showing a small enhancement caused by the IR pulse illuminating the sample at $t = 50$ μs. (b) Emission spectra obtained just prior to (blue circles) and immediately after (red circles) IR excitation showing no change in linewidth or peak position. The fitted two Gaussian curves are indicated by the solid lines.

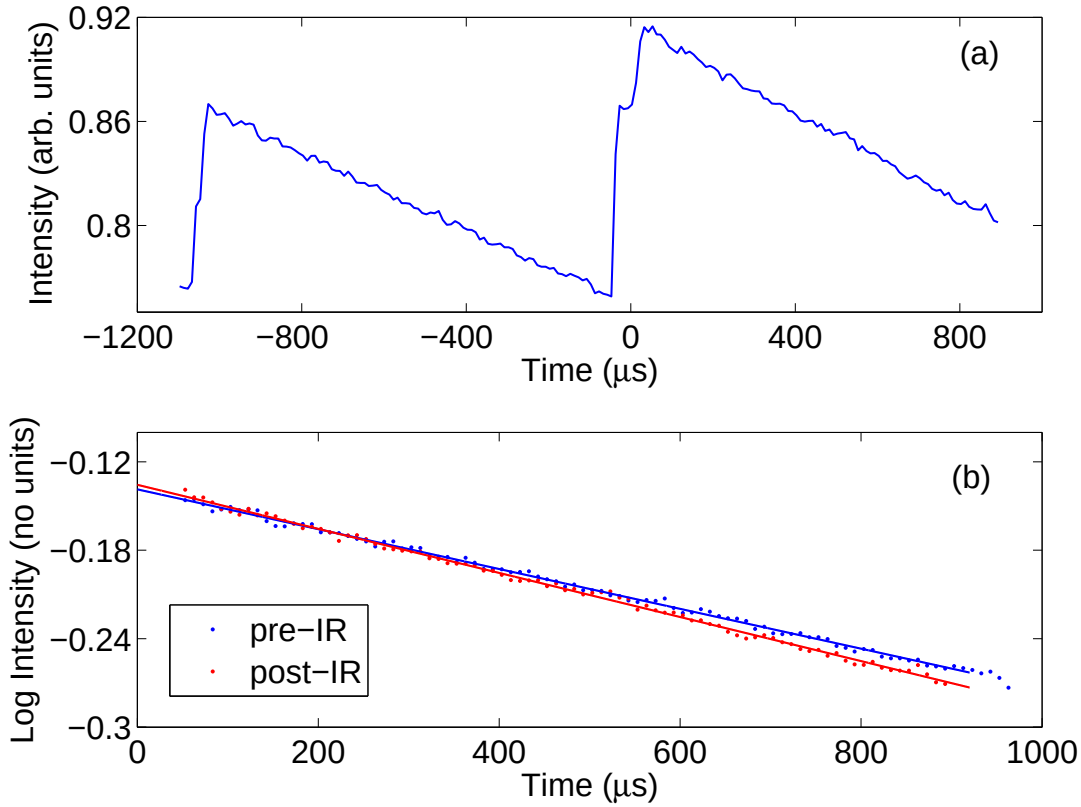

Figure 6.6 (a) Shows the transients over 2 ms at 10 K with two UV pulses occurring at $t = -1060, -60$ μs and the IR pulse at $t = 0$ μs. The decay rate of the transient section without the IR pulse ($t = [-1060, -60]$) appears similar to that of the section with the IR ($t = [0, 860]$). (b) Shows the fitted pre and post IR decay rates.

μs the enhancement may have diminished somewhat. The integrated enhancement (time integrated over $t = [0, 100]$) suggests that there is no difference in total enhancement with delay. However, one should keep in mind that the pre–IR emission decreases by about 7% 600μs after UV illumination (see figure 6.6 (a)) and with the noise level seen in figure 6.7, such a decrease may not be discernable. Note that in figure 6.7 the emission intensity just prior to the IR pulse has been zeroed to ensure that a comparison can be made of the enhancement magnitude. No other normalization has been applied to the transients.

6.7 IR excitation spectrum of MgF_2:Yb^{2+}

As in the CaF_2:Yb^{2+} and SrF_2:Yb^{2+} cases the IR excitation frequency was scanned and a time integrated excitation spectrum was obtained. Figure 6.8 shows that the spectrum is essentially flat between 500 and 1100 cm^{-1} whilst the drop in signal at higher frequencies matches very well the FEL power (shown by the red trace in figure 6.8), which reduces

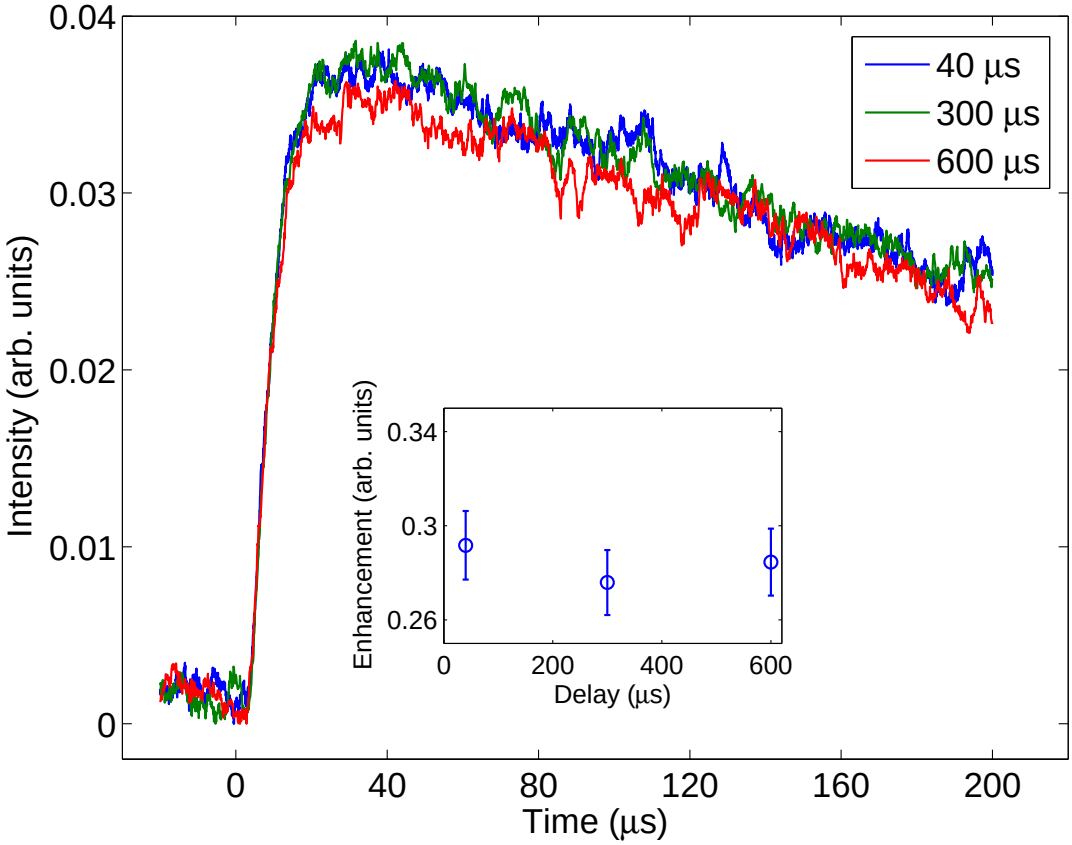

Figure 6.7 Transients recorded at UV – IR delays of 40, 300 and 600 μs at a sample temperature of 10 K, showing similar behaviour independent of delay. The inset shows the integrated enhancement intensity with respect to delay, indicating that they are equal within their uncertainties. The emission intensity just prior to the IR pulse has been zeroed such that the enhancement can be directly compared.

at higher frequencies for the FEL settings used in this experiment.

Examining the post–IR decay rate across the flat region of the excitation spectrum, as illustrated in figure 6.9, shows that the decay rate may be decreasing as the frequency decreases, although the trend is not clear. The decay rates show a variability of approximately 9% between the slowest and fastest rates, however the fits achieved at each frequency point had uncertainties between 5 – 10 %. Given this the variance observed in the decay rates is not significant. This implies that throughout the excitation spectrum the emitting states are identical to those active prior to the incidence of the IR pulse. This fits in with the interpretation that the observed enhancement is due to the liberation of traps much shallower than 400 cm^{-1} increasing the populations of the emitting states.

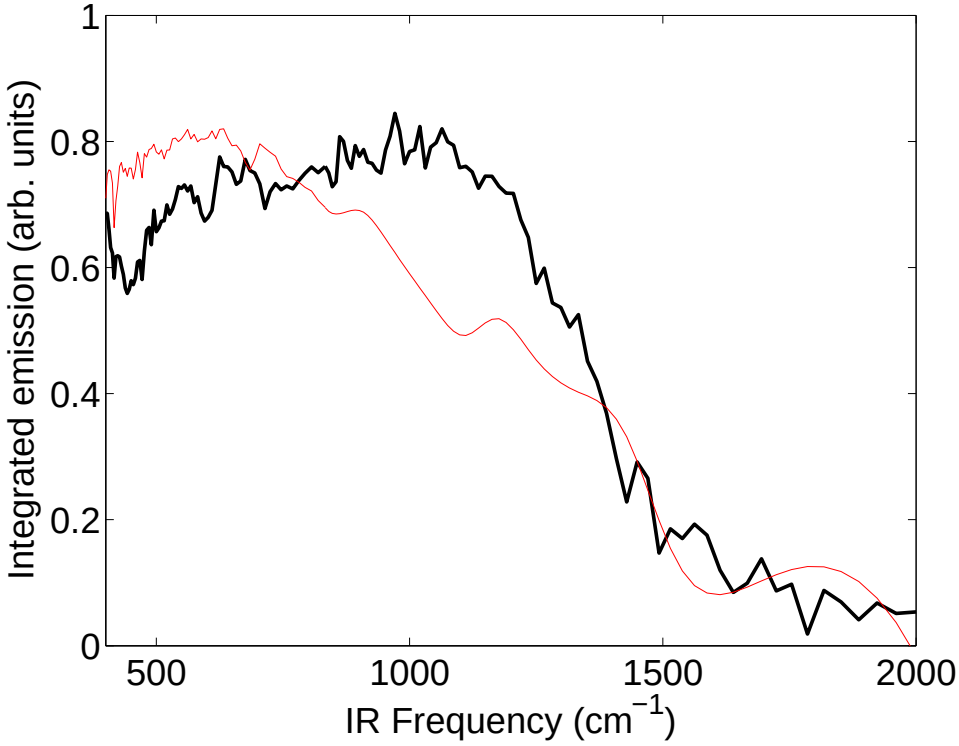

Figure 6.8 Time integrated IR excitation spectrum of MgF_2:Yb^{2+} at 10 K with emission monitored on all frequencies. The response appears to follow the FEL fluence (red curve), measured just prior to the sample.

6.8 UV and IR fluence dependent behaviour of the enhancement

The enhancement intensity showed a linear relationship with variations in UV fluence, up to a measured maximum of 0.13 Jcm^{-2}. The IR fluence was held constant at 11 Jcm^{-2}. The behaviour of the transients can be seen in figure 6.10 (a) and the trend observed in enhancement intensity is shown in figure 6.10 (b).

With the UV excitation fluence at its maximum (0.13 Jcm^{-2}), the IR fluence dependent behaviour was examined and the observed transients are presented in figure 6.11 (a), and the emission intensity as a function of IR fluence is shown in figure 6.11 (b). The transients show that the enhancement increases with increasing IR fluence and a rise time builds in as the fluence increases. At low powers the rise time is simply due to the width of the macro-pulse of FELIX, and is an instrument limited 6 μs. However at the highest IR fluence the observed rise time is about 21 μs.

Figure 6.11 (b) shows the clear onset of saturation as the dependence of the enhancement intensity upon fluence is sublinear. The trend line is fitted to an exponentially saturating

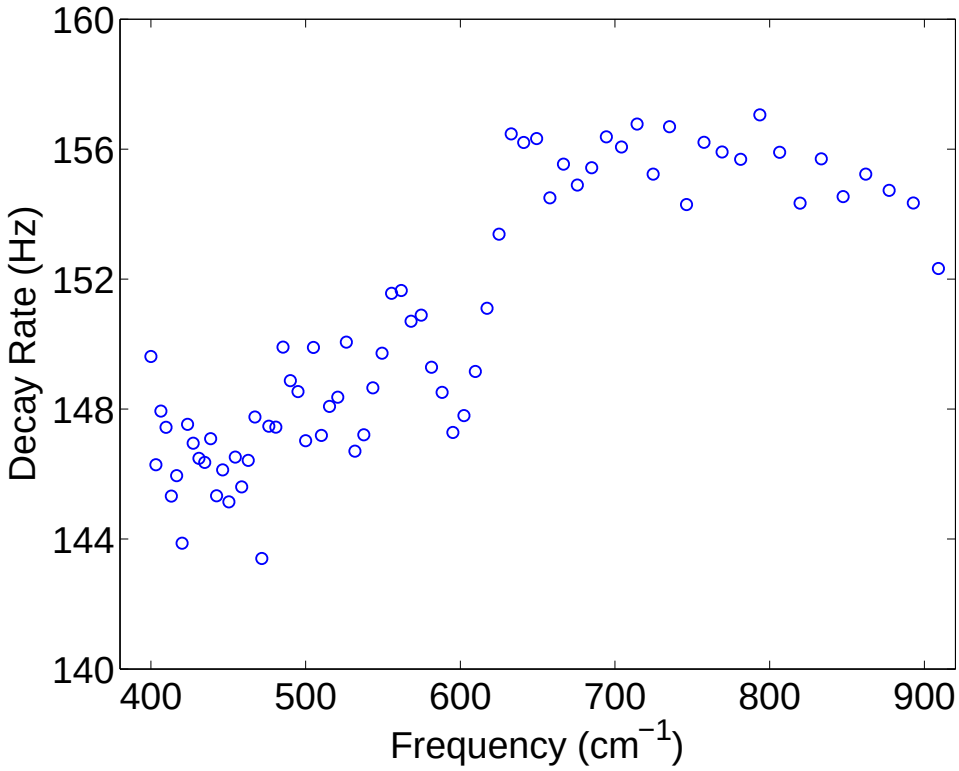

Figure 6.9 Emission decay rates over flat region of IR excitation spectrum from figure 6.8. The rates are estimated by fitting a single exponential decay to the transient just after the termination of the IR pulse.

process described by,

$$I = I_0(1 - \exp(-bF)) \tag{6.1}$$

where I_0 is enhancement caused by the liberation of all available traps, b is a scalar factor computing the influence of a given number of IR photons upon the liberation process and F is IR fluence. For the trend line fitted $I_0 = 0.05 \pm 0.01$ (arb. units) and $b = 0.19 \pm 0.1$.

6.9 Possible explanations for the IR induced photoluminescence enhancement

The observed behaviour of the enhancement may be caused by the liberation of shallow electron traps by the IR pulse or the IR may induce local heating populating the faster emitting state B, located 6 cm^{-1} above the lowest $5d$ state. The case for each of these interpretations is presented.

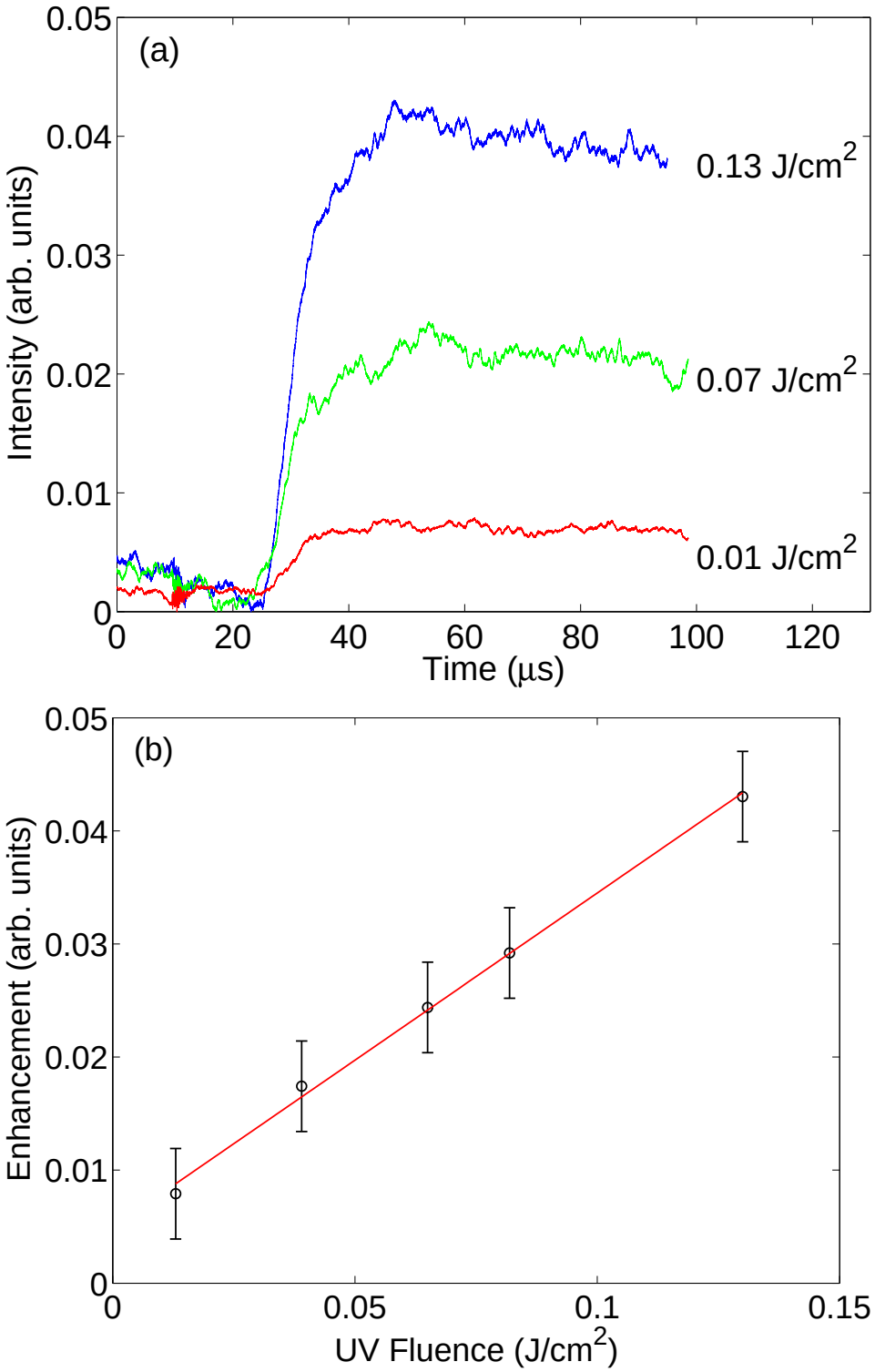

Figure 6.10 UV fluence dependent emission enhancement of the MgF_2:Yb^{2+} under UV excitation at 29850 cm^{-1} at a temperature of 10 K. (a) Shows the transients for three selected fluence values. (b) Shows the observed trend of the enhancement intensity as a function of UV fluence, with a linear fit (red line). The transients were zeroed just prior to the IR at an excitation frequency of 1000 cm^{-1}.

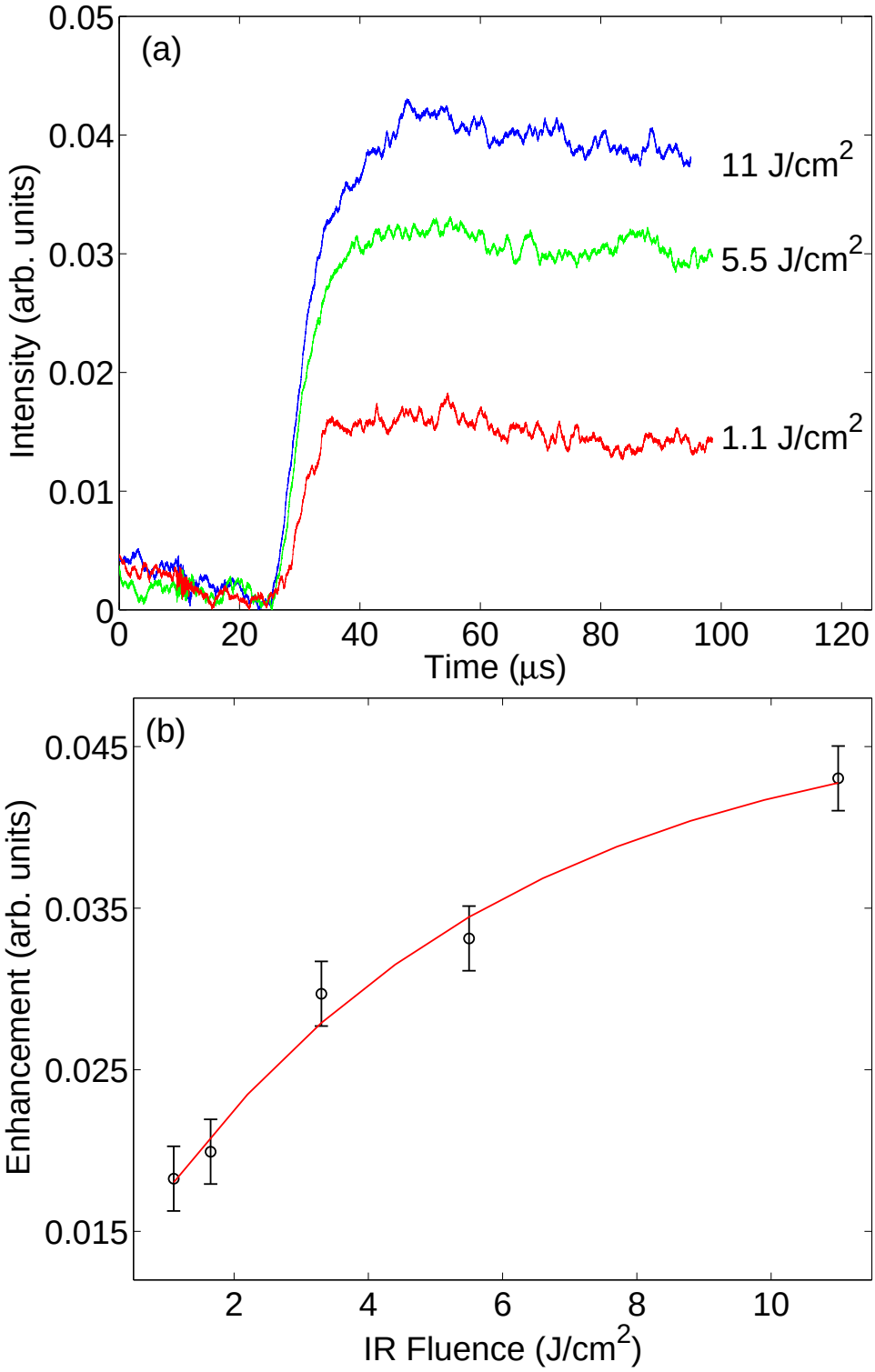

Figure 6.11 IR fluence dependent emission enhancement of the MgF_2:Yb^{2+} under excitation at 1000 cm^{-1} at a temperature of 10 K. (a) Shows the transients for three selected fluence values. (b) Shows the observed trend of the enhancement intensity as a function of UV fluence, with an exponentially saturating fit (red line). The transients were zeroed just prior to the IR pulse.

6.9.1 Liberation of shallow traps by the IR pulse.

The slight increase in emission intensity with no associated change in the emission spectrum and the decay rates indicate that additional oscillators are populating the already emitting state(s). Such behaviour is explained by the IR pulse liberating trapped electrons which are populating the $4f^{13}5d^1$ configuration of the Yb^{2+}, leading to the observed emission properties. The trap states are likely being populated by the application of the UV pulse through photoionization into the conduction band. The production of traps in MgF_2:Yb^{2+} using high-energy ionizing radiation or UV excitation has been previously studied [97–99]. Many of these traps have excited states lying just below the conduction band. For example, the F center first excited state is 565 cm^{-1} below the conduction band [98] and is an efficient intrinsic electron trap.

The behaviour of the excitation spectrum suggests that the traps being liberated do not have depths within the scan region, and the observed response is of the tail resultant from traps occurring at frequencies shallower than 400 cm^{-1}. These can be described with a Coloumb trap model detailed by equation 4.5 for a shallow depth. Additionally the low temperature at which the traps vanish indicates that they are extremely shallow, and a potential barrier of 15 cm^{-1} employed in a Arrhenius activation model causes about 40% of the traps to liberate at 20 K. This value is likely an underestimate of the true trap depth, since previous studies have shown that thermoluminescence is achievable from deeper traps than a simple Arrhenius type consideration would allow [100, 101].

The observed trend of the enhancement with UV fluence shown in figure 6.10 indicates that up to the measured fluence, the UV pulses are not photoionizing enough electrons to saturate the empty traps available to receive these. Saturation identified with an increasing IR fluence, as shown in figure 6.11 is likely caused by the increasing IR depleting the available shallow traps that were induced by the UV pulse. The increasing rise time is likely associated with electrons occupying high–mobility states within the conduction band and reflects the lifetime of the free carrier.

6.9.2 IR induced local heating

While trap liberation is able to explain some of the observations it cannot account for the difference in emission decay rate before and after illumination by the IR pulse. From Lizzo's analysis of the temperature dependent decay lifetimes an increase in the sample temperature from 8 to 9 K leads to a change in lifetime from 7.1 to 6.6 ms, (decay rate

from 140 to 151 s^{-1}). [95] Such an increase is consistent with the change in decay rate observed in figure 6.6. Subsequent to IR illumination the decay rate increases 7% and the emission out of the high frequency peak increases by 6%, which is consistent with a local temperature rise of 1 K. Because the faster emitting B level is located only 6 cm^{-1} above the lowest $5d$ state populating this level would not cause a spectral peak shift observable in the emission spectra obtained in this study.

While the onset of IR absorption in MgF_2 occurs at 1200 cm^{-1} [36], even at 800 cm^{-1} it transmits at about 82% [37]. Thus it is likely that only a small amount of energy is deposited at 1000 cm^{-1} (where the pre/post–IR decay rates are compared). The heat capacity of MgF_2 is appreciably lower than that of CaF_2:Yb^{2+} [102] at low temperatures, thus a temperature rise on the order of 1 K is quite possible. However, given the small heat capacity and the phonon density of states in MgF_2 [103] the flat response of the IR excitation spectrum (figure 6.8) and the slightly decreasing decay rate for an IR frequency range from 900 to 400 cm^{-1} (figure 6.9) is not consistent with heating.

It is likely that both trap liberation and minor local heating occurs under IR excitation, however, with the noise level of the current data it is not possible to conclusively deconvolve the two phenomena.

6.10 Conclusion

Through the analysis of temperature dependent emission spectra obtained with UV excitation we have identified the possibility of an ITE existing within the MgF_2:Yb^{2+} system. With the data obtained via a two–colour experiment we have identified the existence of shallow traps that are populated by the UV and liberated upon IR illumination of the sample.

We have obtained emission spectra that is in agreement with previous measurements conducted by Lizzo et al. [95]. However its analysis has shown that two Gaussians are required to fit the lineshape observed with peaks occurring at 20300 and 21300 cm^{-1} at 10 K. As the sample temperature increases the low frequency line grew in intensity at a much faster rate when compared to the higher frequency line, and both lines broadened. We interpreted the low frequency line as a possible candidate for ITE emission, showing the typical red shift associated with such behaviour. This implied that MgF_2:Yb^{2+}, like BaF_2:Eu^{2+}, may exhibit both $5d$ and ITE emission, with the ITE states occurring slightly above Lizzo's A band. This interpretation may also explain the discrepancy between the

energy levels determined through lifetime modeling and spectral observation in Lizzo's analysis.

In the two–colour experiment the IR pulses were found to cause a small enhancement to the emission intensity. However, the IR did not cause any changes to the emission spectrum and only a slight change in the lifetime of the emission decay. The IR excitation spectrum was found to follow the IR fluence down to a frequency of 400 cm^{-1}. The excitation spectrum coupled with little change in the emission post–IR illumination indicated that the IR was likely liberating traps populated by the UV photoionizing a proportion of the Yb^{2+} centres. The enhancement was found to vanish at a sample temperature of 20 K, indicating that the traps were shallow, confirming that the traps were shallower than this. The enhancement intensity was seen to have a linear relationship with UV fluence, indicating that up to a fluence of 0.13 Jcm^{-2} the number of trap states were not being completely filled via photoionization by the UV. In contrast the enhancement intensity showed the onset of saturation with IR fluence, indicating that the IR was likely depleting all filled trap states.

The small change in decay lifetime is likely due to a small amount of local heating via the absorption of the IR radiation by the MgF_2 lattice. However, heating alone cannot account for the IR excitation spectrum observed. It is likely both mechanisms are driving the observed behaviour, but with the available data it was not possible to deconvolve the two influences.

It was not possible to positively identify any energy level structure with the IR excitation. However, given the energy gap inferred by Lizzo, it is possible that extending the IR below 350 cm^{-1} may find a resonant transition to the possible ITE states.

Chapter 7

Conclusion and possible further experiments

We have employed a novel two–colour photoluminescence enhancement technique to directly probe the energy level structure and dynamic behaviour of ITEs present within CaF_2:Yb^{2+} and SrF_2:Yb^{2+}. Additionally MgF_2:Yb^{2+} has also been examined in order ascertain whether ITE emission is observable from that system.

We successfully accessed electronic states within the ITE and probed them directly with the use of tunable IR excitation subsequent to setting up an excited population of ITEs with UV radiation. We were able to identify sharp transitions within the ITE that would have remained hidden due to the broad featureless emission typically observed from ITEs.

Using a time integrated IR excitation spectrum two sharp peaks were identified at 249 and 1145 cm^{-1} in CaF_2:Yb^{2+} inferred to be due to changes occurring on the $4f$ hole. Based on a semi-empirical crystal field Hamiltonian, coupling the $4f$ hole to an s like delocalized state, the positions and the oscillator strengths for these transitions were well matched. The exchange parameter was found to be $G^3(fs) = 5900$ cm^{-1}. This model was then successfully extended to account for sharp lines observed in the IR excitation spectrum for the SrF_2:Yb^{2+} ITE at 178 and 1284 cm^{-1}. The crystal field parameter B^4 was changed from 800 to 600 cm^{-1} to account for the change in lattice size. The positions and oscillator strengths were well matched for a $G^3(fs) = 7278$ cm^{-1}, the larger exchange parameter indicating that the ITE electron is less delocalized in comparison with the CaF_2:Yb^{2+} case. Broad bands were also observed within the excitation spectra in both cases.

Studying the dynamic behaviour of the CaF_2:Yb^{2+} ITE we found that IR induced intra-excitonic transitions and local heating were the major drivers of population transfer between the two emitting states. A model that took these aspects into account was developed, and was able to account for a variety of observed transients from IR excitation frequency and fluence dependence to sample temperature variations consistently. The

modeling indicated that the broad feature observed in the IR excitation spectrum was due to the two mechanisms dominating at different frequencies. Based on the computed heating spectrum we deconvolved the two effects and estimate that the intra–excitonic absorption lies between 740 – 820 cm^{-1}. The lower frequency 'peak' in the broad feature was found to be caused by local heating, with the maximum occurring at around 600 to 630 cm^{-1}.

The dynamic model was extended to SrF_2:Yb^{2+} with the modification of the heat capacity and thermal conductivity values to account for the differences between the two lattices. In addition to the search space modeled for the CaF_2:Yb^{2+} case, the model was able to account for UV – IR delay dependent behaviour that was observable in the SrF_2:Yb^{2+} ITE system due its faster decay rates. By accounting for the IR induced local heating the intra–excitonic absorption peak of the broadband was found to be at around 785 cm^{-1}.

By extracting the population transfer pathways from the model we show that the intensity of integrated spectra can be misleading if the dynamic behaviour is not well understood or observed. Particularly when dealing with energy levels that are very close together (as the ITE emitting states are) dynamic behaviour of the transitions should be examined where possible. With these considerations we have identified a higher ITE state, occurring between 740 – 820 cm^{-1} in CaF_2:Yb^{2+} and at around 785 cm^{-1} in SrF_2:Yb^{2+}.

In both the cases the modeling showed that the observed IR fluence dependent saturation was due to heating effects. A consistency check of the model was carried out by simulating the transients obtained at sample temperatures of 10, 30 and 50 K for the CaF_2:Yb^{2+} case and 11, 20 and 32.5 K for the SrF_2:Yb^{2+} case. These also confirmed that the non–radiative rate from the higher emitting ITE state to the lowest one is independent of sample temperature.

Examination of the SrF_2:Yb^{2+} dynamic behaviour over a time scale of 100 ms allowed for direct observations of UV driven trap population at a rate of approximately 3% per pulse. The IR pulse liberated these traps, causing them to populate the $4f^{14}$ ground states of the Yb^{2+} centres and these did not appear to contribute to the IR induced emission enhancement.

In CaF_2:Yb^{2+} the spectral behaviour of its emission has shown that the two emitting states are configurationally different. Its ground state recombines with the Yb^{3+} centre with a bond length change of ΔR of -0.169 ± 0.002 Å. Its first excited state recombines with a ΔR of -0.15 ± 0.01 Å, indicating that the bond length of the excited state is longer than

the ITE ground state (and closer to the $4f^{14}$ bond length). Such large configurational changes are the cause of the broad featureless emission observed from this (and other rare–earth ITE) system(s).

This consistency across the two systems and across a large search space shows that the physical interpretations presented for the ITE behaviour is likely valid.

In MgF_2:Yb^{2+} the two–colour experiment was less successful, failing to locate conclusive ITE emission. It was also not able to probe the $5d$ energy structure, however, the IR excitation frequency range available at the time was not particularly suitable for this purpose. However, enhancement that vanished at a sample temperature of 20 K was observed. This enhancement was seen to have identical spectral to the pre–IR emission, and it was concluded that the IR was liberating shallow traps populated by the UV excitation. Additionally the post–IR emission decay rate increased from 140 to 150 Hz, indicating that minute local heating was also occurring.

More interestingly, analysis of the temperature dependent emission spectra showed that two Gaussians are required to fit the observations with peaks at 20300 and 21300 cm^{-1} (at 10 K). As the sample temperature increased the low frequency line grew in intensity at a much faster rate when compared to the higher frequency line, and both lines broadened. We propose that the low frequency line is a possible candidate for ITE emission. This interpretation may also explain the discrepancy between the energy levels determined through lifetime modeling and spectral observation in Lizzos analysis.

7.1 Possible further experiments

The obvious candidate for further experimentation is MgF_2:Yb^{2+}, in order to establish whether the proposed ITE emission is observable. Given that Lizzo finds a higher emitting state occurring at 343 cm^{-1} (using temperature dependent lifetime modeling) the natural course of action appears to be to extend the IR excitation scans to cross this region. Additionally it may be possible to conduct excitation experiments where the observed ZPLs (by Lizzo) are directly excited. This may be able to resolve the two emission peaks observed in our study. Particularly if the lower frequency emission diminishes significantly (or vanishes) it would conclusively show that its origin is not from the $5d$ levels of the Yb^{2+}.

As for the two–colour photoluminescence enhancement experiments, monitoring of the IR

fluence pre and post sample should be added. This will allow for a direct measurement of the IR absorption spectrum while at the same time conducting excitation scans. This may help locate transitions that do not interact with an emitting level within the system. Additionally absorption information can be used to directly compute possible heating effects (rather than relying on nominal absorption spectra of sometimes non comparable samples).

This study has demonstrated that the experiment is able to induce emission from states that do not show any emission under normal circumstances (for example at low temperatures the excited state of the ITEs in both CaF_2:Yb^{2+} and SrF_2:Yb^{2+} are empty, and therefore do not emit). This experiment should be extended to probe the structure and dynamics of $5d$ levels of lanthanide doped materials. Materials where the observed emission is only from spin forbidden states are prime candidates for this technique, especially because of the vast difference in radiative lifetimes expected between spin forbidden and spin allowed states. From the literature it is clear that there are many lanthanides that show only SF emission.

Such an extension will allow for the determination of relevant parameters in crystal field calculations, and will aid in the interpretation of transition energies that are presently somewhat ambiguous. Additionally such extraction of parameters will allow for more *ab initio* calculations to be conducted on a wider variety of materials and symmetries, which may lead to gains in fundamental knowledge of many body systems in the quantum domain.

Appendix A

Properties of CaF_2 relevant to the heating model

A.1 IR absorption properties of CaF_2

CaF_2 has a transverse optical (TO) phonon frequency of 257 cm^{-1} [70], giving a large IR absorption at that frequency [19]. With an increase in frequency the absorption diminishes, following the density of states of the phonon band, with very little absorption occurring past 1000 cm^{-1}. In general the absorption decreases with increasing frequency beyond 257 cm^{-1} [19, 70], however there are resonances present due to the existence of various types of phonons and combinations thereof [104]. As described in chapter 3 the infra-red excitation extends to frequencies far below 1000 cm^{-1} making it vital that the absorption properties of the material are understood in that region.

Figure A.1 shows the manner in which the absorption coefficient α behaves with changing frequency. We can see that α changes by 4 orders of magnitude across the frequency range, meaning that when examining IR excitation properties, both spectrally and dynamically, care must be taken to consider the possible effects of this changing absorption. It is pertinent to note that the absorption presented is due to the host lattice (i.e CaF_2) only, and as such it will not directly influence the emission observed from the dopant. However because of the large change in absorption it will cause indirect effects that must be considered.

When considering the absorption of IR photons into the host lattice, a major concern is the effects caused on the lattice by the absorbed energy. This energy will cause heating within the interaction volume of the IR beam and the sample upon which it is incident. Because the IR beam is typically tightly focused (at a size of 100 μm - see chapter 3 section 3.2) the heating effect is localized, and will not cause the overall ambient temperature of the sample to rise. This causes a sharp temperature gradient to be set up across the beam spot, and causes dissipative cooling through heat transport. Such temperature changes and heat transport can cause differences in the dynamical behaviour of the system, and

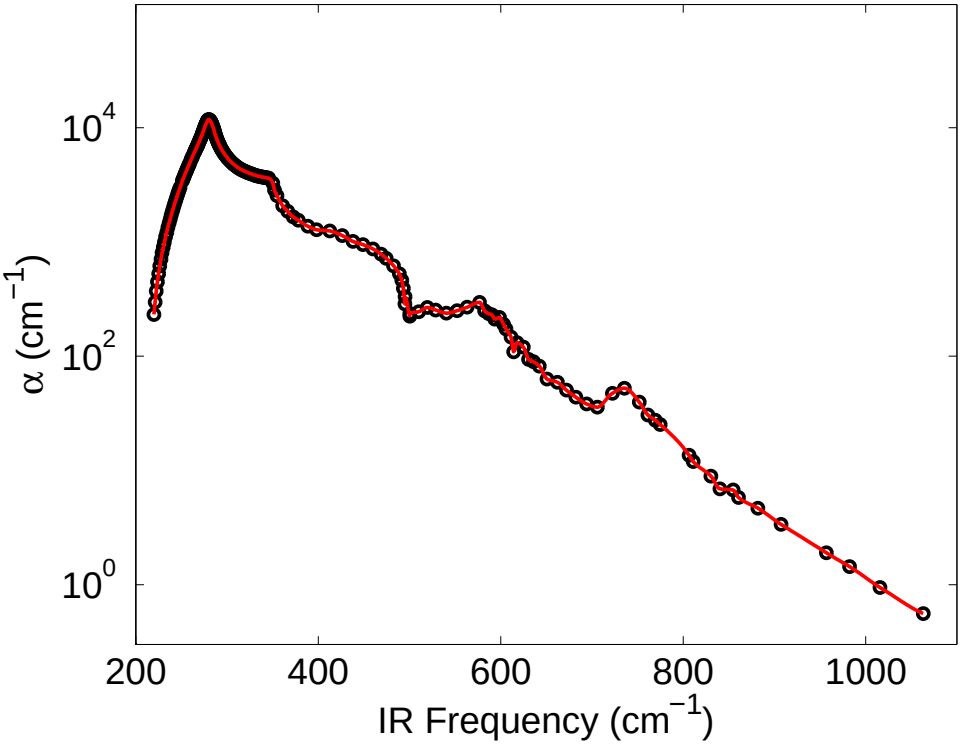

Figure A.1 Absorption of IR radiation in CaF_2 at mid to far frequencies. The peak at 225 cm^{-1} corresponds to the single phonon frequency in CaF_2. The resonances due to combinations of phonons are visible at 590 and 740 cm^{-1}. The absorption is greatly diminished by 900 cm^{-1} and this trend continues with increasing frequency [18]. The figure is adapted from a combination of data presented by Denham et al. [19] and Kaiser [70].

thus careful consideration must be placed upon the effective temperatures established and the time profiles of such temperature changes. Because of this, the rapidly changing low temperature heat capacities [20] and thermal conductivities [21, 22] of the sample material must be considered.

In addition to heating, such changes in absorption can cause obfuscation in the excitation spectra of the sample, as there will be a convolution of changes in the excitation spectra due to absorption by the ITE and states of the dopant materials (the chief concern of these studies) and absorption by the lattice (chiefly manifesting itself through heating effects as described above). When considering the spectral properties of the system it will be important to distinguish between these cases appropriately.

A.2 Low temperature thermal properties of CaF_2

Here we present the behaviour of the low temperature heat capacities and conductivities in CaF_2 with changes in temperature. All the data is obtained from previous studies, mainly conducted on pure CaF_2 crystals. Although there is evidence that the thermal properties of fluorides can change with impurities [23, 30] such data is not universally available in the literature for the temperatures used in our experiments. While there is data available for other impurities such as yttrium [105] in concentrations that are similar to the ones used in our experiments, it is not available in a sufficiently detailed resolution (in the temperature domain) to be usable.

There is high resolution data available for low concentrations of impurities (such as samarium) [21] in CaF_2. However, it is not clear that this behaviour is translatable across all concentrations and types of impurities, especially considering the work of Hayes et al. [105], which shows strong dependences of conductivity on concentration of impurities at low temperatures. Popov et al. also shows that above 40 K, there are significant behavioural differences in thermal properties dependent upon the concentrations of the impurities [23].

A.2.1 Low temperature heat capacity of CaF_2

Here we describe the strong dependence of the heat capacity on temperature. Figure A.2 shows that the heat capacity increases rapidly with temperature, changing over 2 orders of magnitude in the span of 20 K. This implies that while energy deposited in the system will cause the temperature to rise rapidly initially, there will be diminishing increase in temperature with energy absorbed by the crystal lattice.

Given that heat capacity is based primarily on the ability of the host lattice to store energy internally, low concentrations of impurities should not impact the heat capacity significantly [106, 107]. High concentrations of impurities may cause changes in heat capacities if they begin to alter the structure of the lattice significantly, as this will change the ability of the crystal to store energy [107]. However the impurity concentrations encountered (at most 0.1 molar %) in our studies are low enough that they form isolated centres and thus do not cause changes to the structure of the crystal [63]. Given this fact we have used the pure CaF_2 values of heat capacity obtained by Collocott et al. [20] in our considerations of heating caused by the IR absorption into the lattice.

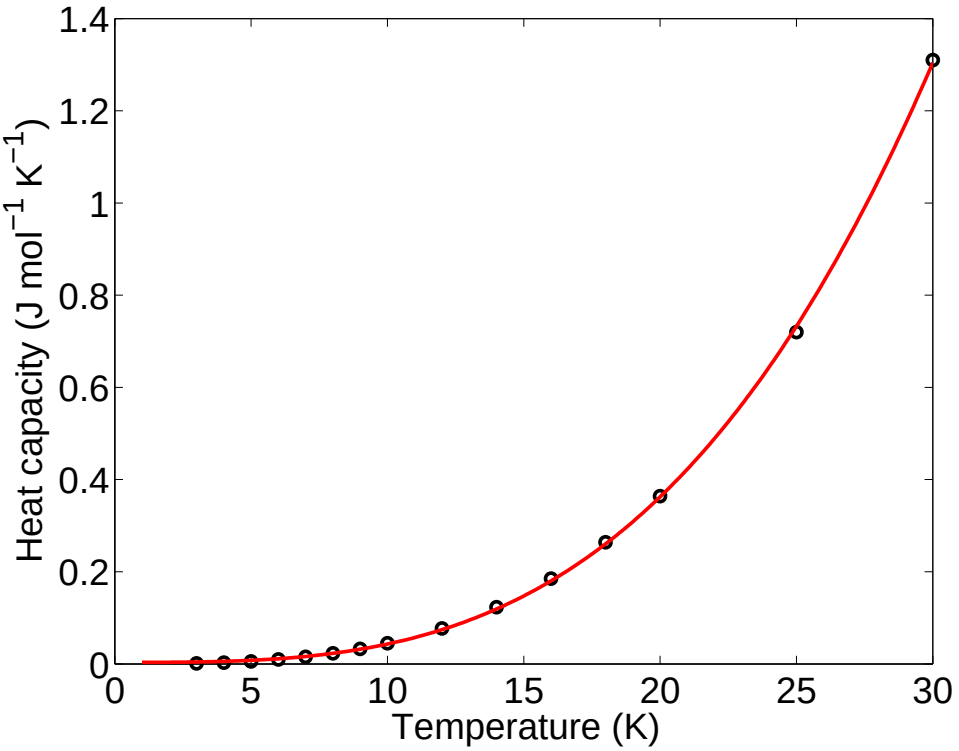

Figure A.2 The low temperature behaviour of heat capacity as sample temperature changes in pure CaF_2. The red line is a polynomial fit indicating the area of interest for the experiments conducted on CaF_2. The heat capacity changes by 2 orders of magnitude in the region of relevant temperatures. The plot is generated from data obtained by Collocott et al. [20].

A.2.2 Low temperature thermal conductivity of CaF_2

Here we describe the strong dependence of the thermal conductivity of CaF_2 on temperature. Figure A.3 shows that the heat capacity initially increases rapidly with temperature, changing by an order of magnitude over the region of interest from 6 to 15 K. However subsequently it decreases as the temperature increases past 15 K towards 50 K. This shows that the heating caused by deposited energy will be conducted away at different rates dependent upon the temperature of the system, meaning that the energy absorbed by the lattice strongly determines how quickly that energy will thermally dissipate towards the rest of the crystal (from the incident point of the IR beam).

The specific implications of the presented variability in conductivity are discussed in section 4.10 with the provision of details of the manner in which different temperatures will dissipate over time.

In addition to the complications caused by the above trend, conductivity appears to be

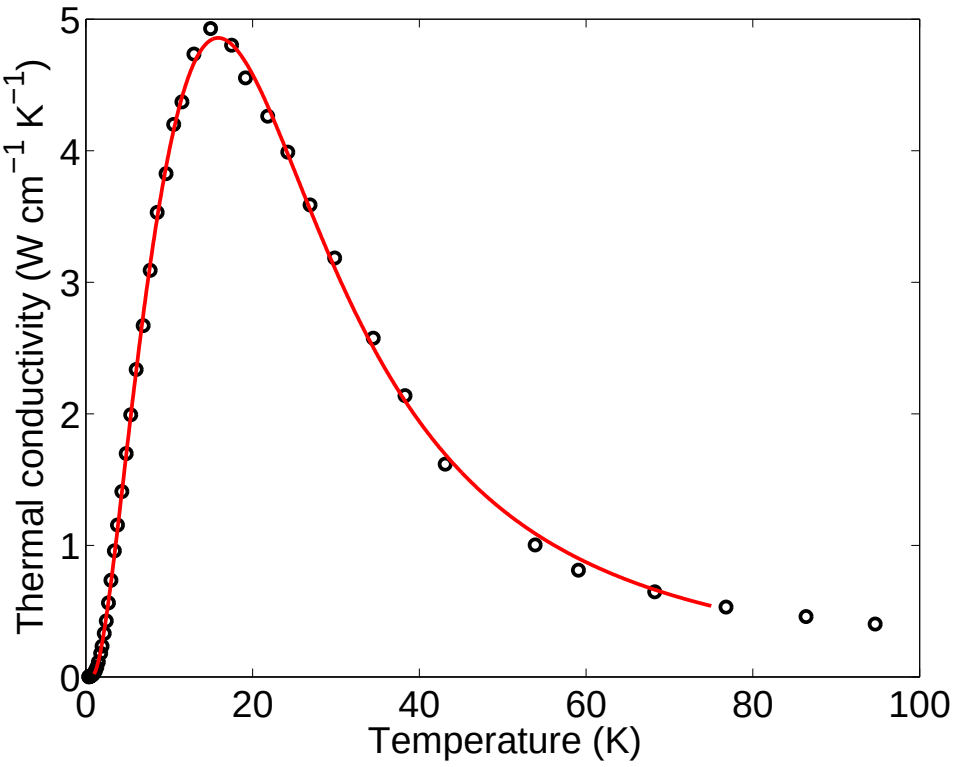

Figure A.3 The low temperature behaviour of thermal conductivity as sample temperature changes in pure CaF_2. The red line is a polynomial fit indicating the area of interest for the experiments conducted on CaF_2. A change by an order of magnitude occurs in the region of relevant temperatures. The plot is generated from data obtained by Harrington et al. [21].

heavily influenced by impurity concentrations, as shown in the figure A.4. It can be seen that this data is across a large range of temperatures, and for the purposes of this study, we require a higher resolution of data between 8 and 40 K.

As mentioned above, in a literature search, the only appropriate data set obtained was for low temperature conductivities was that provided by the work of Harrington [21] for divalent samarium impurities at a molar percentage of 0.04. While the impurity was not identical to the one studied, the concentration of the impurities matches well with the studies carried out (0.05% doping was used in a majority of the experiments, see section 3.1) and Harrington's data was used for considerations of thermal conductivity in CaF_2.

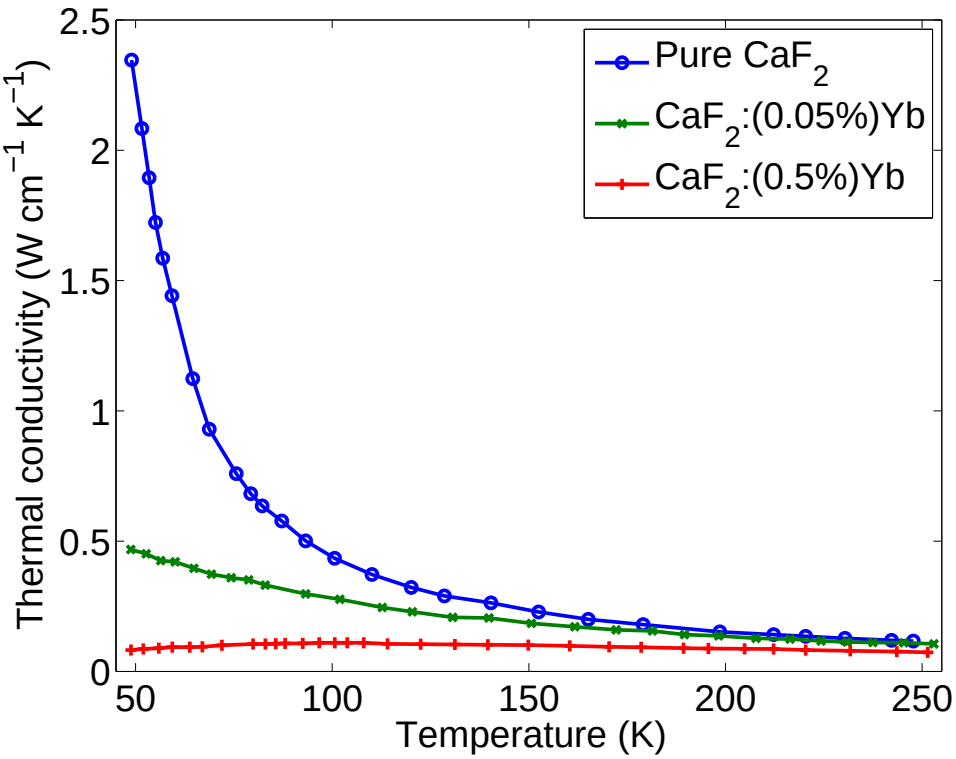

Figure A.4 The temperature dependent behaviour of thermal conductivity as sample temperature changes in CaF_2 crystals doped with varying concentrations of Yb^{2+} impurities. A change by an order of magnitude occurs within the concentration changes presented. The plot is generated from data obtained by Popov et al. [23].

Appendix B

Properties of SrF_2 relevant to the heating model

B.1 IR absorption properties of SrF_2

SrF_2 has a peak IR absorption at 220 cm^{-1} [19]. With an increase in frequency the absorption diminishes, following the density of states of the phonon band, with very little absorption occurring past 1000 cm^{-1}. In general the absorption decreases monotonically with increasing frequency [19, 70], however there are resonances present due to the existence of various types of phonons.

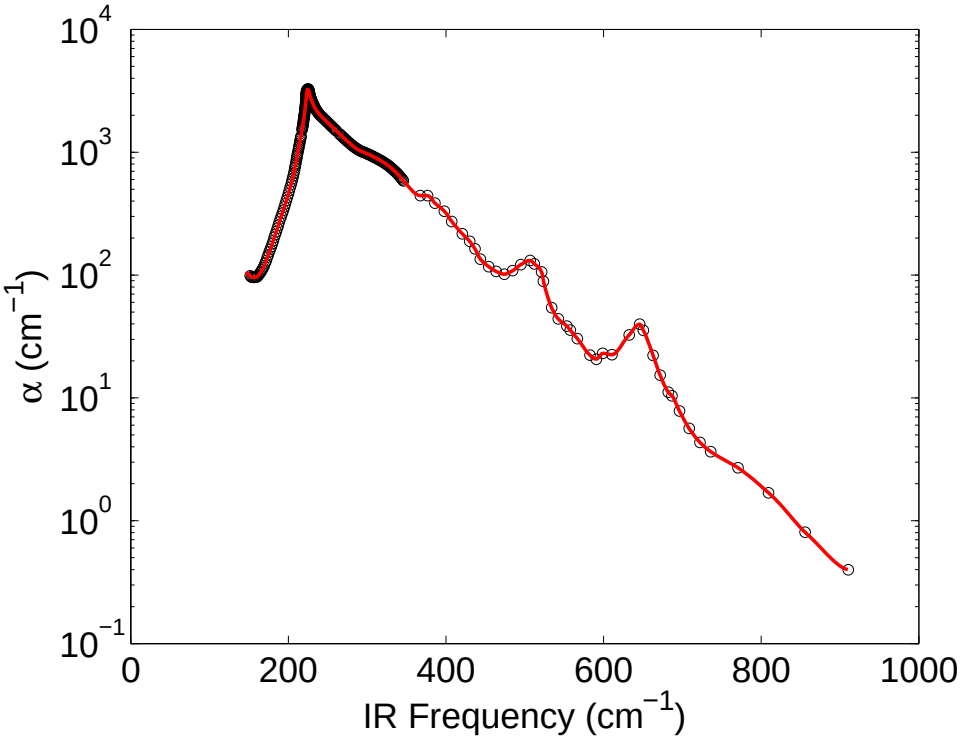

Figure B.1 Absorption of IR radiation in SrF_2 at mid to far IR frequencies. The peak at 200 cm^{-1} corresponds to the single phonon frequency in SrF_2. The resonances due to combinations of phonons are visible at 520 and 690 cm^{-1}. The figure is adapted from a combination of data presented by Denham et al. [19] and Kaiser [70].

As with CaF_2 figure B.1 shows that the absorption coefficient α for SrF_2 changes by 4 orders of magnitude across the frequency range. Because of the considerations outlined previously, taking this absorption into account in our modeling was paramount.

B.2 Low temperature thermal properties of SrF_2

Here we present the temperature dependent heat capacities and conductivities in SrF_2. All the data is obtained from previous studies, mainly conducted on pure SrF_2 crystals.

B.2.1 Low temperature heat capacity of SrF_2

Figure B.2 shows that the heat capacity increases rapidly with temperature, changing over 2 orders of magnitude in the span of 30 K. In comparison to CaF_2, SrF_2 shows a much larger heat capacity for a given temperature. This means that the IR induced temperature change in SrF_2 will be less pronounced in comparison to CaF_2.

B.2.2 Low temperature thermal conductivity of SrF_2

Figure B.3 shows the temperature dependent thermal conductivity in SrF_2. The thermal conductivity initially increases rapidly with temperature, changing by two orders of magnitude over the region of interest from 6 to 15 K. However subsequently it decreases as the temperature increases past 15 K towards 50 K. Compared to CaF_2, the thermal conductivity of SrF_2 is larger by a factor of 3 at its highest. Because of this a temperature perturbation will dissipate much faster in SrF_2.

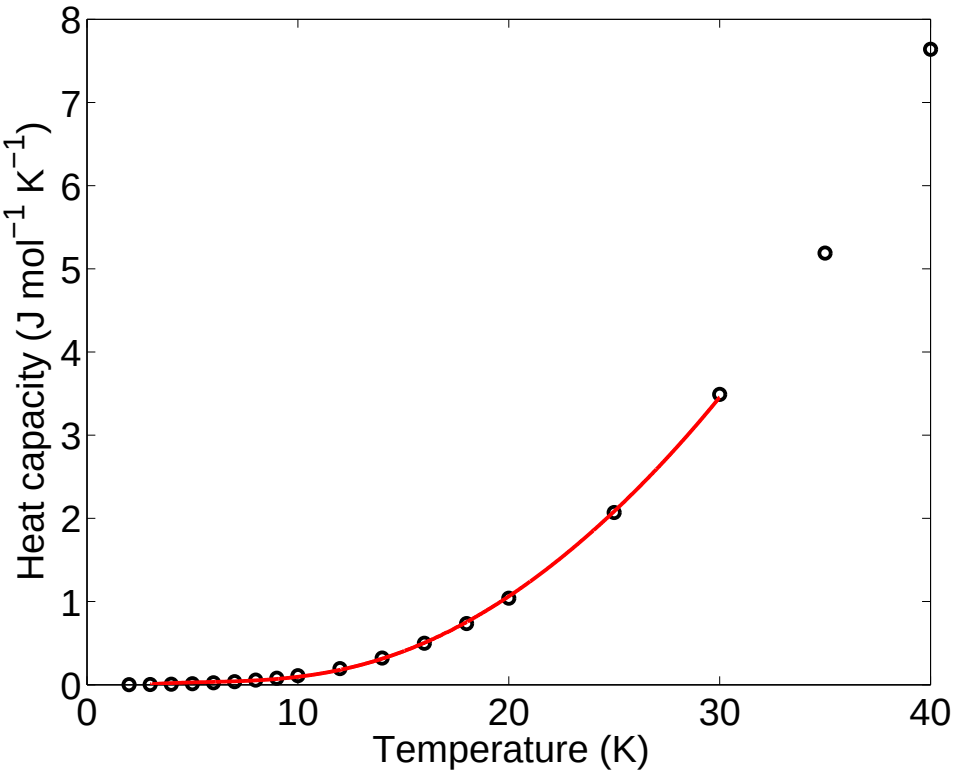

Figure B.2 The low temperature behaviour of heat capacity as sample temperature changes in pure SrF_2. The red line is a polynomial fit indicating the area of interest for the experiments conducted on SrF_2. The plot is generated from data obtained by Collocott et al. [20].

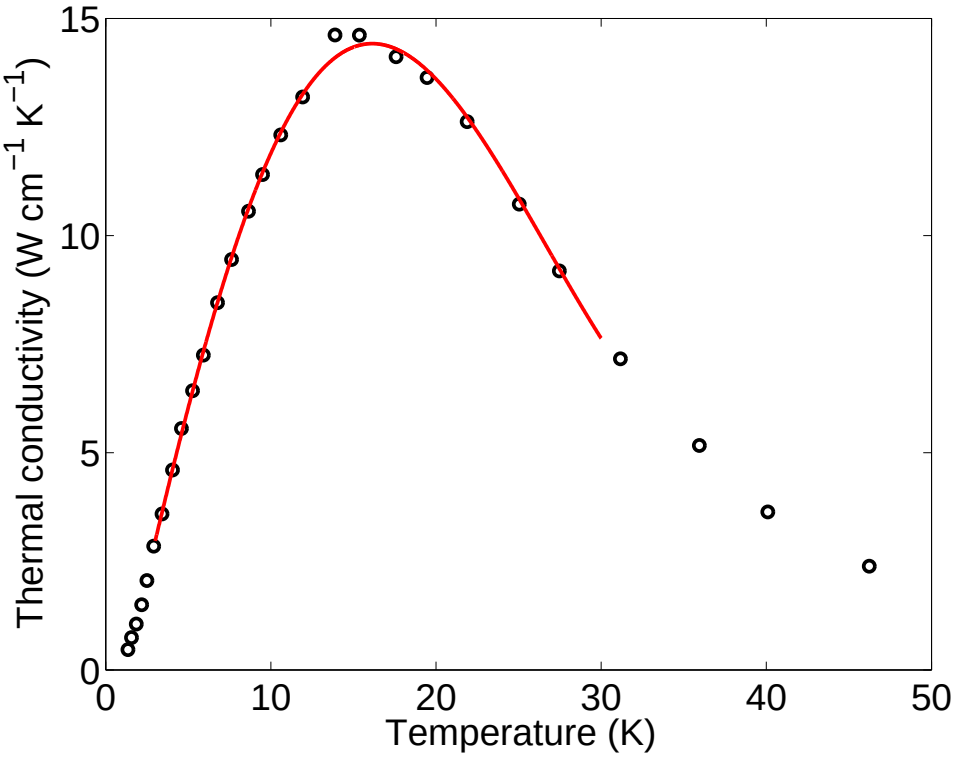

Figure B.3 The low temperature behaviour of thermal conductivity as sample temperature changes in pure SrF_2. The red line is a polynomial fit indicating the area of interest for the experiments performed. The plot is generated from data obtained by Harrington et al. [21].

Appendix C

Details of the modeling of thermal effects due to IR absorption

The evidence presented in section 4.9.3 means that local non–equilibrium heating and the subsequent dissipation of that heat must be examined and taken into account in detail if the dynamic properties of the transients are to be modeled with accuracy. In order to achieve this the manner in which CaF_2:Yb^{2+} heats under illumination by the IR beam is explored.

C.1 IR radiation induced heating of the lattice

The energy contained within the IR pulse can be converted to a change of local temperature by rearranging and generalizing the classical thermal energy equation $Q = mc\Delta T$ to take into account the dependence of heat capacity on the temperature of the material itself. This gives the following expression for ΔT accounting for the heavily temperature dependent heat capacity of CaF_2 at low temperatures:

$$\Delta T = \frac{Q}{mc(T)} \tag{C.1}$$

where Q is the change in energy of a system with mass m and a heat capacity c undergoing a temperature change ΔT [108]. Typically when solving for equation C.1 one assumes that the heat capacity is constant making the process trivial. However in this particular case a different approach must be adopted.

Because the heating occurs due to a time dependent IR pulse, an iterative approach can be taken to compute the local temperature change. The IR pulse shape is known, therefore we may estimate the delivered energy at a given time along the pulse. By normalizing the total integral (from $t = t_i$ to $t = t_f$) of the pulse with υ, such that,

$$\frac{1}{\upsilon}\int_{t_i}^{t_f} F(t)\mathrm{d}t = 1, \tag{C.2}$$

where $F(t)$ is the time dependent pulse shape, an additional coefficient can be utilized that simply reflects the total energy the IR pulse imparts into the lattice in the heating process. Let us now define $f(t) = F(t)/\upsilon$ such that $f(t)$ refers to the normalized time dependent pulse shape.

By assuming that the FEL is operating in the TEM_{00} mode, thus allowing for cylindrical symmetry, the beam shape may be modeled with a Gaussian function in two dimensions by,

$$G(x,y) = G_0 e^{-(\frac{x-x_0}{\sigma_x})^2-(\frac{y-y_0}{\sigma_y})^2}, \tag{C.3}$$

where $G(x,y)$ is the beam energy at a given point (x,y) with a beam shape defined by σ_x and σ_y. Because we assume cylindrical symmetry about the propagation axis of the beam, and centre the beam at $(x,y) = (0,0)$ equation C.3 simplifies to

$$G(x,y) = G_0 e^{-(\frac{x^2+y^2}{\sigma^2})}, \tag{C.4}$$

where $\sigma = \sigma_x = \sigma_y$. As with the time dependent pulse shape, normalizing the total volume of the above Gaussian by setting Γ such that

$$\frac{1}{\Gamma}\iint\limits_R G(x,y)\,\mathrm{d}x\,\mathrm{d}y = \frac{1}{\Gamma}\iint\limits_R G_0 e^{-(\frac{x^2+y^2}{\sigma^2})}\,\mathrm{d}x\,\mathrm{d}y = 1 \tag{C.5}$$

allows for a multiplicative coefficient to set the total energy the Gaussian shaped beam imparts upon the region of interest. R, the region to integrate over can be defined by $-L < x < L$ and $-L < y < L$, where $L = 100$ μm (i.e. a 200×200 μm square region). Given that the Gaussian defined in equation C.4 is not dependent on time, its normalized version (equation C.5) can be thought of as providing a distribution seed function in space for a given amount of energy defined by the multiplicative coefficient. Here σ determines the sharpness of the distribution. By making this coefficient time dependent a change in the imparted energy can be achieved. Let us define $g(x,y) = G(x,y)/\Gamma$ such that $g(x,y)$ refers to the normalized Gaussian basis. Combining the normalized pulse shape (time wise) and beam shape (space wise), it is possible to construct a function that provides the energy Q imparted by the IR pulse at a given time in a given position by,

$$Q(x, y, t) = E_m f(t) g(x, y), \tag{C.6}$$

where E_m is the maximum total energy imparted by the beam over both space and time. This value can be approximated by measuring the IR pulse energy across the frequency range and making an adjustment for the IR absorption by the lattice. When modeling the data however an initial value of E_m was achieved via fitting, then adjusted for the IR absorption (checking that the fitted value was approximately similar to the measured pulse energy). The details of this are provided in section 4.11.

To utilize an iterative procedure for determining the temperature change in time the continuous function previously introduced can be made discrete by introducing a discrete version of $f(t)$ denoted by $f(t_n)$. Because the pulse shape data is discrete in practice this is easily implemented. It is then possible to simply step through time (via a numerical simulation) computing the temperature change at each time step in the following manner:

$$\frac{dT}{dt_n} = E_m \frac{f(t_n) g(x, y)}{c(T(x, y, t_{n-1}))}, \tag{C.7}$$

where the symbols have their previously defined meanings. Here T is a surface defined across (x, y) changing in time. Note that the heat capacity is determined by the temperature established across the region in the previous step, giving a surface of heat capacities across (x, y) dependent upon the temperature at each of the points within the region in the previous step. An assumption is made that the change in temperature is small enough in each step such that the heat capacity between two consecutive steps is similar enough to allow the above calculation. c is initially seeded by establishing a uniform surface of heat capacity prior to the incidence of the IR pulse with the use of the indicated temperature of the sample.

This allows for a temperature surface to be created at a given moment, t_{n+1}, by simply computing the sequence as defined by,

$$T_{n+1} = T_n + \frac{dT}{dt_n}, \tag{C.8}$$

where n is determined by the required time resolution r such that $n = (t_f - t_i)/r$, with t_i and t_f being the start and end times of the IR pulse respectively. Typically r is the same as the time resolution of the data, but in some instances it may be smaller (i.e. the

time step may be smaller). This may happen due to stability problems in solving the heat equation as discussed later.

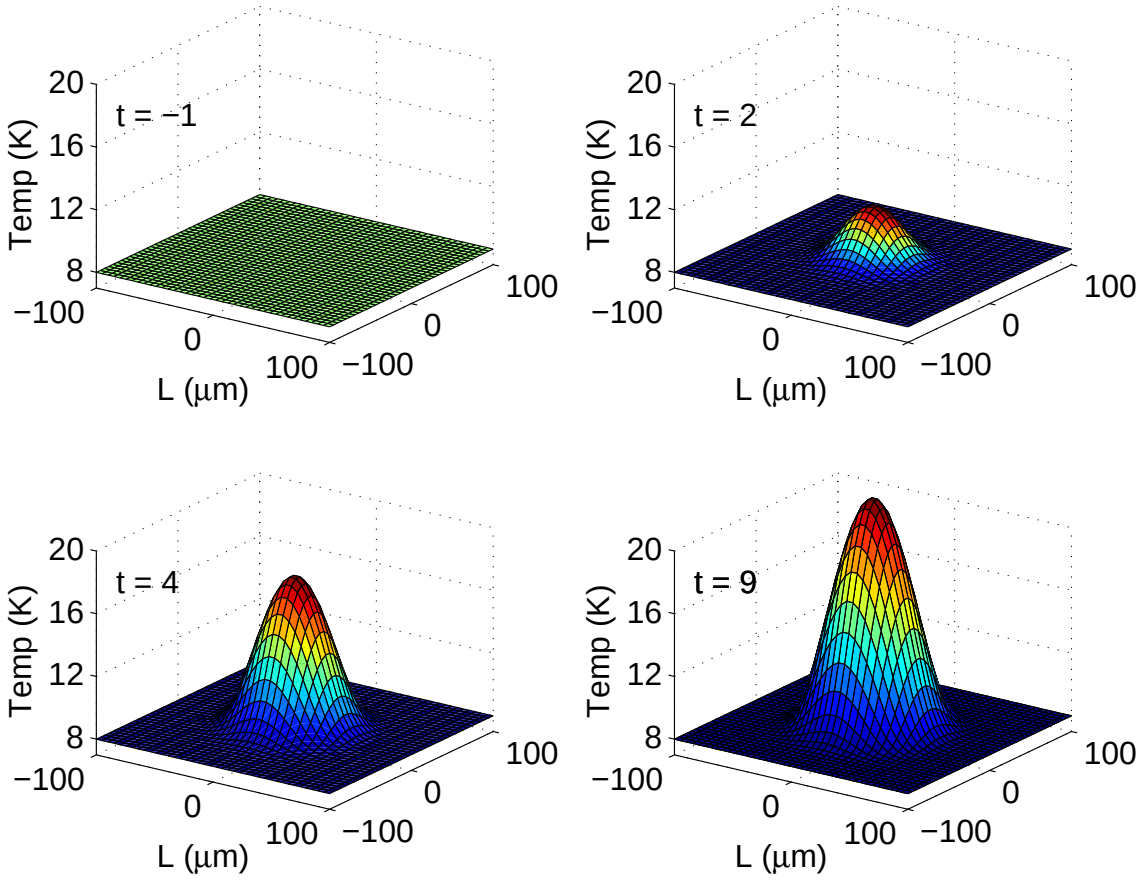

Figure C.1 The evolution of the temperature distribution under heating by the IR excitation. The time lapse presents the temperature distribution just before the incidence of the IR pulse (at $t = -1$ μs) and at points along the IR pulse. The t values shown are in μs. Here we have used a 1.0 mJ energy distribution to induce the temperature change. Note the distortion of the temperature distribution from a Gaussian shape as time progresses.

Figure C.1 displays a time lapse of the heating profile via a series of plots of the temperature distribution at different times along the IR pulse. Notice that the shape of the temperature distribution as it grows is not Gaussian, even though the function inducing the change is. This is further illustrated by figure C.2 and the corresponding 2-D slice across $(0, y)$ displayed next to the relevant distribution plot. This behaviour can be understood by considering the heat capacity (see figure A.2) of the material. As the temperature rises so does the heat capacity of CaF_2, thus causing a distortion in the shape of the temperature distribution.

Furthermore the temperature surface has a greater width when compared to the Gaussian

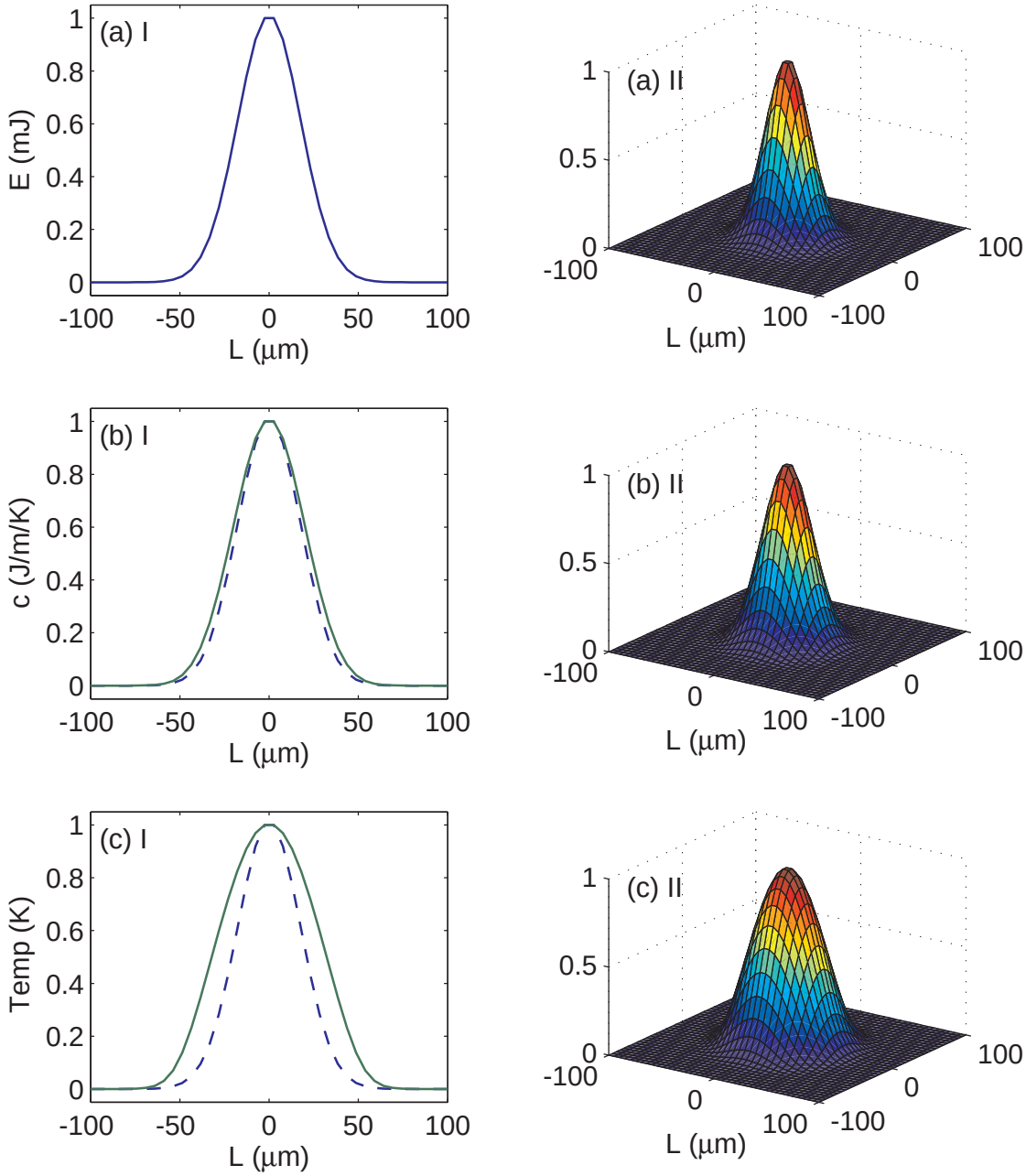

Figure C.2 The distortions that occur in the heat capacity and temperature surfaces upon excitation under the IR pulse, seeded with a Gaussian energy distribution. The two dimensional plots show the respective surface cut across the line $(0, y)$ shown with the solid curve. The seeding energy function is shown on (a) I & II, (b) I & II shows the heat capacity surface, distorted from the energy function and (c) I & II shows the temperature surface, with an even greater distortion. The dashed blue curve indicates the energy function allowing for direct comparison of the distortion. All functions have been normalized such that their domain is $[0, 1]$.

energy distribution that caused the heating. This is again due to the heavy dependence of the heat capacity on the temperature of the lattice. This phenomenon is illustrated in figure C.2. Notice that the heat capacity surface (figure C.2(b)) is also distorted in comparison to the energy distribution. By slicing the distributions along the line $(0, y)$ and examining the two dimensional distribution curve (as in figure C.2(b,c) II) the widening effect is clear.

Such distortions have physical relevance since a change in the total IR energy input will not only cause a change in the temperature, but also a change in the spatial *distribution* of the temperature. This can be seen in figure C.3, where, as the energy input increases the temperature distribution distorts with an increase in width. The 2-D cross sectional plots, shown in figure C.4, allow for direct comparison of the distribution change. Note that the temperatures in figure C.4(b) have been normalized such that their domain is $[0, 1]$, to allow for a better illustration of the changing shapes with total IR energy.

Figure C.3 also shows the influence of the temperature dependent heat capacity on the overall non–equilibrium temperature change. From the wide range of energy inputs displayed it is clear that the rate of growth of the temperature diminishes as the IR fluence (or the corresponding energy input into heating) increases. A clear sublinear dependence exists between the overall maximum temperature reached and the IR fluence, reinforced by the trend presented in figure C.4 (a). Because of the increasing heat capacity the lattice can accommodate a greater amount of energy without requiring a further increase in temperature. However, as we shall see in section C.2 this causes slower cooling, as the greater energy takes longer to dissipate out of the non–equilibrium region. Because the thermal conductivity also depends upon the temperature (section A.2.2), the distortions of the surface will lead to a complex heat flow pattern that is dependent upon the IR energy absorbed by the lattice.

C.2 Modeling the heat dissipation through the lattice

To understand the manner in which the IR induced non–equilibrium temperature changes in our region of interest, the heat equation [87]

$$\frac{\partial T}{\partial t} = \alpha(T)\nabla^2 T, \tag{C.9}$$

where $\alpha(T) = k(T)/c(T)$ is the diffusion coefficient, must be solved. Here $k(T)$ is the

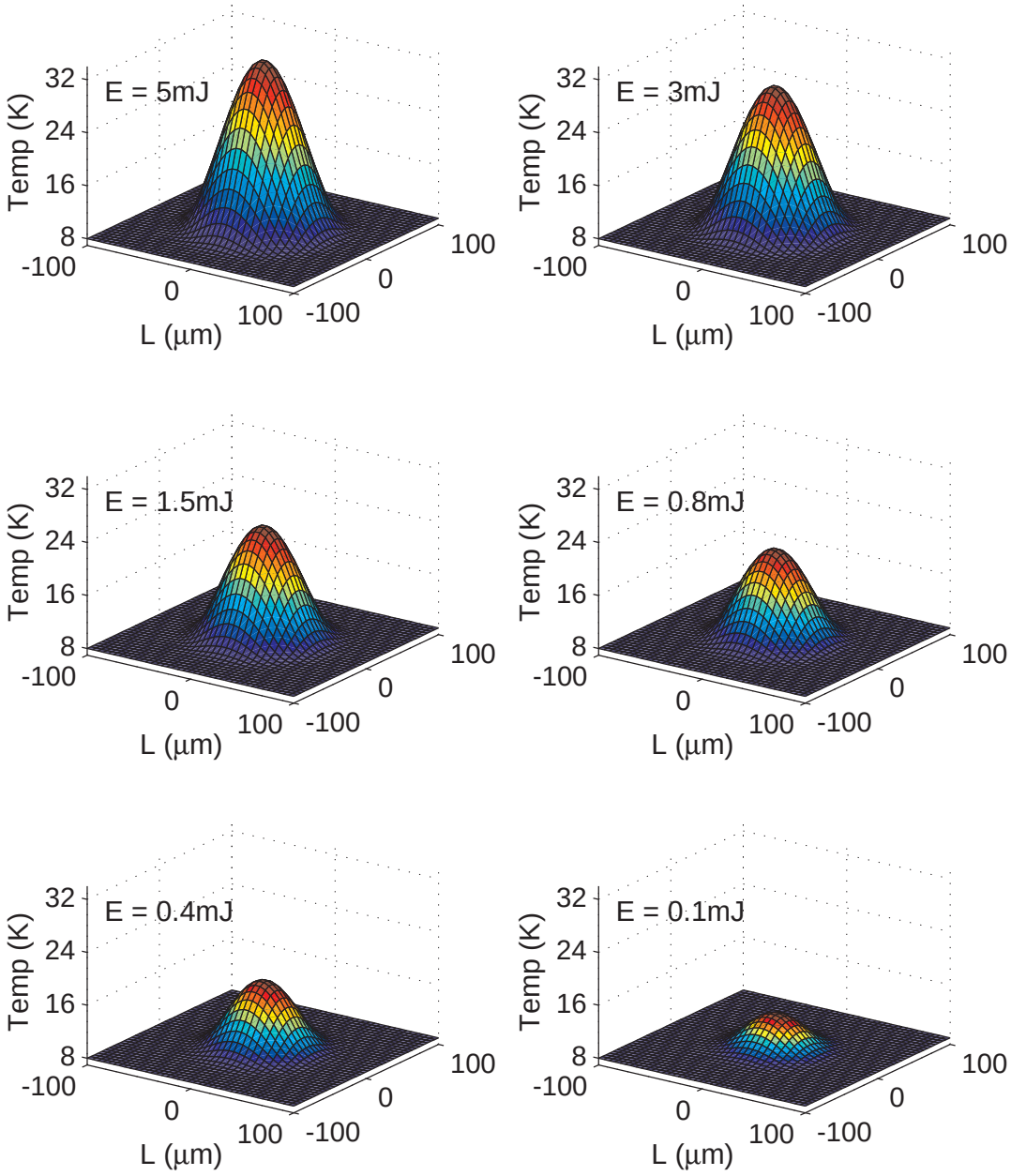

Figure C.3 The temperature distribution just at the moment of termination of IR pulse shown under changing excitation fluence. The E value on each plot indicates the total energy that is used in the heating process. Note that while the temperature distribution gets broader, its peak does not increase linearly with excitation fluence. To obtain these plots E_m was varied in equation C.7.

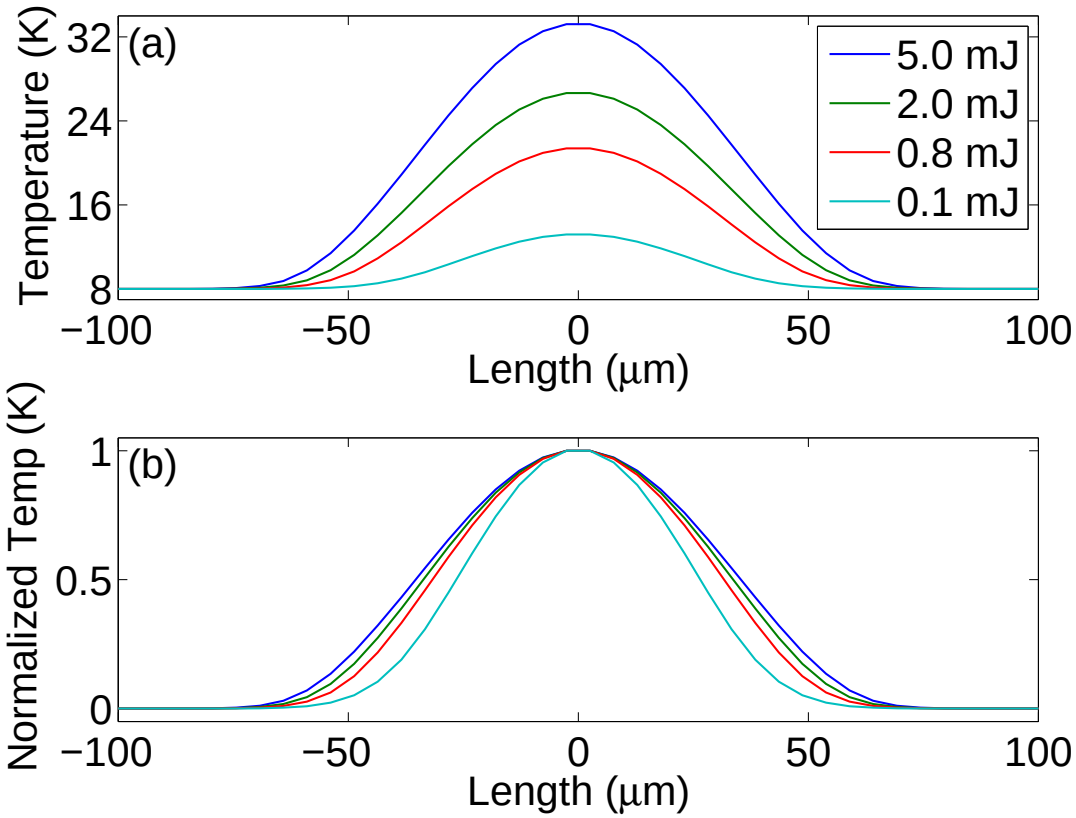

Figure C.4 A 2-D cut along the line $(0, y)$ of selected IR energy values from figure C.3. The sublinear dependence of the overall temperature increase with IR fluence is clear as (a) shows the raw temperature at points along sample's region of interest. Distortions occurring as a result of changing IR energy is better illustrated by (b) which shows the temperature curves from (a) normalized such that they extend over a domain $[0, 1]$.

temperature dependent thermal conductivity. In order to do this several assumptions are made. We assume a cylindrical section of the sample is heated by the IR beam, and that the heat flow will only occur radially outward from the axis z, where z is defined as the axis along which the IR beam propagates. Figure C.5 provides a schematic of the assumptions made about the manner in which the heat dissipates. Note that equation C.9 is modified from the standard heat equation (as presented in Cannon [87]) to account for the temperature dependent behaviour of heat capacity and thermal conductivity encountered here.

The temperature distribution is seeded by equation C.8 prior to the evolution of the dissipation model. We also assume that no heat enters the region of interest externally, specifically this applies to IR radiation absorbed by the lattice outside of the region of interest. Given the symmetries of the system this assumption can be simplified to "*no heat flow occurs along the z axis*," and is an extension of the first assumption above.

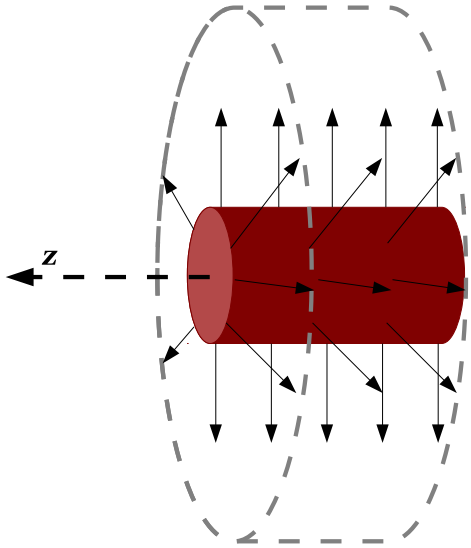

Figure C.5 Schematic illustrating the radial dissipation of heat that is assumed in solving the heat equation. The solid cylinder indicates the emitting region influenced by IR induced non–equilibrium heating. The dashed arrow indicates the axis of the IR beam propagation, defined as the z-axis. The solid arrows indicate the radial heat loss. It is assumed that no heat loss occurs through the parallel surfaces that lay longitudinal to the beam axis.

Because of cylindrical symmetry, the geometry can be further simplified to heat flow between two parallel surfaces, with a given temperature distribution between them. The outside surface in this case is set to be 100 μm from the centre of the beam, which is twice the beam radius in each direction (i.e. a span of 200 μm, with $(0, 0)$ set as the beam centre). This surface is held at the nominal lattice temperature.

Given such boundary conditions equation C.9 is analytically solvable through a variety of methods for well behaved temperature distributions [87, 109] and is extendable to extra dimensions with many types of seeding functions [110, 111]. However in this instance the distorted Gaussian nature of the temperature distribution makes such a solution difficult (as the temperature distribution is not established through a single function). Additionally the temperature dependence of α, established through experimental data (from references [20, 21]), adds a degree of complexity which makes an analytical solution impossible. A numerical method was therefore employed to solve equation C.9.

There are three major approaches for solving partial differential equations numerically, namely the finite element [112], finite difference [88] and finite volume methods [113]. All these methods employ a meshed geometry used to calculate values for the flow based on the initial and boundary conditions. Given the simplicity of the boundary conditions in our system the finite difference method is used to approach equation C.9.

Within the finite difference method there are also three established approaches, the explicit, implicit [89] and the Crank-Nicolson methods [114]. It should be noted that the Crank-Nicolson method is also an implicit method. Both the explicit and implicit methods employ a second order difference for space and a first order forward (explicit) or backward (implicit) difference for time.

The Crank-Nicolson method while generally stable with greater convergent accuracy in comparison to the other methods [115], is also computationally intensive, especially given the time resolution required to match the acquired data. Additionally the manner in which the α surface is computed favours a forward difference in the time domain. Because of this the *Forward-Time Central-Space* (FTCS) method was used. This method is conditionally stable for parabolic partial differential equations (of which the heat equation is one) [89]. In iterative form the solution algorithm can be stated as,

$$\frac{T_i^{n+1} - T_i^n}{\Delta t} = \frac{\alpha_i^n(T)}{\Delta x^2}(T_{i+1}^n + T_{i-1}^n - 2T_i^n), \tag{C.10}$$

where the index i indicates points along the spatial mesh and n indicates the time step through which the algorithm propagates [116]. The other symbols carry their meanings from equation C.9. For a two dimensional temperature function, this can be extended with the addition of an extra index j such that equation C.10 becomes,

$$T_{i,j}^{n+1} = T_{i,j}^n + \alpha_i^n(T)\frac{\Delta t}{\Delta x^2}(T_{i+1,j}^n + T_{i,j+1}^n + T_{i-1,j}^n + T_{i,j-1}^n - 4T_{i,j}^n), \tag{C.11}$$

requiring that for each i, the values of all j points are computed. Given that i and j are of the same length, one can see that the number of computations has now squared. Also notice the factor of 4 in the last term (compared to 2 in the one dimensional case), to account for the additional dimensional terms in equation C.11. The assumption that $\Delta x = \Delta y$ has been made here.

From equations C.10 and C.11 it can be seen that the FTCS method, when used for the heat equation, essentially employs a second order finite difference in space and the forward Euler method [117] in time (because the heat equation is a first order differential in time). Care must be taken when using such a method to ensure stability in the step wise solutions. Even though this is of particular concern in solving hyperbolic PDEs, oscillations in the solutions to parabolic PDEs can also occur if the time step is too large, or the spatial mesh is too fine [115, 116].

A necessary and key condition for convergence of solutions is known as the Courant-Friedrichs-Lewy (CFL) condition, named for the authors that introduced the concept in a 1928 paper [90]. A translated version of this work was published in 1967 [91]. This condition as it applies to equations C.10 and C.11 is,

$$\alpha(T)\frac{\Delta t}{\Delta x^2} < C_m \tag{C.12}$$

where typically, $C_m \leq 0.5$ for the FTCS method [116]. The CFL condition can be thought of as a restriction necessary to allow sufficient time for the "numerically approximated information" to travel spatially through the geometric mesh, set up by Δx. Here α can be thought of as a measure of how quickly the model can propagate (rather than the information the model is computing), thus a greater α will cause the model to compute values along the mesh at points (i, j) without the correct information present in the neighbouring points, leading to stability issues.[1] Under this interpretation $\alpha(T)$ heavily influences the choice of the time step and the size of the spatial mesh. The issue is further complicated because as discussed previously, α changes with temperature, thus as the model propagates in the directions i, j and critically n, the requirements on the time step and mesh size change.

The simplest method to ensure stability was to compute the maximum possible value α will reach and set the time step and mesh size accordingly. To ensure enough spatial resolution in the model the maximum allowable Δx was decided as 3.33 μm. This was determined by examining several temperature distributions at different IR fluences to ensure no information was lost. Such a resolution allowed a beam with a FWHM of 20 μm to be sufficiently well described. Typically though, $\Delta x \approx 1.0$ μm, and α could be as large as 5, causing $\Delta t \approx 0.05$ μs for $C_m = 0.25$. Such a time step was twice the resolution of a typical transient (typically a transient was recorded for about 1000 μs), and while this represents a computation time that is twice as long when compared to a model where the time step is resolution matched to the data, the afforded numerical stability is paramount.

A more sophisticated method with an adaptive time step, where the code continuously checks the CFL condition was attempted. However the introduction of a further conditional check (via a `while` statement) and extra `for` loop elements to deal with a changing time step caused a greater increase in computation time of the model than the gains made

[1] It should be noted however that strictly speaking, α is not a velocity quantity unit wise. However in the context of the CFL condition, the diffusivity of a system can be thought of as a velocity for the model propagation, with units of distance over time. Ultimately the units of this quantity become irrelevant as it is simply a ratio calculation to determine the *numerical* stability of the model

by optimizing the time step size. Such a method is only useful if the solution algorithm were to be "black boxed" for future use.

An algorithm adapted from the FTCS method was thus used for computing the manner in which the IR induced non–equilibrium temperature increase dissipated over the sample, accounting for both the temperature dependent heat capacity and thermal conductivity of the CaF_2 lattice. In general the average temperature of the region $(x, y) = (0 \pm 10, 0 \pm 10)$ was used for subsequent calculations of the thermally influenced rates (e.g. W_{23}). While this approach is not completely accurate, computing the rates at each temperature across the mesh and constructing an emittive model from this was not deemed to provide enough of a gain in accuracy to offset the associated increase in computation time. It is important to remember that these models were subsequently subjected to a least squares fitting scenario, where the model would be run multiple times. Because of this computation time was a relevant factor to consider seriously.

The manner in which the heat dissipates under this model is illustrated in figure C.6 using a cylindrical temperature distribution to set the initial condition. While this is not the modeled temperature distribution that is used in computing the thermal behaviour of the system, the cylinder provides a better illustration of the phenomenon.

The cylindrical distribution quickly dissipates to a Gaussian like shape (at $t = 19.9$ μs). As the subsequent time frames show this shape then distorts as the region cools. This provides an indication of the influence that the temperature dependent $\alpha(T)$ value has on the dynamic thermal behaviour.

From here onwards the term temperature will refer to the temperature used in subsequent calculations, i.e. the computed temperature for a given region of the temperature distribution in (x, y). Any discussion requiring reference to the temperature distribution will have it explicitly stated.

FELIX can sometimes drift spatially when scanning across its frequency range, and because of this a physical offset of a few microns can occur between the peak emitting centre of the sample and the IR beam. In such an event the thermal dissipation is slightly skewed, since the temperature that is affecting the transfers between the states is not the peak temperature of the distribution. To account for this the model was extended to allow the determination of temperature at a given point (x_i, y_i), rather than simply at $(x, y) = (0, 0)$. Figure C.7 shows the influence such an offset has on the time dependent temperature shape. Notice that as the offset increases the peak temperature diminishes,

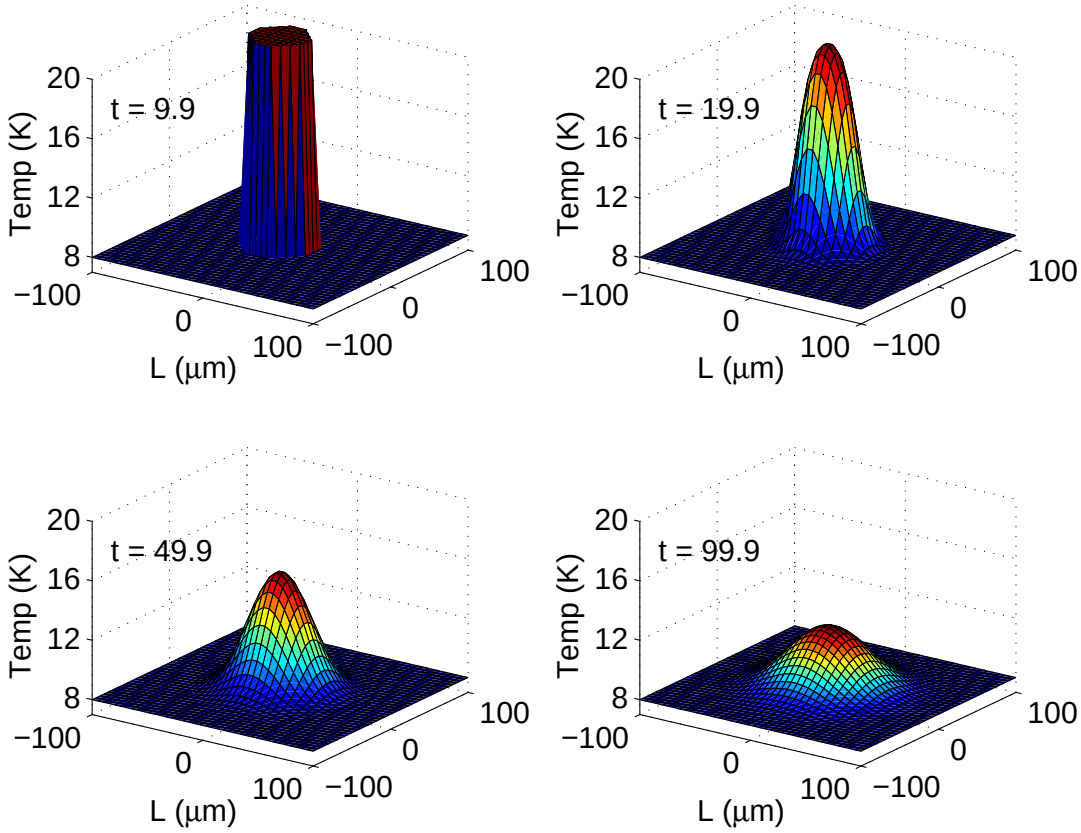

Figure C.6 A time lapse of the dissipation of heat with the initial conditions set by a uniform cylinder with a diameter of 40 μm and a maximum temperature of 20 K. The ambient temperature at the boundary is set to 8 K and is assumed to stay constant. This assumption is valid when considering the relative size of the sample to the beam width. The times indicated are in μs after the initiation of the IR pulse.

but the temperature is sustained for longer (clear in the normalized plot in C.7 (b)). This is because unlike the $(0, 0)$ point, there is heat flowing in to this region as well as out of it.

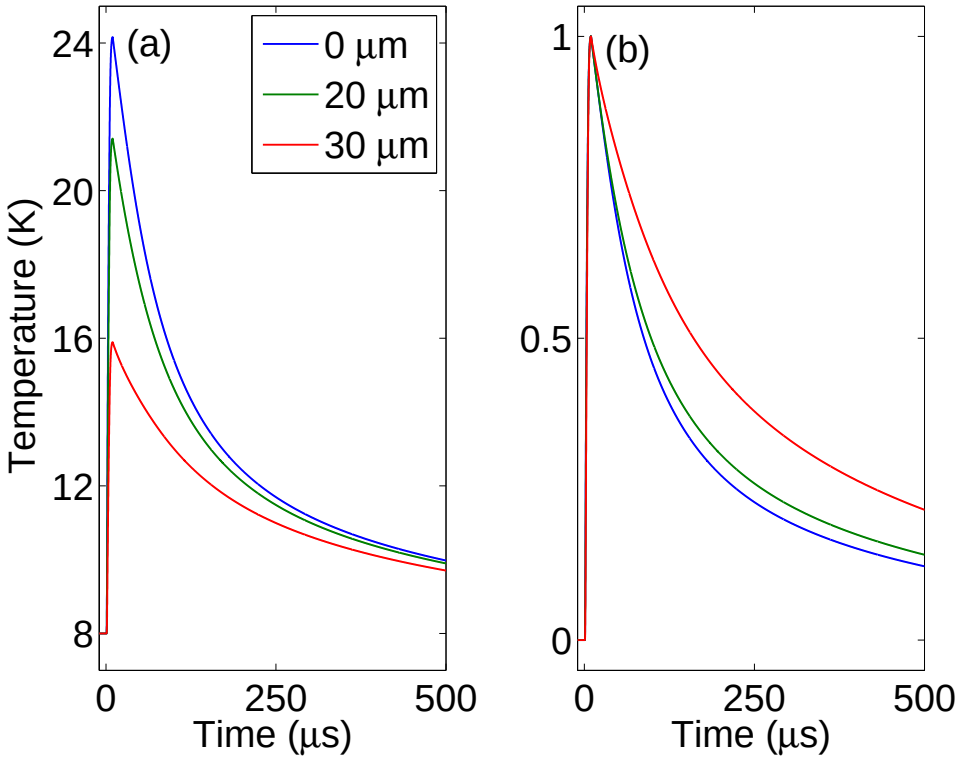

Figure C.7 The manner in which the temperature dissipation curves change when a beam offset is introduced. Naturally the peak temperature drops as one examines the distribution away from the centre of the beam. However the temperature decays slower as the offset increases, because of heat flowing into the point examined. Here (a) shows the calculated temperature curves in their raw form, with (b) showing the curves normalized to the domain $[0, 1]$ allowing for comparison of the decay rates visually.

Appendix D

List of publications

Reid, M. F., Senanayake, P. S., Wells, J–P. R., Berden, G., Meijerink, A., Salkeld, A. J., Duan, C.K., and Reeves, R. J. *Transient photoluminescence enhancement as a probe of the structure of impurity-trapped excitons in* CaF_2*:*Yb^{2+}, *Physical Review B* **84** (2011),113110.

P. S. Senanayake, J–P. R. Wells, M. F. Reid, G. Berden, A. Meijerink, and R. J. Reeves, Electron trap liberation in MgF_2 doped with Yb^{2+} using a two–color excitation experiment, *Applied Physics Letters* **100** (2012), 041902-041902.

P. S. Senanayake, J–P. R. Wells, M. F. Reid, G. Berden, A. Meijerink, and R. J. Reeves, *Impurity-trapped excitons and electron traps in* CaF_2*:*Yb^{2+} *and* SrF_2*:*Yb^{2+} *probed by transient photoluminescence enhancement, Journal of Luminescence* (2011)

R. B. Hughes–Currie, P. S. Senanayake, J–P. R. Wells, M. F. Reid, G. Berden, R. J. Reeves and A. Meijerink. *Site Selective Transient Photoluminescence Enhancement of Impurity-Trapped Excitons in* $NaMgF_3$*:*Yb^{2+}*, Submitted to Phys. Rev. B.* (2013)

References

[1] B. Jacquier and G. K. Liu, *Spectroscopic Properties of Rare Earths in Optical Materials*. Springer Series in Materials Science. Springer, 2005.

[2] G. Sánchez-Sanz, L. Seijo, and Z. Barandiarán, *Yb-doped $SrCl_2$: Electronic structure of impurity states and impurity-trapped excitons*, *The Journal of Chemical Physics* **133** (2010) 114509.

[3] W. T. Carnall, G. L. Goodman, K. Rajnak, and R. S. Rana, *A systematic analysis of the spectra of the lanthanides doped into single crystal LaF*, *The Journal of Chemical Physics* **90** (1989) 3443.

[4] G. W. Burdick and M. F. Reid, *$4f^N \rightarrow 4f^{N-1}5d$ transitions*, vol. 37. North Holland, 2007.

[5] M. F. Reid, L. Hu, S. Frank, C. K. Duan, S. Xia, and M. Yin, *Spectroscopy of High-Energy States of Lanthanide Ions*, *European Journal of Inorganic Chemistry* **2010** (2010), no. 18 2649–2654.

[6] Z. Pan, C. K. Duan, and P. A. Tanner, *Electronic spectra and crystal field analysis of* Yb^{2+} *in* $SrCl_2$, *Phys. Rev. B* **77** (Feb, 2008) 085114.

[7] G. Sánchez-Sanz, L. Seijo, and Z. Barandiarán, *Electronic spectra of Yb-doped $SrCl_2$*, *The Journal of Chemical Physics* **133** (2010) 114506.

[8] M. Grinberg and S. Mahlik, *Impurity-trapped excitons: Experimental evidence and theoretical concept*, *Journal of Non-Crystalline Solids* **354** (2008), no. 35 4163–4169.

[9] B. Moine, B. Courtois, and C. Pedrini, *Luminescence and photoionization processes of Yb^{2+} in CaF_2, SrF_2 and BaF_2*, *Journal de Physique* **50** (1989), no. 15 2105–2119.

[10] C. Pedrini, M. Joubert, and D. McClure, *Photoionization processes of rare-earth dopant ions in ionic crystals*, *Journal of Luminescence* **125** (2007), no. 1 230–237.

[11] P. Dorenbos, *Anomalous luminescence of Eu^{2+} and Yb^{2+} in inorganic compounds*, *Journal of Physics: Condensed Matter* **15** (2003) 2645.

[12] B. Moine, B. Courtois, and C. Pedrini, *Photoconductivity and fluorescence properties of divalent ytterbium ions in fluoride crystals*, *Journal of Luminescence* **48** (1991) 501–504.

[13] D. Lide, *CRC handbook of chemistry and physics: a ready-reference book of chemical and physical data*. CRC Pr I LLC, 2004.

[14] Johnson, E. and Chadderton, L.T., *Anion voidage and the void superlattice in electron irradiated CaF_2*, *Radiation Effects* **79** (1983), no. 1-4 183–233.

[15] R. E. Thoma, *Cation size effects in complex fluoride compound formation*, *Inorganic Chemistry* **1** (1962), no. 2 220–226.

[16] J. Barth, R. L. Johnson, M. Cardona, D. Fuchs, and A. M. Bradshaw, *Dielectric function of* CaF_2 *between 10 and 35 eV*, *Phys. Rev. B* **41** (Feb, 1990) 3291–3294.

[17] G. W. Rubloff, *Far-Ultraviolet Reflectance Spectra and the Electronic Structure of Ionic Crystals*, *Phys. Rev. B* **5** (Jan, 1972) 662–684.

[18] "Calcium Fluoride crystal properties." `http://crystran.co.uk/optical-materials/calcium-fluoride-caf2`. Accessed: 30/08/2012.

[19] P. Denham, G. Field, P. Morse, G. Wilkinson, P. Denham, G. Field, P. Morse, and G. Wilkinson, *Optical and dielectric properties and lattice dynamics of some fluorite structure ionic crystals*, *Proceedings of the Royal Society of London. A. Mathematical and Physical Sciences* **317** (1970), no. 1528 55–77.

[20] S. J. Collocott and J. G. Collins, *Low-temperature heat capacity of alkaline-earth fluorides: SrF_2, BaF_2*, *Journal of physics. C. Solid state physics* **16** (1983), no. 32 6179–6184.

[21] J. A. Harrington and C. T. Walker, *Phonon Scattering by Point Defects in CaF_2, SrF_2 and BaF_2*, *Phys. Rev. B* **1** (Jan, 1970) 882–890.

[22] R. O. Pohl, X. Liu, and E. Thompson, *Low-temperature thermal conductivity and acoustic attenuation in amorphous solids*, *Rev. Mod. Phys.* **74** (Oct, 2002) 991–1013.

[23] P. A. Popov, P. P. Fedorov, S. V. Kuznetsov, V. A. Konyushkin, V. V. Osiko, and T. T. Basiev, *Thermal conductivity of single crystals of $Ca_{1-x}Yb_x$ F_2 solid solutions*, in *Doklady Physics*, vol. 53, pp. 198–200, Springer, 2008.

[24] J.Rubio., *Doubly-valent rare-earth ions in halide crystals*, *Journal of Physics and Chemistry of Solids* **52** (1991), no. 1 101 – 174.

[25] D. J. Newman and B. Ng, *Crystal field handbook*. Cambridge University Press, 2000.

[26] B. Henderson and G. F. Imbusch, *Optical spectroscopy of inorganic solids*. Clarendon Press, Oxford, 1989.

[27] D. Bingham, A. Cormack, and C. Catlow, *Rigid-ion potentials for SrF_2, CaF_2 and GdF_3*, *Journal of Physics: Condensed Matter* **1** (1989) 1205.

[28] S. P. Vernon and M. B. Stearns, *Extended x-ray-absorption fine-structure study of Y^{3+} and Sr^{2+} impurities in CaF_2*, *Phys. Rev. B* **29** (Jun, 1984) 6968–6971.

[29] "Strontium Fluoride crystal properties." `http://www.crystran.co.uk/strontium-fluoride-srf2.htm`. Accessed: 20/08/2012.

[30] P. A. Popov, P. P. Fedorov, V. A. Konyushkin, A. N. Nakladov, S. V. Kuznetsov, V. V. Osiko, and T. T. Basiev, *Thermal conductivity of single crystals of $Sr_{1-x}Yb_x$ F_2 solid solution*, in *Doklady Physics*, vol. 53, pp. 413–415, Springer, 2008.

[31] W. H. Baur and A. A. Khan, *Rutile-type compounds. IV. SiO_2, GeO_2 and a comparison with other rutile-type structures*, *Acta Crystallographica Section B: Structural Crystallography and Crystal Chemistry* **27** (1971), no. 11 2133–2139.

[32] H. Manaa, Y. Guyot, and R. Moncorge, *Spectroscopic and tunable laser properties of* Co^{2+}*-doped single crystals*, *Phys. Rev. B* **48** (Aug, 1993) 3633–3645.

[33] Y. Suzuki, W. A. Sibley, O. H. El Bayoumi, T. M. Roberts, and B. Bendow, *Optical properties of transition-metal ions in zirconium-based metal fluoride glasses and* MgF_2 *crystals*, *Phys. Rev. B* **35** (Mar, 1987) 4472–4482.

[34] R. Nistora, L. Andreici, and N. Avram, *Comparative Study between Energy Levels of Cr^{3+} and CO^{2+} Ions Doped in MgF_2 Crystal*, *Acta Physica Polonica-Series A General Physics* **19** (2009), no. 4 538.

[35] M. Scrocco, *Electron-energy-loss and x-ray photoelectron spectra of* MgF_2, *Phys. Rev. B* **33** (May, 1986) 7228–7231.

[36] A. Duncanson and R. Stevenson, *Some properties of magnesium fluoride crystallized from the melt*, *Proceedings of the Physical Society* **72** (1958), no. 6 1001.

[37] G. R. Hunt, C. H. Perry, and J. Ferguson, *Far-Infrared Reflectance and Transmittance of Potassium Magnesium Fluoride and Magnesium Fluoride*, *Phys. Rev.* **134** (May, 1964) A688–A691.

[38] D. S. McClure and Z. Kiss, *Survey of the Spectra of the Divalent Rare-Earth Ions in Cubic Crystals*, *The Journal of Chemical Physics* **39** (1963) 3251.

[39] E. Loh, $4f^n \rightarrow 4f^{n-1}5d^1$ *Spectra of Rare-Earth Ions in Crystals*, *Physical Review* **175** (1968), no. 2 533.

[40] P. Dorenbos, $f \rightarrow d$ *transition energies of divalent lanthanides in inorganic compounds*, *Journal of Physics: Condensed Matter* **15** (2003), no. 3 575.

[41] B. Wybourne, *Spectroscopic properties of rare earths*. Interscience Publishers, 1965.

[42] S. Lizzo, A. Meijerink, G. J. Dirksen, and G. Blasse, *On the luminescence of divalent ytterbium in* $KMgF_3$ *and* $NaMgF_3$, *Journal of Physics and Chemistry of Solids* **56** (1995), no. 7 959 – 964.

[43] M. Henke, J. Peron, and S. Kck, *Preparation and spectroscopy of* Yb^{2+}*-doped* $Y_3Al_5O_{12}$, $YAlO_3$, *and* $LiBaF_3$, *Journal of Luminescence* **87–89** (2000), no. 0 1049 – 1051.

[44] S. W. Bland and M. J. A. Smith, $4f^{14}$ *to* $4f^{13}5d$ *optical transitions of divalent ytterbium in the potassium and sodium halides*, *Journal of Physics C: Solid State Physics* **18** (1985), no. 7 1525.

[45] A. A. Kaplyanskii and P. P. Feofilov, *The spectra of divalent rare earth ions in crystals of alkaline earth fluorides. ii. europium and yttrium*, *Opt. Spectry.(USSR)(English Transl.)* **13** (1962).

[46] E. Reut, *Characteristics of the broadband luminescence of Eu and Yb ions in crystals with the fluorite structure*, *Optics and Spectroscopy* **45** (1978) 290–294.

[47] E. Reut, *Luminescence of divalent Eu and Yb ions in fluorite-type crystals*, *Optics and Spectroscopy* **40** (1976) 55.

[48] M. V. N. Kaplyanskii, A. A and S. P. L., *Spectra, kinetics, and polarization of the luminescence of CaF_2:Yb^{2+} crystals*, *Opt Spectroscopy* **41** (1976), no. 2 615619.

[49] I. Bersuker, *The Jahn-Teller Effect*. Cambridge University Press, 2006.

[50] C. Pedrini, D. S. McClure, and C. H. Anderson, *Photoionization thresholds of divalent rare earth ions in alkaline earth fluorides*, *The Journal of Chemical Physics* **70** (1979), no. 11 4959–4962.

[51] Pedrini, C., Pagost, P.O., Madej, C., and McClure, D.S., *Photoconductivité due à l'autoionisation de Ce^{2+} dans CaF_2, SrF_2 et BaF_2*, *J. Phys. France* **42** (1981), no. 2 323–330.

[52] D. S. McClure and C. Pedrini, *Excitons trapped at impurity centers in highly ionic crystals*, *Phys. Rev. B* **32** (Dec, 1985) 8465–8468.

[53] B. Moine, C. Pedrini, and B. Courtois, *Photoionization and luminescences in BaF_2:Eu^{2+}*, *Journal of Luminescence* **50** (1991), no. 1 31 – 38.

[54] S. Mahlik, B. Kukliński, Y. Yen, R. Meltzer, and M. Grinberg, *Pressure and temperature dependence of the emission in BaF_2:Eu and SrF_2:Eu*, *Journal of Luminescence* **128** (2008), no. 5 715–717.

[55] S. Lizzo, A. Meijerink, and G. Blasse, *Luminescence of divalent ytterbium in alkaline earth sulphates*, *Journal of Luminescence* **59** (1994), no. 3 185 – 194.

[56] S. Lizzo, E. P. Klein, N. Nagelvoort, R. Erens, A. Meijerink, and G. Blasse, *On the Quenching of the Yb^{2+} Luminescence in Different Host Lattices*, *Journal of Physics and Chemistry of Solids* **58** (1997), no. 6 963 – 968.

[57] S. H. M. Poort, W. P. Blokpoel, and G. Blasse, *Luminescence of Eu^{2+} in barium and strontium aluminate and gallate*, *Chemistry of Materials* **7** (1995), no. 8 1547–1551, [http://pubs.acs.org/doi/pdf/10.1021/cm00056a022].

[58] S. Poort and G. Blasse, *The influence of the host lattice on the luminescence of divalent europium* , *Journal of Luminescence* **72-74** (1997), no. 0 247 – 249.

[59] L. I and M. J, *Atomic Many-Body Theory*. Springer-Verlag Berlin Heidelberg, 2 ed., 1986.

[60] V. Hurtubise and K. F. Freed, *The algebra of effective hamiltonians and operators: exact operators*, *Adv. Chem. Phys.* **83** (1993) 465–541.

[61] B. H. Brandow, *Linked-Cluster Expansions for the Nuclear Many-Body Problem*, *Rev. Mod. Phys.* **39** (Oct, 1967) 771–828.

[62] I. Nicoara, M. Stef, and A. Pruna, *Growth of YbF_3-doped CaF_2 crystals and characterization of Yb^{3+}/Yb^{2+} conversion*, *Journal of Crystal Growth* **310** (2008), no. 7-9 1470–1475.

[63] V. Petit, P. Camy, J.-L. Doualan, X. Portier, and R. Moncorgé, *Spectroscopy of Yb^{3+} : CaF_2: From isolated centers to clusters*, *Phys. Rev. B* **78** (Aug, 2008) 085131.

[64] D. Oepts, A. Van der Meer, and P. Van Amersfoort, *The free-electron-laser user facility FELIX*, *Infrared Physics & Technology* **36** (1995), no. 1 297–308.

[65] B. N. Murdin, "FELIX Free Electron Laser." `http://personal.ph.surrey.ac.uk/~phs1bm/researchinterests.htm`.

[66] H. P. Freund and T. M. Antonsen, *Principles of free-electron lasers*. Springer, 1996.

[67] T. Kwan, J. Dawson, and A. Lin, *Free electron laser*, *Physics of Fluids* **20** (1977) 581.

[68] H. Frank, "FEL Operating Principle Schematic." `http://en.wikipedia.org/wiki/File:FEL_principle.png`.

[69] C. Crisis, "Photo of FELIX Undulators." `http://en.wikipedia.org/wiki/File:Undulator.FELIX.jpg`.

[70] W. Kaiser, W. G. Spitzer, R. H. Kaiser, and L. E. Howarth, *Infrared Properties of CaF_2 , SrF_2 and BaF_2*, *Phys. Rev.* **127** (Sep, 1962) 1950–1954.

[71] W. Hayes, M. C. K. Wiltshire, W. J. Manthey, and D. S. McClure, *Localized vibrational modes induced in CaF_2 by rare-earth impurities*, *Journal of Physics C: Solid State Physics* **6** (1973), no. 13 L273.

[72] B. Fultz, *Vibrational thermodynamics of materials*, *Progress in Materials Science* **55** (2010), no. 4 247–352.

[73] K. Lesniak, *Crystal fields and dopant-ligand separations in cubic centres of rare-earth ions in fluorites*, *Journal of Physics: Condensed Matter* **2** (1990) 5563.

[74] R. D. Cowan, *The theory of atomic structure and spectra*, vol. 3. University of California Press, 1981.

[75] T. S. Piper, J. P. Brown, and D. S. McClure, *fd and $f^{13}d$ Configurations in a Crystal Field, and the Spectrum of Yb^{2+} in Cubic Crystals*, *The Journal of Chemical Physics* **46** (1967), no. 4 1353–1358.

[76] C. Sunta, *Mechanism of phototransfer of thermoluminescence peaks in natural CaF_2*, *Physica Status Solidi (a)* **53** (1979), no. 1 127–135.

[77] C. Sunta, *A review of thermoluminescence of calcium fluoride, calcium sulphate and calcium carbonate*, *Radiation Protection Dosimetry* **8** (1984), no. 1-2 25–44.

[78] A. Pradhan and J. Rassow, *Radiation induced thermoluminescence in CaF_2:Tm detectors*, *Nuclear Instruments and Methods in Physics Research Section A: Accelerators, Spectrometers, Detectors and Associated Equipment* **255** (1987), no. 1 234–237.

[79] J. Qiu, Y. Shimizugawa, Y. Iwabuchi, and K. Hirao, *Photostimulated luminescence in Eu^{2+}-doped fluoroaluminate glasses*, *Applied Physics Letters* **71** (1997), no. 6 759–761.

[80] A. Krumpel, E. Van Der Kolk, D. Zeelenberg, A. Bos, K. Krämer, and P. Dorenbos, *Lanthanide 4f-level location in lanthanide doped and cerium-lanthanide codoped NaLaF by photo-and thermoluminescence*, *Journal of Applied Physics* **104** (2008) 073505.

[81] P. S. Senanayake, J. P. R. Wells, M. F. Reid, G. Berden, A. Meijerink, and R. J. Reeves, *Electron trap liberation in MgF_2 doped with Yb^{2+} using a two-color excitation experiment*, *Applied Physics Letters* **100** (2012) 041902–041902.

[82] O. E. Facey and W. A. Sibley, *Optical Absorption and Luminescence of Irradiated MgF$_2$*, *Phys. Rev.* **186** (Oct, 1969) 926–932.

[83] A. Scharmann, R. Grasser, and M. Böhm, *Thermally stimulated processes in solids*, *Journal of Electrostatics* **3** (1977), no. 1 1–14.

[84] M. F. Reid, P. S. Senanayake, J. P. R. Wells, G. Berden, A. Meijerink, A. J. Salkeld, C. Duan, and R. J. Reeves, *Transient photoluminescence enhancement as*

a probe of the structure of impurity-trapped excitons in CaF_2:Yb^{2+}, *Physical Review B* **84** (2011), no. 11 113110.

[85] P. S. Senanayake, J. P. R. Wells, M. F. Reid, G. Berden, A. Meijerink, and R. J. Reeves, *Impurity-trapped excitons and electron traps in CaF_2:Yb^{2+} and SrF_2:Yb^{2+} probed by transient photoluminescence enhancement*, *Journal of Luminescence* (2011).

[86] I. Izeddin, M. A. J. Klik, N. Q. Vinh, M. S. Bresler, and T. Gregorkiewicz, *Donor-State-Enabling Er-Related Luminescence in Silicon: Direct Identification and Resonant Excitation*, *Phys. Rev. Lett.* **99** (Aug, 2007) 077401.

[87] J. R. Cannon, *The one-dimensional heat equation*, vol. 23. Cambridge University Press, 1984.

[88] G. D. Smith, *Numerical solution of partial differential equations: finite difference methods*. Oxford University Press, USA, 1986.

[89] R. Pletcher, *Computational fluid mechanics and heat transfer*. Taylor & Francis, 1997.

[90] R. Courant, K. Friedrichs, and H. Lewy, *Über die partiellen Differenzengleichungen der mathematischen Physik*, *Mathematische Annalen* **100** (1928), no. 1 32–74.

[91] R. Courant, K. Friedrichs, and H. Lewy, *On the partial difference equations of mathematical physics*, *IBM Journal of Research and Development* **11** (1967), no. 2 215–234.

[92] A. Beer, *Bestimmung der Absorption des rothen Lichts in farbigen Flüssigkeiten*, *Ann. Phys. Chem* **86** (1852), no. 2 78–90.

[93] D. W. Marquardt, *An algorithm for least-squares estimation of nonlinear parameters*, *Journal of the Society for Industrial & Applied Mathematics* **11** (1963), no. 2 431–441.

[94] A. Kiel and W. B. Mims, *Linear Electric Field Effects in Paramagnetic Resonance for* Ce^{3+}-F^- *Tetragonal Sites in Ca*F_2*, Sr*F_2*, Ba*F_2, *Phys. Rev. B* **6** (Jul, 1972) 34–39.

[95] S. Lizzo, A. Meijerink, G. Dirksen, and G. Blasse, *Luminescence of divalent ytterbium in magnesium fluoride crystals*, *Journal of Luminescence* **63** (1995), no. 5 223–234.

[96] D. B. Gatch, D. M. Boye, Y. R. Shen, M. Grinberg, Y. M. Yen, and R. S. Meltzer, *Pressure dependence of the impurity-trapped exciton emission in BaF_2:Eu^{2+} and $Ba_xSr_{1-x}F_2$:Eu^{2+}.*, *Phys. Rev. B* **74** (Nov, 2006) 195117.

[97] R. F. Blunt and M. I. Cohen, *Irradiation-Induced Color Centers in Magnesium Fluoride*, *Phys. Rev.* **153** (Jan, 1967) 1031–1038.

[98] G. P. Summers, *Photoconductivity in MgF_2*, *Journal of Physics C: Solid State Physics* **8** (1975), no. 21 3621.

[99] A. Sergeev and P. Sergeev, *Individual induced absorption bands in MgF_2*, *Quantum Electronics* **38** (2008), no. 3 251–257.

[100] S. Petrov and I. Bailiff, *Determination of trap depths associated with TL peaks in synthetic quartz (350–550 K)*, *Radiation Measurements* **27** (1997), no. 2 185–191.

[101] P. Kivits and H. Hagebeuk, *Evaluation of the model for thermally stimulated luminescence and conductivity; reliability of trap depth determinations*, *Journal of Luminescence* **15** (1977), no. 1 1–27.

[102] S. Todd, *Heat capacities at low temperatures and entropies of magnesium and calcium fluorides*, *Journal of the American Chemical Society* **71** (1949), no. 12 4115–4116.

[103] M. Mostoller, *Phonon density of states for MgF_2*, *Journal of Physics and Chemistry of Solids* **32** (1971), no. 10 2449 – 2451.

[104] M. Elcombe and A. Pryor, *The lattice dynamics of calcium fluoride*, *Journal of Physics C: Solid State Physics* **3** (1970), no. 3 492.

[105] W. Hayes, M. Wiltshire, R. Berman, and P. Hudson, *Infrared absorption and thermal conductivity of CaF_2 containing heavy metal impurities*, *Journal of Physics C: Solid State Physics* **6** (1973), no. 7 1157.

[106] C. Kittel and H. Kroemer, *Thermal physics*. WH Freeman, 1980.

[107] F. Reif, *Fundamentals of statistical and thermal physics*, vol. 11. McGraw-Hill New York, 1965.

[108] H. U. Fuchs, *The dynamics of heat*, vol. 1. Springer, 1996.

[109] R. Haberman, *Elementary applied partial differential equations*. Prentice-Hall Englewood Cliffs, New Jersey, 1983.

[110] G. C. Hsiao and J. Saranen, *Boundary integral solution of the two-dimensional heat equation*, *Mathematical methods in the applied sciences* **16** (2005), no. 2 87–114.

[111] Y. Jarny, M. Ozisik, and J. Bardon, *A general optimization method using adjoint equation for solving multidimensional inverse heat conduction*, *International Journal of Heat and Mass Transfer* **34** (1991), no. 11 2911–2919.

[112] J. N. Reddy, *An introduction to the finite element method*, vol. 2. McGraw-Hill New York, 1993.

[113] R. Eymard, T. Gallouët, and R. Herbin, *Finite volume methods*, *Handbook of numerical analysis* **7** (2000) 713–1018.

[114] J. Crank and P. Nicolson, *A practical method for numerical evaluation of solutions of partial differential equations of the heat-conduction type*, in *Mathematical Proceedings of the Cambridge Philosophical Society*, vol. 43, pp. 50–67, Cambridge Univ Press, 1947.

[115] J. W. Thomas, *Numerical partial differential equations: finite difference methods*, vol. 1. Springer, 1995.

[116] W. H. Press, S. A. Teukolsky, W. T. Vetterling, and B. P. Flannery, *Numerical recipes 3rd edition: The art of scientific computing*. Cambridge University Press, 2007.

[117] L. Euler, *Institutionum calculi integralis*, vol. 1. imp. Acad. imp. Saènt., 1768.